



HAL
open science

Fine tuning of electrostatic interaction between nanomaterials in solutions and at interfaces: towards the fabrication of hybrid functional surfaces

Sribharani Sekar

► **To cite this version:**

Sribharani Sekar. Fine tuning of electrostatic interaction between nanomaterials in solutions and at interfaces: towards the fabrication of hybrid functional surfaces. Other. Université Sciences et Technologies - Bordeaux I, 2013. English. NNT: 2013BOR14811 . tel-00922989

HAL Id: tel-00922989

<https://theses.hal.science/tel-00922989>

Submitted on 1 Jan 2014

HAL is a multi-disciplinary open access archive for the deposit and dissemination of scientific research documents, whether they are published or not. The documents may come from teaching and research institutions in France or abroad, or from public or private research centers.

L'archive ouverte pluridisciplinaire **HAL**, est destinée au dépôt et à la diffusion de documents scientifiques de niveau recherche, publiés ou non, émanant des établissements d'enseignement et de recherche français ou étrangers, des laboratoires publics ou privés.

THÈSE

Présentée à

L'UNIVERSITÉ BORDEAUX 1

École Doctorale des Sciences Chimiques

Par

SRIBHARANI SEKAR

Pour obtenir le grade de

DOCTEUR

SPÉCIALITÉ: Physico-chimie de la Matière Condensée

Modulation de l'interaction électrostatique entre nanomatériaux en solutions et aux interfaces

Vers la génération de surfaces fonctionnelles hybrides

Soutenue le 9 Juillet 2013

En attente de l'avis de :	Mme. BOURGEAT-LAMI Elodie	Rapporteur
	M. STOLL Serge	Rapporteur

Devant la commission d'examen formée de :

Mme. BOURGEAT-LAMI Elodie	Directeur de recherches, CNRS, Lyon	Rapporteur
M. STOLL Serge	Professeur, Université de Genève	Rapporteur
M. CHAPEL Jean-Paul	Chargé de recherches CNRS	Directeur de thèse
M. BERRET Jean-François	Directeur de recherches CNRS, Paris	Examineur
Mme. QI Ling	Solvay, Shanghai	Examineur
M. LECOMMANDOUX Sébastien	Professeur, IPB Bordeaux 1	Examineur
M. RICHETTI Philippe	Directeur de recherches, CNRS	Examineur

Acknowledgements

The work presented in the manuscript was performed between the years February 2010 and May 2013 at Centre de Recherché Paul Pascal (CRPP), affiliated to University of Bordeaux 1. Here I would like to acknowledge many persons for their support for the past three years to tackle me this tough journey.

I am grateful to the French National Research Agency (A. N. R), who funded this “SUGHAR” project and CNRS, for providing me an excellent opportunity to pursue my doctorate under comfortable conditions. My special thanks to the *École Doctorale des Sciences Chimiques* for assisting me in the thesis submission procedures.

I am indebted to thank ***Dr. Elodie Bourgeat-Lami*** and ***Dr. Serge Stoll*** for dedicating their precious time to review the thesis and for their wise remarks and comments. I would also like to thank ***Dr. Jean-Paul Chapel***, ***Dr. Jean-François Berret***, ***Dr. Ling Qi***, ***Prof. Lecommandoux*** and ***Dr. Philippe Richetti*** for participating in the defense committee.

My deepest gratitude to my Ph.D mentor ***Dr. Jean-Paul Chapel***, for accepting me as a graduate student which really made lots of good changes in my life. Many thanks for his massive guidance throughout these three years and for taking care of me since the day I entered into France. He introduced me to various physical characterization techniques. His way of communication provoked me to improve the scientific communication skills. His contribution to my Ph.D and personal life is enormous. I have not only learned a lot about science from him but also how to face the problems in life. His guidance, humor, genuine nature, positive attitude, intelligence, innovative ideas, patience and organizing ability always encouraged me to proceed with the research in a right direction. The mutual understanding between us really worked well to bring out this robust thesis. He taught me to be an independent researcher. His trust on my results fueled me to be more confident and bold. I am highly impressed by his patience especially during the correction of manuscript and presentations. I have really enjoyed working with such an impressive personality that I will surely miss in the future.

Many thanks to ***Joanna Giermanska***, research engineer of our group. She helped me a lot to get along with the CRPP working environment. She was the person to introduce the QCM and contact angle measurements to me. She helped me a lot in carrying out the experiments. Her immense contribution to revise my manuscript was very important that

really helped to bring out this thesis in nice shape. Also she helped me a lot to find the apartment. It was very nice to talk both scientific and non-scientific topics with her. She really became very close to my heart by her love and care. I will never forget the nice time that I had with Joanna and her husband in Pyrenees. It was a nice opportunity to share many ideas with them. Thanks to them for making my stay more comfortable. I expect to see them in India soon.

I would also like to thank *Carlos Drummond*, for having fruitful discussions on synthetic chemistry. I thank for his kind invitation to the party. My special thanks to *Hassan Saadaoui* for helping me to carry out the AFM measurements.

I must thank our collaborator *Jean-Francois Berret*, for allowing me to carry out some ITC experiments in his lab in Paris and for spending time to have fruitful discussions on ITC.

I am very much thankful to *Ling Qi*, not only for introducing the Robotic experiments to me but also for having many useful discussions especially on QCM experiments. She was very friendly and patience to answer many of my questions and doubts on her thesis.

I would like to thank *Emeline Feltrin*, for her assistance in part of my experiments on nanotubes. Her simplicity and friendly attitude always attracts me to mingle with her. We really had a nice time together in Anglet. I wish her a bright future.

I must thank former members *Igor Siretanu*, *Jeanne Marie Lagleize* and *Anne-Sophie Bouchet* for sharing many scientific discussions. Thanks to them for their support and making my working day as pleasant.

Thanks to *Leticia Vitorazi* and *Nowel Ould-Moussa* for helping me to carry out the ITC experiments and also for making my stay comfortable in Paris.

I express my gratitude to all the members from departments of CRPP: reception, mechanic workshop, guardian, library, chemistry department, members of direction branch which help to proceed with university formalities etc, management, instrumentation, transform and computer service and all Ph.D students/postdoctoral fellows for extending their helping hands. Especially to Isabelle Ly and Alain Derre for their assistance in TEM and TGA experiments. I thank CREMEM for permitting me to make high resolution TEM images.

Many thanks to all my former teachers and professors from schools and colleges, especially to my former supervisor **Dr. Satish Patil** from Indian Institute of science, Bangalore, India. He was the first person to provide me the opportunity to enter into the research field. His motivation and encouraging words are the big support in my research carrier. My thanks also extend to my former lab members.

I thank all my well wishers/friends (the list never ends) from schools and colleges in India. This Ph.D program gave a nice opportunity to find many good friends in Europe.

Thousands of thanks to **Eswaran**, a real inspiration in my life. No words to explain his love and care towards me especially on my health. His immense presence is one of the biggest strength for me to pass the hardest time of Ph.D. we have shared several scientific discussions especially on synthetic chemistry. That really helped me a lot in formulating the nanomaterials. His humor sense kept me out of depression. I am really very happy and lucky to continue my life journey with him. I wish him all the best for his thesis.

Finally, my beloved dedication to my family. A special thanks to my mother **Amutha**, the most adorable and extraordinary person to me in the world. She really sacrificed many things for me. I dedicate all my achievements to her. Love you mom!!! Thanks to my father **Sekar**, the first hero in my life. He always taught me to be bold in tough situations. I thank my parents for allowing me to come out of India to make my carrier as I wish and for having trust on me. I thank my lovable and charming sister **Sudha** for her support. She is like my best friend. She helped me to manage with many problems. I wish her a very happy and bright future.

Experience makes one modified

Training makes one qualified, but involvement alone makes everyone satisfied!

So do all work with involvement.

Sribharani Sekar

Pessac, July, 2013

Introduction générale

Au cours des deux dernières décennies, un grand nombre de travaux ont été consacrés à la formation de complexes de polyélectrolytes de charges opposées (PEC). Certains des facteurs clés régissant la formation de PEC tels que la concentration de polyions, la longueur de la chaîne, le rapport de mélange, la température, le pH ou la force ionique ont été examinés pour de nombreux systèmes de polyélectrolytes différents.

Afin d'affiner cette tendance, ces dernières années l'attention a été portée à d'autres espèces de charges opposées tels que les copolymères à blocs double-hydrophiles, les tensioactifs, les dendrimères, les protéines, les nanoparticules et plus récemment les matériaux hybrides. En effet, ces matériaux combinent à la fois des attributs du monde inorganique comme une forte rigidité, une sensibilité magnétique, une meilleure stabilité thermique et des caractéristiques optiques et mécaniques des nanoparticules par exemple et du monde organique comme une flexibilité et une fonctionnalité accrue des macromolécules ou autres polymères. Ces matériaux peuvent offrir un très haut degré de polyvalence en termes de structure, de fonctionnalité et de modularité.

En particulier, la complexation de nanoparticules inorganiques et de polymères organiques a généré beaucoup de travaux en raison des très nombreuses applications potentielles dans divers domaines scientifiques et technologiques comme la science des matériaux, les revêtements, l'encapsulation et la délivrance de principes actifs, la photonique et l'imagerie médicale.

Au-delà des matériaux en volume (3D), la génération de surfaces fonctionnelles hybrides modulables a attiré récemment beaucoup d'intérêt car elle permet de créer des interfaces dites intelligentes alliant avantageusement les propriétés des deux types de briques élémentaires organiques/inorganiques. La génération de ce type de surfaces fonctionnelles à l'échelle nanométrique a déclenché le développement de nombreux procédés de fabrication et d'approches différentes. Déjà dans les années soixante, l'utilisation intelligente de l'interaction électrostatique entre briques élémentaires de charge opposée à une interface solide/liquide avait permis à *Iler* de générer des multicouches par adsorption séquentielle des nanoparticules cationiques et anioniques. Cette approche redécouverte dans les années 90 par *Decher* devint célèbre par la suite grâce à l'utilisation intelligente de complexes de polyélectrolytes. Grâce à l'avènement au cours de la dernière décennie de voies de synthèse de

nanoparticules inorganiques contrôlées et reproductibles, cette méthode dite *couche par couche* (ou *layer by layer* en anglais LbL) a littéralement explosé. Elle est devenu un outil de référence efficace pour élaborer des revêtements multi-échelles organiques/inorganiques, des colloïdes ou des capsules fonctionnels et modulables.

En accord avec cette philosophie, Ling Qi, une ancienne doctorante de l'équipe de Jean-Paul Chapel a mis en avant dès 2008 au travers d'études préliminaires, une nouvelle stratégie de fonctionnalisation de surface qualifiée de *croissance de couche à partir d'une surface* (ou *surface grown layer* en anglais SgL) afin de générer des surfaces fonctionnelles hybrides.

Cette étude préliminaire a démontré qu'il était possible de faire croître en une seule étape des couches hybrides relativement épaisses à une interface fluide/solide au travers d'une modulation très fine de l'interaction électrostatique entre briques élémentaires *stables* de charges opposées (*building blocks* en anglais BB) en fonction de la force ionique de la solution.

Récemment, deux laboratoires académiques, le Centre de Recherche Paul Pascal (CRPP) et Matière et Systèmes Complexes (MSC) associés à deux partenaires industriels, Rhodia et Alcan ont décidé d'étudier plus profondément cette nouvelle approche dans le cadre d'un projet soutenu par l'ANR P³N (Agence Nationale de la Recherche) dénommé SUGHAR autour de couches fonctionnelles hybride développées à partir d'un interface comme illustré dans la Figure I.1.

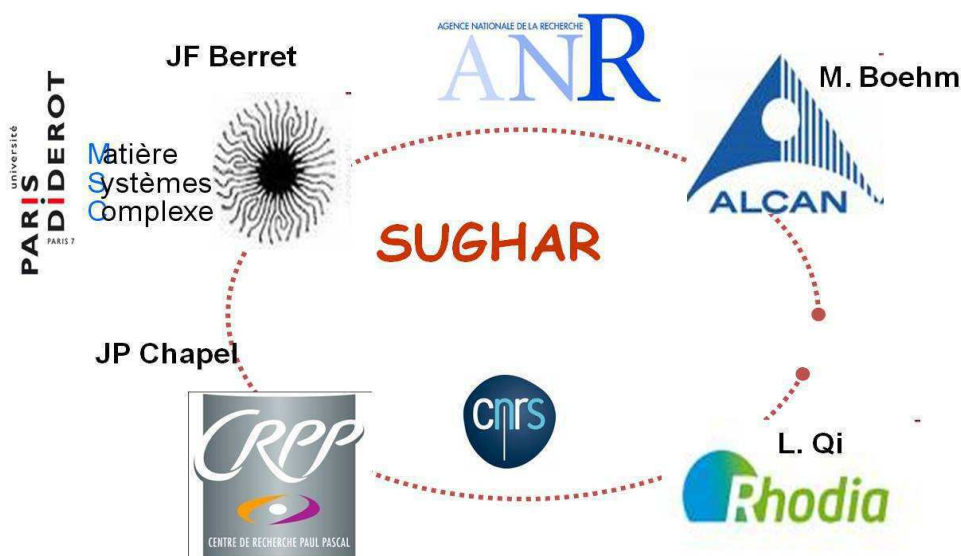


Figure I.1 : Vue schématique des différents partenaires du projet ANR P³N ANR.

Avant d'assembler des nanomatériaux de chargées opposées à une *interface* solide /liquide donnée, il est obligatoire de mieux comprendre et de contrôler leur interaction en *volume*. Dans ce travail de thèse, nous avons tout d'abord étudié plus en profondeur le concept de *transition dessalage* en provenance de la biologie moléculaire et mis récemment en avant dans le monde de la *matière molle* par le groupe de J.-F. Berret à MSC.

La force ionique peut être utilisée efficacement comme paramètre clé afin de contrôler finement l'interaction entre espèces de charges opposées en *volume* même si d'autres paramètres tels que le temps de réaction et d'homogénéisation de la solution jouent un rôle primordial. Des dispersions fortement salines contenant des briques élémentaires de charges opposées où les interactions électrostatiques sont complètement *éteintes* (écrantées) peuvent se transformer lentement en solution *réactive* et déclencher la formation de complexes au travers d'une diminution contrôlée de la force ionique par simple dialyse ou dilution. Le critère clé d'un réglage fin de la complexation électrostatique est alors l'utilisation de nanomatériaux stables à *force ionique élevée* ($> 1\text{M}$).

Malheureusement, la plupart des dispersions colloïdales sont stables qu'en deçà de 10^{-3} - 10^{-2}M en sel, où la stabilité est souvent assurée par simple répulsion électrostatique entre groupes tels que les hydroxydes, les nitrates, les chlorures etc. présents sur la surface des colloïdes lors de l'étape de synthèse. Une diminution de la longueur de Debye conduit à un affaiblissement notable de la force de répulsion électrostatique et à une agrégation/précipitation de la dispersion sous l'effet des interactions attractives de Van der Waals comme le montre la Figure I.2.

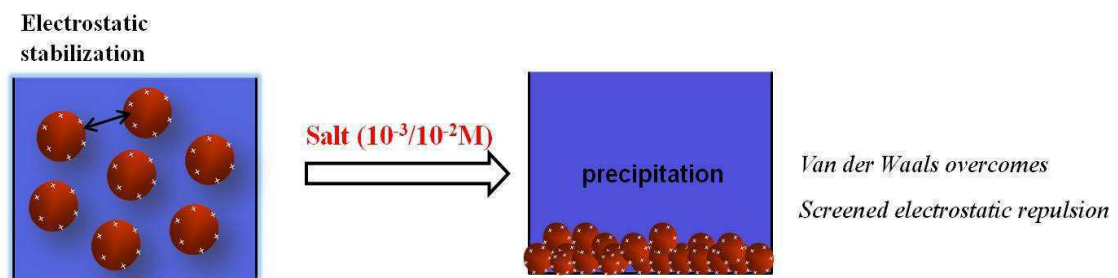


Figure I.2: Représentation schématique de la stabilité électrostatique de "colloïdes nus" en présence de sel.

Le second objectif de ce travail était de développer des dispersions colloïdales à la fois *cationiques* et *anioniques* stables à très faible longueur de Debye (force ionique importante). Cette étape a été réalisée avec succès par la fonctionnalisation de la surface de nanomatériaux (nanoparticules et nanotubes) par des polyélectrolytes faibles *cationiques* et *anioniques* (PEs) afin d'obtenir une stabilisation plus efficace par répulsion électro-stérique. Ce type de fonctionnalisation a ouvert la voie à la mise au point de la complexation entre différents types de nanomatériaux de charges opposées *en volume*, mais également à une *interface* solide /liquide.

Le diagramme représenté dans la figure I. 3 fournit un aperçu rapide des principales étapes suivies dans ce travail de thèse afin de développer des surfaces fonctionnelles grâce à des approches combinées LbL et SgL.

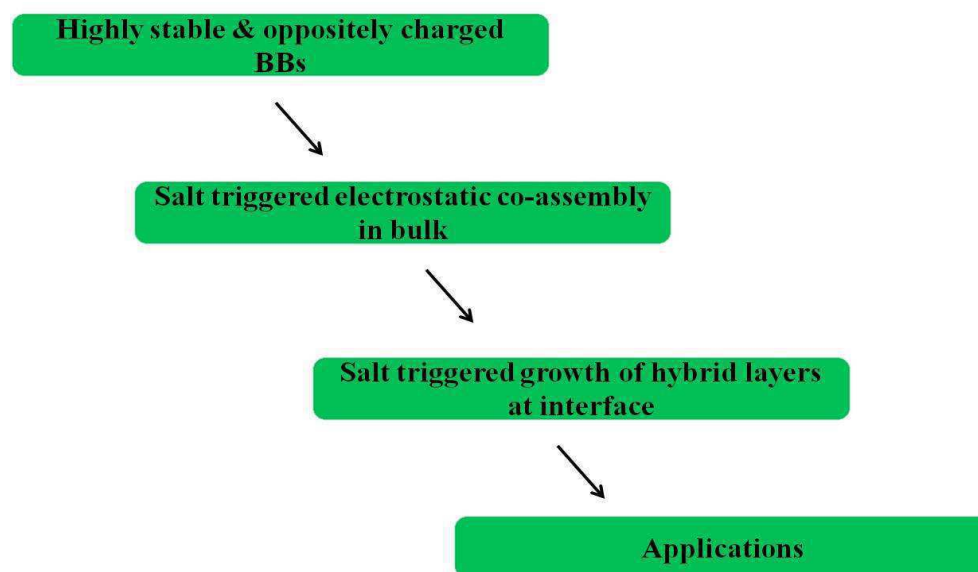


Figure I.3: *Étapes clés développées durant ce travail de thèse afin de générer des surfaces fonctionnelles hybrides à la fois par LbL et SgL.*

Abstract

In this manuscript, one-step bottom-up fabrication of “smart organic-inorganic hybrid functional layers” at a liquid/solid interface were fabricated via a novel surface functionalization pathway termed as “Surface Grown Hybrid Functional Layers” or *SgL* through fine tuning of electrostatic interaction between “highly stable” and oppositely charged nanomaterials as a function of ionic strength of the dispersion. Cationic and anionic nanomaterials based on different hybrid nanoparticles/nanotubes that are very stable towards high saline environment have been formulated. The electrostatic complexation between these oppositely charged nanomaterials has been studied in bulk and at an interface through the concept of “*desalting transition*” pathway. In a second step, the growth of functional hybrid layers directly from a substrate via the novel *SgL* approach was then compared with the conventional Layer-by-Layer approach (*LbL*). Finally the preliminary experiments have shown the potential applications of generated functional surfaces.

Keywords: Electrostatic complexation, hybrid nanomaterials, desalting transition, Layer-by-Layer (*LbL*), functional surfaces.

Centre de Recherche Paul Pascal

115, Avenue Schweitzer

33600 Pessac, Bordeaux - France

Résumé

Des couches fonctionnelles hybrides organiques/inorganiques ont été générées à une interface solide/liquide à l'aide d'une nouvelle technique de fabrication *ascendante (bottom-up)* dénommée *Croissance de Couche à partir d'une Surface (Surface Grown Layers - SgL)* grâce à une modulation très fine de l'interaction électrostatique entre nano-objets de *charges opposés* en fonction de la force ionique de la dispersion aqueuse. Différents nanoparticules/tubes à la fois cationiques et anioniques et très stables vis-à-vis d'un environnement fortement salin ont été développés. La complexation électrostatique entre ces nanomatériaux a été étudiée en solution et près d'une interface au travers du concept de "transition de dessalage". Dans un deuxième temps la croissance de couches hybrides à partir d'un substrat a été étudiée en comparant l'approche SgL et la méthode classique d'adsorption séquentielle *couche par couche (Layer by layer - LbL)*. Des expériences préliminaires ont montré le potentiel de cette approche dans le développement de substrats fonctionnels.

Mots clés : complexation électrostatique, nanomatériaux hybrides, transition de dessalage, couche par couche, surface fonctionnelle.

List of Abbreviations

Materials

SUGHAR: Surface Grown Hybrid Functional Layers
NPs: nanoparticles
PEs: polyelectrolytes
BBs: building blocks
CNPs : cerium oxide nanoparticles
MWCNTs: multi-walled carbon nanotubes
SiNPs: silica nanoparticles
MNIS: multiple non-interacting site
 I_s : ionic strength
 I_0 : initial ionic strength
 I_b : critical bulk ionic strength
Mw: molecular weight
IPEC: inter polyelectrolyte complex
NHS: N-hydroxysuccinimide
EDC.HCl: (1-ethyl-3-(3-dimethyl aminopropyl) carbodiimide hydrochloride)
TEOS: tetraethyl ortho silicate
TMOS: octadecyl trimethoxysilane
APTES: 3-aminopropyl triethoxysilane
EDA: Ethylenedimaine
PAA: poly (acrylic acid)
PDDAC: poly (diallyldimethyl ammonium chloride)
bPEI: branched polyethyleneimine
lPEI: linear polyethyleneimine
PSS: polystyrene sulfonate
PAH: poly(allylamine hydrochloride)
MAPTAC: poly(methacrylamidopropyl trimethyl ammonium chloride)
PTEA-b-PAM: poly(trimethylammonium ethylacrylate)-b-poly(acrylamide)
LbL: Layer-by-Layer
ELbL: electrostatic layer-by-layer
SgL: Surface grown Layers
PEM: polyelectrolyte mulilayers
PS: polystyrene
PET: polyethylene terephthalate
D₂O: deuterium oxide
HCl: hydrochloric acid
HNO₃: nitric acid
NH₄OH: ammonium hydroxide
NaOH: sodium hydroxide
KOH: potassium hydroxide
NH₄Cl: ammonium chloride
NaCl: sodium chloride
NaNO₃: sodium nitrate
w: weak
s: strong

hr: hour
mins: minutes
sec: seconds
DI water: De-ionized water
RT: room temperature

Probing techniques

ITC: Isothermal Titration Calorimetry
DLS: Dynamic Light Scattering
DDLS: Depolarized Dynamic Light Scattering
SLS: Static Light Scattering
QCM : Quartz Crystal Microbalance
AFM: Atomic Force Microscopy
TEM: Transmission Electron Microscopy
FT-IR: Fourier Transform Infrared spectroscopy
UV-Vis: Ultraviolet Visible spectroscopy
NMR: Nuclear Magnetic Resonance spectroscopy
TGA: Thermo Gravimetric Analysis

Parameters

IEP – isoelectric point
RPM – rotation per minute
Z – charge ratio
X – mixing/volume ratio
 R_H – hydrodynamic radius
 R_g – radius of gyration
 ΔH_b – enthalpy of binding
 K_b – binding constant
 ΔS_b – entropy of binding
n – stoichiometry
 ΔG_b – free energy of binding

Table of Contents

Acknowledgement	2
Abstract	5
Resume	6
List of Abbreviations	7
General Introduction	14
Chapter 0: Probing Techniques	22
Introduction	22
Isothermal Titration Calorimetry.....	22
Dynamic Light Scattering.....	24
Static Light Scattering.....	26
Depolarized Dynamic Light Scattering.....	28
Zeta potential.....	30
Streaming potential.....	31
Quartz Crystal Microbalance.....	33
Atomic Force Microscopy.....	35
References	38
PART I	39
Chapter 1: Electrostatic complexation fundamentals	40
Abstract	40
Introduction	41
Experimental section	46
Materials	46
Methods	47
Desalting concept in bulk.....	48
Isothermal Titration Calorimetry.....	49
Results & Discussions	54
Desalting transition of PEs.....	54
Isothermal titration calorimetry.....	58
Asymmetric System.....	58
Symmetric System.....	61
Conclusions	66
References	68
Chapter 2: Highly stable cationic & anionic building blocks (BBs)	71

Abstract	71
Introduction	73
Functionalization of Nanoparticles (NPs)	73
Covalent method.....	74
Non-Covalent method.....	78
General Materials	81
Probing techniques	82
Part I - Cerium oxide nanoparticles (CeO₂ NPs)	85
Introduction	85
Experimental Section	88
Synthesis of bare nanoparticle (CeO ₂).....	88
Synthesis of Anionic Ceria (CPAA _{2k}).....	88
Synthesis of Polyethyleneimine functionalized Ceria (CPEI _{25k}).....	89
Results and Discussions	92
Characterization of bare (CNPs) and anionic Ceria (CPAA _{2k}).....	92
Characterization of Polyethyleneimine functionalized nano ceria.....	96
Conclusions	104
Part II - Carbon Nanotubes (CNTs)	105
Introduction	105
Experimental section	109
Covalent functionalization of MWCNT with short ligands or oligomers.....	109
Non-covalent wrapping of MWCNTs with PEs.....	110
Covalent grafting of MWCNTs (MWCNT-PEs).....	110
Results and discussions	112
Covalent functionalization with short ligands.....	112
Non-covalent functionalization with wrapped PEs.....	115
Covalent functionalization with PEs.....	119
Conclusions	126
Part III - Silica Nanoparticles (SiNPs)	128
Introduction	128
Experimental Section	131
Synthesis of Silica nanoparticles (Stöber method).....	131
Synthesis of APTES functionalized Silica nanoparticles.....	132
Synthesis of Anionic Silica nanoparticles (SiO ₂ -PAA _{5k}).....	132
Synthesis of cationic silica nanoparticles (SiO ₂ -bPEI _{25k}).....	133

Results and Discussions	135
Characterization of APTES and PAA _{5k} functionalized SiNPs.....	135
Conclusions	140
References	141
Chapter 3: Fine tuning of electrostatic complexation between the oppositely charged BBs in bulk	149
Abstract	149
Introduction	150
Experimental section	151
Materials	151
Methods	151
Desalting transition.....	151
Desalting transition by Robotic platform.....	152
Isothermal titration Calorimetry.....	153
Results & Discussions	154
Ceria NPs system	154
Asymmetric system.....	154
Symmetric system.....	160
Carbon nanotubes systems	162
Silica NPs systems	165
Conclusions	168
References	170
PART II	171
Chapter 4: Growth of hybrid layers at a solution/substrate interface	172
Abstract	172
Introduction	173
Surface Grown Hybrid Functional Layers (SgL) approach.....	175
Experimental section	177
Materials	177
Methods	177
Quartz Crystal Microbalance (QCM) experiments	177
Layer-by-Layer self assembly (LbL).....	179
Surface grown hybrid functional layers (SgL).....	180

Results & Discussions	181
Layer-by-Layer self assembly	181
Ceria NPs.....	181
Carbon NTs system.....	188
Silica NPs system.....	194
Surface grown hybrid functional Layers (SgL)	196
Ceria NPs system.....	196
Carbon nanotubes system.....	206
Silica NPs system.....	207
Conclusions	210
References	212
PART III	215
Chapter 5: Toward Applications	216
Abstract	216
Introduction	217
Experimental Section	221
Materials	221
Methods	221
Ceria system.....	221
<i>Wetting properties</i>	221
<i>Anti-corrosive properties</i>	222
Carbon nanotubes system.....	224
<i>Conductivity measurements</i>	224
Results & discussions	226
Ceria system.....	226
<i>Wetting properties</i>	226
<i>Anti-corrosive properties</i>	227
Carbon nanotubes system.....	234
<i>Conductive properties</i>	234
Conclusions	236
References	237
Chapter 6: Conclusions and perspectives	239
General conclusions	239
Future perspectives	246
Appendix	249

Chapter2	249
Chapter3	256
Chapter5	258

General Introduction

Over the past two decades, a large body of work has been devoted to the formation of oppositely charged polyelectrolyte complexes (PECs). Some of the key factors governing the formation of PECs such as polyion concentration, chain length, mixing ratio, temperature, pH and ionic strength^[1-3] were discussed for many different polyelectrolyte systems. As a natural extension, attention has been given in recent years to other oppositely charged species such as block copolymers^[4], surfactants^[5, 6], dendrimers^[7], proteins^[8], nanoparticles^[9] and last but not least to hybrid materials^[10]. These materials indeed combine the attributes of both inorganic and organic worlds like the rigidity, magnetic, thermal stability and optical and mechanical features of the inorganic building blocks^[11, 12] and the flexibility and mechanical stability of the organic macromolecules^[13]. They can offer a very high degree of versatility in terms of structure, functionality and tunability. In particular, the complexation of inorganic nanoparticles and organic polymers has attracted much attention because of their numerous applications in various scientific and technological fields as material science, coating technology, drug delivery, photonics and medical imaging^[14, 15].

Beyond bulk materials, the generation of versatile hybrid functional surfaces has attracted recently a lot of interest as it enables the generation of smart interfaces combining the advantageous properties of both building blocks. The fabrication of such functional surfaces at nanometer level has triggered the development of many different approaches. In the sixties already, the smart use of the electrostatic interaction between oppositely charged building blocks at an interface was pioneered by Iler^[16] to generate *all*-nanoparticles multilayers through the sequential adsorption of cationic and anionic NPs, then rediscovered and brought to fame in the nineties by Decher^[17] using PE complexes. Through the advent of controlled and reproducible inorganic NP synthesis pathways during the last decade this so-called layer-by-layer (LbL) method has literally exploded. It became an efficient benchmark tool to elaborate multiscale organic/inorganic tunable functional coatings, colloids or capsules.

In line with this philosophy, Ling Qi, a former Ph.D student of Dr. Jean-Paul Chapel put forward in 2008 through very preliminary studies a novel surface functionalization strategy termed as “Surface grown Layer (or SgL) to generate hybrid functional surfaces. These preliminary studies showed that it was possible to grow in one step rather thick hybrid layers at a fluid/solid interface through fine tuning of the electrostatic interaction between

General introduction

“stable” and *oppositely* charged building blocks (BBs) as a function of the ionic strength of the dispersion.

Recently, two different academic laboratories, the Centre de Recherche Paul Pascal (CRPP) & Matière et Systèmes Complexes (MSC) together with two industrial partners, Rhodia and Alcan have decided to investigate more deeply this novel approach within the framework of an ANR (Agence Nationale de la Recherche) project named SUGHAR for Surface Grown Hybrid Functional layers illustrated in Figure I.1.

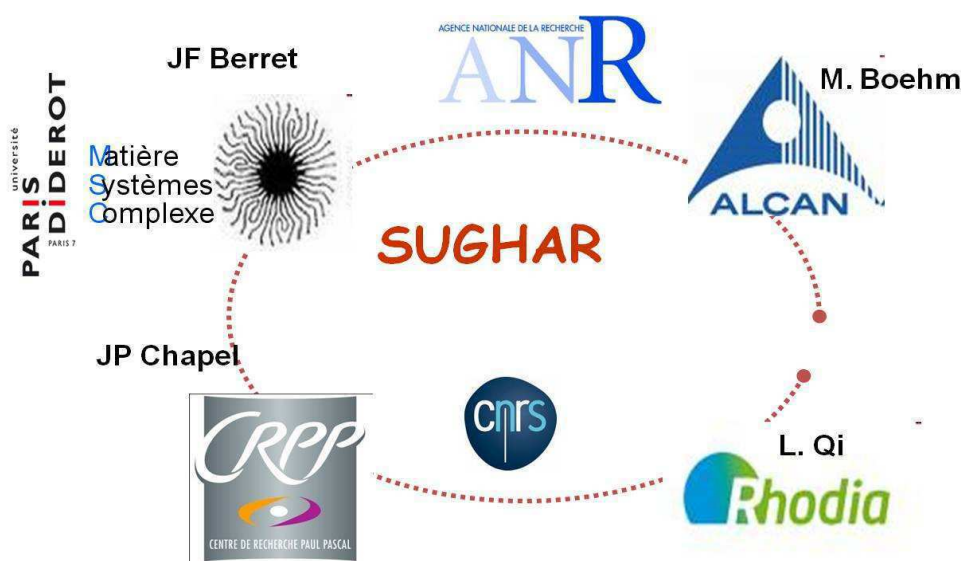


Figure I.1 : Schematic view of the different partner of the SUGHAR P³N ANR project

Before assembling any oppositely charged BBs at a given interface it is mandatory to understand and control their bulk interaction. In this work we have first investigated more deeply the *desalting transition concept* drawn from molecular biology and put forward recently in soft matter worlds by JF Berret’s group ^[18-20]. The ionic strength can be efficiently used as a key parameter to better control the interaction between oppositely charged species in bulk although other parameters such as reaction and homogenization time play a paramount role ^[21, 22]. Highly saline dispersions of BBs where electrostatic interactions are completely turned off (screened), can slowly be turned reactive and trigger the formation of complexes by a slow decrease of the ionic strength through simple dialysis or dilution. The key criterion to achieve a fine tuning of the complexation is then the use of very stable BBs at “*high ionic strength*” (> 1M).

General introduction

Unfortunately most of the colloidal dispersions are not stable beyond 10^{-3} - 10^{-2} M of salt, as stability is often provided through simple electrostatic repulsion between groups such as hydroxides, nitrates, chlorides etc present on the colloid surface during the synthesis step^[23-25]. Decreasing slightly the Debye screening length leads to aggregation/precipitation driven by attractive Van der Waals forces overwhelming electrostatic repulsions^[26] as depicted in Figure I.2.

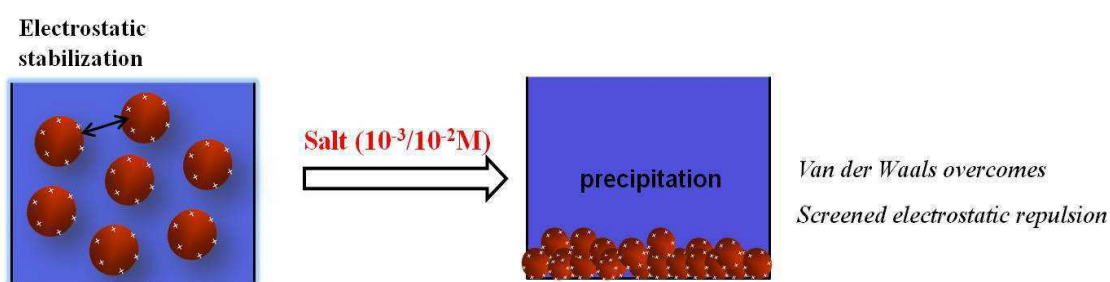


Figure I.2: Schematic representation of electrostatic stability of “bare colloids” in the presence of salt.

The second goal of this work was to develop both *cationic* and *anionic* colloidal dispersions stable at very small Debye lengths. This step has been successfully accomplished by functionalizing the surface of as-synthesized nanomaterials including nanoparticles/nanotubes with preferably cationic/anionic Polyelectrolytes (PEs) in order to obtain more efficient electrosteric stabilization. Functionalization opened the way to the fine-tuning of the complexation between different important type of BBs in the *bulk* but also at substrate/solution *interface*.

General introduction

The flow chart shown in Figure I. 3 provides a quick overview of the key steps followed in this PhD work to develop functional surfaces through *LbL* and *SgL* approaches.

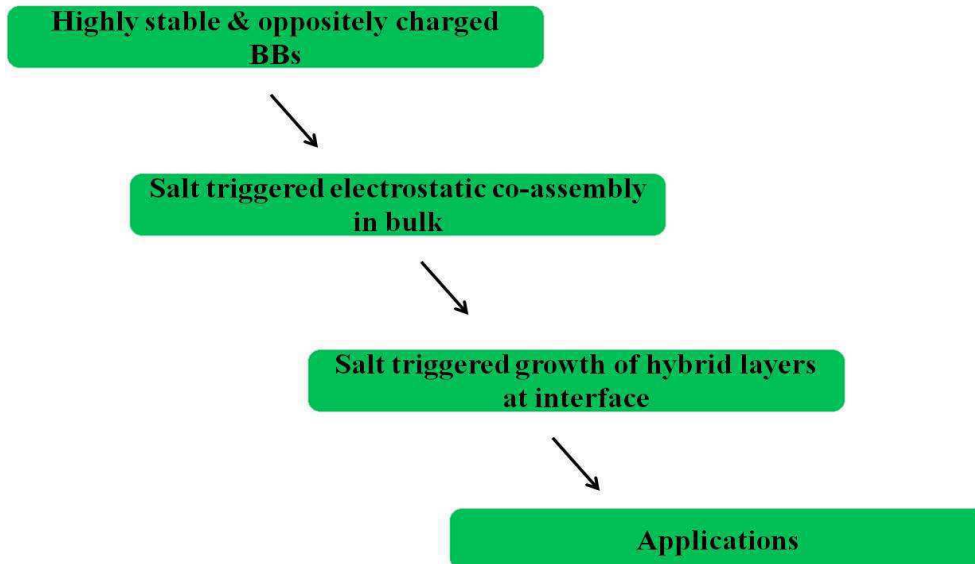


Figure I. 3: *Key steps to achieve functional surfaces.*

Outline of the manuscript

In line with the introduction the manuscript is divided into three parts. The first part (chapter 1, 2, 3) deals with the formulation and electrostatic complexation of oppositely charged components in solution. The fabrication of hybrid functional surfaces based on *LbL* and *SgL* strategy is presented in the second part (chapter 4). The third part highlights through preliminary experiments the potential of these two assembly approaches towards applications (chapter 5).

Chapter 0: *Probing techniques* – presents the basic principle of various characterization techniques and details sample preparation conditions.

Part I: Bulk complexation

In **Chapter 1**, we have investigated the “bulk desalting transition” concept between *pure* and oppositely charged PEs of “asymmetric” (weak/strong) and “symmetric” (weak/weak or strong/strong) systems to demonstrate the generality of this approach. Isothermal Titration Calorimetry (ITC) was carried out to shed some light on the mechanism(s) and the nature of the forces driving the polyelectrolyte complex formation in asymmetric and symmetric systems. This chapter serves as a base for chapter 3.

Chapter 2 describes the development of various highly stable cationic & anionic nanoscale hybrid building blocks of interest based on cerium oxide and silica nanoparticles and carbon nanotubes. This specific chapter is sub-divided into three parts.

I. Cerium oxide nanoparticles (CeO₂ NPs). The first part deals with the formulation of highly stable oppositely charged CeO₂ NPs. Ceria NPs electro-sterically stabilized by short anionic PAA brushes were prepared via precipitation-redispersion protocol based on “direct mixing” method. Highly stable cationic *b*PDI functionalized ceria NPs were synthesized from anionic ceria through the formation of covalent amide bonds via carbodiimide chemistry. The successful functionalization by PEs and the stability toward high ionic strength of the resultant hybrid materials were assessed by various probing techniques.

II. Carbon Nanotubes (CNTs). Functional cationic and anionic MWCNTs were synthesized through the surface modification of bare MWCNTs with short ligands and PEs

based on both covalent and non-covalent approaches. A nice scenario on the salt stability as a function of dispersants and functionalization approaches was put forward.

III. Silica nanoparticles (SiO₂ NPs). Anionic PAA and cationic *b*PEI functionalized SiO₂ NPs via carbodiimide chemistry were developed. The covalent attachment and stability aspects of PAA modified SiO₂ NPs were evaluated by different characterization techniques. Different synthetic strategies were put forward to obtain singlet and stable cationic *b*PEI covered SiO₂ NPs. A thorough characterization of “stable cationic silica” is still under investigation.

Chapter 3 is a combination of chapter 1 and 2. The desalting behavior foreseen in chapter 1 for the pure PEs, is here studied and generalized to hybrid BBs formulated in chapter 2. We have shown the possibility to fine tune in the bulk the interaction between *all*-nanoparticles/carbon nanotubes. The role of secondary forces (hydrophobic, H-bonding, acid-base) in the salt triggered co-assembly process was investigated.

Part II: Towards Functional Surfaces

In **Chapter 4** the “bulk desalting transition” concept was transferred to a solution/substrate interface to fabricate functional hybrid layers based on SgL and LbL complementary. Growth kinetics of both types of hybrid layers was investigated and monitored by Quartz Crystal Microbalance (QCM).

Part III: Towards applications

Chapter 5 highlights the preliminary experiments on the potential applications of hybrid layers based on LbL and SgL strategy to obtain anti-corrosive, conductive and superhydrophilic coatings respectively on aluminum, PET and glass substrates.

Conclusions & Perspectives

General conclusion and future perspectives were drawn in **chapter 6**.

Appendix

The appendix summarizes the extra experiments performed during this work and can serve to ameliorate future works.

References

1. Chollakup, R., et al., *Phase Behavior and Coacervation of Aqueous Poly(acrylic acid)-Poly(allylamine) Solutions*. *Macromolecules*, 2010. **43**(5): p. 2518-2528.
2. Sui, Z., J.A. Jaber, and J.B. Schlenoff, *Polyelectrolyte Complexes with pH-Tunable Solubility*. *Macromolecules*, 2006. **39**(23): p. 8145-8152.
3. Spruijt, E., et al., *Binodal Compositions of Polyelectrolyte Complexes*. *Macromolecules*, 2010. **43**(15): p. 6476-6484.
4. Kabanov, A.V., et al., *Soluble Stoichiometric Complexes from Poly(N-ethyl-4-vinylpyridinium) Cations and Poly(ethylene oxide)-block-polymethacrylate Anions*. *Macromolecules*, 1996. **29**(21): p. 6797-6802.
5. Mezei, A.I., et al., *Effect of Mixing on the Formation of Complexes of Hyperbranched Cationic Polyelectrolytes and Anionic Surfactants*. *Langmuir*, 2007. **23**(8): p. 4237-4247.
6. Pispas, S., *Complexes of Polyelectrolyte-Neutral Double Hydrophilic Block Copolymers with Oppositely Charged Surfactant and Polyelectrolyte*. *The Journal of Physical Chemistry B*, 2007. **111**(29): p. 8351-8359.
7. Miura, N., et al., *Complex Formation by Electrostatic Interaction between Carboxyl-Terminated Dendrimers and Oppositely Charged Polyelectrolytes*. *Langmuir*, 1999. **15**(12): p. 4245-4250.
8. Wen, Y.p. and P.L. Dubin, *Potentiometric Studies of the Interaction of Bovine Serum Albumin and Poly(dimethyldiallylammonium chloride)*. *Macromolecules*, 1997. **30**(25): p. 7856-7861.
9. Berret, J.-F., et al., *Polymer-Nanoparticle Complexes: From Dilute Solution to Solid State*. *The Journal of Physical Chemistry B*, 2006. **110**(39): p. 19140-19146.
10. Fresnais, J., et al., *Universal scattering behavior of coassembled nanoparticle-polymer clusters*. *Physical Review E*, 2008. **78**(4): p. 040401.
11. Nie, Z., A. Petukhova, and E. Kumacheva, *Properties and emerging applications of self-assembled structures made from inorganic nanoparticles*. *Nat Nano*, 2010. **5**(1): p. 15-25.
12. Shon, Y.-S., et al., *Stability and Morphology of Gold Nanoisland Arrays Generated from Layer-by-Layer Assembled Nanoparticle Multilayer Films: Effects of Heating Temperature and Particle Size*. *The Journal of Physical Chemistry C*, 2011. **115**(21): p. 10597-10605.
13. Liu, et al., *Morphology and Mechanical Properties of Multiwalled Carbon Nanotubes Reinforced Nylon-6 Composites*. *Macromolecules*, 2004. **37**(19): p. 7214-7222.
14. Zhang, X.-T., et al., *Self-Cleaning Particle Coating with Antireflection Properties*. *Chemistry of Materials*, 2005. **17**(3): p. 696-700.
15. Wang, Y., et al., *Templated Synthesis of Single-Component Polymer Capsules and Their Application in Drug Delivery*. *Nano Letters*, 2008. **8**(6): p. 1741-1745.
16. Iler, R.K., *Multilayers of colloidal particles*. *Journal of Colloid and Interface Science*, 1966. **21**(6): p. 569-594.
17. Decher, G., *Fuzzy Nanoassemblies: Toward Layered Polymeric Multicomposites*. *Science*, 1997. **277**(5330): p. 1232-1237.
18. Fresnais, J., et al., *Electrostatic Co-Assembly of Iron Oxide Nanoparticles and Polymers: Towards the Generation of Highly Persistent Superparamagnetic Nanorods*. *Advanced Materials*, 2008. **20**(20): p. 3877-3881.
19. Fresnais, J., C. Lavelle, and J.F. Berret, *Nanoparticle Aggregation Controlled by Desalting Kinetics*. *The Journal of Physical Chemistry C*, 2009. **113**(37): p. 16371-16379.
20. Yan, M., et al., *Magnetic Nanowires Generated via the Waterborne Desalting Transition Pathway*. *ACS Applied Materials & Interfaces*, 2011. **3**(4): p. 1049-1054.
21. Qi, L., et al., *Influence of the Formulation Process in Electrostatic Assembly of Nanoparticles and Macromolecules in Aqueous Solution: The Mixing Pathway*. *The Journal of Physical Chemistry C*. **114**(30): p. 12870-12877.

General introduction

22. Qi, L., et al., *Influence of the Formulation Process in Electrostatic Assembly of Nanoparticles and Macromolecules in Aqueous Solution: The Interaction Pathway*. The Journal of Physical Chemistry C, 2010. **114**(39): p. 16373-16381.
23. Chen, H.-I. and H.-Y. Chang, *Synthesis of nanocrystalline cerium oxide particles by the precipitation method*. Ceramics International, 2005. **31**(6): p. 795-802.
24. Pottier, A., et al., *Synthesis of brookite TiO nanoparticles by thermolysis of TiCl₄ in strongly acidic aqueous media*. Journal of Materials Chemistry, 2001. **11**(4): p. 1116-1121.
25. Overbeek, J.T.G., *Recent developments in the understanding of colloid stability*. Journal of Colloid and Interface Science, 1977. **58**(2): p. 408-422.
26. Lanning, O.J. and P.A. Madden, *Screening at a Charged Surface by a Molten Salt*. The Journal of Physical Chemistry B, 2004. **108**(30): p. 11069-11072.

Chapter 0: Probing Techniques

Introduction

In this chapter, we have described the basic principles of different characterization techniques such as Isothermal Titration Calorimetry (ITC), Dynamic and Static Light Scattering (DLS & SLS), Depolarized Dynamic Light Scattering (DDLS), Zeta potential, Quartz Crystal Microbalance (QCM), and Atomic Force Microscopy (AFM). The conditions involved for the sample preparation are detailed. It is suggested that the readers can easily skip this chapter and can refer when it is required.

Isothermal Titration Calorimetry (ITC)

Isothermal Titration Calorimetry (ITC) is a technique widely used to understand the mechanism behind the interaction of oppositely charged components via thermodynamic parameters. In a typical ITC experiment, ligand (L) is titrated into polyelectrolytes PEs (P) solution. [L] and [P] indicates the concentrations of ligands and PEs respectively and V_0 is the volume of the sample cell holding the PEs^[1]. During the injection of ligand into oppositely charged PEs, physicochemical interaction occurs between them. Depending on the type of interaction either the heat is released or absorbed that is proportional to the amount of binding. The raw thermogram was analysed by non-linear least-square fitting method to fit a model to the data. In our binding experiments, we have used multiple non-interacting site (MNIS) model, as the PEs comprises multiple anchoring sites^[1]. In this model, binding of ligand at one site is independent of rate of occupation of other sites of the same PEs. The non-linear least-square along with the MNIS model determined the better values of fitting parameters such as binding constant (K_b), stoichiometry (n) and enthalpy of binding (ΔH_b)^[1],^{2]}. In this model, the equilibrium binding constant K_b is given by^[3],

$$K_b = \frac{\Theta}{(1-\Theta)[L]} \quad (1)$$

In which Θ is the fraction of sites (on the PEs) occupied by ligand, [L] is the free concentration of ligand. The relationship between total $[L_t]$ and free [L] concentration is given by,

$$[L] = [L_t] - n\Theta [P_t] \quad (2)$$

Probing Techniques

Where P_t is the total concentration of PEs and n is the number of binding sites or stoichiometry of the process. By substituting 2 in 1, the quadratic equation (3) is expressed as,

$$\Theta^2 - \Theta \left(1 + \frac{[L_t]}{n[P_t]} + \frac{1}{nK[P_t]}\right) + \frac{[L_t]}{n[P_t]} = 0 \quad (3)$$

The total heat Q associated with the binding of number of moles of ligands with the V_0 volume of $[P_t]$ is given by,

$$Q = n\Theta[P_t]\Delta H_b V_0 \quad (4)$$

Where ΔH_b is enthalpy of binding. Combining the equations 3 & 4, the total heat content involved in the reaction can be expressed as,

$$Q = \frac{n[P_t]\Delta H_b V_0}{2} \left[1 + \frac{[L_t]}{n[P_t]} + \frac{1}{nK_b[P_t]} - \sqrt{\left(1 + \frac{[L_t]}{n[P_t]} + \frac{1}{nK[P_t]}\right)^2 - \frac{4[L_t]}{n[P_t]}} \right] \quad (5)$$

As we calculated the concentration of ligand and PEs as a function of charges, it is convenient to introduce charge ratio $Z = [L_t] / [P_t]$ in the above equation. To simplify the above expression, the term $r = 1/K_b[P_t]$ was introduced and the equation (5) reduced to^[1],

$$Q(Z) = \frac{1}{2} \Delta H_b \left(1 + \frac{n - Z - r}{\sqrt{(n + Z + r)^2 - 4Zn}} \right) \quad (6)$$

From the above equation, K_b , ΔH_b and n were derived. The free energy of binding ΔG_b is then derived from K_b via the equation 7. The entropy ΔS of binding were determined from the enthalpy and free energy of binding through the well known relation (8)^[1,3].

$$\Delta G = -RT \ln K_b \quad (7)$$

$$\Delta S = (\Delta H_b - \Delta G) / T \quad (8)$$

Dynamic Light Scattering (DLS)

Dynamic light scattering (also known as photon-correlation spectroscopy) is a powerful technique to determine the size distribution of the colloidal particles. When the light hits the spherical particles of size much smaller ($\lambda/10$ or around 60 nm) than the wavelength ($\lambda = 540$ nm) of light, the scattered intensity is equal in all the directions, known as Rayleigh scattering. When the particle sizes are larger, a distortion in the scattering direction occurs, known as Mie scattering. For our experiments, Rayleigh scattering theory is applicable, as the spherical particles of the size in the range of 60 nm were subjected to DLS.

The DLS technique measures the time-dependent fluctuations in the scattering intensity I resulting from the Brownian motion of the particles when illuminated by a laser beam. The scattered intensities are then transformed by a correlator into autocorrelation function $g^1(t)$. From which, the diffusion coefficient (D) and in second step the size of the particles can be computed. The first order autocorrelation function as a function of wave vector q and delay time τ can be expressed as follows^[4],

$$g_I^{(1)}(q, \tau) = \lim_{T \rightarrow \infty} \frac{1}{T} \int dt I_1(q, t) \cdot I_1(q, t + \tau) \equiv \langle I_1(q, t_0) \cdot I_1(q, t_0 + \tau) \rangle \quad (9)$$

$$q = \frac{4\pi n}{\lambda} \sin\left(\frac{\theta}{2}\right) \quad (10)$$

Where λ is the wavelength, θ is the scattering angle and n is the refractive index of the medium. The function g^1 measures how quick the particles move away from the initial state due to diffusion. In other words the correlation of their movement decays exponentially with the delay time τ . For the monodispersed particles this decay is a single exponential and the expression can be written as follows,

$$g^1(q, \tau) = e^{(-\Gamma\tau)} = e^{(-q^2 D_t \tau)} \quad (11)$$

Where Γ is the decay rate and related to the translational diffusion coefficient of the particles as follows,

$$D_t = \Gamma(c)/q^2 \text{ or } \Gamma = q^2 D_t = \tau^{-1} \quad (12)$$

Small spherical particles do not possess any angular dependence and therefore the measurement can be done at one angle preferably at $\theta = 90^\circ$. The translational diffusion

Probing Techniques

coefficient can be determined from the equation (12) by substituting θ as 90° . Due to the angular dependence of large particles, it is recommended to perform multi-angle analysis. In such cases, the slope of the plot of Γ vs q^2 results diffusion coefficient. On the other hand, as the larger particles has two contributions such as rotational and translational diffusion coefficient, (termed as collective diffusion coefficient D_c), concentration must be taken into account. In such case, D_c expressed as follows,

$$D_c = D_0 (1 + A_D C) \quad (13)$$

D_0 is the self diffusion coefficient extrapolated at zero concentration and A_D is the second virial coefficient, its sign explains the type of interaction either repulsive or attractive between the particles. In all our experiments, the A_D was positive indicating the repulsive interparticle interactions and results stable solution.

From the self diffusion coefficient, the hydrodynamic radius (R_H) of the particles is calculated through the Stokes- Einstein equation^[5],

$$R_H = \frac{K_B T}{6\pi\eta D_0} \quad (14)$$

Here K_B is the Boltzmann's constant (1.38×10^{-23} J/K), T is the temperature in Kelvin (298 K) and η is the viscosity of the solvent (water, 0.89×10^{-3} Pa.s).

Polydispersity index is used to describe the width of the particle size distribution and it can be related to the standard deviation (σ) of the hypothetical Gaussian distribution of the single particle size divided by the average hydrodynamic radius of the collection of particles (dimers or trimers)^[4],

$$PDI = \frac{\sigma^2}{Z^2} \quad (15)$$

Z is the average size of the cumulants hydrodynamic radius.

For the polydispersed samples, the $g^{(1)}$ function is summation of different exponential decay functions^[4],

$$g^{(1)}(q, t) = \int A(\Gamma) e^{(-\Gamma t)} d\Gamma \quad (16)$$

Probing Techniques

Here $A(\Gamma)$ is the normalized distribution decay rates of different diffusion coefficients and $\Gamma = Dq^2$. From D , by using Stokes-Einstein relationship (14), hydrodynamic radius (R_H) can be determined.

DLS measurements were performed on a BI-9000AT Brookhaven spectrometer. The light source is a laser beam with an incident wavelength of 540 nm. The sample vial made of glass was cleaned with ethanol and dried completely before filling up with the sample solution. In order to avoid interparticle collision, the experiment was performed with low concentration ranging from 0.01 wt% to 0.1 wt%. The thermoregulation is done by water bath and all the experiments were performed at $T = 20^\circ\text{C}$. The autocorrelation function of the scattered intensities was analyzed with the help of CONTIN fitting procedure developed by Steven provencher.

Static Light Scattering (SLS)

In similar to DLS, the particles in the sample are illuminated by laser beam. But instead of measuring time dependent fluctuations, SLS measures the time-averaged scattered intensity of light. From the scattered intensity, Rayleigh ratio R_θ was obtained as follows,

$$R_\theta = \frac{I_A n_0^2}{I_T n_T^2} R_T \sin \theta \quad (17)$$

I_A : residual scattering intensity (sample intensity-solvent intensity)

I_T : toluene scattering intensity

n_T : toluene refractive index

R_T : Rayleigh ratio of toluene

From R_θ we can determine the molecular weight (M_w) and second virial coefficient (A_D) by Zimm representation,

$$\frac{Kc}{R_\theta(c)} = \frac{1}{M_w} + \left[\frac{q^2 R_g^2}{3} \right] + 2A_D c \quad (18)$$

c : concentration

K : optical constant as defined below,

Probing Techniques

$$K = \frac{4\pi^2}{\lambda_0^4 N_A} \left(n_0 \frac{dn}{dc} \right)^2 \quad (19)$$

N_A : Avogadro's constant

λ_0 : laser beam wavelength

n_0 : solvent refractive index

dn/dc : refractive index increments of different solutions were measured using an BELLINGHAM & STANLEY model RF840 refractive index detector in range $c = 10^{-3}$ to 1 wt %.

For very dilute concentrations, the equation (18) reduced to,

$$R_\theta = K M_w C \quad (20)$$

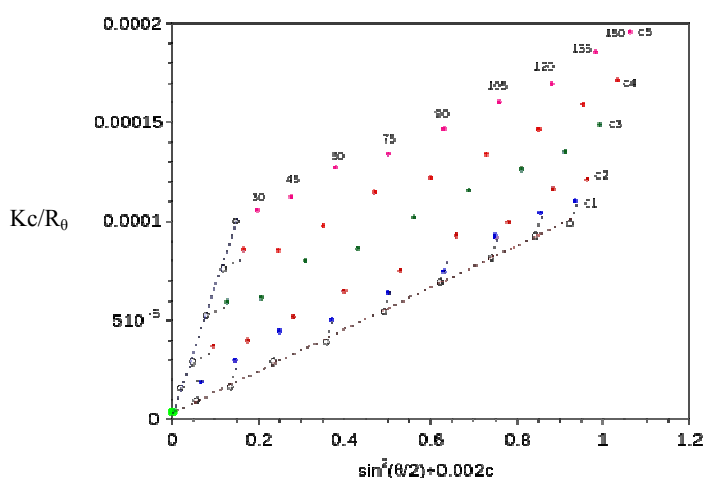


Figure 0. 1: A typical Zimm plot (from Wikipedia).

A typical Zimm plot is shown in the Figure 0. 1, where the experimental points are at all grid points except along the lower line ($\theta = 0$) and the left most line ($c = 0$). Connecting all the grid lines and extrapolating to the lower-left corner, the intercept point gives the M_w (intercept = $1/M_w$). The slopes of the $\theta = 0$ line and the $c = 0$ line respectively gives the radius of gyration (R_g) and second virial coefficient (A_D).

Depolarized Dynamic Light Scattering (DDLs)

Carbon nanotubes (CNTs) cannot be characterized by conventional dynamic light scattering, since their aspect ratio is high, therefore it is necessary to measure both length and diameter which is possible via depolarized dynamic light scattering (DDLs)^[6]. Conventional DLS measures the autocorrelation function of the scattered light with polarization parallel to the incident beam. From the autocorrelation function, translational diffusion coefficient (D_t) is determined and then the hydrodynamic radius can be computed from D_t by using Stokes-Einstein relation.

However in DDLs, the time-dependent fluctuations in the scattered light with polarization perpendicular to the incident beam from the Brownian motion of anisotropic CNTs provide additional information about the rotational (D_r) diffusion coefficient. Thus in DDLs, both polarized ($g_{2,vv}$) and depolarized ($g_{2,vH}$) second order autocorrelation functions can be measured independently at different scattering angles (θ) and are expressed as follows^[7],

$$g_{2,vv}(q,t) = \langle I_{vv}(q,t)I_{vv}(q,0) \rangle / \langle I_{vv} \rangle^2 \quad (21)$$

$$g_{2,vH}(q,t) = \langle I_{vH}(q,t)I_{vH}(q,0) \rangle / \langle I_{vH} \rangle^2 \quad (22)$$

In these equations, q is the scattering vector (equation 10), I is the scattering intensity of light. vv and vH represent the scattering of polarized and depolarized light respectively. As the correlation function decays exponentially with time, the above equations reduced to,

$$g_{2,vv}(q,t) = \exp(-2t/\tau_{vv}) = \exp(-2\Gamma_{vv}t) \quad (23)$$

$$g_{2,vH}(q,t) = \exp(-2t/\tau_{vH}) = \exp(-2\Gamma_{vH}t) \quad (24)$$

τ_{vv} and τ_{vH} are the delay times, extracted from the autocorrelation function of the polarized and depolarized light scattering by the CONTIN process and its inverse related to polarized and depolarized decay rate. The polarized (Γ_{vv}) and depolarized (Γ_{vH}) decay rates are related to translational and rotational diffusion coefficient respectively as follows,

$$\Gamma_{vv} = D_t q^2 \quad (25)$$

$$\Gamma_{vH} = D_t q^2 + 6D_r \quad (26)$$

Probing Techniques

From the translational (D_t) and rotational (D_r) diffusion coefficients, the half-length (a) and half-diameter (b) can be determined by slender body theory^[7],

$$D_t = \frac{K_B T}{6\pi\eta a} \left[\ln\left(\frac{2a}{b}\right) + \ln 2 - 1 \right] \quad (27)$$

$$D_r = \frac{3K_B T}{8\pi\eta a^3} \left[\frac{\left(\frac{a}{b}\right)^2 \left(\ln\left(\frac{a}{b}\right)\right)^2}{\left(\frac{a}{b}\right)^2 \left(\ln\left(\frac{a}{b}\right)\right) (\ln 2 - 1) + 0.65 \left(\ln\left(\frac{a}{b}\right)\right)^2} \right] \quad (28)$$

Here K_B is the Boltzmann constant, T is the temperature and η is the viscosity of water.

In our studies, DDLS measurements were performed at multi-angles starting from 30° to 150° at an interval of 20° , on the ALV-GmbH spectrometer equipped with a digital correlator. Due to the high aspect ratio and anisotropic property, the DDLS experiments were carried out at a wavelength of 634 nm, slit at $400\mu\text{m}$ and the laser power was set to 150mW to avoid thermal convection.

In addition, as the length of the nanotubes is larger, longer time scale is needed to measure the correlation function of the scattered intensities. Furthermore, the scattering intensity of depolarized light is weaker than the polarized one due to various reasons such as optical imperfection in lenses, multiple scattering and lack of high power source^[8]. Therefore the depolarized scattered intensities were collected for 3 hrs, whereas 1 hr was enough to record the polarized light scattered intensities. The autocorrelation functions of the depolarized and polarized scattered intensities were analyzed by CONTIN algorithm. The sample solutions were prepared at infinite dilution in order to avoid percolation of CNTs. The prepared samples were allowed to stay at room temperature for 1 week prior to the measurement to settle down the large aggregates. All the measurements were carried out at $T = 20^\circ\text{C}$ and the temperature was maintained by a water bath.

Zeta potential

Zeta potential (or electrokinetic potential) was determined from the electrophoretic mobility of our hybrid particles suspended in the water. The inherent electric double layer around these particles comprises an inner Stern layer where the ions are strongly bound and an outer diffusive layer. These layers are separated by a boundary, the so called “slipping plane”. The potential difference at this boundary is known as zeta potential.

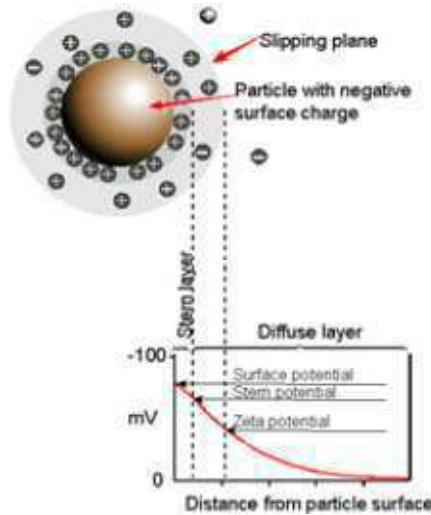


Figure 0. 2: Schematic illustration of zeta potential.

The zeta potential is determined by measuring the rate (or speed) at which these colloidal particles move when an electric field is applied. This is referred to as electrophoresis. The speed is directly related to the magnitude of particle charge or zeta potential. In our experiments, when the hybrid particles are dispersed in aqueous solution, a potential gradient is developed at the liquid/solid interface. When a known electric field (or voltage) is applied between the two electrodes, which are located in the instrument, induces the particles to move with a constant velocity towards the opposite charge of electrode. Positively charged particles move towards cathode. Conversely, the negatively charged ones migrate towards the anode.

The velocity commonly referred as “electrophoretic mobility” (U_E) and from this zeta potential (z) can be determined generally via Henry equation as follows^[9],

$$U_E = \frac{2 \varepsilon z f(\kappa a)}{3\eta} \quad (29)$$

Probing Techniques

U_E is the electrophoretic mobility, z is the zeta potential usually indicated by Greek symbol ζ , ϵ dielectric constant and η is the viscosity of the medium and $f(\kappa a)$ is the Henry correction factor.

Reciprocal of the Debye length κ , often refers to the thickness of the double layer and 'a' indicates the radius of the solid particle. $f(\kappa a)$ indicates the ratio of the particle radius to electric double layer thickness.

The case of $f(\kappa a) \gg 1$, is referred as Smoluchowski approximation. A system, where the colloidal particles are dispersed in aqueous solution containing moderate electrolyte concentration (10^{-3} M salt), fits with the Smoluchowski model. For non-aqueous systems [$f(\kappa a) \ll 1$], Hückel approximation is applicable.

We have performed the electrophoretic mobility measurements for all the formulated nanoparticles and nanotubes using the ZetaCompact device (by Cad Instruments, France). The zeta potential was then deduced from eq. (29). The sample holder is made up of quartz that has to be cleaned prior to use by ultrasonication treatment with water or can be left in strong acid (3N HNO₃) solution for overnight followed by numerous rinsing with water.

The suspension of colloidal particles contained in the quartz cell was illuminated by a laser beam. The voltage was applied to palladium electrodes producing an uniform electric field in the cell. Positively charged particles migrate toward cathode and conversely, negatively charged particles move toward anode. Their movement was observed with a microscope, detected by a camera and analyzed by a high accuracy image analysis software. To avoid the contribution of the fluid movement (under electric field) to the particles mobility, the microscope was focused at the level of stationary layer, where the electroosmotic flow is zero. Therefore only true electrophoretic mobility of colloids was tracked.

Streaming potential

When the zeta potential measurements are carried out at the flat surface, streaming potential technique is often used. Instead of applying an electric field to move through a capillary or porous plug we can force an electrolyte solution to move through a capillary, porous plug or across a channel formed by two plates by applying a pressure gradient. When an electrolyte solution is forced to flow across the solid surface, excess charges near the

Probing Techniques

surface are carried along with the liquid. As a result there is an accumulation of either positive or negative charge at one end of the cell and equal opposite charges at the other end, thereby generating a potential difference (an electric field) across the surface and the measured potential difference is called as streaming potential, denoted by E . This potential opposes further accumulation, causing back conduction by ion diffusion against the direction of flow to attain a steady state by balancing the potential difference.

In our experiments, the streaming potential was recorded using a ZetaCAD instrument. The cell used for the experiments are shown in the Figure 0. 3. The instrument measures the electrical conductivity of the solution, the temperature and the streaming potential.

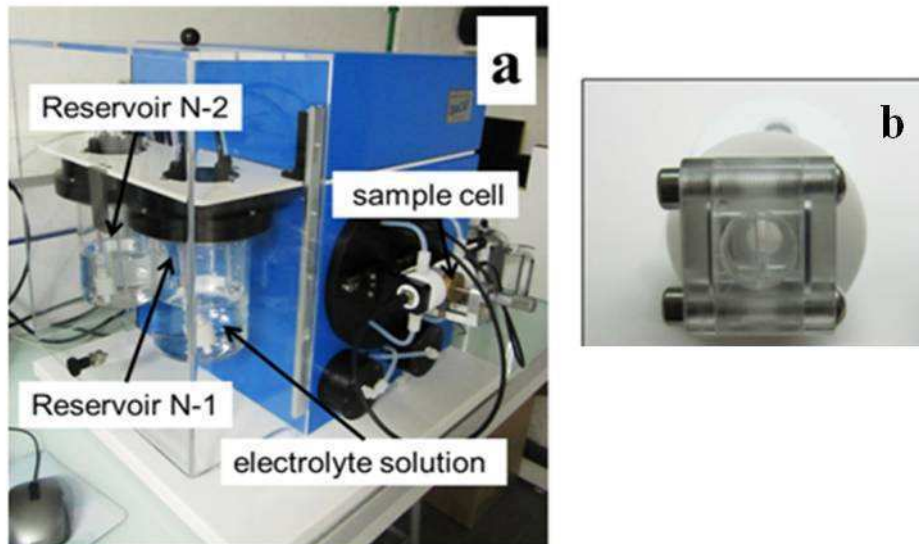


Figure 0. 3: ZetaCAD instrument (a) and ZetaCAD cell (b)(from igor thesis).

The ζ can be calculated from the slope of the streaming potential Vs pressure curve using Helmholtz-Smoluchowski equation^[10],

$$\zeta = \frac{\lambda\eta\Delta E}{\epsilon_r\epsilon_0\Delta P} \quad (30)$$

Where ΔP is a mechanical pressure difference driving the flow of liquid, η is the solution viscosity and λ is the conductivity. ϵ_r and ϵ_0 are the relative dielectric constant of the solvent and permittivity of a vacuum respectively.

Quartz Crystal Microbalance (QCM)

The quartz crystal microbalance is a simple, cost effective, nanogram mass sensitive technique based on the piezoelectric effect. Meaning that when alternating electric current (or potential) is applied to the quartz crystal, a mechanical oscillation (or strain) at its resonant frequency is induced. In common, the fundamental mode of quartz resonates between 5 and 30 MHz, but the commercial devices operate in the 5-10 MHz range. The measured frequency is dependent on many factors such as the thickness of the quartz, electrode and mass of the material deposited on the surface of the crystal. Among several materials, Quartz is the most widely used ones due to its inherent piezoelectric property and commercial availability. There are many ways to cut the quartz crystal. Most commonly AT cut crystals are used because they provide stable oscillation with no temperature fluctuation at room temperature. Furthermore the AT signifies that the crystals are cut at a 35° angle from the Z-axis. The quartz disc is sandwiched between two electrodes made up of gold layer with chromium underlying layer. These electrodes establishing an electric field across the crystal when voltage is applied, are then connected to an oscillator circuit, where the relative shift in the frequency due to the mass adsorption are measured and displayed in the computer.

In our studies, film fabrication was followed in situ by QCM instrument (QCM-D from Q-sense, Sweden) with dissipation (D) monitoring. The D is inversely proportional to the decay time and defined as,

$$D = E_{\text{lost}}/2\pi E_{\text{stor}} \quad (31)$$

Where E_{lost} is the energy lost during one oscillation cycle and E_{stor} is the total energy stored in the oscillator.

When the foreign materials such as inorganic NPs or polymers are deposited at the surface of the crystal, mass increase results in the resonance frequency decrease of the piezoelectric quartz crystal. The quantitative relationship between change in frequency and mass adsorbed was first derived by Sauerbrey in 1959 as shown below,

$$\Delta f = \frac{-2\Delta m f_0^2}{A\sqrt{\rho_q \mu_q}} = -\frac{2f_0^2}{A\rho_q v_q} \Delta m \quad (32)$$

Probing Techniques

In this relationship, f_0 is the resonant frequency of the crystal, A is the active area of the crystal, Δm is the mass change, ρ_q is the density of the quartz (2.648 g/cm^3), μ_q is the shear modulus of the quartz ($2.947 \times 10^{11} \text{ g/cm.s}^2$) and v_q is the shear wave velocity in quartz. In simple form, it can be written as follows^[11],

$$\Delta f = - C_f/n \times \Delta m' \quad (33)$$

Where $\Delta m'$ is the change in mass per unit area (g/cm^2), C_f is the sensitivity factor of the crystal (Hz/g/cm^2) and n is the overtone number. In our experiments C_f is 5.66×10^7 because we have used 5 MHz crystal at 25°C . By knowing the density of the film, thickness can be calculated.

There are three important assumptions to fit Sauerbrey equation.

- The mass adsorbed must be small relative to the mass of the quartz crystal.
- The adsorbed mass should be rigidly adsorbed.
- The adsorbed mass should be uniformly distributed over the crystal.

For thin deposited layers, Δf changes linearly with Δm . When the layers are very thick, the relationship becomes non-linear. The negative sign in equations 1 & 2, indicates that decrease in frequency corresponds to increase in mass and vice versa.

Advances in the quartz crystal microbalance technique allow the mass change measurements at a liquid-solid interface. In such cases, the viscosity η_L and density ρ_L of the liquid near the quartz surface must be taken into account. Kanazawa's equation^[12] for the change in resonant frequency of the crystal due to liquid loading is given by,

$$\Delta f = -f_q^{3/2} \left(\frac{\eta_L \rho_L}{\pi \mu_q \rho_q} \right)^{1/2} \quad (34)$$

Where f_q (Hz) is the resonant frequency of the crystal in air, η_L (N.s/m^2) is the viscosity and ρ_L (Kg/m^3) is the density of the liquid in which the quartz is immersed. μ_q is the shear modulus and ρ_q is the density of the quartz crystal. In our case, moving the 5 MHz crystal from air to pure water at 25°C ($\rho_L = 997$, $\eta_L = 0.89 \times 10^{-3}$), a decrease in fundamental frequency f of 700 Hz was observed.

Probing Techniques

Sauerbrey relationship is applicable as long as the deposited film is thin and rigid. When the overlayers are becoming non-rigid and thick, the relationship underestimates the mass and viscoelastic properties of the deposited film should be taken into account. Combining the frequency and dissipation measurements from multiple overtones one can modelize the thickness, shear elastic modulus and viscosity of viscoelastic film.

In our experiments, the quartz sensor was placed horizontally in a crystal holder and made watertight with the help of Viton O-ring. The small volume of liquid aliquots was delivered to the crystal sensor via orifice tubing with the help of ITC micropump (from ISMATEC). One face of the sensor was in contact with the liquid termed as active side, while the other side was not. The active side of quartz crystals were pre-treated as mentioned in the chapter 4 (UV treatment followed by silanization and spin coated with polystyrene). The frequency and dissipation changes of fundamental and 13 overtones accompanying the mass adsorption and desorption were monitored by the QCM.

Surface roughness and hydrophilicity play important role in the frequency change. Surfaces that are hydrophilic and inhomogeneous entrap water molecules within their cavities and contributing to the mass increase^[12]. In our experiments, this effect was not taken into account as the sensor was covered with smooth and hydrophobic polystyrene layer.

Atomic Force Microscopy

Atomic Force Microscopy is a widely used high resolution imaging technique, invented by Binnig, Quate and Gerber in 1986. The basic mode of the AFM is to image the topography of the sample with the help of a tip that is mounted at the end of a cantilever. Cantilevers usually made up of silicon or silicon nitride, are 100 to 500 μm long and about 0.5 to 5 μm thick. Tips are usually conical or pyramidal shaped and their radius in the range of 1-10 nm. Besides, the tip and cantilever, AFM comprises a cantilever holder, piezo scanner, a deflection detection system and a feedback loop.

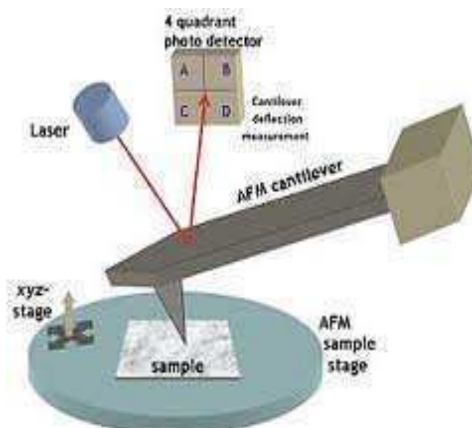


Figure 0. 4: *Schematic representation of Atomic Force Microscopy.*

The sample is placed on the piezoelectric scanner to move it in the X-Y plane. When the tip is brought close to the surface of the sample, the forces acting between the tip and sample surface leads to a deflection in the cantilever according to Hooke's law (35). This deflection is measured by the laser and reflects the forces of interaction towards photodetector. The photodetector converts the deflection into an electric signal. The feedback loop keeps the cantilever signal constant by adjusting the z position of the sample. This height information is finally plotted in the xy-plane and resulting in the topographic picture of the sample.

The Hooke's law expresses the deflection caused by the interaction between tip and surface is as follows,

$$F = k \cdot z \quad (35)$$

Where k is the elastic constant of the cantilever and z is the vertical deflection of the cantilever.

AFM is capable of producing images in a number of modes that includes contact, tapping, electrical and pulsed forces. Of them, tapping or non-contact mode is the most often used one. In this mode, the tip does not contact the sample surface, instead the cantilever is oscillating just below its resonant frequency with amplitude of few tens of nm. When the oscillations occur close to the sample surface, the probe will repeatedly engage and disengage with the surface, restricting the amplitude of the oscillation. The decrease in resonant frequency with the feedback loop maintains a constant oscillation by adjusting the z height of

Probing Techniques

the piezoelectric scanner that resulting an image of the surface topography as mentioned earlier. In addition to the topography, the tapping mode provides information on the mechanical properties of the sample.

In our studies, the image scanning based on tapping mode at room temperature was performed on a Multi ModeIIIa digital instrument. It is equipped with a J-type scanner which has maximum area of 125x125 μm^2 and Z- limit of 5 μm . The analysis of the images was done with the Nanoscope software.

References

1. Courtois, J. and J.F. Berret, *Probing Oppositely Charged Surfactant and Copolymer Interactions by Isothermal Titration Microcalorimetry*. Langmuir, 2010. **26**(14): p. 11750-11758.
2. Freyer, M.W. and E.A. Lewis, *Isothermal titration calorimetry: experimental design, data analysis, and probing macromolecule/ligand binding and kinetic interactions*. Methods in cell biology, 2008. **84**: p. 79-113.
3. Maurstad, G., S. Kitamura, and B.T. Stokke, *Isothermal titration calorimetry study of the polyelectrolyte complexation of xanthan and chitosan samples of different degree of polymerization*. Biopolymers, 2011. **97**(1): p. 1-10.
4. ArzenÅjek, D., *Dynamic light scattering and application to proteins in solutions*.
5. Berne, B.J. and R. Pecora, *Dynamic light scattering: with applications to chemistry, biology, and physics*. 1976: Courier Dover Publications.
6. Badaire, S.p., et al., *In Situ Measurements of Nanotube Dimensions in Suspensions by Depolarized Dynamic Light Scattering*. Langmuir, 2004. **20**(24): p. 10367-10370.
7. Shetty, A.M., et al., *Multiangle Depolarized Dynamic Light Scattering of Short Functionalized Single-Walled Carbon Nanotubes*. The Journal of Physical Chemistry C, 2009. **113**(17): p. 7129-7133.
8. Lehner, D., H. Lindner, and O. Glatter, *Determination of the Translational and Rotational Diffusion Coefficients of Rodlike Particles Using Depolarized Dynamic Light Scattering*. Langmuir, 2000. **16**(4): p. 1689-1695.
9. Deshiikan, S.R. and K.D. Papadopoulos, *Modified Booth equation for the calculation of zeta potential*. Colloid and Polymer Science, 1998. **276**(2): p. 117-124.
10. Szymczyk, A., et al., *Comparison of two electrokinetic methods- electroosmosis and streaming potential - to determine the zeta-potential of plane ceramic membranes*. Journal of Membrane Science, 1998. **143**(1-2): p. 189-195.
11. Crouzier, T. and C. Picart, *Ion Pairing and Hydration in Polyelectrolyte Multilayer Films Containing Polysaccharides*. Biomacromolecules, 2009. **10**(2): p. 433-442.
12. Marx, K.A., *Quartz Crystal Microbalance: A Useful Tool for Studying Thin Polymer Films and Complex Biomolecular Systems at the Solution-Surface Interface*. Biomacromolecules, 2003. **4**(5): p. 1099-1120.

PART - I

Chapter 1: Electrostatic complexation fundamentals

Abstract

We report on the “*desalting*” transition process that enables the tuning of “*electrostatic*” interactions between oppositely charged polyelectrolytes (PEs) of “symmetric” and “asymmetric” systems as a function of the solution ionic strength. Asymmetric systems are composed of a set of weak/strong PEs, whereas symmetric systems comprise a set of weak/weak or strong/strong PEs. We show that in some case the “electrostatic” interactions between oppositely charged macromolecules can be completely turned off at high ionic strength (I_s) and turned back on by a controlled decrease of the salt concentration. Upon dilution with water, this approach enables the controlled co-association of charged species to formulate “organic” electrostatic aggregates of tunable size. We show that the desalting transition is a general phenomenon seen on all PEs pairs investigated and independent of the PEs buildings block features. Even though, specificities like Mw, architecture (linear, branched), weak and strong characters are responsible of some observed differences. Within the same category, the bulk critical salt concentration (I_b) and sizes of the aggregates is a function of the conformation and Mws of the PEs couple. A neat split in I_b is observed between symmetric and asymmetric PEs couples. In particular, the complexation of PEI and PAA chains shows a two step transition in the case of branched chains (*b*PEI) with respect to linear ones. In a second stage, isothermal titration calorimetry (ITC) is carried out to better understand the thermodynamics of polyelectrolyte complexes (IPEC) formation in asymmetric and symmetric systems. Preliminary experiments show that the complexes formation is driven by entropy in all cases, although enthalpy participated to the minimization of the free energy in the symmetric systems (exotherms); likely the signature of secondary forces (hydrophobic effect and/or hydrogen bonding) at play beyond the sole electrostatic interaction. In particular, the IPEC formation of asymmetric systems is purely endothermic and consequently driven by the sole entropy associated with the counter ions (and water molecule) release. In the case of symmetric systems, the IPEC formation is mainly exothermic indicating the presence of extra forces (hydrophobic interactions, hydrogen bonding...) leading to a complexation driven by entropy and enthalpy. Desalting and ITC experiments put forward that beyond electrostatic interaction secondary forces play a key role in the formation of PEs complexes.

Introduction

The “electrostatic complexation”^[1] between oppositely charged polyelectrolytes (PEs) has aroused much attention during the last decades because of their versatile applications in numerous fields such as water and protein purification, coatings, cosmetics, food industry and in drug delivery^[1-6]. PEs are a class of macromolecules which contain chargeable groups in their repeating units. When dissolved in polar solvents such as water, PEs dissociation leads to the generation of charges along its backbone, while releasing the counter ions in aqueous media. Cationic and anionic PEs possess positive and negative macro ions along their chain respectively. PEs can be divided into “strong” or “weak”. Strong PEs have a constant charge density or in other words dissociation is here independent of the solution pH. In contrast, weak PEs have a degree of ionization that strongly depends on pH.

Mixing of aqueous solutions of oppositely charged PEs results in the formation of inter polyelectrolyte complexes (IPECs) with the release of counter ions. The first IPEC formation was investigated by Bungenberg de Jong for the system of gum Arabic-gelatin^[7]. Since then a large number of books and reviews have been devoted to the formation and applications of IPECs. The formation and stability of IPEC depends on PE characteristics such as chain length (Mw), charge density, chain flexibility and some experimental conditions like the mixing order and ratio, polyion concentration, pH, ionic strength and temperature etc^[1, 8, 9]. Among them, charge ratio (Z) is one of the key factors that determines the final morphologies and properties of the complexes. For instance, depending on the charge ratio, the formed IPECs can be either stoichiometrically insoluble or non-stoichiometrically water soluble^[10].

Regarding the complexation mechanism, it has been already shown that the association process between polycation and polyanion is driven by both enthalpy and entropy. The enthalpic change is related to the opposite charge pairing, which strongly depends on the chemical composition of PEs. The entropic contribution arises from the counter ions release initially present along the PEs backbone as a result of binding and from the loss of translational and conformational freedom of PEs chains^[6, 11]. The interplay between enthalpy and entropy gives rise to a variety of complexation behaviors. Although the IPEC formation is primarily driven by electrostatic interactions, a variety of secondary forces such as hydrogen bonding, ion-dipole interactions, hydrophobic interactions and charge

Electrostatic complexation fundamentals

transfer interactions play a crucial role in the association process. These forces are the important parameters in determining the morphology and stability of the complexes.

Complex formation based on electrostatic interactions opened new fields of applications in material as well as in biological sciences, in particular, thin film fabrication via the very popular layer-by-layer approach^[12] and in the design of novel composite materials, where the PEs were found to act as stabilizers for colloids. Increasing number of works have shown that the electrostatic complexation of organic PEs with oppositely charged inorganic nanoparticles (NPs) is a promising way to combine the unique physical properties of NPs with the excellent processability of polymers. These synergistic attributes of hybrid materials emerged their applications in a variety of scientific and technological fields^[13-15]. However under strong electrostatic interactions, the direct mixing or titration of any oppositely charged building-blocks (BBs) generally lead to a macroscopic phase separation or precipitation. Those “precipitates” have a great impact on the mechanical and electronic properties of the resulting materials. The main aim of this study is to find out an efficient processing route to control the electrostatic interactions between any oppositely charged components.

Few years back, as a first step, Berret and co-workers have used charged-neutral block copolymers (also known as double hydrophilic block copolymers) rather than simple homopolyelectrolytes (homoPEs) to control the strong electrostatic attractive driving forces during the complexation with NPs or surfactants. It has been shown that these block copolymers co-assemble with surfactants, NPs, protein, PEs, yielding stable finite “supermicellar” aggregates with core-shell structures^[16-18]. The core was comprised by dense coacervates, made up of oppositely charged components, while the neutral block formed a shell around the core, providing stability through steric repulsion at short range. In the same vein, Qi *et al.*, reported that the direct mixing of NPs with oppositely charged block copolymers gives rise to stable nanoparticle clusters or “hybrid coacervates”^[19]. These reports revealed that with copolymers, under such strong electrostatic interactions, the complexation resulted in the spontaneous formation of thermodynamically unfavorable out-of-equilibrium “kinetically frozen” structures^[19,20].

Further exploration of these “frozen” structures unveiled a new issue: the size and morphology of the coacervates formulated through two different pathways were found to differ from each other^[21]. In addition, spherical electrostatic aggregates prepared from

Electrostatic complexation fundamentals

cationic-neutral block copolymers and surfactants at low concentration were found to transfer to cylindrical aggregates when the mixing concentration and then the probability of interactions were increased. This suggested that the electrostatic coacervate formation strongly depends on the formulation pathway. In comparison to the large body of experimental works performed on the mechanisms, structural characterizations and functionalities, not much attention has been paid to the way how the oppositely charged components are coming into intimate contact. Indeed, understanding the fundamentals behind the electrostatic interactions is a challenging task. As a first attempt, based on many investigations the authors from the Complex Fluid laboratory (joint CNRS/Rhodia institution, NJ, USA) put forward that the electrostatic interaction and therefore the formulation process strongly dependent on the competition between “homogenization time” of the mixed solution and “reaction time” of the individual building-blocks (BBs)^[19-23]. The former depends on the order and/or the speed of mixing (mixing pathway). Whereas the later depends on the initial concentration and the nature/strength of the different interactions taking place (interaction pathway). The electrostatic interactions can then be tuned through either the *mixing or the interaction pathway*.

In order to understand the role of “homogenization time” on electrostatic interactions, Qi and co-workers have used different mixing protocols, including the mixing order and the mixing speed on a system composed of CeO₂ NPs and oppositely charged block copolymer. Their investigations strongly emphasized that high speed injection of NPs into PEs solutions enabled a good control of the strong electrostatic driving force and thereby generated small finite hybrid coacervates with a small polydispersity^[21]. In a subsequent publication, besides tuning the mixing stage, the same authors investigated how the strength of the electrostatic interaction influences the electrostatic complexation^[23, 24].

To investigate the “interaction pathway”, Berret et al have developed the concept of “desalting transition” inspired from molecular biology^[25]. This approach emphasizes the role of the ionic strength to fine tune the electrostatic interaction between oppositely charged components where the complexation is in principle *purely* driven by electrostatic forces. In a first step individual stock solutions were made at a very high ionic strength. Both solutions were then mixed together to get a so called “dormant” or non-reactive solution where the electrostatic interaction between oppositely charged components is completely screened off. Desalting kinetics was then controlled by slowly decreasing the ionic strength (I_s) from 1M (the minimum I_s to totally prevent the complexation), to lower values by dilution or dialysis,

Electrostatic complexation fundamentals

where the electrostatically screened system undergoes an (abrupt) transition at a critical ionic strength (I_b) between a unassociated and a clustered state as depicted in the Figure 1.2. Electrostatic aggregates with sizes ranging from nm to μm , difficult to generate by soft chemistry approaches, found then applications in coating and polishing.

The first desalting kinetics was performed on a system composed of anionic PAA_{2k} coated iron oxide nano crystals and cationic charged-neutral block copolymers and has shown that the controlled removal of the salt via both dialysis and dilution resulted in an abrupt transition at the same ionic strength ($I_b \sim 0.39\text{M}$), suggesting that both desalting processes are acting in a similar way. The resultant electrostatic complexes remained stable over a period of months. Interestingly, a dialysis performed under a magnetic field yielded unidirectional magnetic nanorods, oriented along to the external magnetic field^[26].

In order to understand the role of kinetics behind the desalting transition in the formation of clusters, Fresnais *et al.*, put forward and compared four different formulation techniques such as direct mixing, dilution, dialysis and quenching on a system composed of anionic ceria and cationic block copolymer^[25]. Among the four techniques, except direct mixing, the other three processes used the desalting protocol. Core-shell structures were obtained from direct mixing, whereas “frozen” larger electrostatic aggregates were obtained from desalting processes. An identical I_b was found for all the three desalting processes, suggesting that transition is independent of the desalting rate and process. However, the final sizes of the electrostatic complexes strongly depend on the desalting kinetics. The salt removal rate is then the key parameter that controls here the electrostatic complexation.

In a consecutive publication, Qi *et al.*, have replaced the charged neutral copolymers by homoPEs to investigate the role of a charged corona. Dialysis have showed a transition at $I_b \sim 0.5\text{M}$ and yielded similar aggregates but with much larger sizes than in the copolymer system, showing the generality of the desalting formulation process^[27]. Further investigations revealed that although dialysis yielded reproducible aggregates, it is time consuming and then cannot fit industrial needs. On the other hand, controlled manual dilution presents some advantages. It enables the construction of the phase diagram, easily determines bulk parameters and critical aggregation concentration. But possess some drawbacks too as very large uncontrolled and somehow polydispersed aggregates are generated, due to the non-homogeneity of the dilution rate throughout the sample. These authors put forward that microfluidic mixing can overcome those drawbacks as the flow rate between the dormant

Electrostatic complexation fundamentals

solution and the water can be strictly controlled through known hydrodynamics conditions. From the current discussion, the “desalting” formulation pathway appears to be a very interesting approach to fine tune the electrostatic interaction between oppositely charged BBs made stable at high ionic strength. Furthermore, it allows a control over the size and final morphology of the clusters.

In this Ph.D work, we have investigated deeper this approach on different hybrid building blocks in bulk and at an interface. In the current chapter, we have generalized this electrostatic co-assembly pathway to strong and weak homoPEs and demonstrated that the transition between a dispersed and an aggregated state as function of ionic strength is a general phenomenon independent of the exact nature of the PEs. We have considered asymmetric PEs couples composed of weak/strong PEs ($\text{PAA}_{2\text{k}}/\text{PDDAC}_{100\text{k}}$, $\text{PAA}_{2\text{k}}/\text{MAPTAC}_{400\text{k}}$ and $\text{PAA}_{2\text{k}}/\text{PTEA}_{11\text{k}}\text{-b-PAM}_{30\text{k}}$), whereas “symmetric” ones are composed of weak/weak or strong/strong PEs ($\text{PAA}_{2\text{k}}/\ell\text{PEI}_{2\text{k}}$, $\text{PAA}_{2\text{k}}/b\text{PEI}_{25\text{k}}$, $\text{PAA}_{2\text{k}}/\text{PAH}_{15\text{k}}$ or $\text{PSS}_{75\text{k}}/\text{MAPTAC}_{400\text{k}}$). Upon decreasing the ionic strength as expected, macroscopic flocculate formation has taken place below a critical salt concentration I_b , in all the pairs investigated as expected. For PAA/PAH complex, the interaction(s) cannot be completely turned off even at very high I_s . This series of desalting experiments serve as a base for the formulation of the various hybrid materials in chapter 3, where those PEs act as electro-steric stabilizers for inorganic NPs and carbon nanotubes. It should be noted that in the current work, desalting kinetics was carried out by a slow and manual dilution of the dormant solutions with DI water.

Furthermore, we have performed at a given pH Isothermal Titration Calorimetry (ITC) experiments on some specific pairs of PEs to shed some light on the mechanism that trigger the complexation. Our first motivation is here to acquire a better understanding of the nature of the force(s) at play in “electrostatic” complexation process of oppositely charged PEs, an issue, not very well documented in the literature. More specifically, it might help to understand the neat split/spread in critical I_b observed among the various PEs complexes investigated. In a first step, our preliminary ITC experiments will be performed at low ionic strength ($\sim 10^{-3}$ M). In the future, “desalting” transition will be performed and studied directly inside an ITC cell to better understand the role and impact of salt on the assembly thermodynamics.

Experimental Section

Materials

Homopolyanions used in this study are weak polyacrylic acid (PAA_{2k}) and strong polystyrene sulfonate (PSS_{75k}) PEs. The homopolycations are weak polyethyleneimines (linear & branched) and poly(allylamine hydrochloride) (PAH_{15k}) and strong poly(diallyldimethyl ammonium chloride) (PDDAC_{100k}), and poly(methacrylamidopropyl trimethyl ammonium chloride) (MAPTAC_{400k}). These homoPEs were purchased from Sigma Aldrich. Charged-neutral double hydrophilic block copolymers, poly(trimethylammonium ethylacrylate)-b-poly(acrylamide) abbreviated as PTEA_{11k}-b-PAM_{30k} (values in indices indicate the Mw of the specific blocks) was synthesized by controlled radical polymerization according to MADIX process by Rhodia chemical company and present a strong cationic charged block. Other reagent graded chemicals such as HCl, NaOH and NH₄Cl were used as such without further purification.

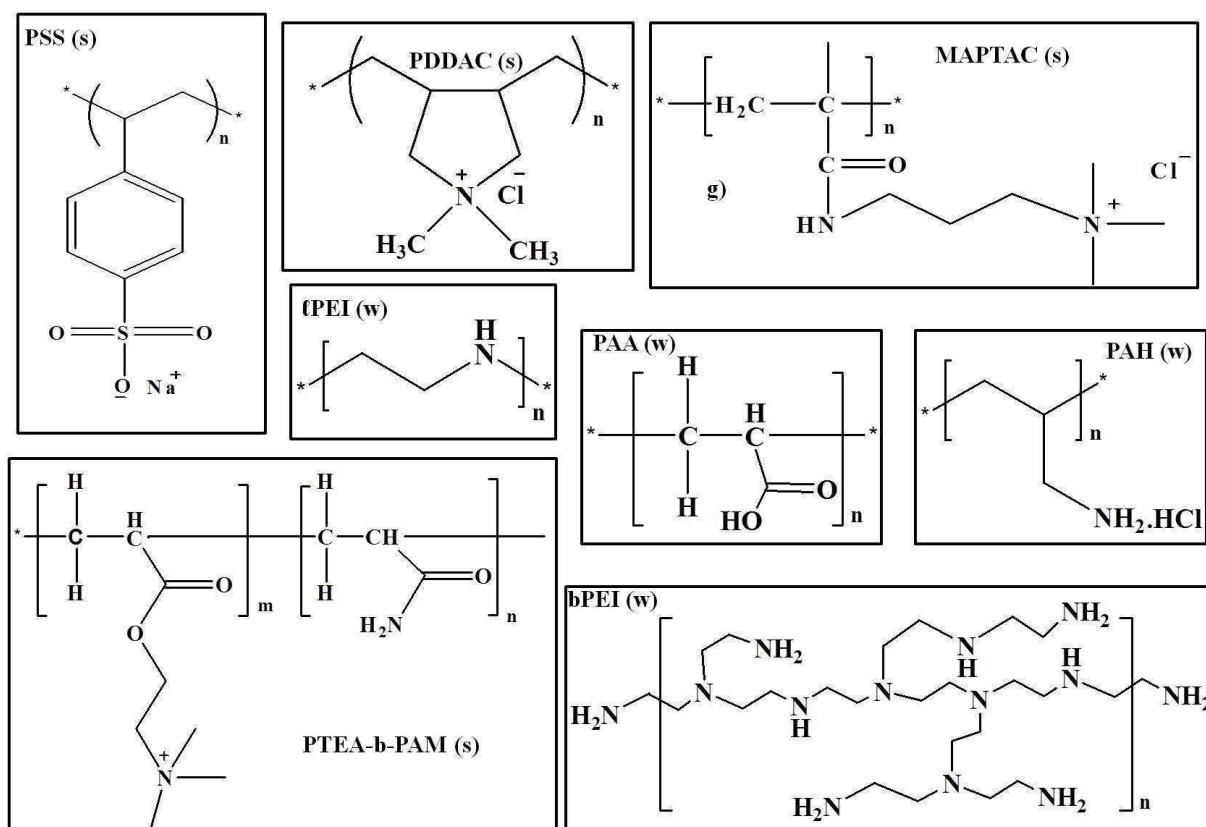


Figure 1.1 : chemical structures of the various anionic and cationic PEs used in this study. s:strong, w: weak.

Electrostatic complexation fundamentals

Name	Mw (g/mol)	Number of repeating units
Polycations		
ℓPEI	2000	46
bPEI	25000	580
PDDAC	100,000-200,000	619
MAPTAC	400,000-1000,000	1818
PAH	15000	160
PTEA-b-PAM	11000-b-30000	70-b-420
Polyanions		
PAA	2000	28
PSS	75000	340

Table 1.1: *Structural characteristics of the PEs used in this study.*

Methods

Charge ratio (Z)

Charge ratio (Z) is defined as the ratio between average structural cationic and anionic charges borne by cationic and anionic PEs respectively (we have calculated the Z by taking number of charge(s) per monomer unit into account).

$$Z = \frac{[\text{cationic}]}{[\text{anionic}]}$$

In case of strong PEs complexation, as their charge density is independent of pH and salt, we consider that the average structural charges are equal to the effective charges.

When at least one of the interacting PEs is weak, as its degree of ionization strongly depends on the pH and salt, the structural charges are not equal to the effective charges and therefore Z is a function of pH and salt. In ITC experiments, as a first approximation, we computed the Z by considering the structural charges = effective charges at a given pH. (Here the term “structural charges” indicate that all the monomer units in the PEs are fully charged).

Mixing ratio (X)

The mixing ratio (X) is defined as the volume ratio of cationic and anionic suspension

$$X = \frac{\text{Volume of cationic PEs (ml)}}{\text{Volume of anionic PEs (ml)}}$$

Desalting concept in “bulk” (*Switching off and on the interaction*)

The mixing of two oppositely charged dispersions at the same concentration and at high ionic strength results in a clear-dormant solution where the electrostatic interaction between the components is completely *switched off*. The interaction between opposite species can be resumed or *switched back on* by the controlled removal of the salt either by dialysis or dilution resulting in a turbid-reactive solution via the spontaneous association of the reacting species. The bulk transition from a clear non-clustered state to a (turbid) clustered state at a particular ionic strength is denoted as the “critical ionic strength” I_b , for a given pair of oppositely charged BBs. Beyond, clusters are formed via a nucleation and growth process. By fine tuning the ionic strength and the rate of salt removal, the size of the clusters can be tuned from nanometer to micrometer level.

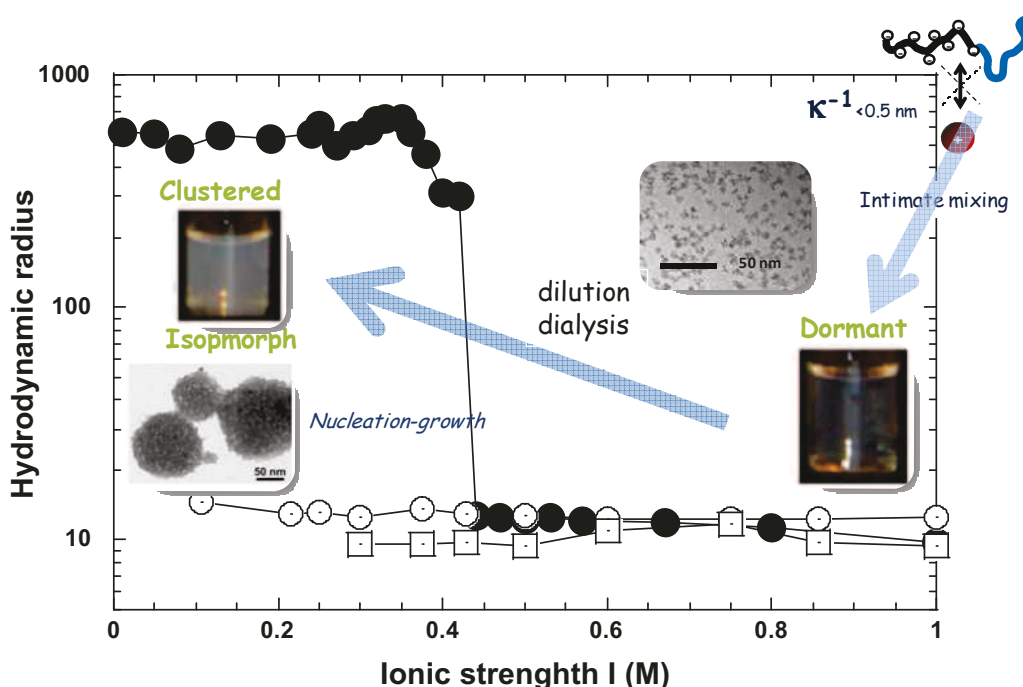


Figure 1.2 : Hydrodynamic radii (R_H) as a function of ionic strength between oppositely charged species (closed symbols). Open symbols represent R_H values for individual species.

Electrostatic complexation fundamentals

Stock solutions of each individual PEs were prepared at a concentration of 0.1 wt% and at a pH of 7. The electrostatic interactions between oppositely charged PEs of “asymmetric” and “symmetric” systems were completely *switched off* by bringing their mixed dispersions into high initial ionic strength (I_0) of 1M and 4M respectively with the addition of NH_4Cl . At this stage, the dispersions yielded clear “dormant” solutions, indicating that oppositely charged species were not yet associated. Drop-by-drop addition of DI water turned the “dormant” solutions into “reactive” ones giving rise to an abrupt transition at I_b for each different couple. Below I_b , large aggregates were formed. Hydrodynamic radii (R_H) were monitored by DLS throughout the dilution process.

Isothermal Titration Calorimetry (ITC)

ITC^[28] is a technique of choice to help to understand the complexation mechanisms on a thermodynamic point of view. Using this approach milli, micro and pico level molar binding constants can be determined. No prior labeling or immobilization is required. As experiments are programmed, operator involvement and thereby mistakes can be largely avoided. ITC is most commonly used in the literature to understand biological assembly processes. Very few reports are however devoted to polyelectrolyte complexation^[29-32]. In those studies, complexes formation are driven by either enthalpy or entropy or by the combinations of both effects, and then depends on various parameters such as pH, salt, temperature and polymer chain length^[33]. Before going into discussion on the systems put under scrutiny in this work, it is worthy to introduce the basic principles and experimental protocols of ITC.

Basic principles of ITC

The chemical or physical interaction between molecules is always accompanied either with the release or absorption of heat. ITC^[28] is a fast and robust quantitative physical technique which directly measures the heat change occurred during the interaction under adiabatic conditions. Typically, the basic concept of ITC is to maintain the temperature and pressure equal between the reference and sample cell. Depending upon the nature of the interactions between the molecules, the heat is either released or absorbed and associated with exothermic or endothermic processes respectively. For an exothermic reaction, the heat evolved will be transferred to the surroundings in order to maintain the temperature equal

Electrostatic complexation fundamentals

between the cells; whereas in an endothermic process, heat will be supplied from the surroundings. As mentioned earlier, ITC measures the rate at which the heat is exchanged. The measured heat (released or absorbed) will be directly proportional to the amount of binding. The heat measurement allows direct determination of some thermodynamic parameters such as binding constant (K_b), enthalpy (ΔH_b), and stoichiometry (n) of the interaction from the binding isotherm curve through an appropriate fitting model when available. The free energy (ΔG_b) of binding is then derived from K_b , via the well known relationship (1). The complexation entropy (ΔS_b) is then determined from the enthalpy and free energy of binding through equation (2).

$$\Delta G_b = -RT \ln K_b \quad (1)$$

$$\Delta G_b = \Delta H_b - T \Delta S_b \quad (2)$$

Where, R = universal gas constant, T = absolute temperature in Kelvin

Thermodynamic parameters such as enthalpy and entropy of binding provide information as well on secondary forces. Thus a single ITC measurement can potentially describe the complexation mechanism or the driving forces at play via the structural features of the components or building blocks (BBs) used.

Experimental protocols of ITC

A typical ITC instrument is shown in the Figure 1.3. It consists of two identical cells called reference and sample cell, made up of thermal conducting materials such as hastelloy or gold and kept inside an adiabatic jacket. Normally the reference cell is filled up with the buffer or water used to prepare the sample solution. The sample cell is loaded with 1.5 ml of one of the components (for instance PEs), which can be introduced manually with the help of a μ syringe. The controlled delivery of titrant (PEs of opposite charge) is automated by a motor-driven injection syringe comprising a stirrer at the end, which ensures the thorough mixing of components. Generally, a single ITC experiment contains at least 5 to 20 injections of titrant. The volume of the titrant to be injected depends on the operator, and is generally in the 10-20 μ l range. The delivery of titrant into the sample cell is carried out at a constant rate. A sensitive thermocouple measures the temperature difference between the cells (ΔT_1) and between the cell and jacket (ΔT_2). A constant power signal is applied to the reference cell.

Electrostatic complexation fundamentals

Heater located on the sample cell will be activated by this signal via a feedback loop when there is a need to maintain isothermal condition. During successive injections of the titrant, heat is either released or absorbed, depending upon the nature of the interactions between the macromolecules. For endothermic processes, the feedback circuit activates the heater of the sample cell in order to maintain the temperature equal between the cells. The reverse is true for exothermic reactions where the feedback loop is deactivated.

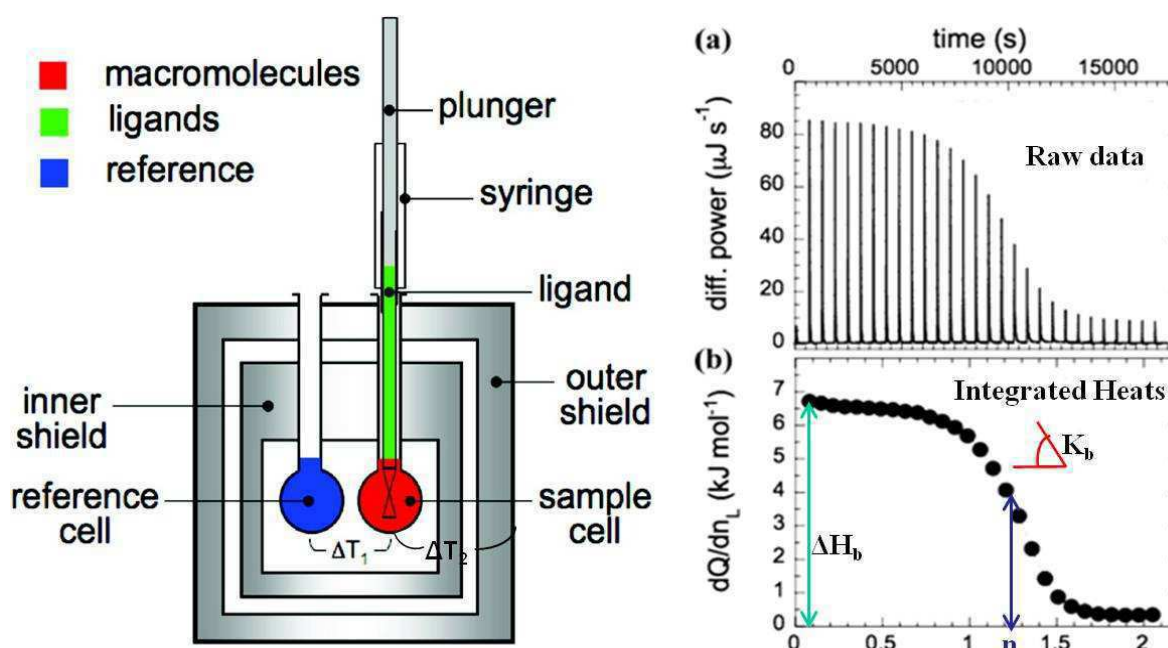


Figure 1.3 : Schematic representation of ITC.

The right panel of Figure 1.3 shows a typical ITC data. The top curve represents the differential power (DP) or heat flow as a function of time and contains a series of signals. Each signal is associated with a heat exchange. The decrease in intensity of signals after the neutralization point is attributed to the heat of dilution of the titrant. In other words, the observed complexation signal is a combination between the heats of association, the heat of dilution of titrant and the small heat generated by the stirring. Prior to the data analysis, it is then necessary to normalize the DP curve. Normalization is done by subtracting the heat of dilution of titrant from the heat of binding. It is recommended to perform an identical and separate experiment to measure the heat associated with the titrant alone (the aliquot is added to the solvent (buffer/water) in the sample cell in the absence of the oppositely charged PEs).

Electrostatic complexation fundamentals

The data are analyzed in this work using the *Multiple non-interacting site model* (MNIS)^[34] which assumes that oppositely charged macromolecules comprising several binding sites interact in an uncorrelated way. The reaction stoichiometry n denotes the number of non interacting binding sites available on each macromolecule ($n=1$ defines the single site binding model). The measured quantity represents the derivative of the heat with respect to the number of moles of titrants injected, noted $dQ/dn_t \equiv \Delta H_b$. In the framework of the MNIS model ΔH_b then reads:

$$\Delta H_b(Z) = \frac{1}{2} \Delta H_b^0 \left(1 + \frac{n-Z-r}{\sqrt{(n+Z+r)^2 - 4Zn}} \right) \quad (3)$$

Where Z is the charge ratio as defined earlier, $r = 1/K_b[M]$ and n is the stoichiometry. Expression (3) exhibits a sigmoidal decrease of the exchanged heat as a function of charge ratio Z . The thermodynamic signature of the complexation can then be determined by a nonlinear least-square fit to the data. In a second step, the variation in entropy and overall free energy (ΔS_b and ΔG_b) can be determined via equations 1 & 2.

Key steps to perform a neat ITC experiment:

ITC is a very sensitive tool and therefore needs a keen attention throughout the experiment which includes sample preparation, cleaning of the cells, loading of injection syringe, sample and reference cell^[35].

1) In order to avoid problems arising from foreign materials and air bubbles, all the experimental samples should be filtered and degassed immediately prior to loading. In sample preparation, concentration (C) is a very important parameter together with pH and salt concentration. For a neat experiment, C should be well optimized and should be calculated accurately as the heat effects are directly proportional to the amounts of binding. At very low C , the evolved heat will be very difficult to measure. Whereas for large C , accurate determination of K_b will be hampered, as the interaction between the component is very fast, hindering the monitoring of a characteristic sigmoidal curve due to the sharpness of the transition.

Electrostatic complexation fundamentals

2) Extreme care should be taken while filling the sample cell to avoid air bubbles. Introduction of bubble results in a very poor baseline signal. The volume of the titrant should be large enough to enable numerous small injections to ensure a complete complexation and get a better fit.

3) Parameters such as C , pH and salt should be identical between titrant and titrate. There should be enough time between successive injections to permit the relaxation of the baseline to its original value.

ITC experiments were performed on a VP-ITC instrument at 25°C at a stirring speed of 307 rpm. The sample cell was filled with 1.45 ml of one of the interacting PEs. Whereas 0.28 ml of the titrant (oppositely charged PEs) was taken in a syringe. Each experiment proceeds with preliminary injection of 2 μ L of titrant followed by subsequent 28 injections of 10 μ L of titrant over 20s with an interval of 10-20 mins between injections.

Stock solutions of PEs were prepared by dissolving calculated amount of PEs in aqueous media. The calculations of PEs concentrations were made by taking their molar charge (Z) into account. The pH of PEs solutions was adjusted with the help of HCl or NaOH to attain pH 7. The sample solutions were degassed for 10 min prior to loading. The heat associated with the complexation of PEs was recorded as a function of time. In our experiments the DP curves were not normalized, since the signals of the aliquot dilution give the idea about the completion of the complexation process whose value is negligible.

Results and Discussions

Desalting transition of PEs

Figure 1.4 displays the hydrodynamic diameter (D_H) as a function of the ionic strength of the electrostatic complexes formed between various oppositely charged PEs. In all 5 systems investigated, a small D_H at initial ionic strength (I_0) (1M or 4M) assures the effective screening of the interaction and the “dormant” nature of the PEs solution. Stepwise dilution of the salt concentration upon addition of DI water triggers then the co-assembly or association of oppositely charged components at lower I_s . The sizes of the “organic” complexes were found to slightly increase with decreasing I_s .

Just before passing through a sharp transition, at a critical concentration I_b (specific to the PEs pair investigated), very large complexes were generated due to the accomplishment of maximum complexation. The occurrence of a full complexation at I_b is indeed governed by the charge compensation between the cationic and anionic species, which tend to grow electrostatic complexes in an uncontrolled manner^[36]. In the case of PSS/MAPTAC pair, in addition to the charge balance between the oppositely charged species, the very large Mw of MAPTAC tends to generate “infinite” complexes as can be seen in the Figure 1.4.

For pairs comprising weak PEs where effective charges are not equal to structural ones, some cationic or anionic species will be either in excess or deficient resulting in finite non-stoichiometric charged complexes. Depending on the system and PEs features (Mw, weak/strong nature) either very large organic complexes or macroscopic flocculates were formed.

The measured diameter (~400 nm) for the set comprising the block copolymer (PTEA-b-PAM) was lower than all the other comparative systems, suggesting that the interaction was much stronger in the case of homoPEs as anticipated. Indeed the presence of the neutral corona is somehow shifting the local stoichiometry away from $Z = 1$, arresting rapidly the growth of the structure. It should be noted that in the case of direct mixing, the complexation generates core-shell structures with the neutral block outside, creating then smaller structures. For homoPEs, charge compensation generates larger structures. In case of MAPTAC, the clusters are very large (> 1000 nm) suggesting the role of high M_w in promoting inter complexes bridging as well. The formation of large organic aggregates is not

necessarily reversible (de-association occurs upon increasing back the ionic strength to higher values ($>I_b$)) and depends on the couple studied.

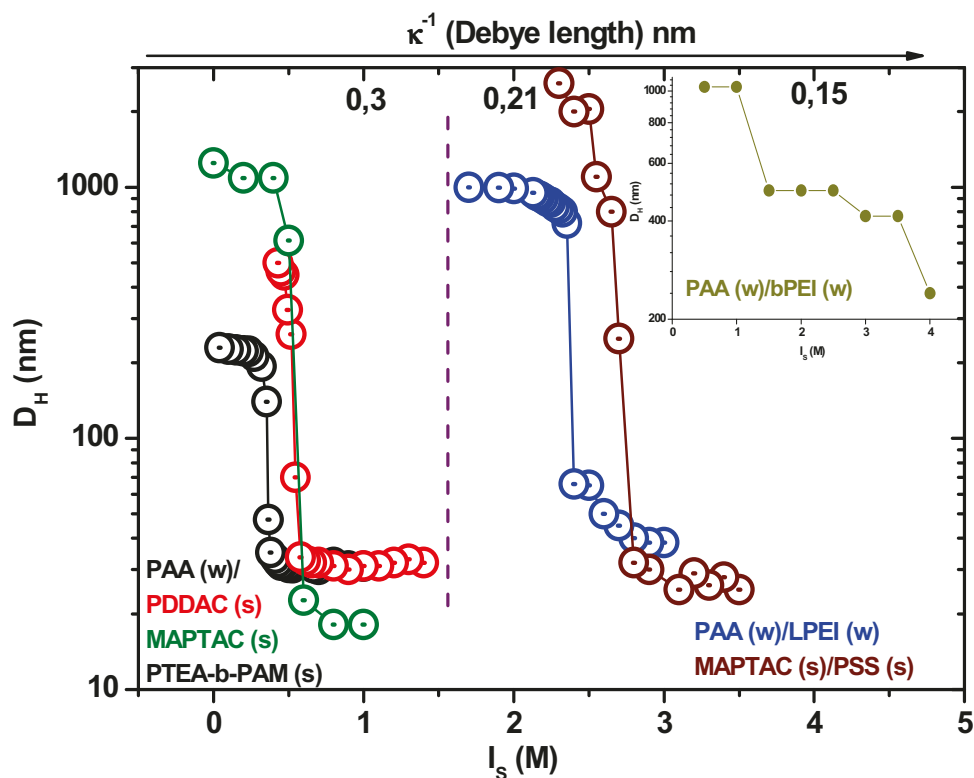


Figure 1. 4 : Hydrodynamic diameters as function of I_s for “asymmetric” and “symmetric” systems. [Complexation of PAA with PTEA_{11k}-b-PAM_{30k}, black; PDDAC, red; MAPTAC, green; PEI_{2k}, blue; Complexation of MAPTAC with PSS, brown].

In the case of the PAA/PEI pairs, the complexation based on $bPEI_{25k}$ required 4M of NH_4Cl to obtain a “visually clear” solution, whereas a clear solution was observed at 3M for the interaction of ℓPEI_{2k} with PAA_{2k}. At first sight, this trend suggests that Mw plays an important role in the complexation. Indeed, the observation revealed that the higher $bPEI$ Mw shifted the I_b to a higher concentration of salt. This finding was in good agreement with the report by Etrych and co-workers^[37] showing that with large Mw, the interaction is much stronger due to higher charge density and therefore higher concentration of salt are necessary to screen completely the electrostatic interaction.

Electrostatic complexation fundamentals

A closer look to the DLS data revealed that the measured D_H for the $bPEI_{25k}/PAA_{2k}$ pair at 4M is much larger than the individual D_H of both free PEs (12 nm for $bPEI$ and 6 nm for PAA). This implies that the complexation is stronger and is likely driven not only by electrostatic interaction but also by H-bonding interactions between non-protonated amine groups ($-NH_2$) of $bPEI$ and $-COOH$ groups of PAA. As a result the interaction between both PEs cannot be completely switched off even at high salt concentration ($\kappa^{-1} < 0.15$ nm). This is not the case for ℓPEI , where the interaction can be completely switched off due to much larger number of secondary amine ($-NH$) groups with respect to $-NH_2$, unable to form strong H-bonds.

The insert of the Figure 1.4 shows the desalting transition between $bPEI_{25k}$ and PAA_{2k} . The transition proceeds via two stages (at 3.5M and at 1.5M) and corresponds to ion-pair and large aggregates formation respectively, as explained later on in the ITC section. Etrych *et al.*,^[37] reported a higher I_b value for high Mw PEs. In the case of $bPEI_{25k}$ PEs, an abrupt transition was observed at a lower concentration of salt, far away from the first stage. If one looks closely, the transition for the branched system is not “abrupt” but rather step-wise. This is certainly influenced by the conformational effects of $bPEI$ chains. High Mw $bPEI$ chains will be much less extended due to its branched nature as compared to linear ℓPEI . The addition of high concentration of salt further promotes a compact globular structure. As a result, some of the counter ions will be trapped inside the globular network thereby preventing the macro cations to interact fully with macro anions. Unlike ℓPEI , the compact $bPEI$ architecture provides then a reduced accessibility for PAA chains at high I_s ^[38].

Further dilution with water favors the release of trapped counter ions by increasing the spacing between branches^[39], which in turn loosen the compact structure of $bPEI$ at high ionic strength. As a result, the short PAA chains can diffuse easily and interact with the branched chains. This hypothesis implies that $bPEI$ chains shifted down the I_b as they require more water to release their trapped counter ions, and giving an easy access to macro anions. As mentioned earlier, high Mw PEs should normally form large size aggregates. Here the reduced size of the $bPEI/PAA$ aggregates compared to $\ell PEI/PAA$ ones was likely due to the condensing ability of $-NH_2$ of $bPEI$ with $-COOH$ group of PAA^[40], a feature not seen for ℓPEI where $-NH_2$ groups are very few. The role of counter ions release during complexation strongly depends here on the dilution stage.

Electrostatic complexation fundamentals

Furthermore effective “screening” was not found for the PAA/PAH system, even beyond 3M where hydrophobic interactions are suspected to play a role as both individual PEs are known to have hydrophobic behavior (surface activity) at high salt concentration. Tirrell and co-workers^[41] have shown however that at high NaCl concentration, the stoichiometric complexes obtained from this PEs pair successfully underwent a transition from precipitated to highly transparent state. It is therefore necessary to pay more attention to this system and figure out the origin of these contradictory results.

We have shown here that the previous copolymer based co-assembly strategy could be generalized to strong and weak polyelectrolytes. The “desalting transition” is then a “universal phenomenon” independent of the nature of the PEs considered^[42]. Nevertheless, Mws and possible conformations of PEs^[37] have a great impact on the onset of the transition I_b and the size of the final aggregates. Furthermore, those results emphasize that the electrostatic complexes formation is strongly influenced by secondary forces such as H-bonding and hydrophobic interactions. Our observations clearly indicate that salt is an efficient parameter to tune the electrostatic interactions when the complexation is driven solely by electrostatic forces. This trigger will be used in chapter 3 to control the co-assembly of oppositely charged hybrid BBs.

Besides, Figure 1.4 displays a neat split in I_b between symmetric and asymmetric systems. Secondary forces, Mw and architecture might be the key factors behind this spread. Their impacts on the complex formation must be investigated in near future. In order to increase our understanding of the mechanism(s) driving the complexation, preliminary ITC experiments between oppositely charged PEs from symmetric and asymmetric systems in the absence of salt will now be discussed. It should be noted however, that the monitoring of the “desalting transition” itself inside an ITC cell is a perspective experiment beyond the scope of this Ph.D and will be planned in the near future.

Isothermal Titration Calorimetry

Asymmetric System

Electrostatic complexation between PAA_{2k}/PDDAC_{100k} PEs

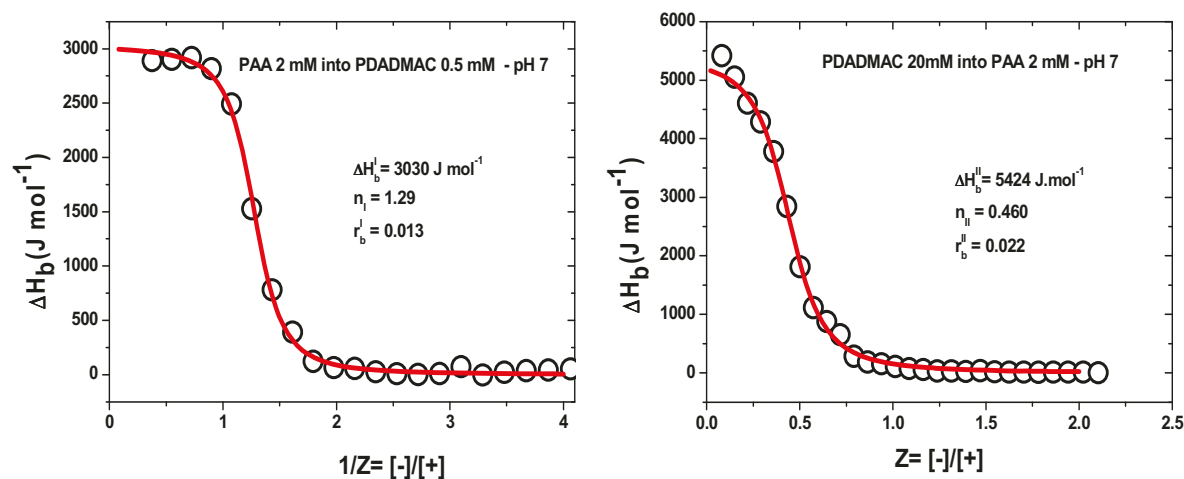


Figure 1. 5 : Type I and II ITC binding isotherms at pH=7 resulting from the addition (left) of a 2mM PAA solution into a 0.5 mM PDDAC solution and (right) of 20mM PDDAC solution into a 2mM PAA solution. Red lines represent the MNIS fit to the data.

PAA/PDDAC is one of the most frequently used pairs for IPEC formation in solution and at interface as well. The IPEC formation is predominantly driven by ion-dipole interactions between $-\text{COOH}$ groups of PAA and quaternary nitrogen atoms of PDDAC. We have measured the complex formation enthalpy at pH ~ 7 as PAA is almost fully ionized (PDDAC is independent of pH). ITC experiments were carried out in two ways: PAA was injected into PDDAC (type I experiment), or PDDAC was injected into PAA (type II). The derivative of the heat changes was expressed as a function of the charge ratio (Z). As seen in Figure 1.5, both types of experiments showed a typical sigmoidal drop of the binding isotherm as more titrant was injected. In both cases, the complexation was associated with an endothermic (“positive ΔH ”) process.

What can we say at this stage? Many reports in the literature are showing both positive and negative enthalpy for experiments performed on the same system (but likely not the same conditions) suggesting that we are still away from complete understanding. The complexation free energy ΔG , between oppositely charged PEs might include several contributions including the release of the counter ion, the partial removal of the hydration

Electrostatic complexation fundamentals

shell around ionized groups and the formation of the complex itself. Bringing a chloride anion and a sodium cation together in water for example is an endothermic process and not an exothermic process as one could imagine. This highlights the high complexity of such thermodynamic signature. Nevertheless, we can likely say that when the complexation is exothermic (negative ΔH) both enthalpy and entropy changes favor the complexation giving rise to much stronger complexes.

At pH = 7, the PAA chains are almost fully ionized (pKa 4.5) and offer more “coulombic” binding sites for the strong PDDAC polycations resulting here in a purely endothermic complexation suggesting a complexation driven by entropy through the release of the counter-ions. The different thermodynamic quantities drawn from the MNIS model are gathered in Table 1.2. The entropy contribution clearly dominates the complexation process for both types of experiment.

Type	$n=[+]/[-]$	$K_b (M^{-1})$	$\Delta G (kJ.mol^{-1})$	$\Delta H_b (kJ.mol^{-1})$	$-T.\Delta S (kJ.mol^{-1})$
I	1/1.29=0.77	1.49×10^5	-29	3.03	-32
II	0.46	2.25×10^4	-24.4	5.4	-29.8

Table 1. 2: *Thermodynamic parameters for the complexation of PAA_{2k}/PDDAC_{100k} PEs.*

The binding isotherms corresponding to different mixing orders yielded different results for the reaction stoichiometry n pointing again that thermodynamic quantities associated with out of equilibrium processes depend strongly on the formulation pathway. Both n were found different than 1 suggesting that the PAA chains were not fully ionized at pH=7 (and that effective charges were indeed different than structural charges). The entropy contribution to the overall free energy is in both cases the leading term as expected.

In the raw data (not shown here), the slight exothermic behavior seen after the saturation point in type I accounts for the binding of the titrant PAA chains with water molecules. Whereas the slight endothermic behavior seen after the saturation point in type II might be attributed to H-bond breaking by the titrant PDDAC chains. We have furthermore noticed that macroscopic precipitation only occurs in type I experiment whereas in type II, soluble complexes were observed. As PDDAC concentration was set higher, the large M_w chains wrapped the already formed aggregates giving rise to a “cationic” electro-steric

Electrostatic complexation fundamentals

stabilization of the complexes. It is important to notice that the pH is not constant during the complexation phenomena due to the release of H^+ ions from PAA.

But this endothermic behavior is not necessarily the rule for the PAA/PDDAC couple as recently reported by Alonso^[43] and Ekaterina et al^[44]. They have shown that mixing PAA and PDDAC chains at acidic pH resulted in an instantaneous macroscopic precipitation, whereas no interaction took place at high pH. The authors showed that the complexes formation is not only driven by electrostatic interactions but other secondary forces as a function of the pH are at play.

Their comprehensive study concluded that hydrogen bonding through which water molecules were linked to PAA, indeed ruled the complexation. This H-bonding or the amount of water linked to PAA was found to increase linearly with pH. This hydrated shell is an unfavorable environment for PDDAC to complex with PAA. At low pH, where PAA is less hydrated, PDDAC strongly binds with PAA and forms ion-pairs. The heat released here (exothermic) overcomes the heat required to break the few existing hydrogen bonds. The determination of negative enthalpy at acidic pH associated with exothermic process suggested that the overall interaction was strong (but no quantitative information was given).

With increasing pH, the heat associated with the binding was found to decrease and almost shifting to endothermic process, indicating a weaker complexation at high pH. At high pH, as PAA is highly hydrated, PDDAC must break much more $-H$ bonds to complex with PAA. In order to break the $-H$ bonds and favor the complexation, the system must absorb (endothermic) more heat from the surroundings as indicated by an enthalpy, close to zero at this stage. This endothermic character implies that the complexation at high pH, favored by an increase in overall entropy with the release of water molecules overcomes the heat lost through the binding of oppositely charged macro ions.

Symmetric Systems

Electrostatic complexation between PSS_{75k}/PDDAC_{100k} strong PEs

In this section, the complexation thermodynamics between two strong PEs is investigated. It should be noted that the charge densities of strong PEs are almost constant over a wide pH range. ITC experiments were carried out in two ways: PSS was injected into PDDAC (type I) or PDDAC was injected into PSS (type II).

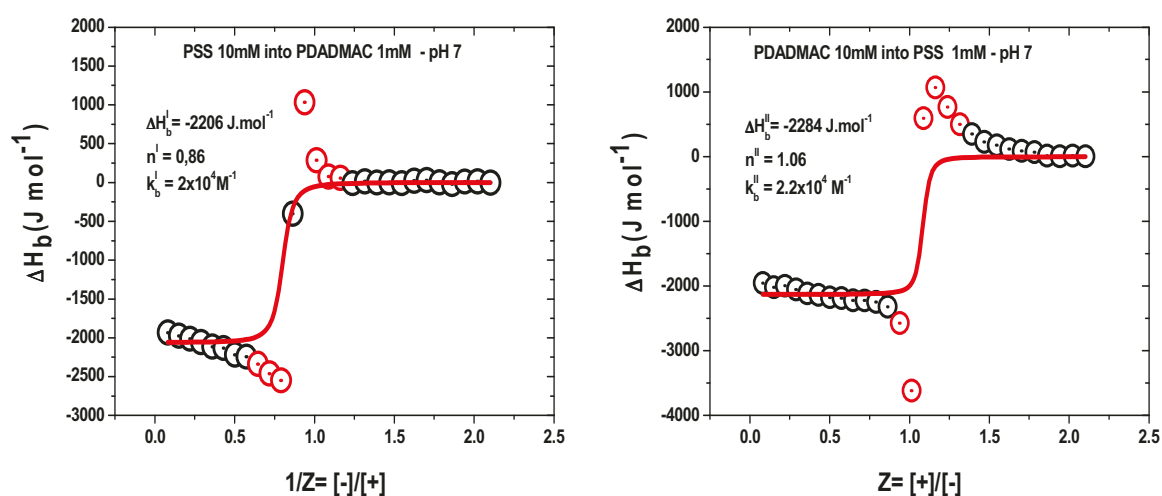


Figure 1.6 : Type I and II ITC binding isotherms at pH=7 resulting from the addition (left) of a 10 mM PSS solution into a 1 mM PDDAC solution and (right) of 10 mM PDDAC solution into a 1mM PSS solution. Red lines represent the MNIS fit to the data performed off the peaks.

Figure 1.6 indicates that both type of experiments are associated with exothermic processes suggesting that the symmetric complexation between PSS and PDDAC at pH 7 is much stronger than with the asymmetric PAA/PDDAC system and involve likely different other interactions than the electrostatic one. We can see clearly the presence of overshots in both types of experiments close to the saturation point. A feature that is not included in the MNIS model which assumes a smooth sigmoidal variation of the evolved heat. In order to retrieve some information, we did not consider the peaks in the fitting procedure as seen in Figure 1.6 (red points)^[45].

Electrostatic complexation fundamentals

The different thermodynamic quantities drawn from the MNIS model are gathered in the Table 1.3.

Type	$n=[+]/[-]$	$K_b (M^{-1})$	$\Delta G (kJ.mol^{-1})$	$\Delta H_b (kJ.mol^{-1})$	$-T.\Delta S (J.mol^{-1})$
I	1/0.86=1.16	2×10^4	-24.1	-2.2	-21.9
II	1.06	2.2×10^4	-24.4	-2.4	-22

Table 1. 3: *Thermodynamic parameters for the complexation of PSS/PDDAC.*

The complexation occurs for both types close to $n=1$ indicating a maximum complexation at charges stoichiometry. We recall that here the charge ratio Z is directly estimated via the structural charges born by the backbones as both PEs are strong. Although both the enthalpy and entropy are here driving the complexation, the entropy represents however the main contribution^[46, 47] ($\sim 90\%$) through the release of the counter-ions and water molecules trapped in iceberg structure around hydrophobic patches (see below). The strong exothermic behavior (together with the significant overshoot seen just prior the neutralization) originated likely from the swelling-shrinking and further aggregation of IPECs. Indeed, in the previous asymmetric system, PAA chains formed H-bonds with water molecules, whereas in the present case, instead of forming H-bonds, the “hydrophobic” backbones (six-membered aromatic rings of PSS and five-membered rings of PDDAC) of both strong PEs disrupted water molecules. In order to avoid such disruptions, water molecules minimize their free energy through the formation of 3D structured “cage” network where they can be connected through H-bonding. The cage like structures have indeed restricted mobility and therefore will be easily entrapped inside IPEC matrixes, inducing the swelling of the complexes through the increase of the osmotic pressure; providing a less favorable environment for the complexation.

In order to minimize the free energy, the enthalpic contribution counteracts via the strong “electrostatic interaction” between sulfonate and quaternary ammonium groups. The heat loss as a result of binding of PEs will then be utilized by the entrapped water molecules to expel themselves from the matrix to the bulk solution with the release of counter ions by breaking the dynamic hydrogen bonding between them. Consequently the hydrophobic aromatic rings of both PEs interact via hydrophobic interaction^[48] while the sulfonate and quaternary ammonium interact through strong electrostatic interaction. These strong

Electrostatic complexation fundamentals

interactions promote the shrinking of IPEC and form insoluble stoichiometric complexes with a maximum heat released. This plausible explanation concludes that the strong association between strong PEs is driven by a combination of hydrophobic and electrostatic interaction. The observed overshoot for type II is associated with the formation of huge electrostatic aggregates favored by PDDAC chains bridging the already formed smaller aggregates. The appearance of endothermic peaks after the saturation point might be influenced by Na-Cl formation^[39].

Electrostatic complexation between PAA_{2k}/bPEI_{25k} weak PEs

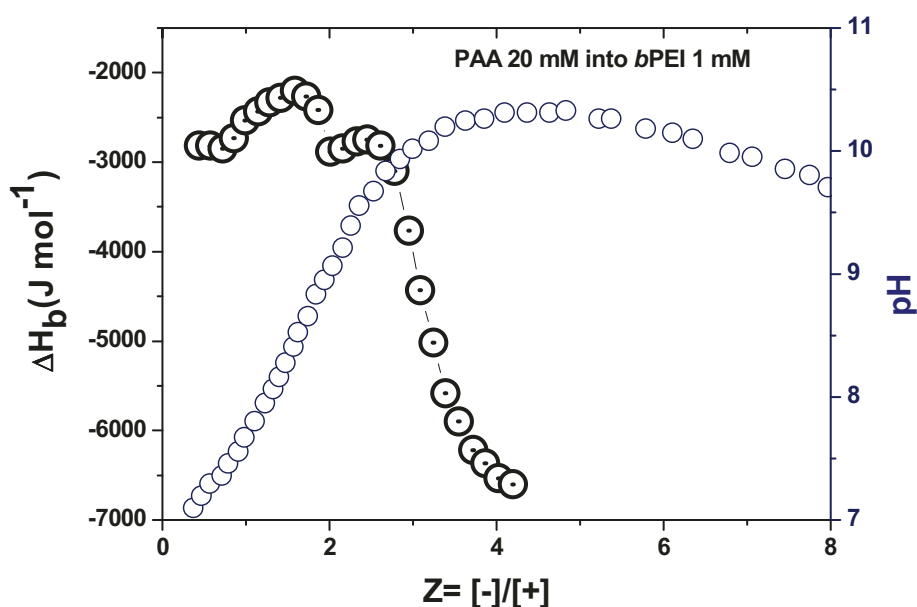


Figure 1.7 : Incomplete ITC titration of 20 mM solution of PAA_{2k} into 1 mM solution of bPEI_{25k} accompanied by a variation of pH during the complexation. pH monitoring was made outside of the ITC with a pH meter cell in order to handle more solution).

Figure 1.7 shows the binding isotherm of low Mw PAA_{2k} chains with branched bPEI_{25k} chains at pH-7. It is important to note that at this specific pH, nitrogen and carboxyl groups from polybase and polyacid respectively can be present in both ionized and non-ionized forms. Furthermore, bPEI offers 3 types of amines (primary, secondary and tertiary

Electrostatic complexation fundamentals

amines) with very different pK_as. It is then very difficult to figure out accurately the effective charge ratio Z at a given pH.

The strong exotherm reveals that the association is driven here again by both enthalpy and entropy. The binding isotherm curve clearly shows that the complexation is a two-step process in agreement with the two stages complexation observed in the desalting transition (see Figure 1. 4). Unfortunately, the titration is incomplete likely due to a continuous proton transfer between the weak PEs. The detailed interpretation behind the complexation process is then difficult to capture entirely. Indeed, the isothermal curve was stopped after the charge ratio 4, because a further addition of titrant was not possible as it exceeded the cell capacity. The initial concentrations must then be tuned beyond the sole volume to enable a full titration.

Tentatively, the observed increase in pH during the titration might indicate the consumption of protons released by the PAA chains (acid, proton donor) by the weak *b*PEI chains (base, proton acceptor). Consequently, the protonated *b*PEI amines interact with the COO^- groups of the PAA through H-bonding and form ion-pair intermediates ($\text{COO}^- \text{---} \text{NH}_3^+$, carboxylate salt intermediate) illustrated by the presence of two distinct peaks in the isothermal curve. In agreement with Maustrad et al^[49], the first one is likely associated with the formation of carboxylate salt intermediates between ---NH_3^+ and ---COO^- groups ; the second reflects the aggregation of those intermediates via bridging/wrapping triggered by the large *b*PEI chains. The large exotherm drop observed then is associated with the hydration of PAA chains by water molecules.

Due to the incompleteness of the titration, the thermodynamic features cannot be derived. Albeit reports^[50] have shown that the end point of the titration curve between polyamines and polyacids was normally ruled by entropy. This observation might hold here as well through the large release of the entrapped counter ions in the branched structure of *b*PEI.

Generally a complete complexation occurs at charge stoichiometry. Accurate calculations must then be done in near future to determine the effective charge ratio between *b*PEI and PAA, in order to observe the real end point associated with this complexation process. It is important to pay more attention in determining the number of charges on each type of amines at a given pH for both *l*PEI_{2k} and *b*PEI_{2.5k} PEs.

Electrostatic complexation fundamentals

Finally, this specific ITC experiment suggests that a complete understanding of the complex formation between weak-weak PEs is complicated due to the continuous variation of pH during the titration and the presence of different interactions such as electrostatic and H-bondings. In order to understand the real influence of H-bonding on the complexation, it would be interesting in the future to perform the ITC experiment in the presence of urea, a known H-bonding breaker. Nevertheless, such ITC experiment highlights that conformational effects, M_w s and the protonation state of different types of amines are playing an important role in the complexation process and cannot be forgotten.

Conclusions

We have shown that the desalting transition triggered by the electrostatic interaction is a general phenomenon seen on all PE pairs investigated and independent of the PE building block features. Although the specific characteristics of each oppositely charged component induce some differences, the pathway between an aggregated and unaggregated state triggered by the sole electrostatic interaction presents a “universal behavior” independent of the features of PE building blocks. More specifically, it highlights a neat split in I_b between the symmetric systems (weak/weak, strong/strong PEs) and asymmetric ones (weak/strong PEs). The salt concentration required to *turn off* the “electrostatic” interaction between the PEs of symmetric systems was found higher than for asymmetric ones. Furthermore, the sizes of the aggregates depended strongly on the nature of the complexing macromolecules such as block or homopolymers, linear or branched structure and Mws. In the case of *bPEI*_{25k}, the transition proceeds throughout a two-step process indicative of the formation of ion-pair and aggregates. The conformation of *bPEI* played an important role in delaying the I_b to lower concentration of salt.

On the thermodynamics point of view, ITC gave basic and useful information on the complexation between the oppositely charged PEs of asymmetric and symmetric systems. The preliminary experiments showed that the complexes formation was driven by entropy in all cases, although enthalpy participated to the minimization of the free energy in the symmetric systems (exotherms); likely the signature of secondary forces at play beyond the sole electrostatic interaction as the hydrophobic effect and/or hydrogen bonding. Indeed, the IPEC formation of the asymmetric system was purely endothermic and consequently driven by the sole entropy associated to the counter ions (and water molecule) release. In the case of both symmetric systems, the IPEC formation was mainly exothermic indicating the presence of extra forces (hydrophobic interactions, hydrogen bonding...) leading to a complexation driven by entropy and enthalpy.

Furthermore, ITC experiments revealed that the PAA/*bPEI* complexes formation was associated with a two steps process well correlated with the two stages observed in the desalting transition. The absence of end point in the complex formation of weak PEs suggests that attention must be paid ahead to estimate the effective charge ratio and the pH at a given concentration in order to get good ITC data and derive useful thermodynamics parameters; especially for PEs like *bPEI* presenting all three types of amines. Finally, the desalting and

Electrostatic complexation fundamentals

ITC experiments put forward that beyond electrostatic forces, secondary forces play a key role in the formation of PEs complexes.

References

1. Lankalapalli, S. and V.R.M. Kolapalli, *Polyelectrolyte complexes: A review of their applicability in drug delivery technology*. Vol. 71. 2009. 481-487.
2. Wang, Y., J.Y. Gao, and P.L. Dubin, *Protein separation via polyelectrolyte coacervation: Selectivity and efficiency*. *Biotechnology Progress*, 2008. **12**(3): p. 356-362.
3. Bhatia, S.R., S.F. Khattak, and S.C. Roberts, *Polyelectrolytes for cell encapsulation*. *Current Opinion in Colloid & Interface Science*, 2005. **10**(1-2): p. 45-51.
4. Philipp, B., et al., *Polyelectrolyte complexes-recent developments and open problems*. *Progress in Polymer Science*, 1989. **14**(1): p. 91-172.
5. Schmitt, C., et al., *Structure and Technofunctional Properties of Protein-Polysaccharide Complexes: A Review*. *Critical Reviews in Food Science and Nutrition*, 1998. **38**(8): p. 689-753.
6. Anajwala, C. and S. Dakhara, *Polyelectrolyte complex: A pharmaceutical review*. Vol. 1. 2012. 121-127.
7. Bungenberg-de-Jong, Elsevier, 1949: p. 335.
8. Sui, Z., J.A. Jaber, and J.B. Schlenoff, *Polyelectrolyte Complexes with pH-Tunable Solubility*. *Macromolecules*, 2006. **39**(23): p. 8145-8152.
9. Spruijt, E., et al., *Binodal Compositions of Polyelectrolyte Complexes*. *Macromolecules*, 2010. **43**(15): p. 6476-6484.
10. Lemmers, M., et al., *The influence of charge ratio on transient networks of polyelectrolyte complex micelles*. *Soft Matter*, 2012. **8**(1): p. 104-117.
11. Berret, J.F., *Stoichiometry of Electrostatic Complexes Determined by Light Scattering*. *Macromolecules*, 2007. **40**(12): p. 4260-4266.
12. Decher, G., *Fuzzy Nanoassemblies: Toward Layered Polymeric Multicomposites*. *Science*, 1997. **277**(5330): p. 1232-1237.
13. Reyes, D.R., et al., *Micropatterning Neuronal Cells on Polyelectrolyte Multilayers*. *Langmuir*, 2004. **20**(20): p. 8805-8811.
14. Schmidt, I., et al., *Spatial Structure and Composition of Polysaccharide-Protein Complexes from Small Angle Neutron Scattering*. *Biomacromolecules*, 2009. **10**(6): p. 1346-1357.
15. Wagner, K., et al., *Direct Evidence for Counterion Release upon Cationic Lipid-DNA Condensation*. *Langmuir*, 1999. **16**(2): p. 303-306.
16. Bronich, T.K., et al., *Effects of Block Length and Structure of Surfactant on Self-Assembly and Solution Behavior of Block Ionomer Complexes*. *Langmuir*, 1999. **16**(2): p. 481-489.
17. Yokota, K., et al., *Stabilization and controlled association of inorganic nanoparticles using block copolymers*. *EPL (Europhysics Letters)*, 2007. **69**(2): p. 284.
18. Berret, J.F., K. Yokota, and M. Morvan, *Interactions Between Polymers and Nanoparticles: Formation of <<Supermicellar>> Hybrid Aggregates*. *Soft Materials*, 2004. **2**(2-3): p. 71-84.
19. Qi, L., et al., *Organic versus hybrid coacervate complexes: co-assembly and adsorption properties*. *Soft Matter*, 2008. **4**(3): p. 577-585.
20. Qi, L., et al., *Stability and Adsorption Properties of Electrostatic Complexes: Design of Hybrid Nanostructures for Coating Applications*. *Langmuir*, 2007. **23**(24): p. 11996-11998.
21. Qi, L., et al., *Influence of the Formulation Process in Electrostatic Assembly of Nanoparticles and Macromolecules in Aqueous Solution: The Mixing Pathway*. *The Journal of Physical Chemistry C*. **114**(30): p. 12870-12877.
22. Qi, L., et al., *Redispersible Hybrid Nanopowders: Cerium Oxide Nanoparticle Complexes with Phosphonated-PEG Oligomers*. *ACS Nano*, 2008. **2**(5): p. 879-888.
23. Qi, L., et al., *Influence of the Formulation Process in Electrostatic Assembly of Nanoparticles and Macromolecules in Aqueous Solution: The Interaction Pathway*. *The Journal of Physical Chemistry C*, 2010. **114**(39): p. 16373-16381.

Electrostatic complexation fundamentals

24. Destremaut, F., et al., *Microfluidics with on-line dynamic light scattering for size measurements*. Lab on a Chip, 2009. **9**(22): p. 3289-3296.
25. Fresnais, J., C. Lavelle, and J.F. Berret, *Nanoparticle Aggregation Controlled by Desalting Kinetics*. The Journal of Physical Chemistry C, 2009. **113**(37): p. 16371-16379.
26. Fresnais, J., et al., *Electrostatic Co-Assembly of Iron Oxide Nanoparticles and Polymers: Towards the Generation of Highly Persistent Superparamagnetic Nanorods*. Advanced Materials, 2008. **20**(20): p. 3877-3881.
27. Qi, L., et al., *Influence of the Formulation Process in Electrostatic Assembly of Nanoparticles and Macromolecules in Aqueous Solution: The Interaction Pathway*. The Journal of Physical Chemistry C. **114**(39): p. 16373-16381.
28. Freyer, M.W. and E.A. Lewis, *Isothermal titration calorimetry: experimental design, data analysis, and probing macromolecule/ligand binding and kinetic interactions*. Methods in cell biology, 2008. **84**: p. 79-113.
29. Bharadwaj, S., R. Montazeri, and D.T. Haynie, *Direct Determination of the Thermodynamics of Polyelectrolyte Complexation and Implications Thereof for Electrostatic Layer-by-Layer Assembly of Multilayer Films*. Langmuir, 2006. **22**(14): p. 6093-6101.
30. Feng, X., M. Leduc, and R. Pelton, *Polyelectrolyte complex characterization with isothermal titration calorimetry and colloid titration*. Colloids and Surfaces A: Physicochemical and Engineering Aspects, 2008. **317**(1-3): p. 535-542.
31. Oppermann, W. and T. Schulz, *Interaction between oppositely charged polyelectrolytes in aqueous solution*. Makromolekulare Chemie. Macromolecular Symposia, 1990. **39**(1): p. 293-299.
32. Nyström, R., et al., *Mixtures of cationic starch and anionic polyacrylate used for flocculation of calcium carbonate-influence of electrolytes*. Colloids and Surfaces A: Physicochemical and Engineering Aspects, 2004. **234**(1-3): p. 85-93.
33. Priftis, D., N. Laugel, and M. Tirrell, *Thermodynamic Characterization of Polypeptide Complex Coacervation*. Langmuir, 2012. **28**(45): p. 15947-15957.
34. Wiseman, T., et al., *Rapid measurement of binding constants and heats of binding using a new titration calorimeter*. Analytical Biochemistry, 1989. **179**(1): p. 131-137.
35. Pierce, M.M., C.S. Raman, and B.T. Nall, *Isothermal Titration Calorimetry of Protein-Protein Interactions*. Methods, 1999. **19**(2): p. 213-221.
36. Yan, M., et al., *Magnetic Nanowires Generated via the Waterborne Desalting Transition Pathway*. ACS Applied Materials & Interfaces. **3**(4): p. 1049-1054.
37. Etrych, T., et al., *Polyelectrolyte complex formation and stability when mixing polyanions and polycations in salted media: A model study related to the case of body fluids*. European Journal of Pharmaceutical Sciences, 2005. **25**(2-3): p. 281-288.
38. Borisov, O.V. and E.B. Zhulina, *Effects of ionic strength and charge annealing in star-branched polyelectrolytes*. The European Physical Journal B-Condensed Matter and Complex Systems, 1998. **4**(2): p. 205-217.
39. Laugel, N., et al., *Relationship between the Growth Regime of Polyelectrolyte Multilayers and the Polyanion/Polycation Complexation Enthalpy*. The Journal of Physical Chemistry B, 2006. **110**(39): p. 19443-19449.
40. Sun, C., et al., *Molecular Dynamics Simulations of DNA/PEI Complexes: Effect of PEI Branching and Protonation State*. Biophysical journal, 2011. **100**(11): p. 2754-2763.
41. Chollakup, R., et al., *Phase Behavior and Coacervation of Aqueous Poly(acrylic acid)-Poly(allylamine) Solutions*. Macromolecules, 2010. **43**(5): p. 2518-2528.
42. Yan, M., et al., *Magnetic Nanowires Generated via the Waterborne Desalting Transition Pathway*. ACS Applied Materials & Interfaces, 2011. **3**(4): p. 1049-1054.
43. Alonso, T., et al., *Study of the multilayer assembly and complex formation of poly(diallyldimethylammonium chloride) (PDADMAC) and poly(acrylic acid) (PAA) as a function of pH*. Soft Matter, 2012. **9**(6): p. 1920-1928.

Electrostatic complexation fundamentals

44. Litmanovich, E.A., et al., *Unusual Phase Behavior of the Mixture of Poly(acrylic acid) and Poly(diallyldimethylammonium chloride) in Acidic Media*. *Macromolecules*, 2010. **43**(16): p. 6871-6876.
45. Kim, W., Y. Yamasaki, and K. Kataoka, *Development of a Fitting Model Suitable for the Isothermal Titration Calorimetric Curve of DNA with Cationic Ligands*. *The Journal of Physical Chemistry B*, 2006. **110**(22): p. 10919-10925.
46. Qiao, B., J.J. Cerda, and C. Holm, *Poly(styrenesulfonate)-Poly(diallyldimethylammonium) Mixtures: Toward the Understanding of Polyelectrolyte Complexes and Multilayers via Atomistic Simulations*. *Macromolecules*. **43**(18): p. 7828-7838.
47. Bucur, C.B., Z. Sui, and J.B. Schlenoff, *Ideal Mixing in Polyelectrolyte Complexes and Multilayers: Entropy Driven Assembly*. *Journal of the American Chemical Society*, 2006. **128**(42): p. 13690-13691.
48. Bai, G., et al., *Microcalorimetric Evidence of Hydrophobic Interactions between Hydrophobically Modified Cationic Polysaccharides and Surfactants of the Same Charge*. *The Journal of Physical Chemistry B*, 2007. **111**(39): p. 11453-11462.
49. Maurstad, G., S. Kitamura, and B.T. Stokke, *Isothermal titration calorimetry study of the polyelectrolyte complexation of xanthan and chitosan samples of different degree of polymerization*. *Biopolymers*, 2011. **97**(1): p. 1-10.
50. Kono, K., F. Tabata, and T. Takagishi, *pH-responsive permeability of poly(acrylic acid)-poly(ethylenimine) complex capsule membrane*. *Journal of Membrane Science*, 1993. **76**(2-3): p. 233-243.

Chapter 2: Highly stable cationic & anionic building blocks (BBs)

Abstract

We report on the formulation of various oppositely charged hybrid nanoscale building blocks (BBs) that are stable in highly saline conditions, composed of inorganic nanomaterials as core and organic charged polymers as shell. The inorganic material put under scrutiny are nanoparticles of cerium oxide (CeO_2), silica (SiO_2) and Multi-walled carbon nanotubes (MWCNTs). The shell (or corona) is built from either cationic branched polyethyleneimine (bPEI) or anionic polyacrylic acid (PAA) chains. The bare colloidal dispersions share the tendency to aggregate beyond 10^{-2}M which hurdles any further assembly/complexation triggered by the ionic strength. We address the issue of overcoming the aggregation via the surface modification of the different BBs with PEs. In this context, the well known “grafting to” together with “direct mixing” explores the successful covalent functionalizations of nanocolloids with cationic and anionic PEs of opposite charges via the formation of amide linkages between complementary functional groups of amine and acid, mediated by water soluble EDC.HCl / NHS as coupling agents. The impact of non-covalent functionalization with PEs on the stabilization of MWCNTs is investigated. On the other hand, anionic CeO_2 NPs are solely developed by pure electrostatic adsorption of PAA brushes on the surface of bare CeO_2 NPs via precipitation-redispersion protocol based on “direct mixing”.

The resulting cationic and anionic hybrid materials of CeO_2 , SiO_2 and CNTs are stabilized via electrosteric forces. FT-IR and NMR spectra evidenced the covalent functionalization for all the formulated hybrids except anionic ceria, where the NPs were functionalized by electrostatic and coordination interactions. Whereas cross experiments such as DLS, DDLS, TGA and TEM experiments confirmed the successful “encapsulation” of organic charged polymers over the inorganic cores. Dynamic light scattering and zeta potential are used to investigate the stability features of these hybrid BBs under high ionic strength and a large pH range. Light scattering demonstrates that formulated core-shell structures exhibited excellent and prolonged stability in high saline conditions up to 4M of NH_4Cl . The results obtained demonstrate that covalent attachment of PEs is a promising way to obtain highly stable hybrid NPs dispersions. This unique property turned out those core-

Highly stable & oppositely charged building blocks

shell NPs as suitable candidates to build-up functional complexes in bulk and at surfaces through the fine tuning of “desalting transition” where clusters with different morphology are generated by a controlled electrostatic co-assembly process between oppositely charged components.

Introduction

Functionalization of Nanoparticles (NPs)

As described in the introduction, one of the goals of this Ph.D work is to formulate colloidal materials that will be highly stable at high ionic strength (I_s) which can be accomplished via the functionalization of colloids surface with macromolecules or PEs^[1]. This short survey indeed represents the various functionalization strategies of NPs with PEs which were developed during the last decade. The following section helps to understand the advantages and disadvantages of each method. At the end of the discussion we have put forward the most appropriate approach which fulfills our primary goal.

In general, hydrophilic NPs are functionalized by charged PEs which can be cationic or anionic. This helps to increase the surface charge and prevent aggregation of the colloids via stabilizing electro-steric forces. On the other hand hydrophobic NPs were widely modified by copolymers comprising hydrophilic and hydrophobic segments. Hydrophobic parts are generally aromatic compounds adsorbed on the particles surface through π - π interaction while the hydrophilic part interacts with the solution media. Charge density regulated by pH, Mw, structure and size of the polymers, surface charge of the particle altogether play an essential role for effective stabilization^[2]. PEs can be incorporated on nanoparticle surface by two different approaches i) Covalent (chemisorption) where the polymers are permanently linked to the NPs and ii) Non-covalent (physisorption) based on reversible adsorption. The former can be further divided into two categories namely i) One pot synthesis, where the formation of nanoparticle and coating with monomer/PEs occur simultaneously and ii) two step synthesis, in which the nanoparticles are first synthesized and then coated with the desired PEs. They are further classified into two categories such as i) “grafting to”, where the end group of as-prepared PEs are chemically tethered on the surface of nanomaterials via ester or amide linkage ii) “grafting from”, in which the monomers are first introduced on the surface and afterwards the polymerization of desired monomer occurs by an initiating agent. The second non-covalent approach is based on weak interactions such as Van der Waals, hydrogen bonding, hydrophilic-hydrophobic and electrostatic interaction. Among which, direct mixing is an emerging approach based on electrostatic interactions to formulate hybrid materials by simply pouring the NPs dispersions into PEs dispersions.

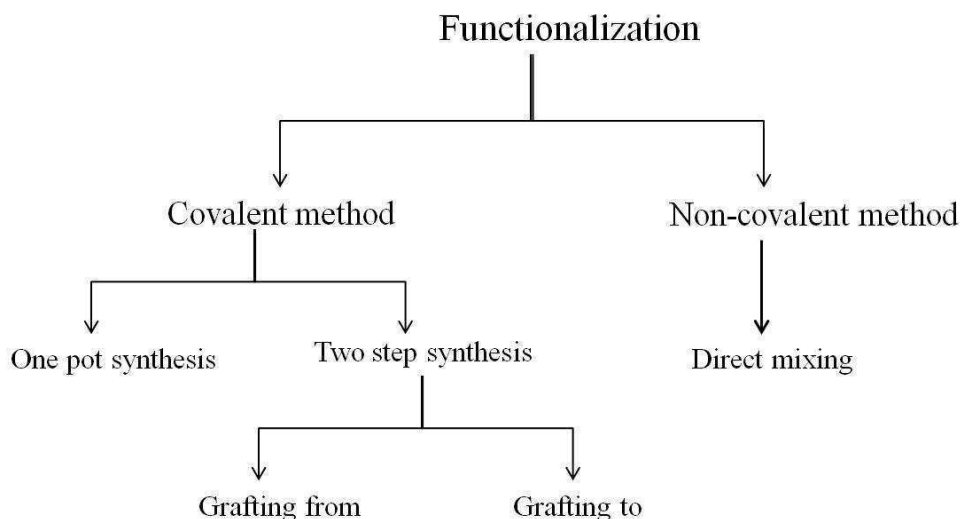


Figure 2.1 : *Different strategies for the functionalization of NPs.*

Covalent method

One-pot synthesis

As stated earlier, the fabrication of inorganic NPs from the metallic salt takes place in the presence of PEs. In that case PEs serve both as a template (nanoreactor) thereby controlling the particle size and distribution and as a stabilizing agent to avoid aggregation. The ratio of PEs to the molecular precursor and grafting density of PEs play an important role to control the size of the nanoparticles. Coating with several homo and copolymers has been successfully performed on various metal, metal oxide and semiconductor nanoparticles and was carried out via several routes namely i) coprecipitation^[3, 4] of metal salt solutions assisted by base ii) chemical reduction of metal salt^[5, 6] iii) thermal decomposition of molecular precursor^[7, 8] iv) hydrolysis^[9, 10] v) irradiation^[11, 12].

Among them chemical reduction was widely used to coat the surface of NPs. Instance, PSS encapsulated Au colloids were synthesized by chemical reduction of HAuCl_4 in the presence of reducing agent EDOT. The obtained composite acts as good catalyst in the conversion of nitro into amino groups and exhibits excellent stability in 3M NaCl ^[13]. NaBH_4 assisted reduction of CuSO_4 in PAA^[14] and PdCl_2 in PAA^[15] generated corresponding CuNPs and PdNPs each coated with the single adlayer of PAA. In the former case controlled oxidation transformed the CuNPs into nanocubes. Some literatures have shown that the wrapping PEs act as a reducing agent for metal salt without the need of external reducing

Highly stable & oppositely charged building blocks

agents. For instance Bronstein et al^[16] demonstrated the synthesis of stable AuNPs from AuCl₃ in the presence of PEI-g-PEO graft copolymer where the amine groups of PEI segment act as a reducing agent to form gold colloids.

Although the One-pot synthesis is widely used for surface functionalization, it has some limitations and drawbacks. Indeed it yields only small size NPs, due to the interference of PEs during the nucleation step^[17].

Two step synthesis

PEs are here coated on preformed NPs via “grafting from” and “grafting to” techniques. In the former, an initiator is first immobilized on the surface of NPs and afterwards the polymerization of desired monomers takes place from the surface. While in the later, the active end groups of the commercially available PEs chains are tethered to the surface. Both of these grafting techniques were found to be an effective way for the surface modification of NPs. These grafting techniques improved the dispersion stability of colloids in a large number of organic solvents. But each has its own advantages and disadvantages.

Grafting from

In the “grafting from” approach, the polymer is grown outward from the nanoparticles surface by radical polymerization through different strategies namely ring opening metathesis polymerization (ROMP), atom transfer radical polymerization (ATRP), reversible-addition fragmentation chain transfer (RAFT), nitroxide-mediated polymerization (NMP). This grafting from technique has been successfully applied to many metal oxides (titanium, iron, nickel, zinc, magnesium) and semi-conductors (CdSe and CdS) NPs surfaces. Among the various strategies available ATRP and RAFT have been widely used where respectively ATRP and RAFT agent acts as an initiator. All the above mentioned routes rely to anchor one end of the initiator species on the desired NPs surface and then the graft polymerization of desired monomers proceeds from the other end of the initiator under appropriate conditions. Although, the primary scope behind this modification is to prevent the aggregation of NPs, more attention has been given to improve the dispersibility of hybrids in organic solvents. An increasing number of works were carried out on the inorganic core of iron and silica NPs. Of which iron NPs receive more attention as they are less toxic, biodegradable and their excellent magnetic property can be exploited in Magnetic Resonance Imaging (MRI)^[18].

Highly stable & oppositely charged building blocks

Independent of the core type, the key step to achieve stable dispersion is an irreversible interaction between initiators and the metal particle surface. If the initiators are not permanently linked, NPs tend to aggregate due to their high surface energy^[19, 20]. For instance, chloropropionic acid (ATRP initiator) physisorbed on MnFe_2O_4 surface^[21], yield aggregated dispersion due to the weak non covalent and reversible interaction between anchored carboxyl moiety and NPs surface. The issue was circumvented by silane and chloro initiators^[22, 23]. For instance, Sun *et al.*^[24] successfully replaced the oleic acid and established the covalent bond between their novel silane initiator “2-bromo-2-methyl-N-(3-(triethoxysilyl)propyl) propanamide” and particle surface of Fe_3O_4 . The initiator functionalized NPs graft polymerized with styrene monomer and produce PS brushes around the core assisted by copper catalyst.

Although “grafting from” technique is able to provide high grafting density of PEs on NPs surface, it has several disadvantages, and requires harsh conditions typically high temperature, large amount of catalyst and long reaction time to achieve desired Mw. Furthermore it is tedious to remove the catalyst completely from the final polymers^[25]. In case of RAFT polymerization, the RAFT agents are not commercially available and their synthesis involves multistep with low yields^[26]. In conclusion, all the radical based polymerizations involve long synthetic pathways to achieve a desirable hybrid material thus they are time and energy consuming approach.

Grafting to

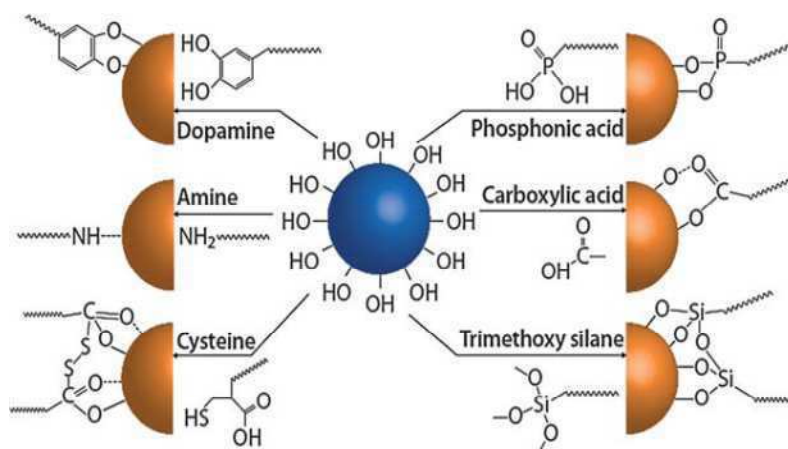


Figure 2.2 : Attachment of several functional groups on Fe-OH NPs.

Highly stable & oppositely charged building blocks

Unlike “grafting from”, “grafting to” allows control over Mw and PDI as the prefabricated polymers are utilized. This method is a versatile way to modify the NPs surface where the active end groups of polymers reacts with complementary functional groups on surface of nanoparticles. The polymers employed are commercially available or sometimes synthesized via anionic, radical or other polymerization techniques. Several groups such as carboxyl, alkyl silane, phosphonic acid, alkyl, aromatic amines and thiols can be covalently attached to the metal surfaces and those functionalities indeed act as a cross linker between PEs and NPs via the formation of covalent linkages as shown in the Figure 2.3^[27].

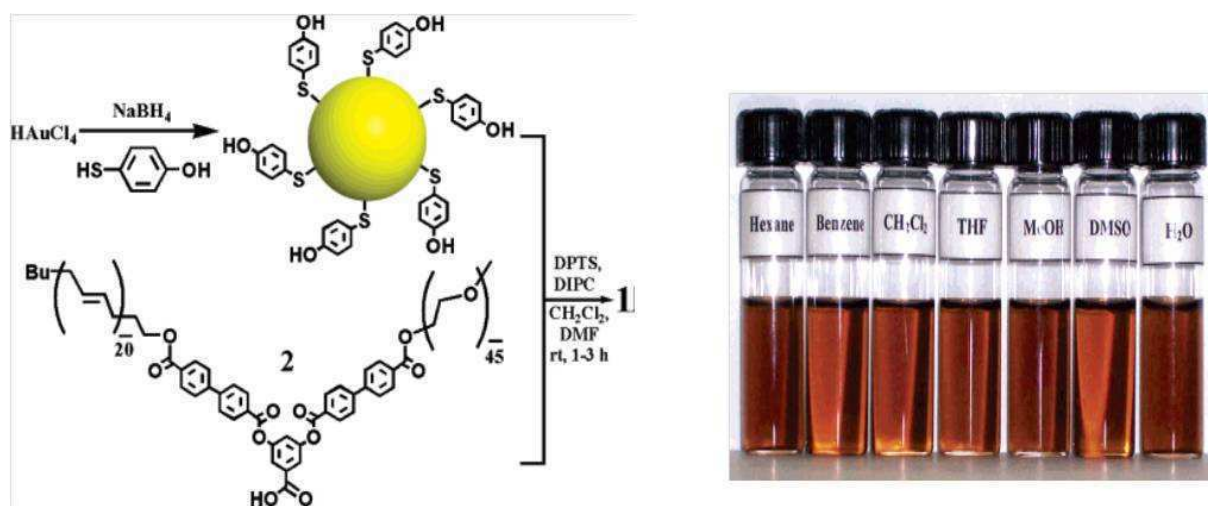


Figure 2.3 : Synthesis of V-shaped AuNPs (left), and their solubility in a variety of solvents (right).

V-shaped amphiphilic polymers comprising polybutadiene-polyethyleneglycol (PB-PEG) having carboxyl group as their meeting point underwent the esterification reaction with hydroxyl group of mercaptophenol functionalized AuNPs via thiol cross linker. The resultant amphiphilic hybrid NPs were soluble in a broad range of solvents^[28]. Unfortunately in “grafting to”, the number of polymer chains grafted per particle is not high but can be accomplished by other techniques such as “click chemistry”^[29]. Click chemistry being a growing synthetic approach in conjugate preparation and mainly takes place between azide and alkyne in the presence of copper catalyst. It exhibits numerous applications almost in all fields due to its reliability, selectivity and simplicity.

Highly stable & oppositely charged building blocks

The first report of click reactions together with RAFT explored the surface modification of silica NPs by homo and block copolymers. Functionalization of alkyne terminated PS, PAAm and PS-*b*-PMA synthesized by RAFT/ATRP with the azide modified silica NPs using click reaction in presence of Cu catalyst, indeed offered high grafting densities^[30].

As can be seen from the above discussions, the “grafting to” has several advantages such as control over PDI, Mw allowing a thorough characterization of the polymer solution before coating the NPs. However, some limitations do exist, like the difficulty in achieving high grafting densities. Although it can be satisfied by click chemistry, the later possess drawbacks as special operating conditions and some specific groups such as azide and alkyne on both NPs and polymer chains, thereby involving many steps and thus a time and energy consuming approach as well.

Most of the works in the literatures were however focused mainly on generating stable dispersion of NPs in non aqueous solvents. Very few papers were indeed devoted to the stability of hybrid materials building blocks towards high ionic strength.

Non-Covalent method

Direct mixing

“Direct mixing” is an emerging platform where hybrid materials are fabricated by simply mixing dilute dispersions of NPs and PEs. The formulation of hybrid materials is mainly driven by electrostatic adsorption of charged PEs with oppositely charged colloids. This versatile technique is a promising pathway to coat single NP with an adlayer of PE and provides an excellent opportunity to tune the physio-chemical properties of the resulting electrosteric stabilized hybrid nano materials. In addition the adsorbed PEs allow subsequent deposition of various species based on this approach or via other methods such as “grafting to”. Direct mixing has received more attention in recent years due to the ease and scaling up properties of the process. Besides, achieving much higher yield or grafting density is more simple as compared to “grafting to” and “grafting from” approaches. Further, it is a reliable way to produce various novel morphological composites. For instance Decher *et al.*,^[31] formulated different morphological nano and micro pouches via this protocol by fine tuning the concentration and charge ratio between basic polyelectrolyte, NPs and multivalent ions.

Highly stable & oppositely charged building blocks

As compared to fabrication and characterization of composites, the formulation process has received much attention. Few literatures associated with the formulation process showed that indeed the order of addition of inorganic NPs and PEs affects the final morphology. Based on report from Chen^[32] and Naderi^[33], in 2010, researchers from COMPASS laboratory paid special attention on formulation process of coacervates. The authors reported that among various available mixing pathways^[34-36] such as powder-powder, powder-solution, solution-solution, the last one is the most appropriate process as it minimizes the gradient in the charge ratio (Z). At the same time, they have mentioned that the solution-solution mixing pathway does not reproduce necessarily an identical final morphology of the nanocomposites. These results strongly imply that the electrostatic coacervates formation is a formulation dependent process. Further investigations revealed that the main reason which restricts the formation of same final morphology is that formulation is an out of equilibrium process and highly dependent on the interplay between the reaction time (strength and nature of interaction) and homogenization time (mixing pathway and time). This urged the authors to go a step further to deeply explore the influence of mixing and interaction pathways on the final morphology of composites.

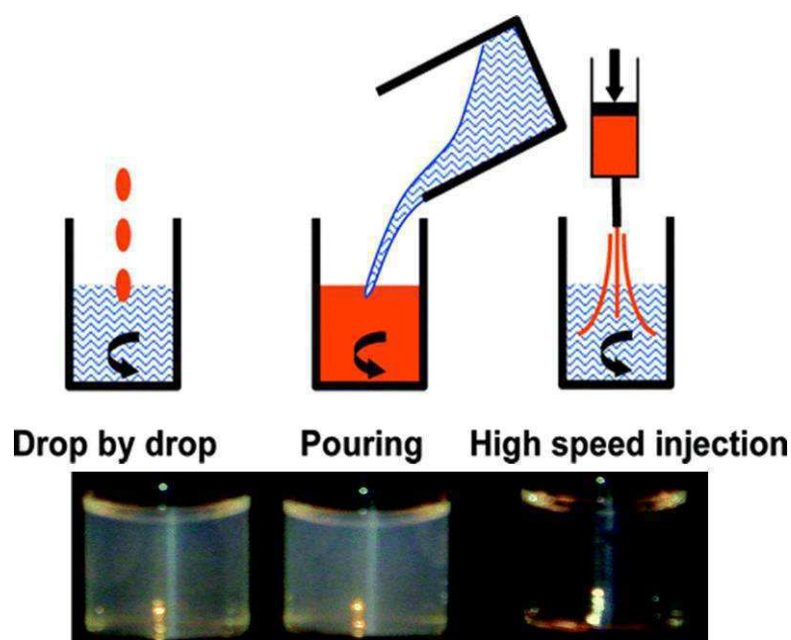


Figure 2.4 : *Different mixing orders and homogenization speeds.*

In order to understand the influence of mixing pathway, the authors have employed different mixing conditions such as “mixing order”^[34] i.e. the order of addition of one

Highly stable & oppositely charged building blocks

component into the other and mixing or homogenization speed which includes pouring, drop by drop addition, high speed injection with the help of syringe, on a system of ceria NPs and double hydrophilic block copolymers.

The investigation strongly emphasizes that high speed injection of NPs solution into polymer solution resulted in individual colloids with small polydispersity. Fast injection triggered a fast homogenization thus minimizing any local concentration inhomogeneities. Whereas other mixing pathways such as pouring, drop by drop addition and the reverse mixing order resulted in large aggregates clearly evidenced by light and neutron scattering, and cryo TEM experiments.

These authors stabilized ceria NPs with phosphonated end functionalized PEGyl oligomers using the same strategy. Freeze drying of the resulting solution yielded hybrid powder with the capacity to redisperse as single colloid in variety of organic solvents^[37].

More generally, the complexation of polymers with NPs requires some mechanical input such as ultrasound or shear treatment to produce a stable dispersion. However Berret *et al.* modified the surface of CeO₂ NPs by short homopolyelectrolytes PAA chains via electrostatic adsorption by precipitation-redispersion^[38] method without any mechanical assistance.

The method was later developed to stabilize maghemite NPs. Both anionic PE coated NPs exhibited stability in wide range of pH and ionic strength^[39]. Unlike PEGyl polymers, the PAA corona allowed further deposition or functionalization with different molecules. These observations encouraged us to exploit the “High speed injection of NPs to PEs” strategy throughout this manuscript to functionalize various NPs and nanotubes surface with various PEs. We have used homopolymers rather than copolymers to have a charged rather than a neutral corona. The high stability of such formulated building blocks triggered our work on the fine tuning of the electrostatic interactions between oppositely charged building blocks in bulk and at surfaces, discussed in upcoming chapters.

General Materials

Chemicals and polymers

Polyacrylic acid of different Mw (g/mol) ~2000 (2k), ~5000 (5k weight average, 50% w/v solution), ~130,000 (130k, number average), ~450,000 (450k, viscosity average) and different Mw of Polyethyleneimines (PEIs) 50% w/v solution of 750,000 (Mn 60k), 2000 (2k) and branched Polyethyleneimine (bPEI_{25k}) having Mw of 25,000 (25k), and cross linkers such as EDC.HCl (1-ethyl-3-(3-dimethyl aminopropyl) carbodiimide hydrochloride), NHS (N-hydroxysuccinimide), and Ethylenedimaine (EDA), Thionyl chloride, TEOS (tetraethyl ortho silicate), APTES (3-aminopropyl triethoxysilane), Ninhydrin were purchased from Sigma Aldrich and used without purification. Cerium oxide nanoparticles were kindly supplied by Rhodia Company. MWCNTs used in this study were received from Arkema (batch 6077) whereas the other reagent graded chemicals such as HNO₃, NH₄OH, HCl, H₂SO₄, NaOH, NH₄Cl and NaNO₃ were used as such without further purification.

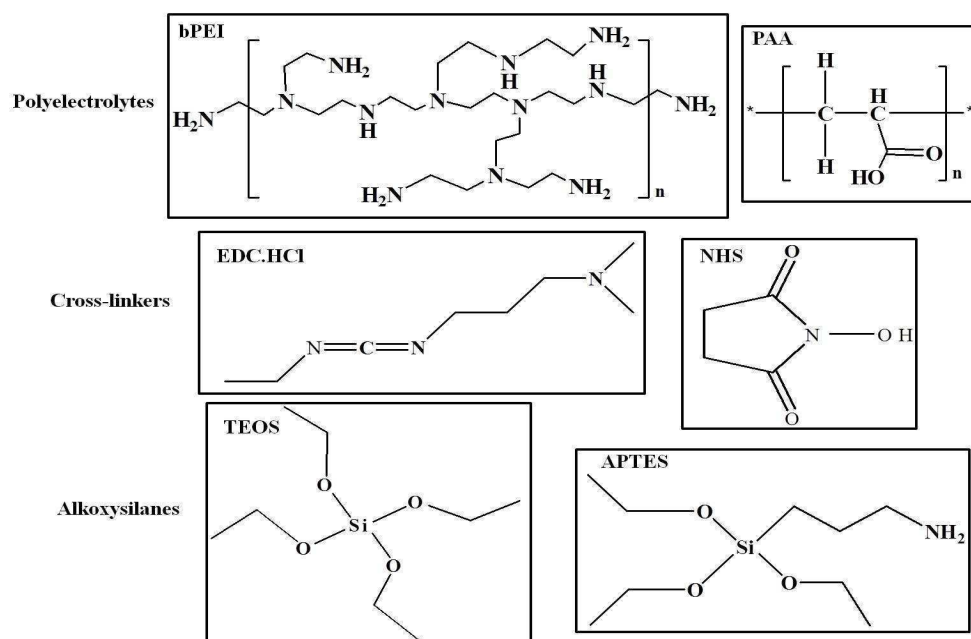


Figure 2.5 : Molecular structure of the different PEs, cross linkers and alkoxysilanes used in this study. Polymers of all Mw [a] polyethyleneimine (PEI), 25% primary, 50% secondary and 25% tertiary and b) polyacrylic acid (PAA)]. Cross-linkers [c] 1-Ethyl-3-(3-dimethylaminopropyl) carbodiimide (EDC) and d) N-Hydroxysuccinimide (NHS)]. Alkoxysilanes [e] Tetraethyl orthosilicate (TEOS) and f) (3-Aminopropyl) triethoxysilane (APTES).

Probing techniques

Characterization (for more details see “chapter 0”)

UV-Vis spectrometer

UV-Vis experiments were carried out for ceria based blocks. By taking bare nanoceria as reference, the concentration of particles in the polymer conjugate was determined by UNICAM UV-Vis spectrometer. All the measurements were carried out at room temperature and at wavelengths ranging from 200 nm to 500 nm. Dil.HNO₃ of pH~1.5 was used as a reference for bare ceria whereas for other BBs the baseline correction was done with DI water.

FT-IR spectroscopy

FT-IR spectra were recorded on NICOLET 6700 FT-IR spectrometer having diamond as reference material. All the samples were recorded in their solid state except for the polymers alone.

Nuclear Magnetic Resonance (NMR) Spectrometer

¹H NMR spectra were recorded at room temperature with a JEOL ECS400 (400MHz) using D₂O as solvent.

Dynamic Light Scattering (DLS) & Static Light Scattering (SLS)

The average hydrodynamic radii (R_H) of bare and polymer functionalized “spherical” NPs were determined by DLS at 90°. Except bare cerium oxide NPs (CNPs at pH~1.5) and Silica NPs (pH~5), all the other polymer covered NPs were measured at neutral pH. The R_H of free polymers such as PAA_{130k}, PAA_{450k} and PEI_{60k} were measured at different angles before and after ultrasonication to estimate their final molecular weight after chain scission. Mw of CNPs and PAA functionalized CeO₂ (CPAA_{2k}) NPs were determined from SLS (Zimm plot construction). Saline stability of functional NPs comprising spherical cores were monitored by DLS only at 90°. All the experiments were carried out at 20°C at an incident wavelength of 532 nm. The impact of salt on CNT-polymer nano composites was measured at an angle of 90° and at a wavelength of 644 nm to minimize absorption.

Depolarized Dynamic Light Scattering (DDLS)

CNTs cannot be characterized by conventional DLS, because of an aspect ratio far from 1 leading to distinct translational (D_t) and rotational (D_r) diffusion coefficients. DDLS enables the separate measurement of D_t and D_r , and the subsequent determination of both the length and the diameter of the “semi-rigid” CNTs. The dimensions of functional CNTs prepared at 10^{-3} wt% were determined by DDLS experiment carried out at 20°C at multiple angles starting from $\Theta=30^\circ$ to $\Theta=150^\circ$ at an interval of $\Theta=20^\circ$ at a wavelength of 644nm. The samples were prepared 1 week prior to the measurement to allow the large aggregates to settle down. In order to avoid thermal convection the power of the laser was set to 30mW and the slit at $400\mu\text{m}$. The scattered intensity was collected at each angle for 1.5 hrs and 1 hr for depolarized and polarized light respectively. The autocorrelation functions of the scattered light were analyzed by CONTIN program to obtain decay rates (Γ) and from that dimensions of all functional CNTs were determined according to the literature^[40] (see chapter “0”).

Thermo Gravimetric Analysis (TGA)

TGA measurements were conducted on SETARAM TAG24 from ambient temperature to 1000°C at a heating rate of $5^\circ\text{C}/\text{min}$ under argon atmosphere using 10mg of sample.

Zeta potential measurements

Zeta potential measurements were performed on Zeta Compact CAD instrument with a dispersion concentration of 1mg/ml and 0.01mg/ml for ceria, silica and CNT composites. The ionic strength was set to 10^{-3}M for short ligands attached CNTs (otherwise CNTs dispersion crashed out) and 10^{-2}M for all types of composite materials with the addition of NH_4Cl . In all experiments pH was adjusted with 0.1M HCl and NaOH.

Transmission Electron Microscopy (TEM)

High Resolution Transmission Electron Microscopy (HRTEM) was performed on bare and hybrid NPs solutions prepared at concentration of 0.1 wt% in water. A drop of solution was deposited on holey carbon grids. The drop was blotted with filter paper and subsequently stained with OsO_4 vapors in order to impart the contrast to species. The grid was then scanned under TEM microscope at a higher magnification and at liquid nitrogen temperature.

Highly stable & oppositely charged building blocks

High Power ultrasound

The ultrasound is generated with the help of Branson "Digital Sonifier S-450D" (maximum power = 400 W), equipped with a microprobe from titanium based alloy with a diameter of 3 mm. The vibration amplitude applied is 30% of the maximum vibration amplitude (228 microns) which corresponds to a power of 20 W for the given conditions and is performed by direct immersion of the microprobe into the desired suspension under ice bath to avoid the dispersion from heating and to maintain a constant temperature.

Part I - Cerium oxide nanoparticles (CeO₂ NPs)

Introduction

Among several metal oxide nanoparticles, cerium oxide nanoparticles (CNPs) also termed as “nano ceria” are one of the most wanted rare earth building blocks (BB) in today’s life since it is an excellent candidate to fulfill many industrial requirements^[41]. These particles aroused much attention in recent years owing to their special properties such as optical, catalytic, high refractive index, high specific surface area, good UV absorber, anti-oxidant and scavengers for free radicals^[42-48]. These properties broaden the applications of CNPs in various fields ranging from catalysis to cosmetics, coatings, polishing, sensor and biology^[49-53].

CNPs can be synthesized via various methods which include chemical vapor deposition (CVD)^[54], flame spray pyrolysis^[55], precipitation^[56], microemulsion^[57], combustion^[58], hydrothermal^[59] and microwave-hydrothermal methods^[60]. Of which the last one is facile and provides rapid synthesis of ceria nanorods too, but suffers drawback as it is expensive to carry out. Among the above methods, hydrothermal is an effective way to synthesize ultrafine particles usually prepared from tetravalent cerium salt precursors^[61]. All these synthetic methods produce CNPs at low pH (< 2) where the stability is imparted via electrostatic and short range hydration repulsions. The resulting acidic “as synthesized” colloidal solution is not suitable for physiological applications as they are not very stable under physicochemical parameters such as pH and salt.

For instance, Katherine *et al.*^[62] has studied the stability of CNPs under mono and divalent salts. In their study, the electrophoretic measurements and time resolved DLS together proved that an increase in concentration of mono and divalent salts beyond some extent destabilizes the colloids via formation of aggregates. Aggregation is enhanced by the attachment of particles as a consequence of weakening of electrostatic repulsion brought by the screening effect of added salt. Those aggregates lack homogeneous dispersion and hinder any further applications. The above behavior clearly indicates that physicochemical parameters especially salt stability is a key characteristic to enable the applications of CNPs in commercial, biological and environmental usage. On the contrary, only fewer reports were dealing with the stability issue of these particles under saline conditions.

Highly stable & oppositely charged building blocks

Earlier studies clearly reveal that wrapping CNPs with dispersants such as small ligands, surfactants and PEs improved the dispersibility and stability by controlling the surface interactions between nano building blocks via the formation of thin organic layer (corona, shell or adlayer) around the core^[63-66].

Small ligands such as PPEG, citric, ascorbic and oleic acids^[37, 67, 68] stabilize CNPs mainly via electrostatic adsorption. These organic functionalities improved the dispersibility and stability under wide range of pHs. The salt stability assessment indicates that citrate and PPEG coated nanoceria are stable in 1M of NaCl and NH₄Cl as well. But long term stability was not achieved. Destabilization of the dispersion and therefore aggregate formation occurs in time. This is due to the desorption of organic coatings as they are solely adsorbed physically, the interaction between ceria surface and organic corona is easily weakened by salt^[39]. Despite, citric and ascorbic coated ceria found application in biotransformation in cucumber plants where the organic shell played a key role in transformation by promoting particles dissolution into roots^[69].

On the other hand, polymer coated ceria composites are of great interest now-a-days due to applications in many fields^[70]. Studies on ceria composites prove that polymeric coatings do not affect the intrinsic properties of ceria. Indeed they facilitate the CNPs to show pH dependent unique properties thereby broadening their applications^[71]. In biological fields, the surface charge of the polymer coating helps to determine the toxicity of NPs on exposure to living cells^[72].

Besides, PEs functionalization offers both dispersibility and long term stability under salt. Unlike small ligands, PAA stabilized nanoceria sols, termed here as CPAA_{2k}, prepared by precipitation-redispersion method^[38] remains stable under 1M of salt for a long period of time^[39]. This is due to the fact that PAA chains are strongly adsorbed onto the ceria surface via their multisite attachments through electrostatic and heterometallic coordination interactions (Lewis acid-base).

So far, CPAA is the only ceria composite showing a high saline stability. No other stability reports were found especially on the cationic side. This triggered us to formulate highly stable cationic ceria as well. Bare “cationic ceria” is not stable in high molarity of salt and precipitate above 0.3M (into a shallow minimum). The formulation was carried out from CPAA as PAA functionality enables further functionalization with several moieties including cationic PEs.

Highly stable & oppositely charged building blocks

Among various cationic PEs, our choice was made to bPEI_{25k}, a weak PEs that partially dissociate as a function of the pH, offering then an extra control for the complexation and therefore widely used in NPs functionalization, biological and medicinal applications^[73, 74]. Moreover the amine functionality easily forms covalent bond with acid moieties under appropriate conditions^[75]. Even after functionalization with the NPs surface, the residual amine groups of bPEI_{25k} permit further complexations/interactions. This might bring multiple functionality, dynamic properties and applications to such composite NPs.

We report in the following section a facile route to synthesize highly stable cationic ceria NPs from CPAA_{2k} through the formation of covalent amide bond between amine groups of cationic bPEI and acid groups of PAA using EDC/NHS as cross linkers. We put forward important attributes such as i) confirmation of the covalent grafting ii) stability under high saline conditions.

Experimental Section

Synthesis of bare nanoparticle (CeO₂)

CNPs were synthesized via hydrothermal method, as described elsewhere. In short, thermohydrolysis of an acidic solution of cerium-IV nitrate salt $[\text{Ce}^{4+}(\text{NO}_3^-)]_4$ at high temperature (70°C) results in homogeneous precipitation of CNPs^[76]. The sizes of the particles were controlled by the addition of hydroxide ions during the thermohydrolysis. High resolution transmission electron microscopy (HRTEM) has shown that the nanoceria (bulk density $\rho = 7.1\text{g/cm}^3$) consists of isotropic agglomerates of 2 to 5 crystallites with typical size of 2 nm and faceted morphologies. As synthesized, CNPs are stabilized by combination of long range electrostatic forces and short range hydration interactions (including strongly bound or condensed nitrate ions). The hydrodynamic diameter is 8-10nm, depending upon synthetic conditions. The bare CNPs at pH 1.5 have a zeta potential $\zeta = +30\text{ mV}$ and an estimated structural charge of $Q_{\text{CeO}_2} = +300e$. The charges are compensated by nitrate anions in the Sternand diffuse layers surrounding each particle^[77]. Cryo-TEM analysis has give a polydispersity index $s = 0.15 \pm 0.03$ for the CNPs^[78].

Synthesis of Anionic Ceria (CPAA_{2k})

CNPs surface was wrapped with short PAA_{2k} chains through the Precipitation-Redispersion pathway^[38] based on a direct mixing protocol. In short, mixed solutions of CNPs (pH 1.5) and PAA (pH 3.5) were prepared by simple mixing of dilute solutions prepared at the same weight concentration c (1 wt%). The relative amount of each component can be monitored by the volume ratio X between particles versus polymer solutions. $X=1$ was chosen here. In a very recent publication from our group, a great attention has been paid to the mixing pathway (mixing order and homogenization speed). To optimize the formulation and to generate singlet PAA wrapped CNPs, high speed injection (using a syringe) of NPs into PAA solutions was followed. The formulation leads to macroscopic precipitation because at such low pH (~2) hydrogen bonding occurs between CeO₂ NPs surface and protonated PAA chains. After homogenization of the solution under stirring for one hour at room temperature, the pH was slowly increased by drop by drop addition of NH₄OH (0.1M). Above pH 8, the solution turned transparent due to the repulsion between the charged polymer chains covering the NPs. The size and the stability of CPAA_{2k} under salt were

Highly stable & oppositely charged building blocks

monitored by DLS. The molecular weight and the number of polyelectrolyte chains per particle were figured out with the help of SLS.

Synthesis of Polyethyleneimine functionalized Ceria (CPEI_{25k})

Polyethyleneimine functionalized ceria particles were synthesized from anionic ceria through the formation of amide bonds between –COOH groups of PAA present on the particle surface and –NH₂ groups (primary amines) of either PEI 60k, 25k or 2k by using EDC.HCl and NHS as cross linkers. 3 different formulation pathways were investigated to optimize the process.

Pathway I.

In short, anionic ceria NPs were suspended as a powder in a calculated amount of PEI of desired M_w. After adjustment of pH to 8, 2:2 equivalents of cross linkers (EDC/ NHS) calculated with respect to CeO₂-PAA_{2k} were dissolved in water, then added to the above mixture and stirred for 1 day at 50°C. The resulting product was purified and finally dissolved in water. The resulting solution appeared turbid due to presence of large aggregates (for more details see *Appendix I*).

Pathway II.

CeO₂-PAA_{2k} NPs dispersion at pH 8 was added in one shot to the calculated amount of PEI_x (pH – 11.25). After stirring at room temperature for 15 min, the pH of the reacting mixture was adjusted from 11.1 to 8. As in pathway I, cross linkers were then added and the reaction mixture was stirred for 24 hrs at 50°C. The resulting intense yellow colored viscous mixture was precipitated, centrifuged and purified. Their dispersion yielded slightly turbid solutions for all M_w investigated. The presence of such *small aggregates* is likely due to the sudden drift in the pH value of the reaction mixture during the addition of the NPs to the PE solution leading to the desorption of PAA chains from the NPs surface (for more details see *Appendix I*).

Pathway III.

The combination of “direct mixing” and “grafting to” explores the formulation of stable cationic bPEI_{25k} functionalized ceria from CPAA_{2k}. EDC.HCl and NHS were used as cross linkers in order to establish covalent amide bonds between COOH groups of CPAA and

Highly stable & oppositely charged building blocks

NH₂ groups of bPEI_{25k}^[79, 80]. The above trial experiments, guided us to improve the efficient grafting of PEI chains on individual colloids.

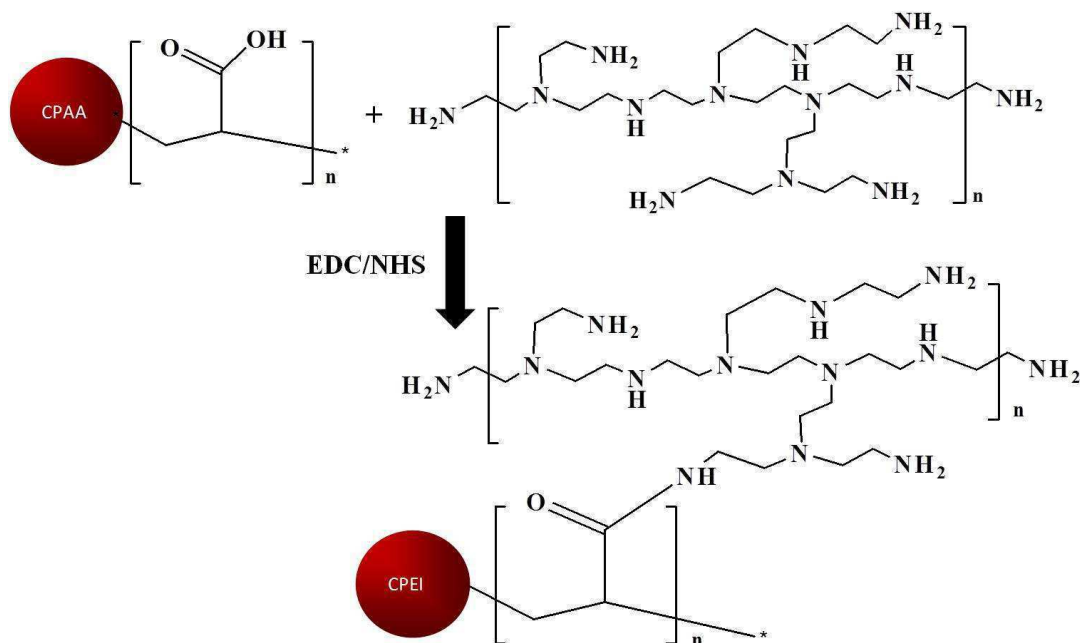


Figure 2.6 : Schematic representation of the synthetic route followed to generate stable cationic ceria via the formation of amide bonds between CPAA_{2k} and bPEI_{25k}.

CPAA_{2k} (pH 8) was added in one shot to bPEI_{25k} (pH 5 attained with HCl from native pH 11.25) at equal volume and concentration (0.1 wt%). A clear transparent solution indicated that aggregates were not formed at this stage. bPEI chains were allowed to physically adsorb on the particle surface by stirring the mixture at room temperature for 15 min. The aqueous solution of 2:2 equivalents of EDC.HCl/NHS calculated with respect to PAA moieties was added to the electrostatic complexes. The stirring was then continued for 1 day at room temperature. The solution was centrifuged at 5000 RPM for 20 min to get rid of unreacted particles if any and subsequently supernatant was subjected to dialysis. The latter was performed in Amicon ultra centrifugal filter device of MWCO 30000 at 4000 RPM for 15 min to remove loosely bound polymer chains. This purification process was repeated until the extract which is collected at the bottom of the tube showed a colorless solution with Nin-Hydrin reagent which typically yields deep violet color with PEI. The redispersion of the yellow paste collected from the filter part of the Amicon device in water resulted in

Highly stable & oppositely charged building blocks

transparent solution indicating that there were no aggregates present at the end of process as well. This strongly suggests that bPEI_{25k} chains are grafted on individual particles of CPAA_{2k}. The cationic particles (named as CPEI_{25k}) obtained were characterized by probing techniques to confirm the functionalization.

The above synthetic functionalization route was extended (PEI_{2k} and PEI_{60k}) in order to understand the impact of the Mw on the nanocomposite stability. Among the composites formulated, CPEI_{25k} exhibited excellent stability. Although the chemistry was successful in formulating CPEI_{2k} and CPEI_{60k}, the stability efficiency was influenced by the chain lengths. Indeed, PEI_{60k} PE can potentially wrap several particles together, as its chain length is quite large. However as a result, small aggregates comprising “trimers” or “tetramers” are generated which presumably influence the overall stability. PEI_{2k} PEs being much smaller, lack to encapsulate the particle completely and moreover contains a much smaller number of effective primary amines able to react covalently with the –COOH groups of the CPAA_{2k} NPs. This outcome forced us to increase the amount of PEI_{2k} PEs chains over the CPAA_{2k} NPs (at least 40 times greater by volume), in order to fully cover the NPs surface, reducing then the fraction of inorganic materials in the complexes.

The complete encapsulation/functionalization of CPAA_{2k} by bPEI_{25k} was appropriate and efficient, avoiding drawbacks seen with the smaller or larger chains. Therefore we have more specifically investigated the CPEI_{25k} system.

Results and Discussions

Characterization of bare (CNPs) and anionic Ceria (CPAA_{2k})

Light scattering

Bare CNPs provided by Rhodia and homemade anionic ceria were thoroughly characterized by DLS and SLS to determine size and Mw respectively. Self diffusion coefficient (D_0) was calculated independently for both dispersions at varying concentrations ranging from 0.1 wt% to 1 wt%. Average hydrodynamic radii (R_H) of bare and PAA coated nanoparticles were found to be $R_H = 4.3 \pm 0.2$ nm and $R_H = 9.3 \pm 0.5$ nm from their respective self-diffusion coefficient (D_0) through the Stokes-Einstein relationship. Mw, Rayleigh ratio (R_Θ) and second virial coefficient (A_2) were deduced from the generated Zimm plots. The latter was constructed by measuring the scattering intensities at different concentrations and angles (from 50° to 130° with a step of 20°).

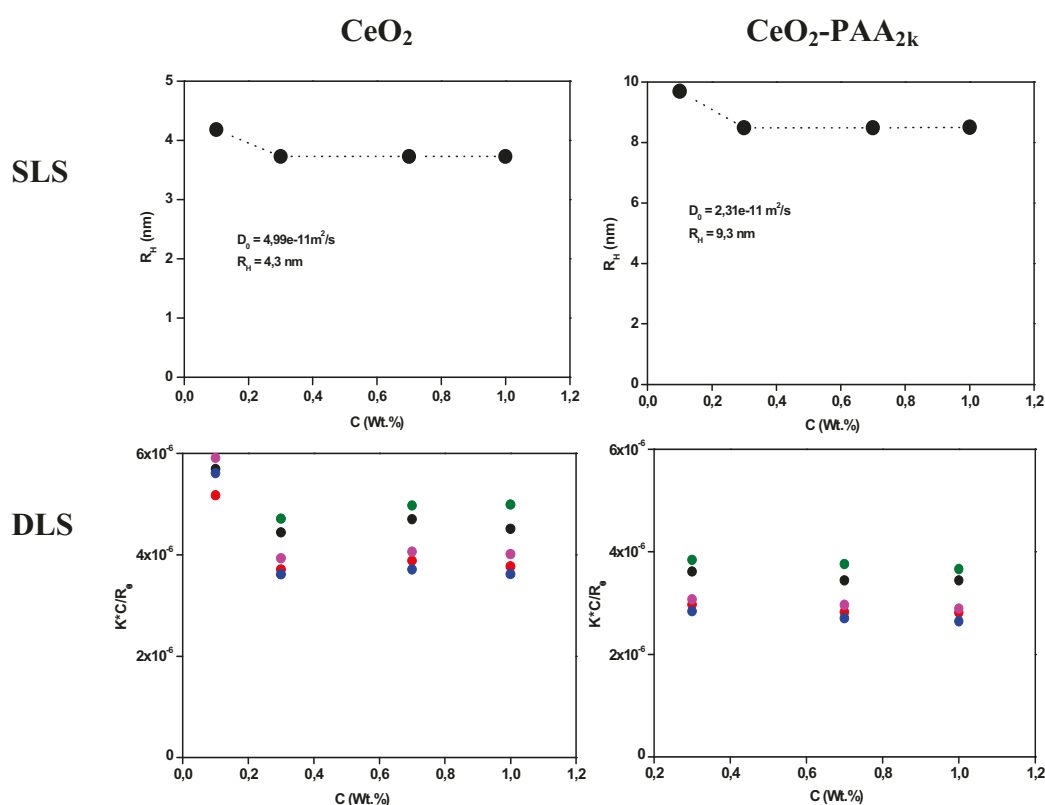


Figure 2.7 : Hydrodynamic radii (R_H) and reduced scattering intensity (k^*C/R_Θ) of bare and PAA coated ceria as a function of concentration from 0.1 wt% to 1 wt%.

Highly stable & oppositely charged building blocks

The Figure 2.8 shows the hydrodynamic radii distribution of bare CeO_2 and CeO_2 - PAA_{2k} measured by DLS. As can be seen, the mean value shifted from $R_H = 4.3 \text{ nm}$ ($s=0.35$) to $R_H = 9.3 \text{ nm}$ ($s=0.5$) indicative of the functionalization of the bare NPs by the short anionic polyelectrolytes. The comparison of a ΔR_H of 5 nm with the theoretical contour length of a 2k PAA (7 nm)^[81], suggests that 2 nm of the chain (or 6 COOH groups) interacts with the NPs surface and 5 nm (or 16 COOH groups) is sticking out into the solution. Furthermore, the additional small peak seen for the bare NPs and indicative of the presence of small aggregates disappears after the functionalization due to a higher and more efficient electro-steric repulsion between the NPs.

The insert displays the TEM image of bare and PAA coated CNPs at $c = 0.1 \text{ wt}\%$. The value of 10 nm for CPAA_{2k} lies in close agreement with the R_H measured by DLS, indicating the presence of PAA brush around CNPs. The well dispersed state of CPAA_{2k} proves that the sols were not aggregated due to the repulsion exerted by the polymer chains.

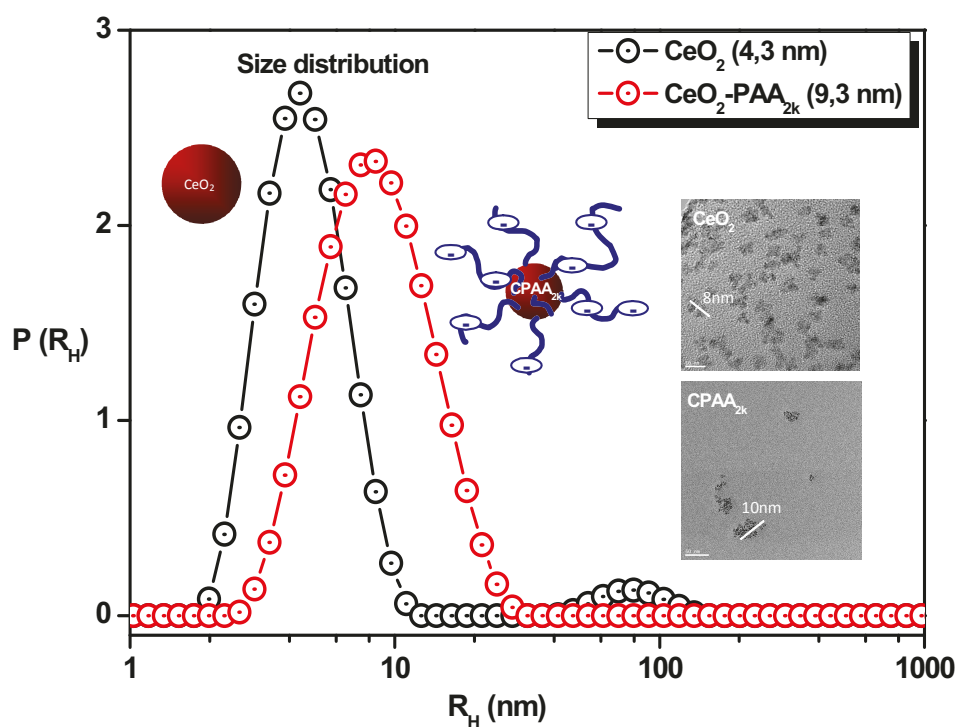


Figure 2.8 : Hydrodynamic radii (R_H) distribution of bare CNP (black) and CPAA_{2k} (red) NPs.

Determination of number of polymer chains on CPAA_{2k}

To obtain more quantitative results on this system, the Rayleigh ratios were measured on both dispersions as a function of the CeO₂ weight fraction. The two slopes are different because the Rayleigh ratio is proportional to K and M_w. The slopes of the linear regression for CeO₂ and CeO₂-PAA_{2k} are 0.202 and 0.153 respectively. The number of adsorbed PAA chains per NPs can then be computed from the difference between the two slopes. Using equation (1) described in earlier publications^[38], one finds $n_{ads}=40 \pm 10$ PAA per CeO₂ NP with $M_w^{CeO_2} = 192,000$ g/mol (and $M_w^{CeO_2-PAA} = 280,000$ g/mol) as determined by SLS.

$$\frac{R^{CeO_2-PAA}}{R^{CeO_2}} = \frac{K^{CeO_2-PAA}}{K^{CeO_2}} \left(1 + n_{ads} \frac{M_w^{PAA}}{M_w^{CeO_2}} \right)^2 \quad (1)$$

The organic corona represents then 32 % of the NP's weight and bears 640 negative charges. A result confirmed by ATG measurements which give a quite similar value of 35 % for the polyelectrolytes corona (or $N_{ads} \sim 35$ PAA per NPs).

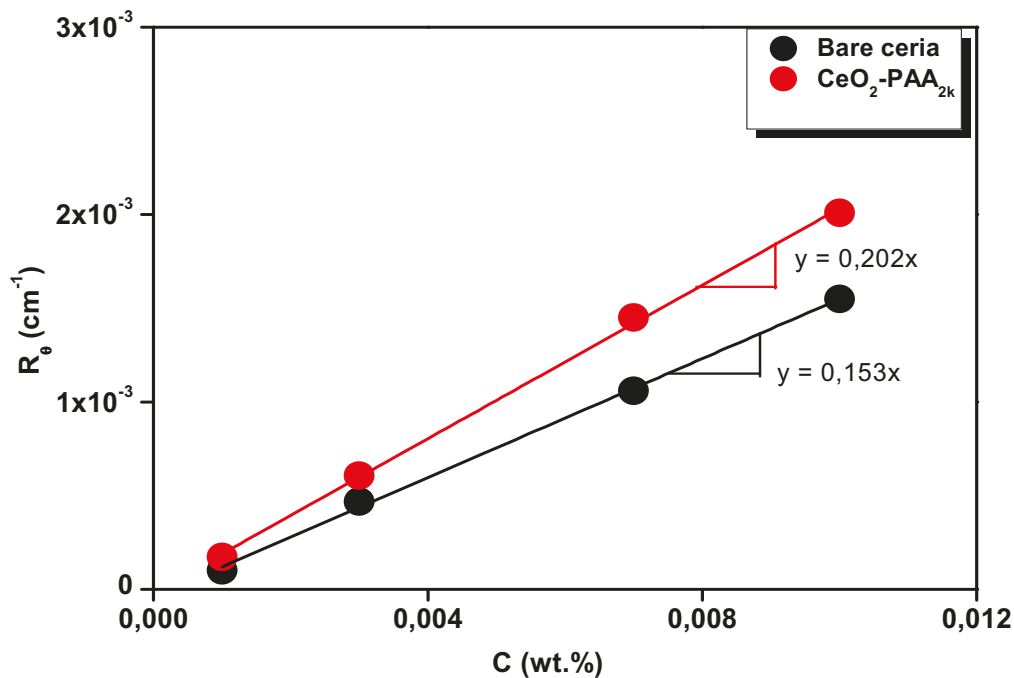


Figure 2.9 : Rayleigh ratios of bare CNP (black) and CPAA_{2k} NPs solution (red) vs the CeO₂ weight fraction.

Stability of CPAA_{2k} under high salt concentration

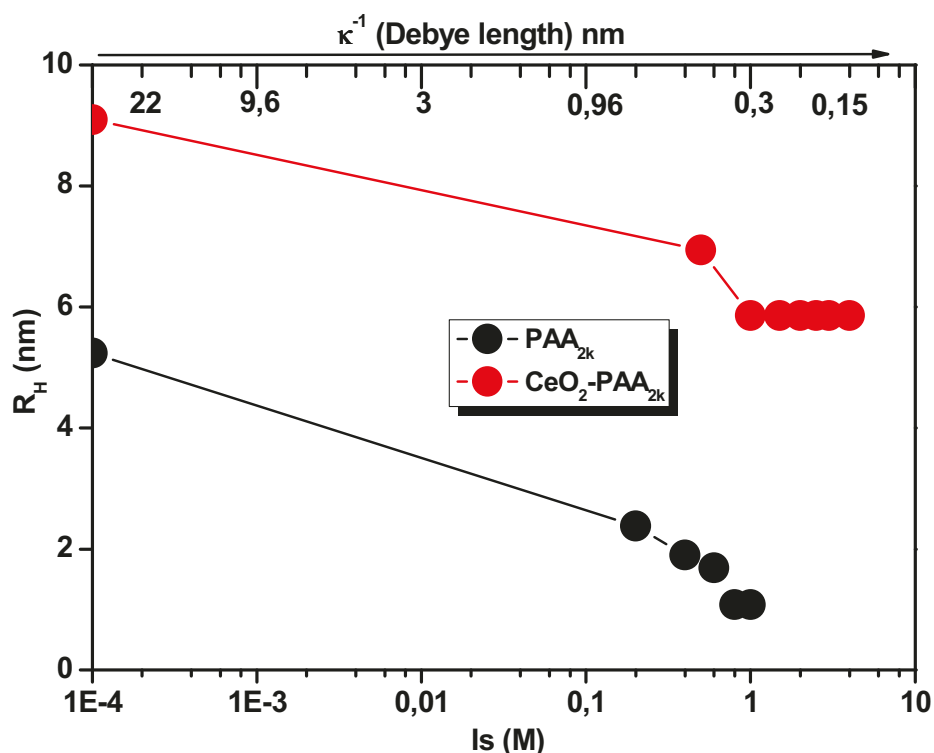


Figure 2.10 : R_H values of PAA_{2k} chains (black) and CPAA_{2k} NPs (red) as a function of ionic strength (I_s) [NH_4Cl].

The above graph represents the stability of the formulated sols upon the addition of NH_4Cl . As can be seen in Figure 2.10 no aggregation of the NPs is visible up to 4M NH_4Cl due the very efficient electro-steric stabilization provided by the short polyelectrolyte. As expected the NPs size starts to decrease slightly with increasing ionic strength due to the shrinkage* of the PAA chains from an extended worm like structure to a more coiled conformation^[82] and stabilizes above 1M where the electrostatic repulsion between charged monomers is completely screened (Debye length $\kappa^{-1} < 0.3$ nm).

*Shrinkage of polymer chains is induced by counter ion condensation of added salt with ionic groups of polymer chains. As a result of this ionic-pair ($\text{COO}^- \text{-NH}_4^+$) formation, number of effective charges which are responsible for repulsion are reduced. Contrary, the counter ions induce attraction within the chain and thereby promote the contraction in size of polymer brush around the NPs^[83].

Characterization of Polyethylenimine functionalized nano ceria

Stable cationic ceria nanoparticles were synthesized as shown in the figure 2.6. Activation of acid group of CPAA_{2k} by EDC.HCl/NHS is essential to carry out the reaction in a controlled manner. bPEI_{25k} was covalently attached to activated CPAA_{2k} by a simple condensation reaction between primary amine groups of bPEI_{25k} and –COOH groups of CPAA_{2k} with the subsequent elimination of water molecules [79, 80].

UV-Vis spectroscopy

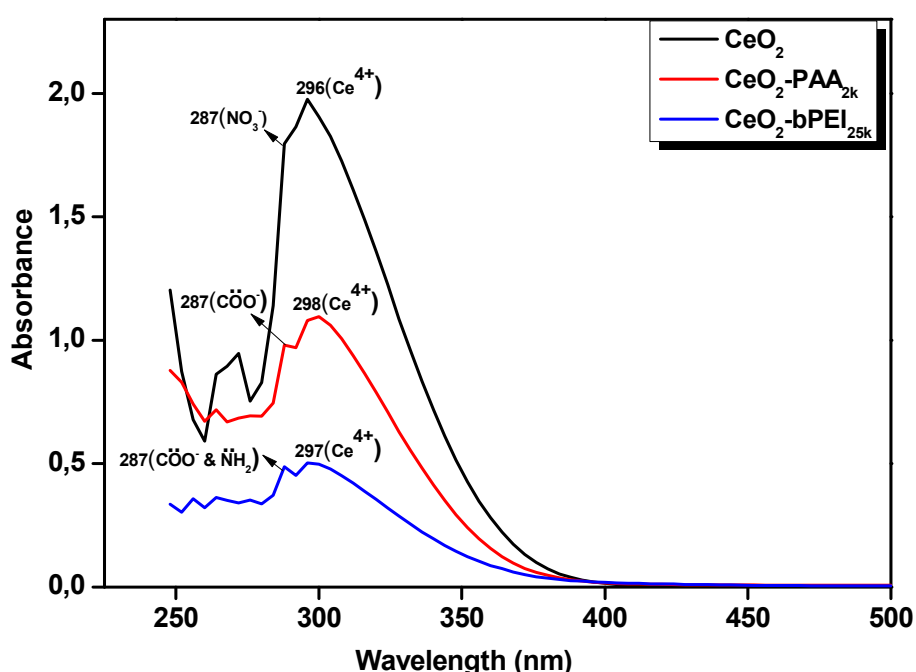


Figure 2.11: UV-Vis spectra of bare and PEs coated ceria NPs solutions. Bare (black line), PAA_{2k} coated (red line), and bPEI_{25k} functionalized ceria NPs (blue line).

The polymers used in this study are UV inactive. Ceria being a good UV absorber^[84], the absorption intensity directly relates then to the fraction of ceria (Figure 2.11). The appearance of absorbance peaks at 296 nm in all system studied indicates the presence of CNPs in the Ce⁴⁺ state^[85]. We have noted an enhancement of the 287 nm peak from bare to CeO₂-bPEI_{25k} NPs, suggesting possibly an increase of the population of electron donating species such as O and N in CPAA and CPEI respectively evidencing the successful functionalization of bare ceria with PAA and PEI PEs. Since PEI acts as a reducing agent, it donates more lone pairs of electrons to the NPs. Furthermore the PEI grafting changed the

color of the dispersion from yellowish to intense yellow due to the auxochromic effect of amine groups. From the graph below, it was deduced that 50% and 25% of CNP is present in PAA and PEI matrix. These findings are in close agreement with TGA results.

FT-IR spectroscopy

The FT-IR spectra of CPAA_{2k}, bPEI_{25k} and CPEI_{25k} are shown in Figure 2.12. A characteristic band at 3361 cm⁻¹ in CPEI_{25k} can be assigned to -NH asymmetric stretching vibration of bPEI_{25k}^[86]. Two bands at 2952, 2837 cm⁻¹ can be assigned to -NH symmetric and -CH stretches of bPEI_{25k} and PAA backbones respectively. The disappearance of the characteristic band at 1694 cm⁻¹ (attributed to the free carbonyl C=O stretching of free acid) indicates that the carbonyl groups are not free and attached to the low electronegative atom of nitrogen thus forming the covalent C-N bond.

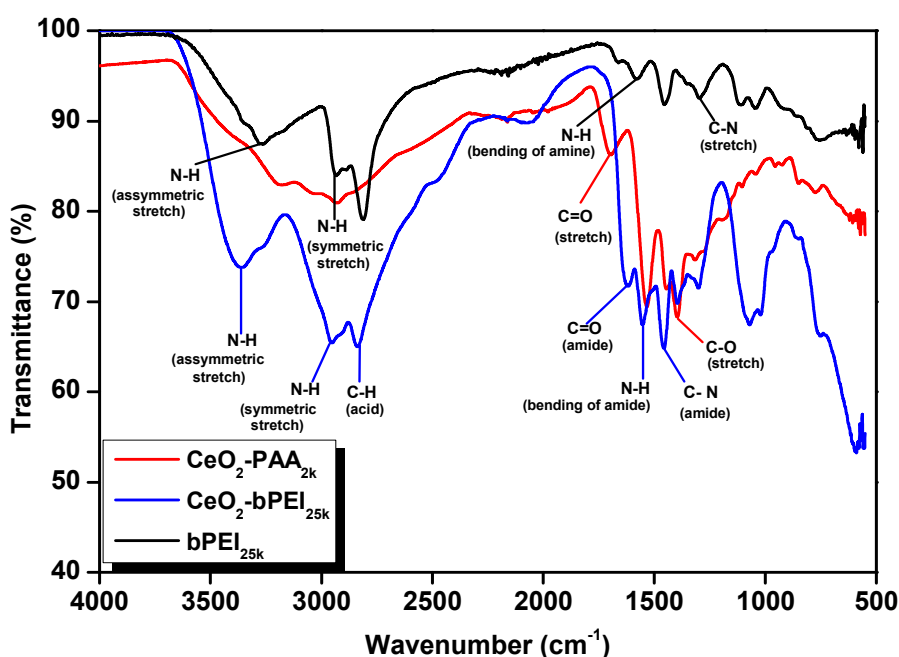


Figure 2.12 : FT-IR spectra of CeO₂-PAA_{2k} and CeO₂-bPEI_{25k} NPs together with bPEI_{25k} free chains.

The appearance of the new peak at 1616 cm⁻¹ is mainly associated with the C=O stretching of amide (-CONH), and the absorbance band at 1553 cm⁻¹ and 1478 cm⁻¹, which originate from -NH bending and -C-N stretching vibrations^[87, 88] between CPAA_{2k} and bPEI_{25k} clearly indicating the successful formation of amide bonds between -COOH groups

of PAA and $-\text{NH}_2$ groups from $\text{bPEI}_{25\text{k}}$ mediated by EDC.HCl/NHS. These results were further evidenced by ^1H 1-D NMR.

^1H Nuclear Magnetic Resonance (NMR) spectroscopy

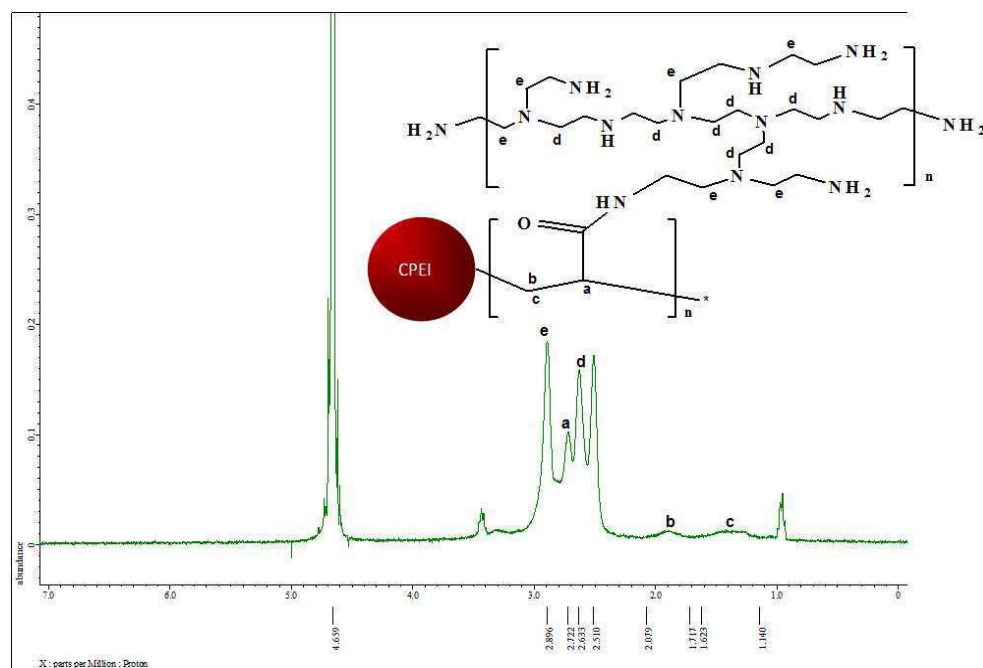


Figure 2.13 : ^1H NMR of $\text{CeO}_2\text{-bPEI}_{25\text{k}}$.

The ^1H 1-D NMR spectrum of $\text{bPEI}_{25\text{k}}$ functionalized CNPs ($\text{CPEI}_{25\text{k}}$) is shown in Figure 2.13. The appearance of the multiplet at 1.140 ppm – 2.079 ppm assigned as b, c corresponds to the $-\text{CH}_2$ protons while the presence of a peak at 2.722 ppm denoted as a, corresponds to the $-\text{CH}$ protons of acrylic acid in $\text{CPAA}_{2\text{k}}$ ^[89]. The absence of characteristic acid peak at 12.00 ppm suggests that $-\text{OH}$ groups are involved in condensation reaction. Backbone $-\text{CH}_2$ protons of parent $\text{bPEI}_{25\text{k}}$ should normally appear in the region between 2.4-2.5 ppm. Their shift from 2.5 ppm to upfield between 2.5 ppm and 2.896 ppm assigned as e, d in $\text{CPEI}_{25\text{k}}$, indicates that the nitrogen atoms of $\text{bPEI}_{25\text{k}}$ are attached to the high electronegative carbonyl groups present on the corona of the $\text{CPAA}_{2\text{k}}$ NPs^[41]. The absence of $-\text{OH}$ and shift of $\text{bPEI}_{25\text{k}}$ signal together give strong evidences for the formation of amide bonds as a result of acid-amine reaction. More quantitatively, it was determined from the integral value of ^1H NMR spectra that 80% of the carboxyl groups present on $\text{CPAA}_{2\text{k}}$ were reacted with $\text{bPEI}_{25\text{k}}$ forming then amide bonds.

Zeta potential of CPEI_{25k}

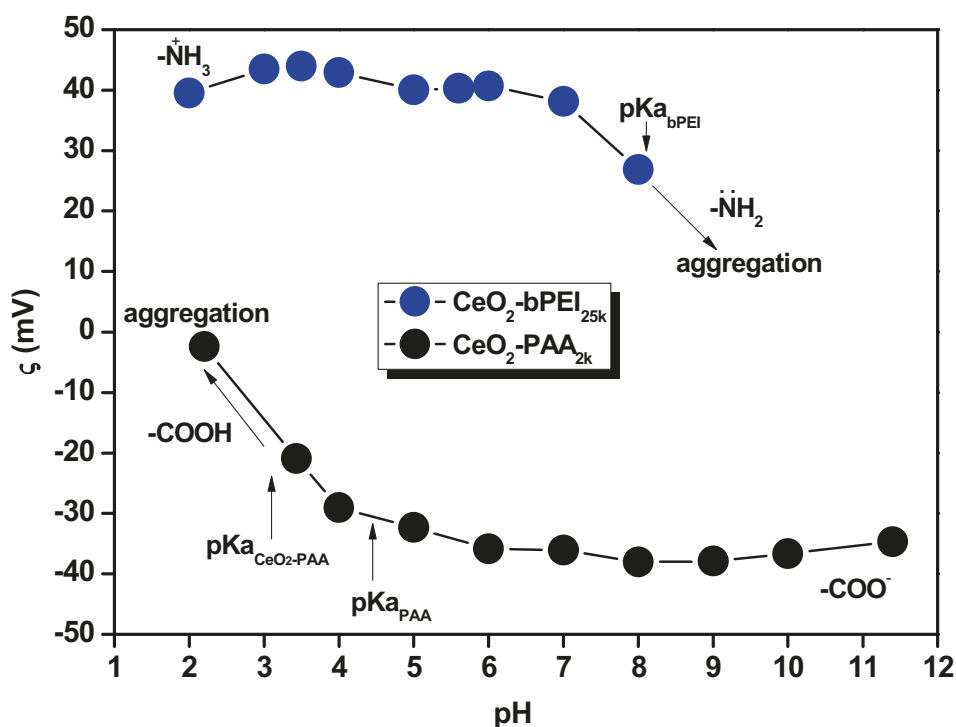


Figure 2.14: Zeta potential measurements of anionic and cationic CeO₂ NPs as function of pH at constant ionic strength of 10⁻² M NH₄Cl.

Independent zeta potential measurements as a function of pH were carried out on both types of nanocomposite solutions. Figure 2.14 depicts the investigation of surface charge density and stability of the dispersions over a broad range of pH. At high pH the carboxylic groups of PAA^[90] are fully ionized giving rise to a high zeta potential (-40 mV) as well. This value slowly decreases toward lower pHs as expected for a weak polyacid where the dispersion started to aggregate through hydrogen bonding between protonated COOH groups and some uncovered areas on the CeO₂ NP surface.

Symmetrically, at low pH, amines groups of bPEI are protonated^[91] giving rise to a high zeta potential of + 40 mV. This value slowly decreases towards higher pHs in agreement with the weak cationic nature of the corona^[92]. Above pH 9, it was not possible to carry out the measurement anymore because the dispersion started to aggregate likely due to the formation of carboxylate-ammonium salt intermediates^[93, 94] when some unamidated PAA chains present in the CeO₂-bPEI_{25k} structure met with the residual -NH₂ group of neighboring NPs corona. In both cases the presence of a plateau below pH 5 for bPEI and

above pH 6 for PAA suggests a maximum coverage of both PEs chains around the inorganic NPs core^[95].

Surface chemistry of colloidal materials can be easily altered by the functionalization step. There is a strong interplay between solid material and dispersants. Study on Isoelectric point (IEP) helps to understand the influence of colloid on stabilizing agent or vice versa. In Figure 2.14, the two IEPs were never attained, as the measurement was concentration dependent. This result highlights that functionalization with PAA shifts the IEP of ceria to lower pH values, in good agreement with the report by Sun *et al* ^[96]. C_{PAA}_{2k} NPs IEP will likely be below pH 2. Since we were at the maximum electrode sensitivity, further investigations at lower pH cannot be done. Furthermore the presence of a stable dispersion (-20 mV) at low pH indicates that the presence of nanoceria slightly shifting down the pK_a ^[97, 98] of PAA to lower pH values. In case of C_{PEI}_{25k}, the NPs might have shifted the pK_a of amines to high pH values, but due to intermediate formation (aggregation) it cannot be determined. A detailed explanation will be given for covalent MWCNT-PEs composites.

Dynamic Light Scattering

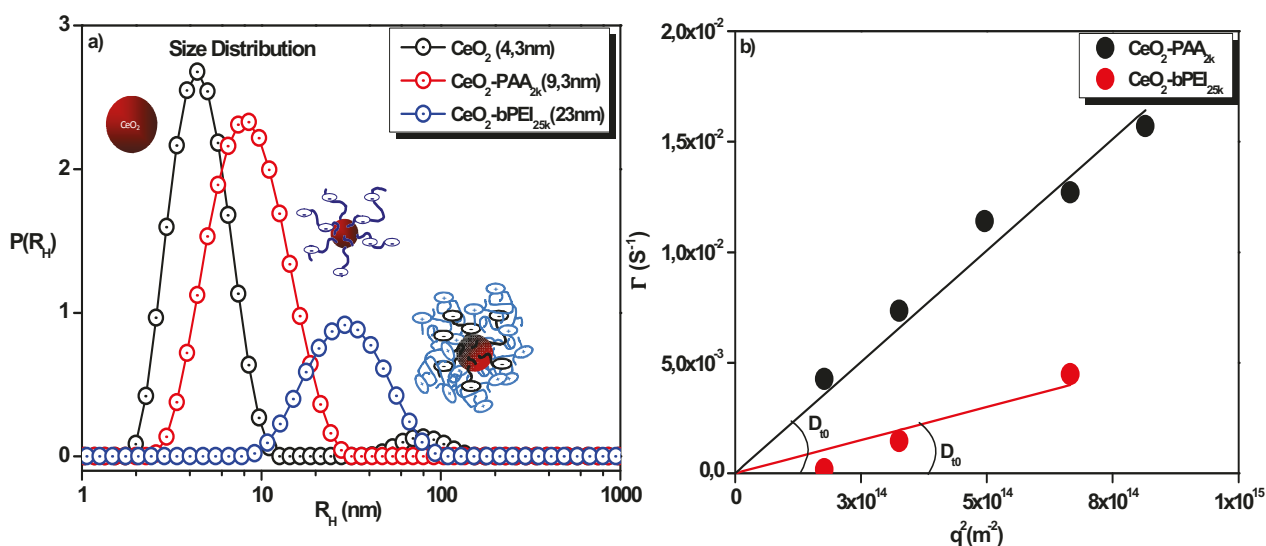


Figure 2.15 : a) Hydrodynamic radii (R_H) distribution of bare ceria, C_{PAA}_{2k} and C_{PEI}_{25k} NPs. b) self diffusion coefficients of PAA and PEI functionalized particles: $\Gamma = D_1 q^2$

Highly stable & oppositely charged building blocks

As evidenced in Figure 2.15 the covalent functionalization of the CPAA_{2k} NPs scaffold with bPEI_{25k} shifted up as expected the R_H from 9 nm to 23 nm ($s = 0.52$). It should be noted that the bPEI_{25k} chains have a theoretical contour length of 130 nm, much longer than the size of the CPAA_{2k} NPs. This might lead to the formation of multimers as suggested by a broader size distribution of the CPEI_{25k} NPs.

specimen	dn/dc (cm ³ .g ⁻¹)	R_H (nm)	Mw (g.mol ⁻¹)	Rg (nm)
CeO ₂ (CNP)	0.197	4.3±0.35	190887	3.33
CeO ₂ -PAA _{2k} (CPAA _{2k})	0.160	9.3±0.5	282224	7.2
CeO ₂ -bPEI _{25k} (CPEI _{25k})	not performed	23±0.52	not performed	17.8

Table 2. 1: *Molecular weight (Mw), refractive index increments (dn/dc), hydrodynamic radii (R_H), radii of gyration of bare and PEs (PAA & bPEI) coated ceria (R_g) NPs.*

Thermo Gravimetric Analysis (TGA)

The below figure represents the TGA of bare and polymer functionalized ceria NPs. TGA determined the weight percentage of inorganic nanoparticles in the nanocomposites. The weight loss of the bare NPs estimated to 4 wt% is attributed to the elimination of strongly bound water molecules. The weight loss of CPAA_{2k} composite between 70°C and 210°C is rather small (15%) and corresponds to dehydration associated with the formation of anhydride like structures. A significant decomposition of CPAA_{2k} begins at about 210°C and ends at 500°C. This weight loss (25%) represents the release of CO₂ due to the decarboxylation of anhydride and the formation of acrylic acid monomers via chain scission (depolymerization). No noticeable weight changes are observed up to 1000°C indicating the presence of a purely inorganic NPs^[99].

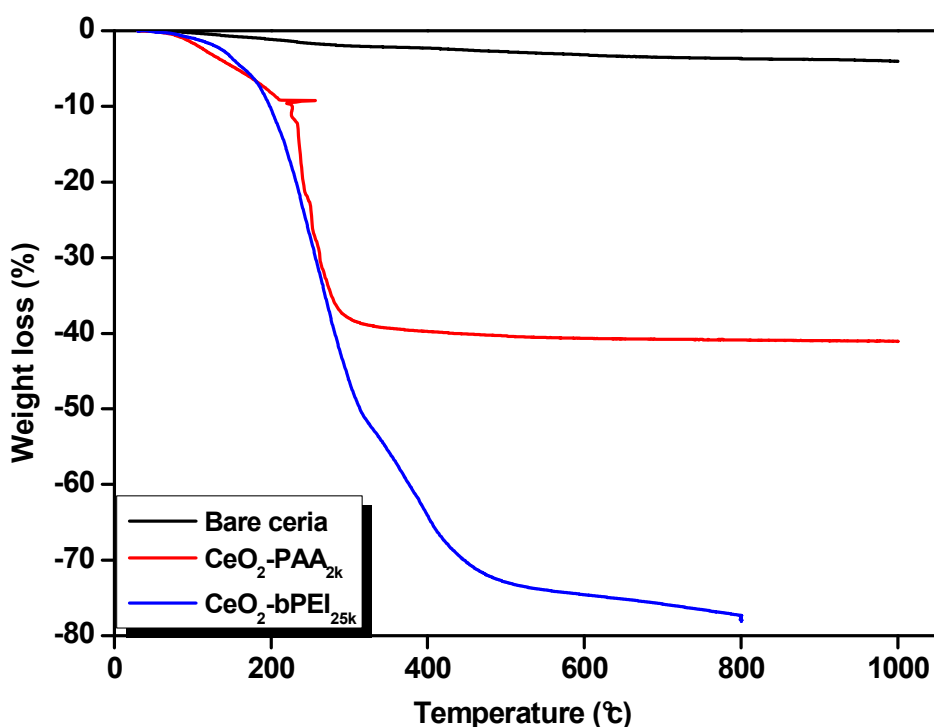


Figure 2.16 : *Weight loss vs temperature of bare and polymer coated CNPs.*

The bPEI functionalized ceria showed two distinct weight loss stages. A first rapid decomposition stage between 150°C and 300°C, and rather a steep slope attributed to the removal of water, ammonia, main polymer chain scission and release of CO₂ and imides^[100]. The increased weight loss (47%) as compared to CPAA_{2k} (25%) indicates the successful transformation of amines into amides^[101]. Furthermore a relatively slower weight loss between 300°C and 600°C associated with imidization and hydrogen transfer reactions, accounts for many unsaturated products followed by final decomposition of polymer chains^[100]. From TGA results, we were able to figure out that 3 bPEI chains are present per CPAA_{2k} NPs. Relative amount of ceria in CPAA_{2k} and CPEI_{25k} composites was determined up to 57% and 20% respectively.

Stability under High Ionic Strength

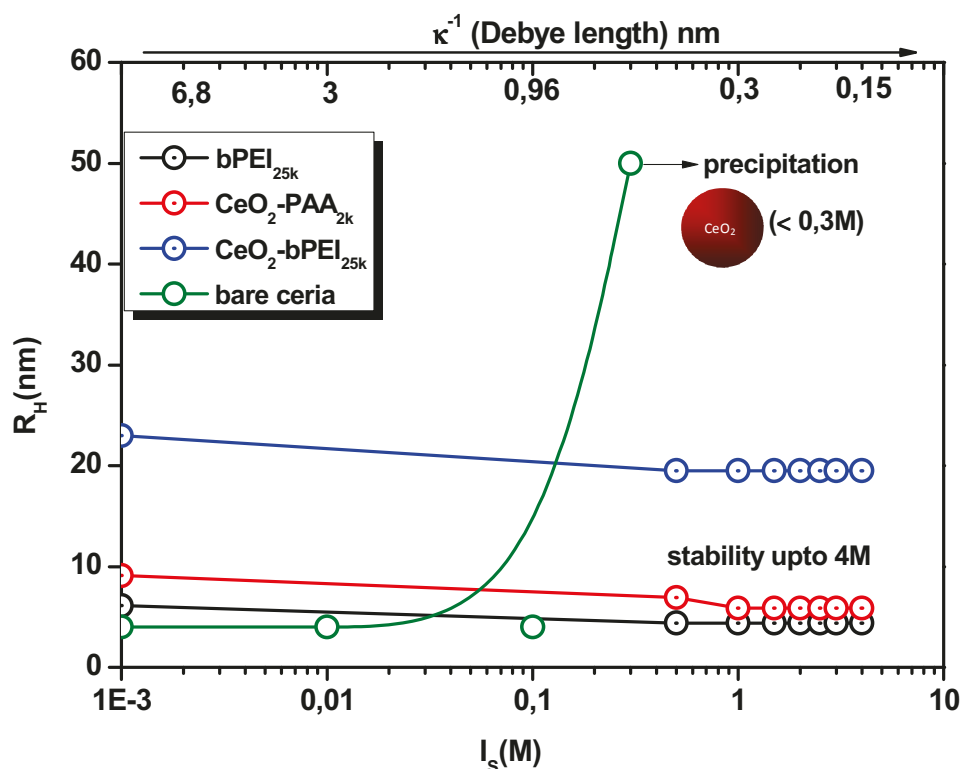


Figure 2.17 : R_H values of bPEI_{25k} and CPEI_{25k} NPs as a function of the ionic strength [NH₄Cl].

The measurement of hydrodynamic radii as a function of the ionic strength evidenced the remarkable stability of CPEI_{25k} towards high ionic strength. A sudden drop in size from 23 nm to 19.5 nm is attributed to the shrinkage of PEI chains as a result of counter ion condensation of salt^[83, 102, 103] as mentioned earlier. The R_H values stabilize then above 0.5-1M where the electrostatic interaction is completely screened off. Stabilization is then provided by the steric repulsions up to 4M. The stability assessment indicates that bPEI functionalized cerium oxide nanoparticles remains well dispersed in high saline medium even after several months.

Conclusions

Functionalization of cerium oxide nanoparticles with anionic and cationic polymers improved their stability over a wide range of pH and ionic strengths via efficient electrosteric interactions. Anionic particles were formulated by electrostatic (and coordination) adsorption of PAA_{2k} chains onto the surface of the NPs through a direct precipitation-redispersion mixing protocol. “Grafting to” combined with “direct mixing” successfully generated versatile bPEI functionalized CNPs from anionic CNPs via robust carbodiimide chemistry.

FT-IR and NMR spectroscopic studies gave strong evidences for the covalent attachment of bPEI_{25k} to PAA corona of CPAA_{2k}. Electrophoretic mobility showed that both cationic and anionic composites were stable under a broad range of pH. Furthermore PAA functionalization dramatically altered the IEP of inorganic materials to lower pH, while its pKa was slightly shifted to lower pH values by CNPs. Light scattering experiments determined the differences in M_ws, R_{Hs} and the number of polymer chains per particle [$N_{\text{ads}} = 40/\text{CeO}_2 \text{ NP}$].

TGA experiments have shown that 57% and 20% of CNPs were respectively present in anionic and cationic composites and determined the number of polymer chains grafted per NPs in case of bPEI chains coated NPs [$N_{\text{ads}} = 3/\text{CPAA}_{2k}$]. Excellent stability in high ionic strength up to 4M was exhibited by both PAA and bPEI coated nano ceria. We will take advantage of this high stability to fine tune the electrostatic interaction between oppositely charged NPs in the chapter 3.

Part II - Carbon Nanotubes (CNTs)

Introduction

Carbon nanotubes (CNTs) are one of the famous allotropic forms of carbon, accidentally discovered during the large scale synthesis of fullerenes by Iijima^[104] in 1991 gave a fascination to the nanoscience. The electron microscope analysis of first discovered “MWCNT” reveals that the nanotubes were constructed by the cylindrical structure of graphite sheets closed with hemifullerenes at their end. Depending upon the number of graphene sheets (a monolayer of sp^2 bonded carbon atoms) rolled they can be referred as Single walled nanotubes (SWNTs), Double Walled Nanotubes (DWNTs) and Multi-Walled Nanotubes (MWNTs) where one, two and multiple graphene sheets are present respectively. On the other hand, depending upon the angle at which the graphene sheets can be rolled, CNTs can be discriminated into different forms such as “arm chair”, “chiral” and “zig-zag”. Of which arm chair is metallic, whereas the other two are either metallic or semiconducting, depending upon the band gap of the structures^[105]. In this manuscript MWCNTs are preferred as the SWCNTs can be easily damaged by functionalization.

MWCNTs are usually prepared via various synthetic methods which include Arc-discharge, Laser ablation and Chemical Vapor deposition (CVD)^[106]. Each method has its own advantages and disadvantages. Among them CVD is widely used for large scale production. Higher yield of MWCNTs were obtained from pyrolysis of benzene^[106]. High pressure carbon monoxide (HiPCO) yields CNTs with high purity. All the above methods produce common impurities such as amorphous carbon, metal nanoparticles and fullerenes along with CNTs. It is essential to remove these impurities as they significantly alter the properties of CNTs^[105]. Oxidation^[107] is very common and effective procedure to purify CNTs in comparison with physical methods.

CNTs are promising candidates for numerous applications due to their unique properties such as special structural features, high aspect ratio, mechanical strength, electrical and thermal conductivity^[108]. Although CNTs have the above exciting properties, the main drawback is that they are very difficult to disperse in water or in any other organic solvents as they prevail as bundles due to the intrinsic van der Waals attraction between themselves^[105]. This lack of solubility hinders their application in many fields. Several attempts have been

Highly stable & oppositely charged building blocks

carried out to overcome the dispersion barrier which includes physical (mechanical) and chemical methods.

Physical methods include ultrasonication, high shear mixing, grinding and ball milling^[109]. These mechanical methods not only exfoliate the bundles but also destruct CNTs structures. For instance, as reported by Lu et al, ultrasound treatment introduces more defects such as bent and buckling thereby damages the tubes. Prolonged sonication causes thinning of the tubes by peeling the graphitic layers. Besides, the dispersions produced by mechanical methods do not possess long term stability since there is no existence of repulsive force to overcome van der Waals attraction^[110]. Chemical methods comprising surface functionalization adopt both covalent and non-covalent approach. Covalent methods introduce defects by changing the hybridization state from sp^2 to sp^3 while adding “chemical functionalities” on the tubes surface.

“Oxidative purification”^[107] is a well known covalent method to decorate the tubes surface with oxygen containing groups mainly carboxyl, hydroxyl and ester, brought by strong oxidizing agents such as HNO_3 , H_2SO_4 and H_2O_2 often combines with heat or ultrasound treatment. This aggressive acid treatment not only covalently adds the chemical moieties to graphite tubes but also produces shorter tubes by etching (cutting) the long tubes in sites where the structures are highly damaged. Thus opening the caps of the tubes and thereby removing the impurities (amorphous carbon and metal nanoparticles). Among them “carboxyl functionality” is the most used oxygen bearing group which preferentially adds to the edge where defects are already present (pentagonal or seven-membered rings) than to the side walls of the tubes.

The treatment method/time and the combination of acids vary from authors to authors. The first liquid phase oxidation method was reported by Esumi et al^[111] describing that refluxing MWCNTs with nitric acid or mixture of nitric/sulfuric acids enhances the dispersion of tubes in water and ethanol through etching. A comparative study on activity of different oxidizing agents such as HCl, refluxing nitric acid, $H_2SO_4+H_2O_2$ (piranha solution) and $NH_4OH+H_2O_2$ towards the oxidation of MWCNTs was deeply investigated by Datsyuk *et al.*^[112]. This study concludes that vigorous nitric acid treatment introduces more carboxyl functional groups on MWCNTs. The presence of carboxyl moieties exfoliates the bundles through electrostatic repulsion between the adjacent tubes thereby stabilizing the dispersion.

Highly stable & oppositely charged building blocks

The carboxyl functional groups extended the solubility range of nanotubes from aqueous solution to organic media via the formation of amides and esters with amines and alcohols respectively. The chemistry based on carboxyl functionality is vast and aroused more attention as it facilitates further functionalization with other molecules^[113, 114] such as small ligands, macromolecules, nanoparticles and biomolecules, dendrimers etc.

As the chemical oxidation is more effective at the end cap, several other strategies were followed to improve side wall functionalization including fluorination, ozonation, cycloaddition and radical mediated reactions, nucleophilic and electrophilic addition reactions^[113]. Unfortunately the covalent side wall functionalization degrades the novel properties of CNTs^[105] due to the disruption of π -conjugation.

On the other hand, non-covalent functionalization based on adsorption forces such as van der Waals and π -stacking interactions receives considerable attraction because the decoration occurs without disturbing the electronic structures of tubes. Surfactants and polymers were extensively used and functionalization occur exohedrally. The wrapping mechanism strongly depends on thermodynamic parameters.

Surfactants are amphiphilic molecules having hydrophilic head and hydrophobic tail group. Surfactants serve as a good dispersing agent below their critical micelle concentration (CMC). The dispersants can be either ionic or non-ionic. In case of ionic surfactant, the head group interacts with solvent whereas the tail lies on the CNTs surface to reduce the surface tension between the solvent and CNTs thus preventing the tubes from aggregation in an efficient way by steric or electrostatic repulsion. On the other hand, in case of non-ionic dispersants hydrophobic interactions play a major role. Usually surfactants assisted dispersion process is accompanied with ultrasonication. The later treatment simplifies the wrapping process by separating the individual tubes from bundles thereby the surfactant molecules can easily access the individual tubes and encapsulate them^[115]. The most commonly used surfactants are SDS, CTAB, NaDDBS.

Wrapping with surfactants has disadvantage that it is a reversible process. Therefore bundles can be reformed since the dispersant can be easily removed from the surface of the tubes. In addition, presence of surfactant in composites can degrade the transport properties of resulting material as reported by Bryning *et al.*^[116]. Besides, surfactant induces crystallization in some cases which markedly affects the transparency of the composites^[117].

Highly stable & oppositely charged building blocks

Contrary, polyelectrolytes (PEs) are promising candidates to replace surfactants. PEs incorporation to tubes surface is accomplished by covalent or non-covalent approach. The resulting composites make dispersions both in aqueous and organic solvents. The first polymer nanocomposite having CNT as filler was prepared by Ajayan *et al.*^[118]. The important features of composites are that they exhibit pH responsive properties. PE shells allow further functionalization with other molecules via their active ends. Further, embedding CNTs into polymer matrix simplifies the processibility of composites and improves the thermal and mechanical properties of polymers. The main challenge behind the fabrication of CNT-polymer composites is the efficient loading of nanotubes into the polymer matrix.

In common three methods called solution blending, melt blending and in-situ polymerization are widely used to prepare nanotube/polymer composite^[119]. The first two methods based on non-covalent approach are not efficient to produce long term stable dispersions as the interacting forces are weak between PEs and CNTs^[120]. “In-situ” enables covalent functionalization of PEs to tubes either via “grafting from” or “grafting to” strategies. The main drawback of “grafting from” is that the reaction conditions are so strict. Contrary, “grafting to” is amenable, requires simple reaction conditions and is mostly initiated from carboxyl functional groups. Several homo and copolymers such as PLLA, PVA, PSV, PPEI-EI, epoxy and polyurethane were incorporated to the tubes surface via amide and ester linkages^[121-125]. The main intention behind this PEs attachments was to improve the dispersion stability of CNTs in aqueous and in organic solvents in order to utilize their unique properties in many fields. But not much attention has been given to impact of factors such as pH and salt on dispersion stability.

Herein, we report on the generation of cationic and anionic CNTs with the help of small oligomers and PEs based on both covalent and non covalent approach. A nice scenario on dispersion stability of tubes with respect to salt is demonstrated. Thorough investigations on stability parameters assure that covalent attachment of bPEI_{25k} and PAA_{5k} respectively to acid and amine modified CNTs improves their dispersibility and renders the dispersions stable in high ionic strength.

Experimental section

Covalent functionalization of MWCNT with short ligands or oligomers

As pointed out earlier, introduction of oxygen containing groups on the tubes surface is one of the ways to cut or purify the tubes. It was accomplished by the following simple procedure^[126]. The as-received MWCNTs (Arkema batch 6077) were first subjected to purification by refluxing them in sulfuric acid for 5hrs at 110°C to remove impurities. The resulting solution was filtered to retrieve the CNT “pulp”. It was then many times washed with water to reach neutral pH and eventually lyophilized to get a powder.

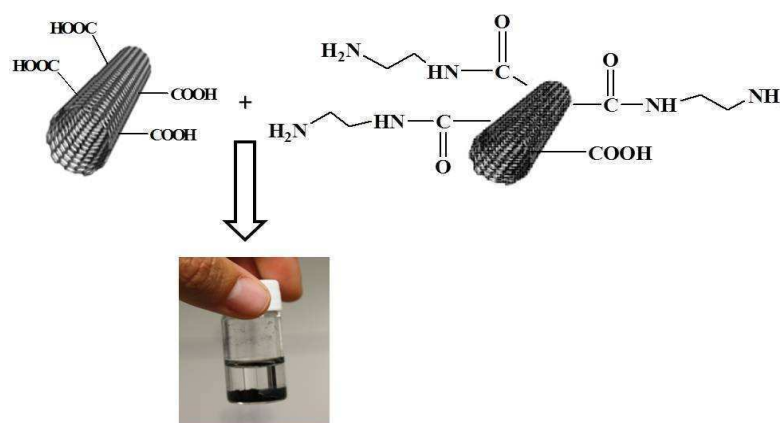


Figure 2. 18 : *Mixing of oppositely charged short ligand (MWCNT-COOH and MWCNT-NH₂) functionalized MWCNTs.*

In order to introduce carboxylate moieties on the surface of the tubes they were suspended in 3.6M nitric acid and subjected to sonication for 5 minutes to get homogeneous dispersion and then kept under reflux for 3 days with stirring in a RB flask. The resulting dispersion was diluted with water and filtered through PVDF membrane of pore size 0.45µm. The resulting paste was lyophilized to obtain a powder and hereafter denoted as MWCNT-COOH or O-MWCNTs. In a second step, acid decorated tubes were converted into acid chlorides by refluxing them with SOCl₂ at 70°C for 12 hrs. After the removal of excess SOCl₂, EDA was covalently attached to chloride functionality via amide linkage by refluxing in dehydrated toluene at 70°C for 24 hrs^[127]. The pasty product obtained after filtration was subjected to several washings with ethanol and DI water. The wet product was freeze-dried to obtain solid material and named as MWCNT-NH₂. The aminated tubes were likely slightly

Highly stable & oppositely charged building blocks

bundled and later were exfoliated by grafting with PEs. The acid and amine functionalized tubes were subjected to preliminary characterizations and both dispersions stability was investigated visually. It should be noted that the mixing of anionic and cationic CNTs dispersions precipitated as expected as shown in the Figure 2.18.

Non-covalent wrapping of MWCNTs with PEs

Anionic and cationic functional tubes were obtained by wrapping the as received bare MWCNTs with both cationic and anionic weak PEs (PAA_{130k/450k} and PEI_{60k}). Wrapping was carried out with the assistance of ultrasonication based on solution blending protocol^[128]. The pH of the PAA solution prepared from both Mws was adjusted to ~5 (near to the pKa of free PAA chains). Whereas the functionalization by PEI chains was performed at different pHs of 5, 8, and 10, as they possesses all types (1°, 2°, 3°) of amines, to understand the effect of charge on dispersion stability. Trial experiments suggested that, it is essential that PEs should not be fully charged to maintain some hydrophobicity to trigger/facilitate the adsorption on the CNTs surface via hydrophobic interactions^[129]. In all cases, the optimum ratio of MWCNTs to PEs was set to 1:3 by volume, with the bare MWCNTs and PEs concentration always maintained at 0.1 wt%.

Microprobe was directly immersed into the mixture of MWCNTs and PEs. The ultrasound was applied as pulses at intervals of 0.5s on and 0.2s off for 2 hrs under ice bath. Different Mw of PEs were used as dispersants to understand their influence on dispersion stability. The resulting materials were characterized by FT-IR and DDLS. Visual investigation was made on the stability issues.

Covalent grafting of MWCNTs (MWCNT-PEs)

Covalent attachment of PEs to MWCNTs is likely an effective way to improve both dispersibility and stability. bPEI_{25k} and PAA_{5k} grafted tubes were synthesized from MWCNT-COOH and MWCNT-NH₂ respectively through the formation of amide bonds using EDC.HCl and NHS^[79, 80, 130] as cross linkers by a combination of “grafting to” with “direct mixing”. The synthetic strategy to obtain PEs functional CNTs is quite similar to the fabrication of stable cationic ceria NPs.

Shortly, 0.1wt% of MWCNT-COOH at pH 8 was added at one shot to equal concentration of bPEI_{25k} at pH 5 at a volume ratio ($X = \text{volume of CNTs}/\text{volume of PEs}$) of

Highly stable & oppositely charged building blocks

0.1. No aggregates formation occurred during this fast injection, as indicated by a transparent final solution. The PEs were physically adsorbed on CNTs surface via electrostatic interaction under stirring at RT for 15min. Covalent bonds between CNTs and PEs were established by the addition of aqueous solution of cross linkers. The stirring was further continued for 24 hrs at RT. The resulting black solution was centrifuged to get rid of unreacted bundles. Subsequently the supernatant was dialyzed and purified with the same protocol as for CPEI_{25k} NPs. The purified product collected from the filter part was dried under vacuum.

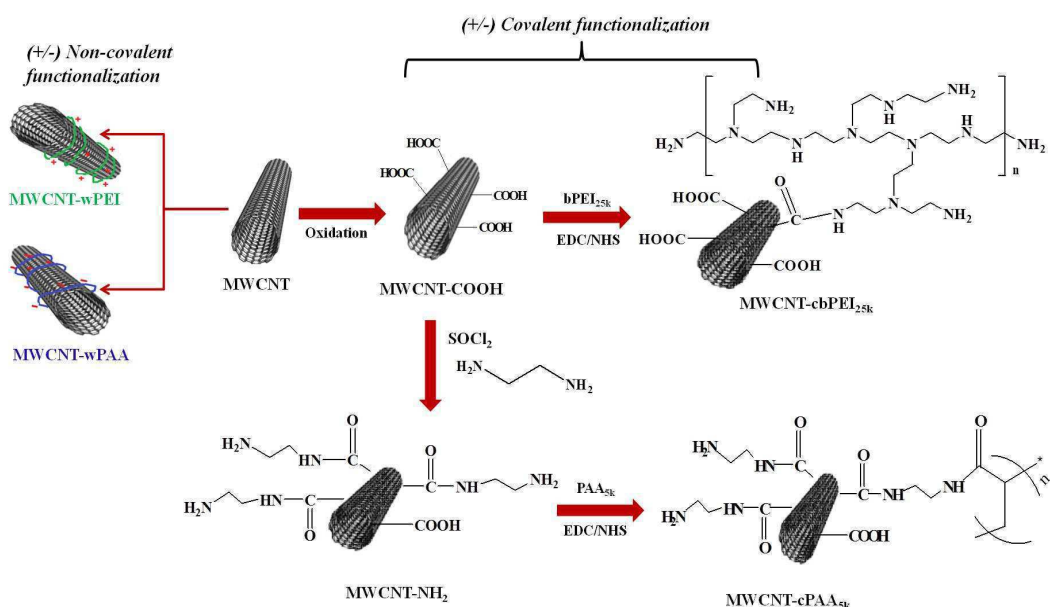


Figure 2.19: Schematic representation of Non-covalent / Covalent functionalization of MWCNTs with PEs and small ligands.

In a similar fashion, anionic functional tubes were fabricated. Aminated tubes at pH 2.5 were added at one shot to PAA_{5k} solution at pH 8 at a volume ratio of 0.1. All the other reaction conditions and processes such as the addition of cross linkers, centrifugation, dialysis and purification was carried out exactly under the same protocol as for cationic tubes except the size of dialysis device. Since PAA_{5k} chain length is smaller than bPEI_{25k}, dialysis was performed in an Amicon device of MWCO 10000 to remove free polymer chains and then dried under vacuum. Both resulting conjugates denoted as MWCNT-cPAA_{5k} and MWCNT-cbPEI_{25k} were characterized by analytical techniques to confirm the covalent functionalization.

Results and discussions

Covalent functionalization with short ligands

FT-IR spectroscopy

Incorporation of ethylenediamine to acid functional group was confirmed by FT-IR spectra. The presence of characteristic bands at 3150cm^{-1} and 3017cm^{-1} in aminated tubes is assigned to -NH and -CH stretching vibrations of ethylenediamine backbone. Appearance of characteristic amide bands at 1574 cm^{-1} and at 1406 cm^{-1} associated with N-H bending and C-N stretching respectively, gives a clear evidence that ethylenediamine was covalently attached to oxidized nanotubes^[131]. In MWCNT-NH₂ the presence of characteristic acid peaks with reduced intensity at 1658 cm^{-1} and at 1069 cm^{-1} corresponding to free -C=O and -C-O stretching respectively, suggests that the conversion to amines is not complete and still some carboxyl groups are left unreacted. Due to the dispersibility issues in D₂O, the oxidized and aminated tubes were not characterized by NMR.

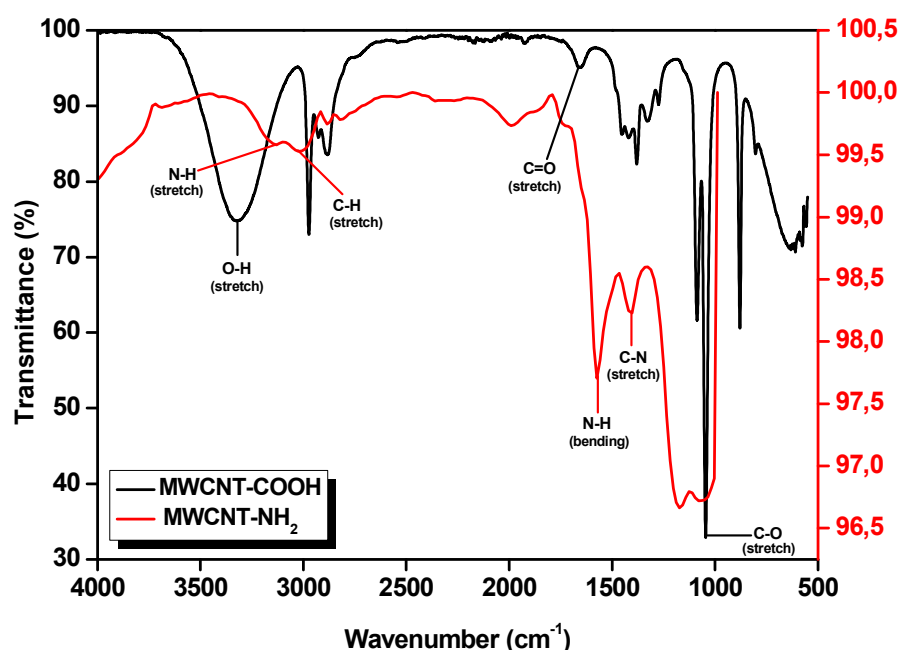


Figure 2.20 : FT-IR spectra of functional MWCNT-COOH and MWCNT-NH₂.

Depolarized Dynamic Light Scattering (DDLs)

Rotational (D_r) and translational diffusion (D_t) coefficients calculated from the decay rates of scattered intensities of depolarized and polarized light^[40] at different angles allowed to determine the dimensions of acid and amine functionalized tubes with the help of equations 27 & 28 (see chapter 0).

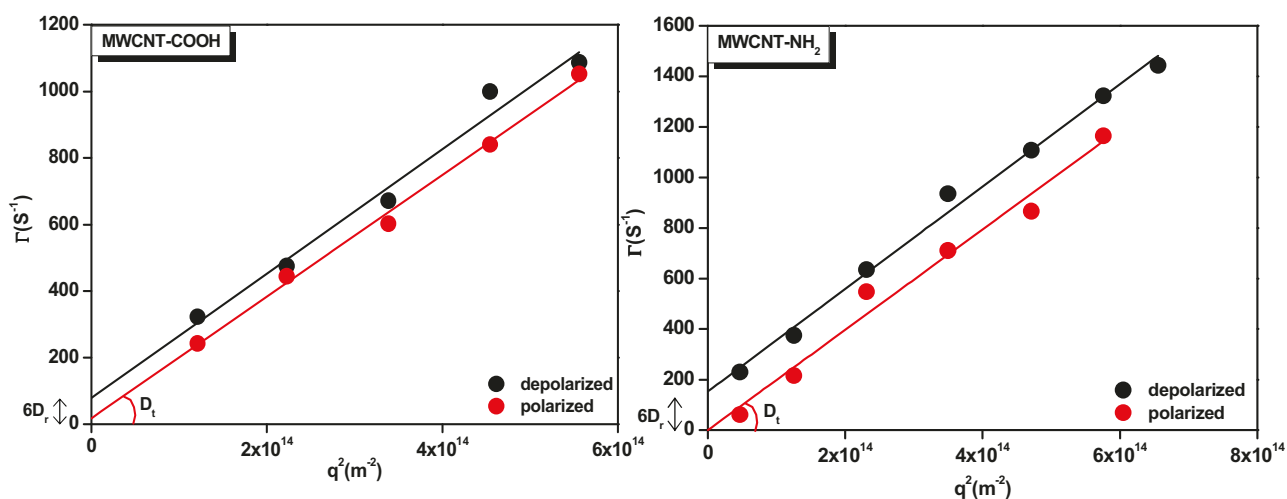


Figure 2.21 : Plots of decay rates as a function of q^2 for MWCNT-COOH (left) and MWCNT-NH₂ (right): $\Gamma = D_t q^2 + 6D_r$.

In Figure 2.21, the slopes of the polarized plots correspond to D_t , whereas the intercepts of depolarized plots correspond to $6D_r$. By substituting these values in equations^[40] 27 & 28, the mean diameter and length were determined for both types of tubes.

sample	D_t ($\mu\text{m}^2/\text{s}$)	D_r (s^{-1})	L (nm)	D (nm)
MWCNT-COOH	1.87	13	1024±51	13±0.65
MWCNT-NH ₂	1.99	25.5	750±37	26±1.3

Table 2. 2 : Length and diameters of short ligand functionalized tubes.

Highly stable & oppositely charged building blocks

As expected, a mean diameter of ~ 14 nm found out for the MWCNT-COOH tubes together with the mean length of 1024 nm, is in agreement with the AFM images (chapter 4). In the case of MWCNT-NH₂ however, the mean diameter is found to be around 26 nm with a similar mean length (~ 750 nm). This diameter is twice as large as for individual MWCNT-COOH tubes likely indicating the presence of aggregates. As MWCNTs were introduced in their solid form, EDA was not able to access individual tubes and functionalization might here occurred on bundles. As 1 week is necessary before performing any DDLs experiment to settle down very large aggregates, the formation of MWCNT-NH₂ dimers might also have occurred during this induction time due to a slightly hydrophobic nature of the EDA.

Ionic strength stability

Two independent experiments were carried out to understand the effect of NH₄Cl on acid and amine functionalized tubes, each prepared at a concentration of 10⁻³ wt%. In both solutions, addition of 10⁻²M and 10⁻¹M caused immediate precipitation. Whereas in case of 10⁻³M, precipitation was delayed and observed on the next day. This indicates that addition of salt triggers the formation of large aggregates via the screening of the electrostatic interactions. No steric force is able in this case to take over the weak electrostatic repulsion and to balance the attractive van der Waals forces.

Zeta potential of acid and amine functionalized MWCNTs

Independent investigation was made on dispersion stability of acid and aminated tubes as a function of pH. The results are similar to the ceria nano composites. IEP were never reached due to the concentration issues. In agreement with reports by Lee *et al.*^[127], oxidized tubes are negatively charged at all pH. The surface charges are less negative at low pH due to protonation of carboxylate moieties in acidic region, yet the dispersion remains stable. The stability at low pH is indeed influenced by sp² hybridization of MWCNT backbone which shifts the pKa of -COOH groups to lower value. Charge density increases linearly with pH due to the ionization of acid moieties. Dispersion stability at high pH is maintained via the electrostatic repulsion between the adjacent acid functionalized tubes.

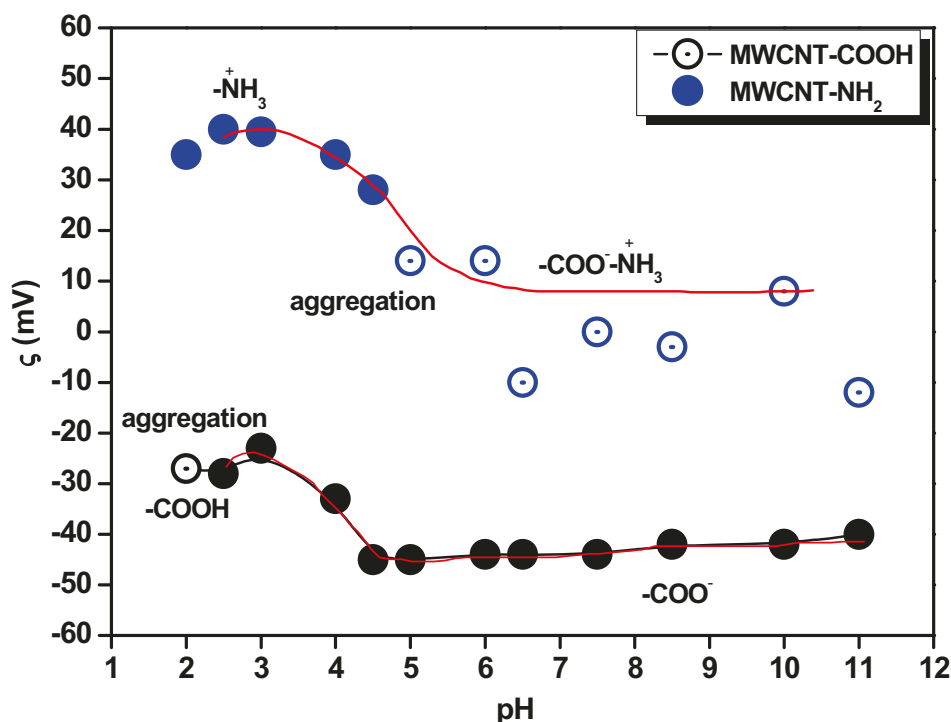


Figure 2. 22 : Zeta potential of MWCNT-COOH and MWCNT-NH₂ tubes as a function of the solution pH, at constant ionic strength of 10⁻³ M NH₄Cl.

A symmetric behavior was observed for MWCNT-NH₂ tubes. Surface charge decreases linearly with pH increase, as the amines are not charged at high pH. The observed precipitation of the dispersion before reaching the amine pK_a suggests the formation of carboxylate-ion intermediates (-COO-NH₃⁺)^[93, 94], between residual carboxyl groups (-COO⁻) of aminated tubes and amine groups of adjacent tubes. Whereas, at low pH aminated tubes are stabilized via the electrostatic repulsion exerted by the protonated amine shells.

Non-covalent functionalization with wrapped PEs

FT-IR spectroscopy

In MWCNT-PAA_{130k/450k} the presence of a broad band between 3000 and 3500 cm⁻¹ is attributed to OH stretching of PAA chains. In anionic composites, appearance of two peaks at 1700 cm⁻¹ and at 1230 cm⁻¹ associated with -C=O and -C-O stretching of acid

respectively,^[132] confirms the presence of PAA on the tube surface. On the other hand, in the case of MWCNTPEI_{60k}, the presence of two peaks at 1580 cm⁻¹ and at 1450 cm⁻¹, attributed to -NH bending and C-H deformation together with two other peaks around 2955 cm⁻¹ and 2829 cm⁻¹ corresponds to -NH asymmetric and symmetric vibrations of the PEI_{60k} backbone^[86], suggesting a successful wrapping of bare MWCNTs with cationic PEI chains.

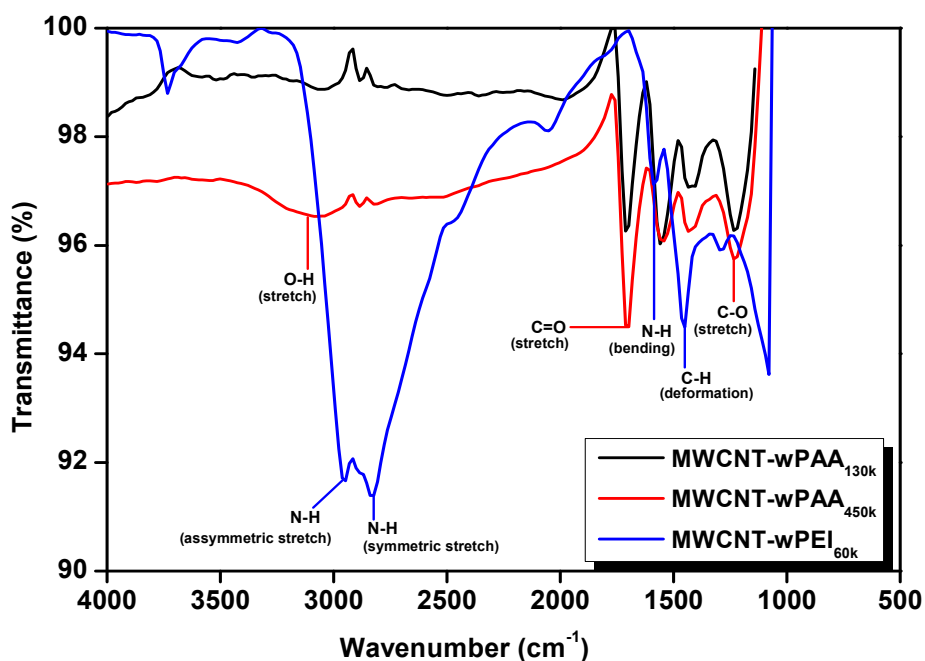


Figure 2.23 : FT-IR spectra of MWCNT-wPAA_{130k}, MWCNT-wPAA_{450k} and MWCNT-wPEI_{60k} tubes.

Final Mw of the PEs after ultrasonication

As mentioned earlier, different PEs Mws were used for non-covalent functionalization. Indeed, the ultrasonication step not only breaks the “van der Waals bundles” of the above tubes, but cuts the wrapping chains as well. It is hence necessary to estimate the final Mw of the PEs chains to really understand the effect of Mw on the stabilization of the tubes. As R_H is known to be proportional to the radius of gyration (R_g) of the chains, which in turn is a function of the molecular weight Mw.

$$R_g \propto M_w^{\nu}$$

with ν , the Flory expression, equal to 3/5 in good solvent, it then turns out that

Highly stable & oppositely charged building blocks

$$M_{wf} = \left(\frac{R_{Hf}}{R_{Hi}} \right)^{5/3} \cdot M_{wi} \quad (2)$$

where i = before the ultrasound treatment, f = after the ultrasound treatment

Polymer M_{wi}	130k (PAA)	450k (PAA)	60k (PEI)
R_{Hi}	1.49×10^{-07}	2.05×10^{-07}	7.05×10^{-08}
R_{Hf}	6.31×10^{-08}	7.24×10^{-08}	3.96×10^{-08}
M_{wf}	31k	80k	21k

Table 2.3: *Molecular weight (M_w) of cationic and anionic PEs before and after ultrasonication.*

It is clear from the Table 2.3 that the ultrasound step cuts the PEs chains. High molecular weight chains are then needed to accomplish the complete wrapping of the tubes to get the expected stability. The chosen M_w should not be however too large to avoid CNTs bridging. In the case of PAA_{450k}, the M_w after treatment drops to 80k with chains sufficiently large to trigger aggregation by wrapping more than one tube. The wrapping strategy is then a slight balance between the chain initial and final M_w , and the charge density of PEs as a function of pH.

DDLs of non-covalent PE-CNTs composites after ultrasonication

DDLs experiments were carried out in the case of MWCNT-PEI_{21k} and MWCNT-PAA_{31k}, with same conditions as for acid and aminated tubes, and the results are presented below. Length and diameter of PEI_{21k} and PAA_{31k} wrapped MWCNTs were figured out from the corresponding D_t and D_r , which are shown in the Table 2.4.

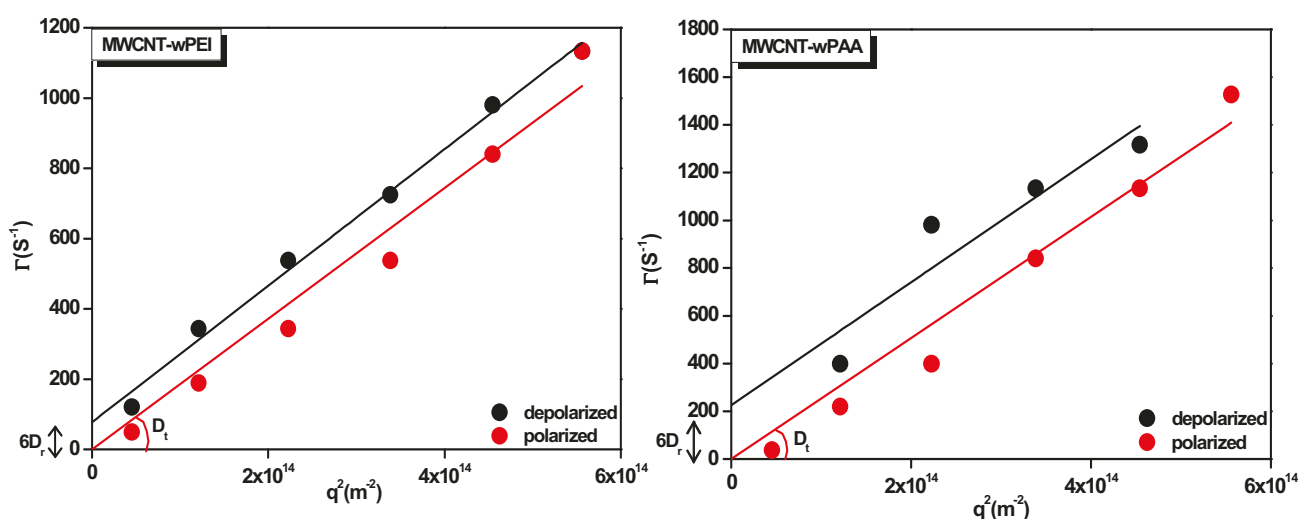


Figure 2. 24 : Plots of decay rates as a function of q^2 for MWCNT-wPEI (left) and MWCNT-wPAA (right): $\Gamma = D_t q^2 + 6D_r$.

sample	D_t ($\mu\text{m}^2/\text{s}$)	D_r (s^{-1})	L (nm)	D (nm)
MWCNT-wPAA _{31k}	2.53	37.5	1011±51	16±0.8
MWCNT-wPEI _{21k}	1.86	12.8	1031±52	14±0.7

Table 2.4: Dimensions of oppositely charged wrapped MWCNTs.

A diameter close to 15 nm is obtained for both tubes. It should be noted that even though we are likely beyond the resolution of the DDLS technique, the diameters are well agreed with the size of the functionalizing shell ($-\text{COOH} < \text{PEI}_{21\text{k}} < \text{PAA}_{31\text{k}}$).

Ionic strength stability

Stability of PAA and PEI wrapped MWCNTs were independently investigated upon addition of NH_4Cl . Anionic and cationic dispersions remained stable until 10^{-1}M for at least 24 hrs, which is two orders of magnitude higher than the short ligand functionalized tubes (MWCNT-COOH, MWCNT-NH₂). Prolonged stability was not possible and the dispersion eventually precipitated after 1 day due to the fact that the wrapping density was likely not enough to sustain stability over longer period of time and/or desorption of some physisorbed PEs chains.

Trial experiments were carried out to further improve the stability of the dispersion. The ultrasonic wrapping step was performed in the presence of 1M NH_4Cl for 1h. The Debye screening length is here very small (0.3 nm) a sign of decrease of the electrostatic interaction between the PEs and consequently likely increase the chain adsorption density around the bare MWCNTs. Indeed, the dispersion stability was improved transiently for more than 24 hrs at 1M NH_4Cl . The weak interaction between wrapped PEs and bare tubes triggered the desorption of PEs from the tubes surface with time^[120, 133], resulting in bundles formation. These observations suggest that PEs are very good dispersants but covalent attachment would be a reliable way to achieve prolonged stability under high saline conditions.

Covalent functionalization with PEs

Cationic and anionic covalent nanocomposites were synthesized as shown in the Figure 2.19. Activation of acid group of MWCNT-COOH and PAA_{5k} by EDC.HCl / NHS is crucial for effective functionalization. bPEI_{25k} and PAA_{5k} were covalently attached to MWCNT-COOH and MWCNT-NH₂ respectively via the formation of amide linkage between the primary amine and acid moieties.

FT-IR spectroscopy

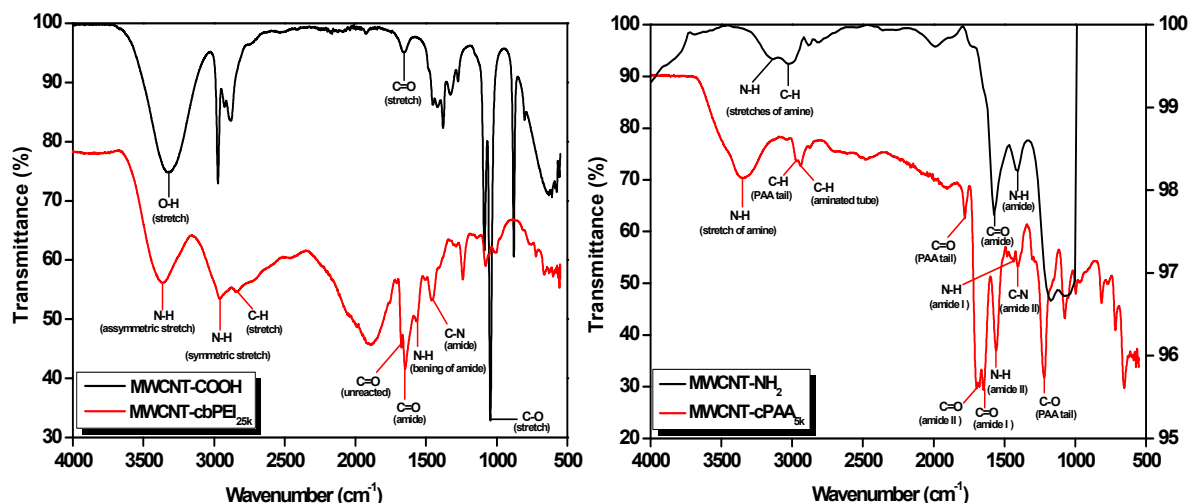


Figure 2.25 : FT-IR spectra of covalently functionalized MWCNTs. (Left: MWCNT-cbPEI_{25k} in comparison with MWCNT-COOH) and (Right: MWCNT-cPAA_{5k} as compared to MWCNT-NH₂).

Highly stable & oppositely charged building blocks

The FT-IR spectra of “parent” and PEs (PAA_{5k} and bPEI_{25k}) tethered nanotubes are shown in the Figure 2.25. The interpretation is quite similar to FT-IR spectra of functional nano ceria, as the same polymers (but different in Mws) are used. Briefly, in comparison with oxidized tubes, characteristic bands at 3370 cm⁻¹ and at 2958 cm⁻¹ in MWCNT-bPEI_{25k} are assigned to –NH asymmetric and symmetric stretching vibrations of bPEI_{25k} backbone^[86] respectively. The reduced intensity of the bands at 1658 cm⁻¹ and 1069 cm⁻¹, attributed to carbonyl C=O and C-O stretching of acid, reveals that some acid groups are left free. Appearance of new peaks at 1648 cm⁻¹, 1560 cm⁻¹ and 1461 cm⁻¹ respectively associated with C=O stretching, –NH bending and –C-N stretching of amide (-CONH)^[87, 88], assures the successful formation of amide bonds between –COOH groups of oxidized tubes and –NH₂ groups of bPEI_{25k}.

In Figure 2.25 (right), the presence of a narrow band at 3357 cm⁻¹ in anionic composite corresponds to –NH stretching vibration of amine groups of parent nanotubes^[134]. The bands at 2972 cm⁻¹ and 2935 cm⁻¹ corresponds to –CH stretching vibrations of acrylic acid and ethylenediamine backbone respectively. Appearance of new peaks at 1779 cm⁻¹ and 1219 cm⁻¹ responsible for –C=O and C-O stretching of residual COOH groups^[132], assures the successful attachment of PAA_{5k} to aminated tubes. An additional proof is shown by the appearance of characteristic amide stretchings^[87, 88] at 1686 cm⁻¹, 1555 cm⁻¹ and at 1405 cm⁻¹, designated as amide II in MWCNT-PAA_{5k} in order to differentiate from the already existing amide link, resulting from ethylenediamine functionalization (and assigned as amide I). Both bPEI_{25k} and PAA_{5k} covalent functionalizations were further confirmed by ¹H NMR.

¹H Nuclear Magnetic Resonance (NMR) spectroscopy

The ¹H 1D NMR spectra of MWCNT-bPEI_{25k} and MWCNT-PAA_{5k} are shown in Figure 2.26. As mentioned earlier, protons from –CH₂ backbone of bPEI_{25k} alone normally appears in the region between 2.4-2.5 ppm. Their shift from 2.5 ppm to upfield between 2.7 ppm and 3.194 ppm (a broad multiplet) are assigned as a in MWCNT-bPEI_{25k}, evidencing the covalent attachment of primary amine groups of bPEI_{25k} to high electronegative carbonyl group of MWCNT-COOH^[79].

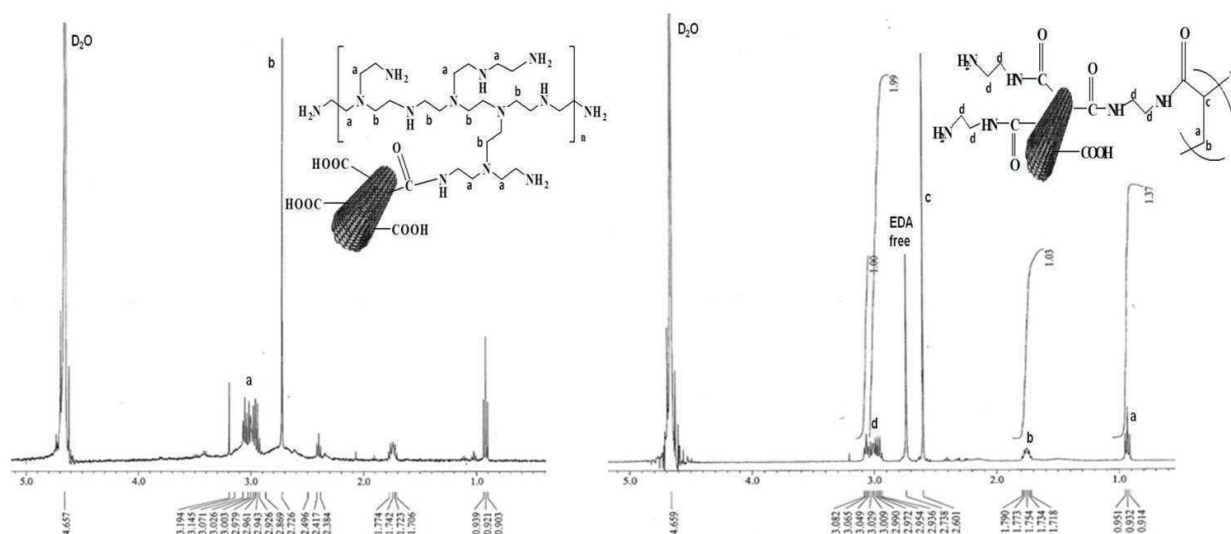


Figure 2. 26 : ^1H NMR of $b\text{PEI}_{25k}$ (left) and PAA_{5k} (right) functionalized MWCNTs.

In MWCNT- PAA_{5k} , the presence of multiplet from 1.718 ppm to 1.790 ppm and a triplet at 0.932 ppm is attributed to $-\text{CH}_2$ protons of the PAA_{5k} backbone. The appearance of $-\text{CH}$ protons in downfield at 2.601 ppm as compared to parent PAA_{5k} (2.9 ppm), indicating the deshielding of $-\text{CH}$ protons, as a result of electron density shift from their adjacent $-\text{C}=\text{O}$ group to nitrogen atom, confirms the incorporation of PAA_{5k} to ethylenediamine via amide linkage^[89]. Consequently, $-\text{CH}_2$ protons of EDA shift to upfield as compared to as-received EDA (2.74 ppm)^[135], and appear as multiplet between 2.94 ppm to 3.082 ppm, representing the attachment of the amine groups (of this ligand) to high electronegative carbonyl groups. The resonance at 2.74 ppm indicating the presence of unreacted parent ligand suggests that conversion to amide is not complete. From the integral value of the spectra it was deduced that 80% and 72% of carboxyl and amine groups of MWCNT- COOH and aminated tubes were respectively modified by $b\text{PEI}_{25k}$ and PAA_{5k} .

Zeta potential measurements

Electrophoretic mobility measurements as a function of pH were carried out on both types of nanocomposite dispersions. The interpretation is similar to functional nano ceria composites as the corona of CNT composites were built from the same PEs.

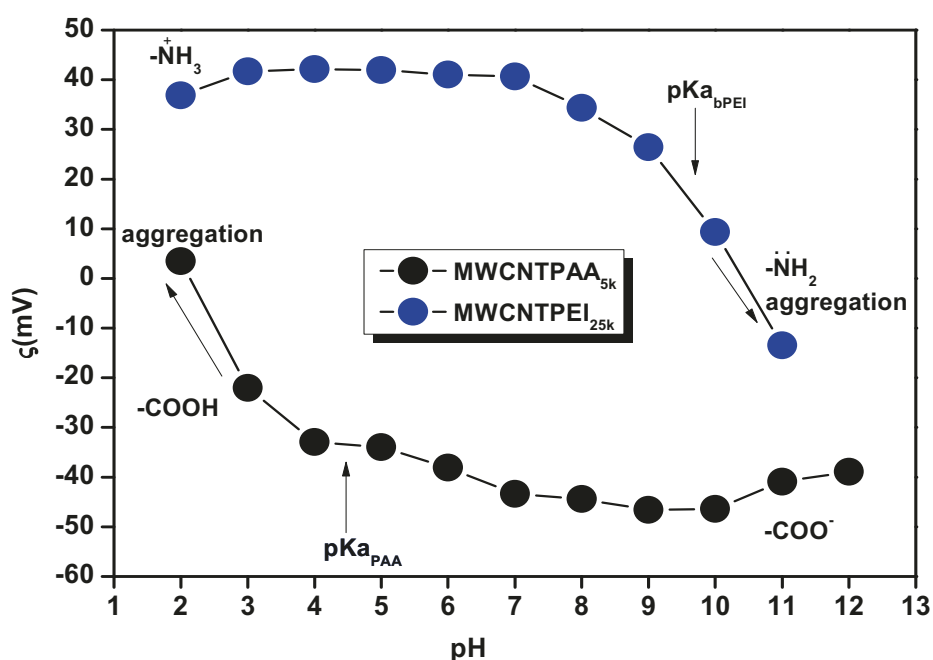


Figure 2. 27 : Zeta potential of cationic (top curve) and anionic (bottom curve) MWCNTs nanocomposites.

Anionic composites are more stable at basic pH, due to the high ionization degree of PAA chains which stabilizes the dispersion via electrosteric repulsion. At acidic pH, the sols were destabilized by aggregate formation due to the protonation of carboxylate moieties. A reverse behavior is shown by MWCNTPEI_{25k}. Stable dispersions are obtained at low pH, as the amine groups of corona are protonated and then more positive at acidic pH. Destabilization occurred when the pH was raised above the pKa of PEI, due to the lack of sufficient repulsion provided by amine groups. The average ζ values are +40 mV and -40 mV for bPEI_{25k} and PAA_{5k} stabilized CNTs respectively. As explained previously, modification with PEI and PAA chains respectively shifts the IEP of parent CNTs to higher and lower pH values^[96]. The appearance of stable dispersions beyond pKa values of free PEs emphasize that MWCNT backbones shifting down the pKa of $-\text{COOH}$ ^[127] of PAA to lower pH values, whereas shifting up the pKa of $-\text{NH}_2$ groups of bPEI to higher pH values.

Depolarized Dynamic Light scattering (DDLS)

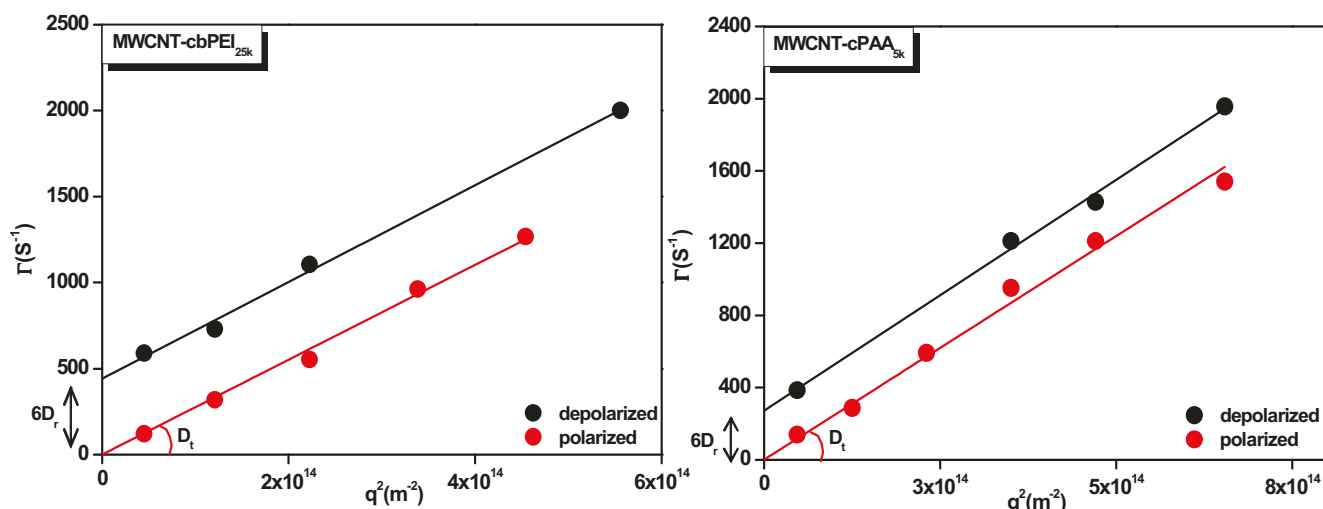


Figure 2.28: Γ as a function of q^2 for MWCNT-cbPEI_{25k} (left), MWCNT-cPAA_{5k} (right).

DDLS experiments give a similar lengths for both anionic and cationic MWCNTs around 500-700 nm, somehow smaller than parent MWCNT-COOH and MWCNT-NH₂ tubes. A supplementary functionalization step (chemistry + sonication) might explain shortening of tubes. Interestingly, we note an increased diameter of cationic and anionic PEs functionalized MWCNTs as compared to their respective parent tubes. Furthermore, PEI_{25k} chains possessing a much larger Mw than PAA_{5k} chains, give slightly larger MWCNTs as one might expect as seen in the Table 2.5.

Functional MWCNTs	D_t ($\mu\text{m}^2/\text{s}$)	D_r (s^{-1})	L (nm)	D (nm)
MWCNT-COOH	1.87	13	1024±51	13±0.65
MWCNT-cbPEI _{25k}	2.75	73.3	550±28	20.5±1.03
MWCNT-NH ₂	1.99	25.5	750±37	26±1.3
MWCNT-cPAA _{5k}	2.47	45.1	620±31	18.8±0.94

Table 2.5: Dimensions of PEs functional MWCNT nanocomposites.

Highly stable & oppositely charged building blocks

The functionalization was further confirmed by TEM experiment which is in close agreement with DDLs. HRTEM images shown below correspond to oppositely charged covalent hybrids. The presence of additional layers on CNT composite materials gives direct evidences for the presence of PEs. Grafting with bPEI_{25k} and PAA_{5k} increased the diameter of cationic and anionic tubes respectively by 5 nm and 3 nm in comparison with their respective parent materials. The visualization of polymeric coatings on CNTs is not much significant, due to the low contrast of polymers.

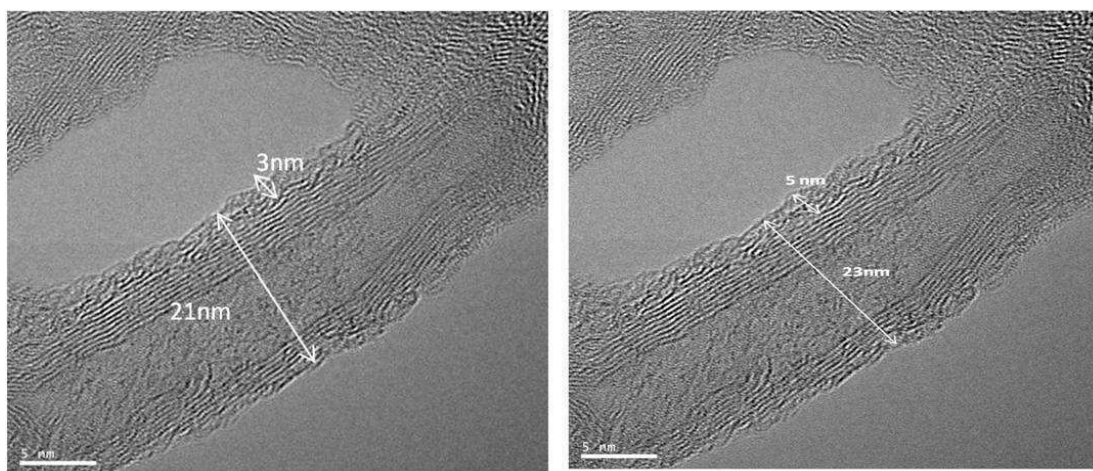


Figure 2. 29 : HRTEM images of MWCNT composites MWCNT-cbPEI_{25k} (right), MWCNT-cPAA_{5k} (left).

Ionic strength stability

Influence of the ionic strength on the stability of anionic and cationic CNTs covalent nanocomposites are investigated as a function of NH₄Cl concentration. The slight decrease in size of bPEI functionalized tubes is due to the shrinkage of the organic corona through the salt screening effects as described earlier^[83, 102, 103]. Debye lengths vary here from 3 nm (10⁻²M) down to 0.15 nm (4M). Beyond 0.5M, where the electrostatic interaction is very low, steric repulsion stabilizes both the dispersions. Interestingly, in the case of PAA CNT composites a slight increase in size is observed at high Is due to the chain swelling, enhanced via hydrophobic interactions^[136]. Both PEs functionalized MWCNT nanocomposites dispersions present then very high stability at high ionic strength (up to 4M) over many months. Stability of MWCNTs was then increased by 3 orders of magnitude.

Highly stable & oppositely charged building blocks

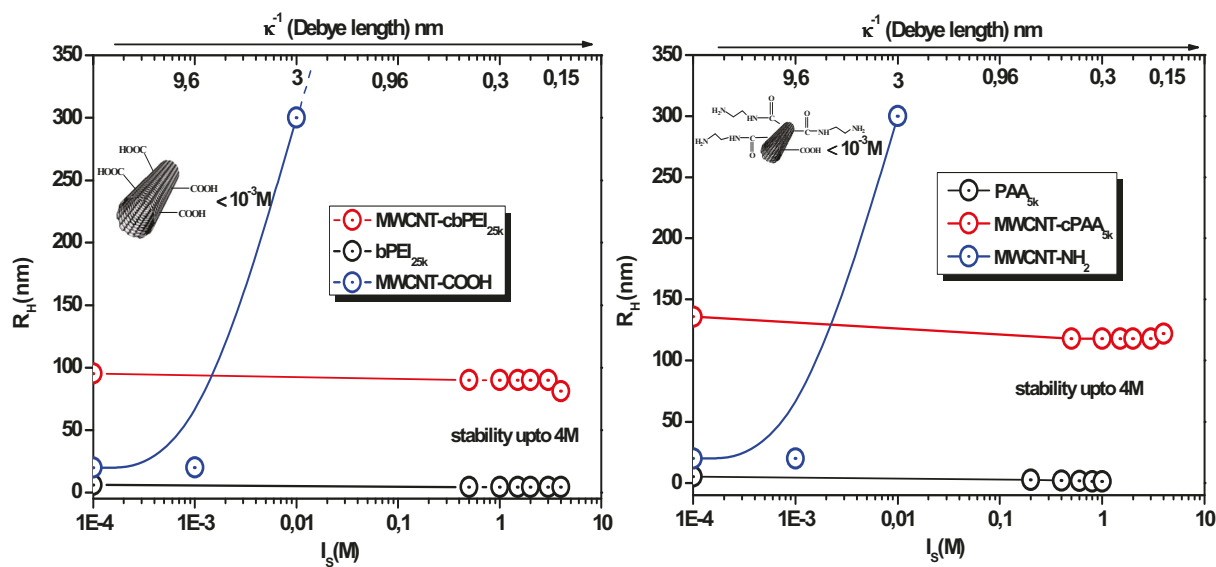


Figure 2. 30 : Stability of MWCNT-bPEI_{25k} (left) and MWCNT-PAA_{5k} (right) in comparison with their respective parent PEs under increasing ionic strength $[NH_4Cl]$.

Conclusions

Unique properties made carbon nanotubes (CNTs) as most wanted material in nanoscience. In the past years, the dispersibility issues of CNTs were overcome via functionalization. Herein, for the first time, besides dispersion, we have shown a special concern on their stability features especially towards high ionic strength, an important criteria which makes CNTs as suitable building blocks to generate functional materials (see following chapter). The impact of functionalization strategy as well as the value of the dispersants on MWCNTs stability was investigated using short ligands and charged macromolecules through both covalent and non-covalent grafting strategies.

The covalent attachment of short ligands such as carboxyl and amine groups via amidation to the CNTs tube surface were confirmed by cross FT-IR and DDLS experiments. The occurrence of destabilization even under moderate concentration of salt (10^{-3}M) indicated that the charge density, an essential parameter to get electrostatic stabilized dispersions, was not enough to exert a sufficient repulsion to overcome strong attractive van der Waals forces. A result that triggered the use of charged macromolecules and their electrosteric stabilization potential.

Non covalent MWCNTs-PEs composites were fabricated with the help of ultrasonication via the wrapping of cationic or anionic PEs over bare pristine CNT tubes. Significant FT-IR stretching bands together with increased tubes diameters measured by DDLS suggested a successful non-covalent functionalization of MWCNTs by PEs. Estimation of the final Mw of the macromolecules at the end of ultrasonication treatment step highlighted the real role of charges and Mw of PEs on the dispersion stabilization. Large Mw PEs caused aggregation likely through bridging, whereas short chains were unable to fully wrap tubes surfaces.

Stability of non covalent CNT composite dispersions was improved up to two orders of magnitude (10^{-1}M) as compared to MWCNT-COOH and MWCNT-NH₂. The addition of salt during the wrapping step transiently (24 hrs) improved the stability up to 1M. The appearance of a precipitation suggested that long term stability could be efficiently accomplished by a covalent attachment of PEs to the surface of the MWCNTs.

Finally anionic PAA_{5k} and cationic bPEI_{25k} chains were covalently tethered on aminated and oxidized tubes respectively via amide linkage mediated by carbodiimide cross

Highly stable & oppositely charged building blocks

linkers. FT-IR and ^1H NMR characterization confirmed the successful covalent attachment of anionic and cationic PEs onto their respective parent tubes. DDLs and TEM experiments gave strong evidences for presence of PEs chains on the tubes surface as shown by increased diameters. Furthermore nanocomposite solutions exhibited excellent stability in high ionic strength up to 4M of NH_4Cl for many months without any precipitation. Covalent attachment of weak anionic and cationic PEs is then a reliable way to generate stable CNT BBs, able to participate in a second step to the generation of functional materials.

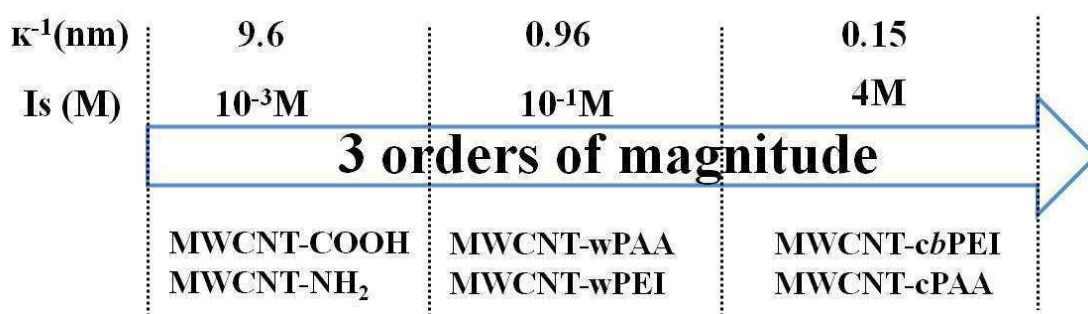


Figure 2. 31 : *Stability scenario of functional MWCNTs.*

Part III - Silica Nanoparticles (SiNPs)

Introduction

Silica Nanoparticles (SiNPs) are ubiquitous and one of the most reviewed materials of metal oxide NPs class. They are used in plethora of applications include coatings, sensors, catalysis and biology because of their unique properties such as high specific surface area, pore volume, pore size and chemical reactivity, cheap and easy handling^[137].

Sol-gel, microemulsion and flame synthesis are commonly used techniques to synthesize SiNPs. The major drawbacks of flame and microemulsion methods are difficulty in controlling size, morphology and removal of surfactants respectively. Whereas sol-gel approach is widely used and an effective route to develop SiNPs^[138]. The pioneer work of Stöber in 1968^[139], explored the synthesis of monodispersed spherical silica nanoparticles based on sol-gel approach via hydrolysis and condensation of TEOS in the presence of ammonia in ethanol medium. The size of the particles ranging from nanometer to micrometer can be varied by altering the concentration of reactants and reaction conditions such as temperature and time.

Typical surface silanol groups (Si-OH) promote spontaneous aggregation between adjacent particles via H-bonding^[137]. Protonation/deprotonation of surface silanol groups determines the surface charge of SiNPs. Many reports have shown that the rate of aggregation of SiNPs strongly depends on various external parameters such as pH, salt and temperature^[140, 141]. Metin *et al.*^[141] investigation leads to apparent conclusion that in comparison with other parameters (pH and temperature), electrolyte addition has great impact on stability, as they effectively compress the electric double layer, enhances the aggregation via particle-particle interaction. The authors pointed out that as compared to monovalent ions, divalent cations cause severe aggregation. This behavior makes SiNPs as unsuitable candidate to target many biological applications. In addition the aggregates affect unique properties, hamper the processibility, homogeneous dispersion and other potential applications. The aforementioned barriers were circumvented by physical (mechanical) and chemical methods. Disaggregation and hence dispersion alone was improved by mechanical methods which include ball milling and ultrasonication^[137]. But suffer severe drawbacks as they highly destruct the shape and size of NPs.

Highly stable & oppositely charged building blocks

Previous comprehensive reports showed that surface engineering based on chemical method is a powerful approach to achieve both dispersibility and stability. It can be accomplished either via physical or chemical interactions of stabilizing agents with NPs surface. The main drawback of physisorption is that the weak interaction between modifier and particle surface initiate aggregation. Chemical modification or chemisorption is more attractive and reliable way, as the interaction between the stabilizer and particle are much stronger.

Silane coupling agents and polymers were widely used for chemisorption. Silane coupling agent is a bifunctional molecule, comprising hydrolyzable groups at one end and organofunctional groups at the other end. Typical hydrolyzable groups are chloro, methoxy and ethoxy, which react with the –OH groups of surface silanol to establish covalent Si-O-Si bond. Among various available coupling agents, APTES is the most commonly used one which acts as a catalyst during the sol-gel synthesis of SiNPs. APTES terminates the particle surface with primary amine groups and finds applications in biological field. Although, the silane functionalization improves the dispersibility both in aqueous and in organic solvents, they provide insufficient barrier against high Is. Albeit, the main advantage of amine groups is that they allow further accessibility to other molecules and polymers.

On the other hand surface modification of SiNPs by PEs is an effective way to improve the interfacial properties and compatibility of particles with external factors. The covalent attachment of PEs to NP surface can be achieved either via “grafting to” or “grafting from”. As described in *Functionalization of NPs*, “grafting from” possesses complications such as it requires specific conditions and involves many steps. Although the grafting density is low, “grafting to” is the simplest and convenient way to formulate silica-polymer nanocomposites.

Several homo and copolymers were successfully grafted to silica nanoparticles surface. Among them, PAA and PEI were extensively studied because of their intrinsic properties such as biocompatibility, conformational changes, environmental response and commercial applications. Incorporation of these PEs to silica surface was carried out via several procedures. For instance, Heikkinen *et al.*^[142] followed two different methods to graft PAA on SiNPs. In the first method, PAA was first end functionalized with imidazole and subsequently formed amide bond with APTES modified SiNPs at low temperature in next step. Whereas in second method, MgCl₂ catalyzes the formation of covalent ester linkage

Highly stable & oppositely charged building blocks

between glycidoxy functionalized silica and PAA. Both of the above methods proceed through multistep reactions, where either the PEs end or metal NPs surface were preferably modified by appropriate agents followed by their incorporation with complementary groups. Removal of catalyst in second method may need special attention. In contrast, Suzuki *et al.* modified amine terminated SiNPs surface by PAA in one step, but requires harsh condition such as the reactants were heated at 140°C in DMF to establish amide linkage^[143]. All the aforesaid grafting experiments were carried out in DMF, its high boiling point (154°C) requires high temperature purification process in order to remove them completely from end product which may break the covalent linkage.

In this work, we got around previous methods drawbacks. The aqueous solution of PAA grafted SiNPs were formulated in one step in absence of catalyst under mild conditions using carbodiimides as coupling agents between APTES modified SiNPs and PAA_{5k}. Dispersion stability of nanocomposites was investigated as a function of pH and ionic strength. Jiang *et al.*^[144] have shown that PAA grafted SiNPs are stable under 1M of NaCl and CaCl₂. In the present system, we have broaden the investigation range.

There are several literatures dealing with the synthesis of PEI functionalized SiNPs^[145-147]. Different synthetic routes were developed although only the direct mixing approach was successful as explained later on.

Experimental Section

Synthesis of Silica nanoparticles (Stöber method)

Silica nanoparticles (SiNPs) were synthesized by hydrolysis and condensation of TEOS in aqueous solution of ethanol catalyzed by NH_4OH ^[148]. The sizes of particles can be varied by tuning the ratios between base and alkoxide. In the present work, we have synthesized spherical SiNPs in a range of ~ 45 nm using sol-gel process. In a typical synthesis, 2.9 ml of NH_4OH was dissolved in 50 ml of ethanol, to which 1.25 ml of TEOS was added drop wise to initiate the hydrolysis. The cloudy suspension was kept under stirring overnight. The final white suspension was centrifuged at 4000 rpm for 15 min and finally dispersed in DI water and stored.

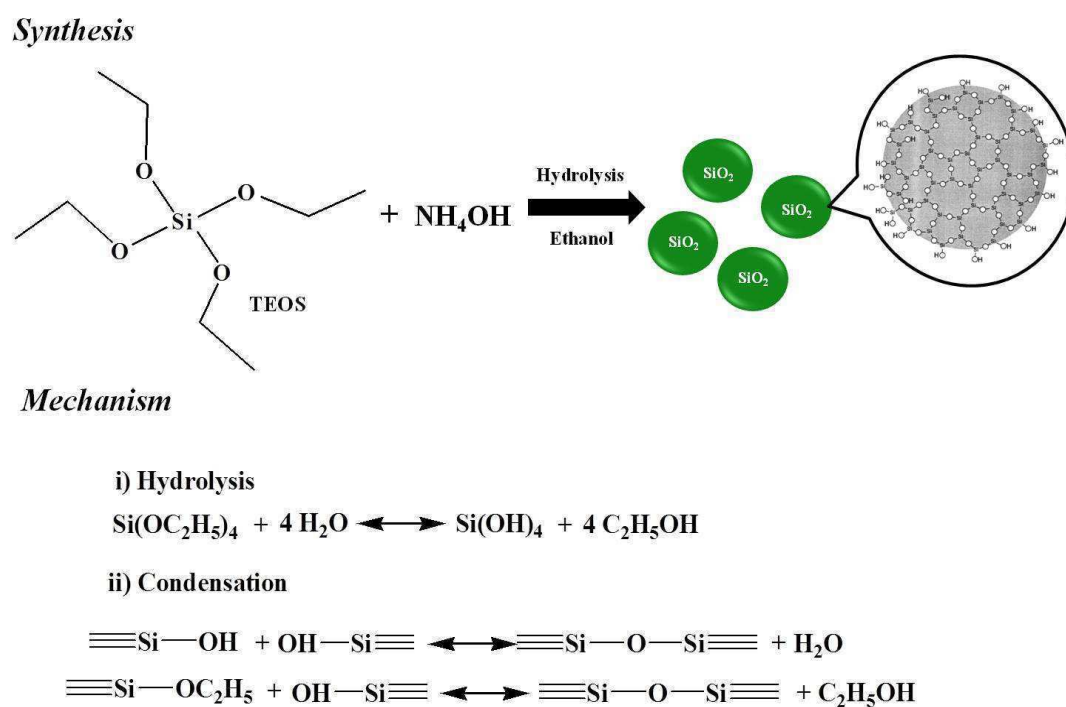


Figure 2.32 : Synthesis and mechanism of formation of silica nanoparticles^[149].

Synthesis of APTES functionalized Silica nanoparticles

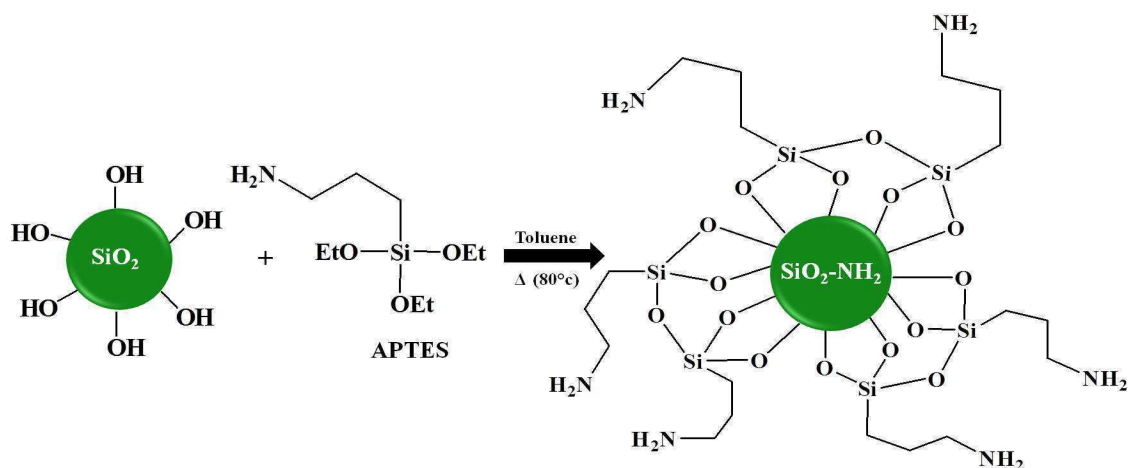


Figure 2.33 : Synthesis of APTES functionalized silica colloids.

APTES (3.5g) in toluene (15ml) was added drop wise to the toluene (50ml) suspension containing silica colloids (2.5g). The mixture was refluxed at 80°C overnight^[143]. After cooling, the suspension was centrifuged and dispersed in water and then stored.

Synthesis of Anionic Silica nanoparticles (SiO₂-PAA_{5k})

PAA_{5k} was covalently grafted onto APTES modified silica via amide linkage mediated by cross linkers (EDC.HCl / NHS) based on combined methods of “grafting to” and “direct mixing”.

In short, APTES modified SiNPs at pH 6 were added at one shot to PAA_{5k} at pH 8 at a volume ratio of 0.1. The aqueous solution of 2:2 equivalents of cross linkers was added to the mixture and stirred at RT for 1 day. PAA uncovered particles are separated by centrifugation. The supernatant was dialyzed in Amicon device of MWCO 10000 to remove loosely bound polymer chains. The purification was monitored by conductivity measurements. At the end, the white paste collected from filter part was dried and referred as SiPAA_{5k}. It was then subjected to various characterizations in order to confirm the covalent functionalization and their stability features.

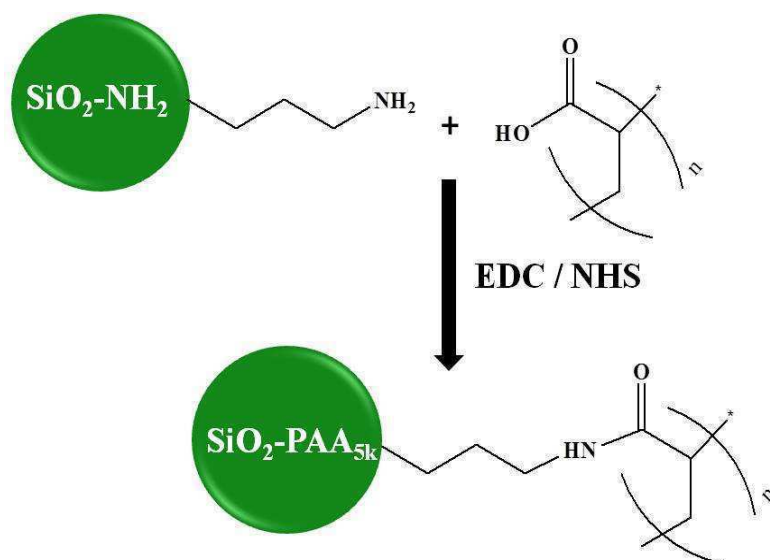


Figure 2. 34 : Schematic representation of synthesis of stable anionic silica via the formation of amide bonds between PAA_{5k} and APTES modified Silica.

Synthesis of cationic silica nanoparticles (SiO₂-bPEI_{25k})

Three different synthetic strategies were investigated to obtain singlet silica NPs covered with bPEI_{25k}. In *strategy I*, bPEI_{25k} was covalently linked to APTES modified silica NPs via imine bonds using glutardialdehyde as a cross linker. The large visible aggregates indicated that the aldehyde promoted the cross linking between the terminal amine groups of starting material. To overcome this drawback, in *strategy II*, bPEI_{25k} functionalization was carried out from TEOS without the need of any cross-linkers. But met the same drawback likely influenced by the chain length of bPEI_{25k} (for more details see appendix II). In order to manage this issue strategy III was implemented.

Strategy III

This strategy follows the combination of “direct mixing” with “grafting to”. Here the bPEI_{25k} functionalized particles are synthesized from anionic silica nanoparticle (SiPAA_{5k}) via amide linkages. In a typical synthesis, SiPAA_{5k} NPs at pH 8 were added at one shot to bPEI_{25k} at pH 5 at a volume ratio of 0.1. The aqueous solution of 2:2 equivalents of cross linkers was added to the mixture and stirred at RT for 1 day. The obtained suspension was dialyzed in Amicon device of MWCO 25,000 to remove loosely bound PEI chains. The purification was monitored with the help of ninhydrin. At the end, the white paste collected

Highly stable & oppositely charged building blocks

from filter was dried and referred as $\text{SiO}_2\text{-bPEI}_{25k}$, highly stable cationic silica NPs. The visual saline stability assessment indicates that the formulated sols are stable under high concentration of salt up to 4M NH_4Cl .

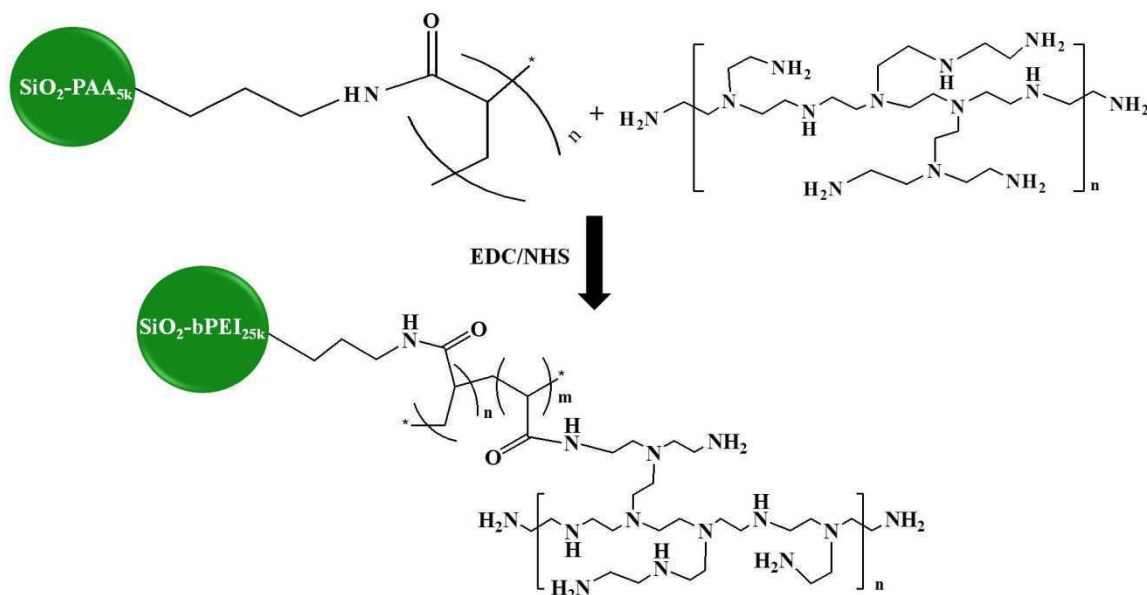


Figure 2. 35 : *Synthesis of bPEI functionalized silica nanoparticles from anionic silica.*

The stability features are encouraging result. Albeit, from this we cannot assure the successful covalent functionalization of bPEI, as the parent material itself is stable under high salt content. Therefore characterizations such as FT-IR, NMR, zeta has to be done in near future in order to prove the presence of covalent bond and successful modification of anionic silica NPs by cationic polymers. It should be noted however that the mixing of cationic and anionic silica NPs leads well to precipitation.

The major drawback of this synthesis route is a reduced concentration of inorganic material in the final composite as the volume ratios are low. In other words, the NPs suspension is indeed diluted by the addition of PEs.

Results and Discussions

Characterization of APTES and PAA_{5k} functionalized SiNPs

FT-IR spectroscopy

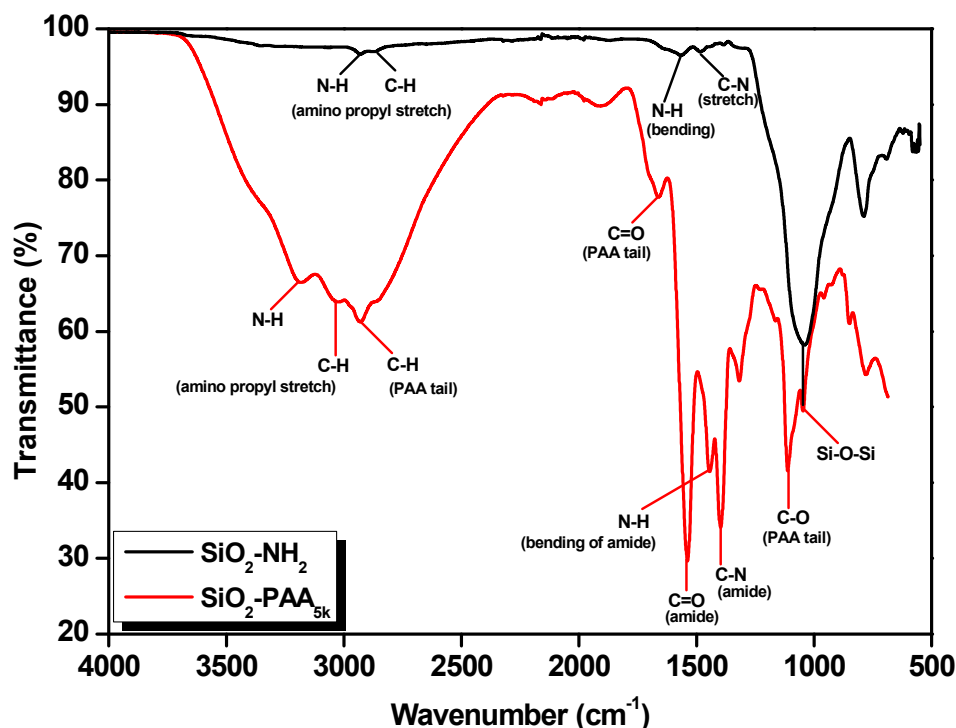


Figure 2. 36 : *FT-IR spectra of aminopropyl and PAA modified Silica nanoparticles.*

The FT-IR spectra of APTES and PAA modified silica nanoparticles are shown in the Figure 2.36. The covalent attachment of APTES is confirmed by the presence of characteristic siloxane stretching at 1040 cm^{-1} . The appearance of bands at 2928 cm^{-1} , 1566 cm^{-1} and 2865 cm^{-1} respectively responsible for -NH stretching, -NH bending and -CH stretching vibrations of aminopropyl backbone^[150] gives additional proof for the successful modification by APTES.

In comparison with APTES modification, the presence of additional bands at 3027 cm^{-1} , 1705 cm^{-1} and 1112 cm^{-1} respectively associated with -CH , -C=O and -C-O stretching of residual acid groups indicating the presence of PAA^[132]. The successful incorporation of

PAA to amine terminated NPs by cross linkers is evidenced by the appearance of characteristic amide stretchings^[87, 88] at 3181 cm^{-1} , 1664 cm^{-1} , 1397 cm^{-1} and 1538 cm^{-1} , attributed to $-\text{NH}$, $-\text{C}=\text{O}$, $-\text{C}-\text{N}$ stretching and bending.

Dynamic Light scattering (DLS)

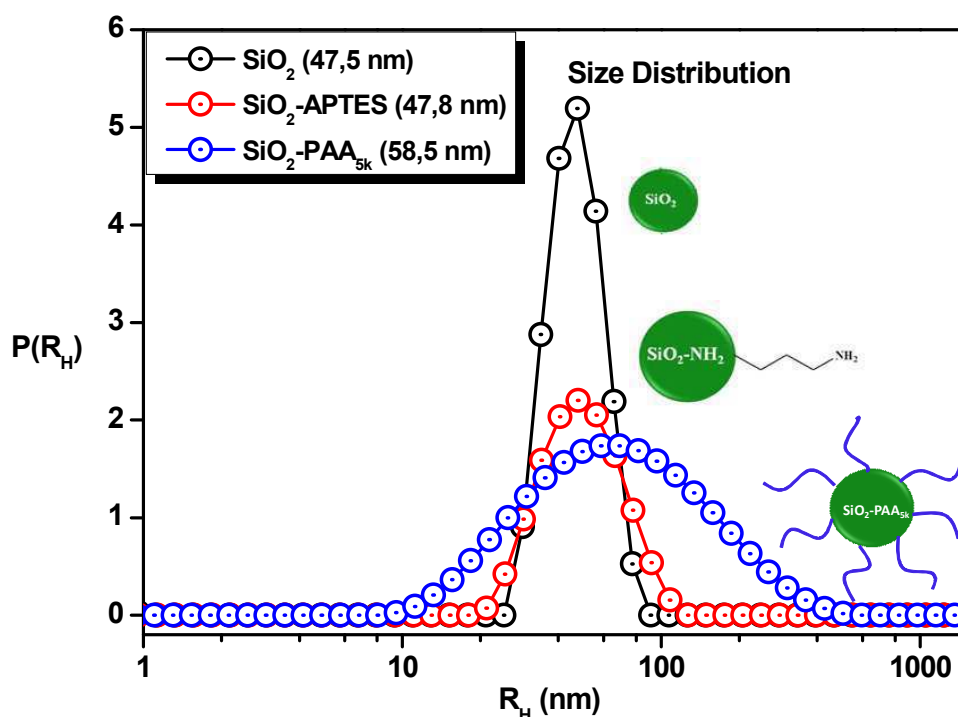


Figure 2. 37: Hydrodynamic Radii (PR_H) distribution of bare silica, APTES-silica and $\text{SiO}_2\text{-PAA}_{5k}$.

The increase in R_H and the broadening of distribution of $\text{SiO}_2\text{-PAA}_{5k}$ as compared to bare and APTES modified silica NPs give direct evidences for the successful attachment of PAA chains. The experimentally determined mean $R_H = 58\text{ nm}$ calculated from D_0 is larger than the $R_H = 48\text{ nm}$ of amine functionalized particles. The difference of $\sim 10\text{ nm}$ is associated with an increase in the corona thickness as a consequence of PAA chain attachment. The theoretically calculated fully extended (contour) length of PAA_{5k} chains is about 16 nm . The difference of 6 nm as compared to experimentally determined value ($\sim 10\text{ nm}$) expresses that $1/3$ of the PAA backbone was strongly bound to the particle surface. The remaining $2/3$ of the chains are sticking out into the aqueous solution and stabilizes the colloids via electrosteric repulsion. No significant difference is noticed between the R_H of amine terminated and bare particle since the chain length of APTES is only 0.2 nm .

Transmission Electron Microscopy

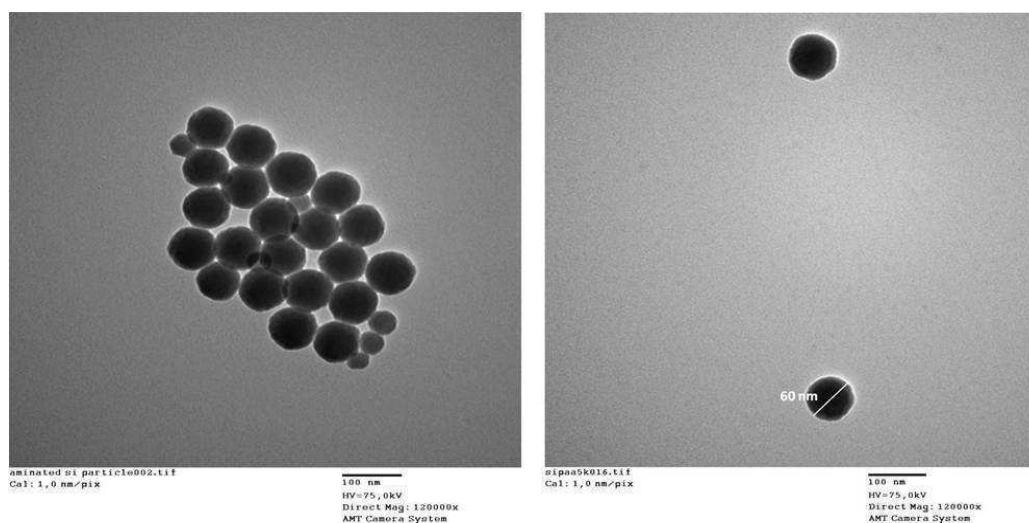


Figure 2. 38 : TEM images of APTES functionalized silica (left) and $\text{SiO}_2\text{-PAA}_{5k}$ (right).

The images shown in the Figure 2.38 correspond to amine and PAA modified silica nanoparticles. The presence of a significant bright shell around the core confirms the presence of APTES and PAA chains. The well dispersed state of anionic silica nanoparticles as compared to its parent material is influenced by the chain length of PAA_{5k} . The size measured from TEM experiment is in close agreement with DLS data, giving additional proof for the presence of the organic layer around the inorganic NPs.

Zeta potential

Figure 2.39 explores the stability of $\text{SiO}_2\text{-PAA}_{5k}$ as a function of pH. The absence of flocculation and high negative zeta potential (-40 mV) at basic pH (beyond the pKa) confirms the grafting of PAA chains onto NPs. The occurrence of destabilization at extreme acidic pH is due to the protonation of carboxylate moiety. The above exploration concludes that grafting with PEs broaden the stability range of NPs with respect to pH. Indeed, bare SiO_2 NPs are stable at high pH, where they are fully charged and at low pH, where short range hydration forces stabilize the NPs. At intermediate pH however (pH 4 to 6), the dispersion is unstable (no hydration forces anymore and very weak electrostatic repulsion close to the SiO_2 NPs IEP) and precipitate. The PAA modification shifting down the IEP of APTES modified

SiNPs to lower pH values^[147]. Whereas SiNPs slightly shifting down the pKa of PAA chains as already pointed out for CeO₂ and CNT nano building blocks^[97, 98].

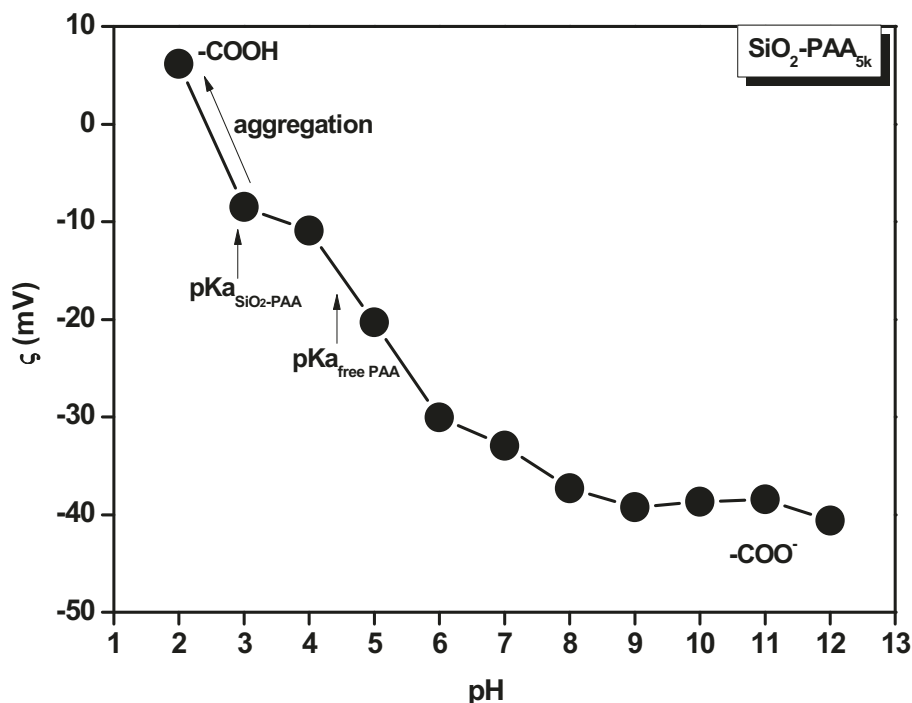


Figure 2.39 : Zeta potential of PAA functionalized silica nanoparticles ($\text{SiO}_2\text{-PAA}_{5k}$).

Ionic Strength stability

Figure 2.39 clearly shows that the dispersion of PAA_{5k} grafted silica nanoparticles remains stable upon the addition of up to 4M of NH₄Cl. The initial R_H drop at about 0.5M is again due to the shrinkage of PAA chains^[144]. Dispersion stability is then provided by the electrosteric repulsion between PAA chains. No significant variation of R_H is seen by DLS over months, indicating that PE grafting is a reliable way to obtain long term stable dispersions in saline conditions.

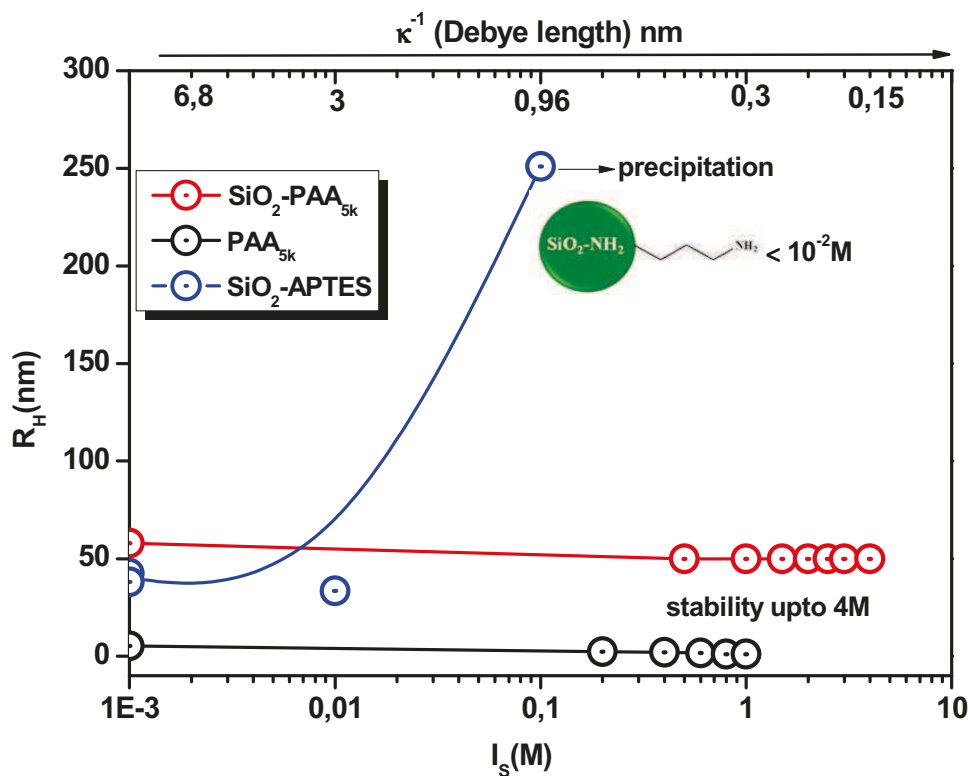


Figure 2.40 : Hydrodynamic Radii (R_H) of $\text{SiO}_2\text{-PAA}_{5k}$ and free PAA chains as a function of the ionic strength $[\text{NH}_4\text{Cl}]$.

Conclusions

We have proposed a facile route to synthesize core-shell silica nanoparticles which overcomes the drawbacks of previous methods. Grafting of PAA chains onto silica nanoparticles were successfully accomplished under mild conditions. Silica nanoparticles terminated with amine functionality formed amide bonds with –COOH groups of PAA using carbodiimides coupling agents. Probing techniques confirmed the covalent attachment of anionic PAA chains onto the SiO₂-NH₂ NPs. Covalent grafting of PAA chains enhanced the stability of silica NPs under a wide pH and ionic strength range. The high stability of SiO₂-PAA_{5k} NPs triggers their use in electrostatically co-assembled structures with other oppositely charged stable building blocks. We have also synthesized cationic silica NPs. But we did not fully characterize due to lack of time. They will be used for co-assembly with anionic silica NPs in near future.

References

1. Bourgeat-Lami, E., *Organic-Inorganic Nanostructured Colloids*. Journal of Nanoscience and Nanotechnology, 2002. **2**(1): p. 1-24.
2. Iijima, M. and H. Kamiya, *Surface modification for improving the stability of nanoparticles in liquid media*. Kona Powder Particle J, 2009. **27**: p. 119-129.
3. Wan, S., et al., *Fe₃O₄ Nanoparticles coated with homopolymers of glycerol mono(meth)acrylate and their block copolymers*. Journal of Materials Chemistry, 2005. **15**(33): p. 3424-3430.
4. Lutz, J.-F.o., et al., *One-Pot Synthesis of PEGylated Ultrasmall Iron-Oxide Nanoparticles and Their in Vivo Evaluation as Magnetic Resonance Imaging Contrast Agents*. Biomacromolecules, 2006. **7**(11): p. 3132-3138.
5. Lowe, A.B., et al., *Facile Preparation of Transition Metal Nanoparticles Stabilized by Well-Defined (Co)polymers Synthesized via Aqueous Reversible Addition-Fragmentation Chain Transfer Polymerization* Journal of the American Chemical Society, 2002. **124**(39): p. 11562-11563.
6. Chou, K.-S. and Y.-S. Lai, *Effect of polyvinyl pyrrolidone molecular weights on the formation of nanosized silver colloids*. Materials Chemistry and Physics, 2004. **83**(1): p. 82-88.
7. Li, Z., et al., *One-Pot Reaction to Synthesize Biocompatible Magnetite Nanoparticles*. Advanced Materials, 2005. **17**(8): p. 1001-1005.
8. Di Luccio, T., et al., *Controlled Nucleation and Growth of CdS Nanoparticles in a Polymer Matrix*. The Journal of Physical Chemistry B, 2006. **110**(25): p. 12603-12609.
9. He, Y.-q. and Y.-h. Ping, *Nano-composite TiO₂-PI via sol-gel process*. Materials Chemistry and Physics, 2003. **78**(3): p. 614-619.
10. Xu, H., et al., *Room-temperature preparation and characterization of poly (ethylene glycol)-coated silica nanoparticles for biomedical applications*. Journal of Biomedical Materials Research Part A, 2003. **66**(4): p. 870-879.
11. Lu, H.W., et al., *Silver nanocrystals by hyperbranched polyurethane-assisted photochemical reduction of Ag⁺*. Materials Chemistry and Physics, 2003. **81**(1): p. 104-107.
12. Karadas, F., et al., *X-ray-Induced Production of Gold Nanoparticles on a SiO₂/Si System and in a Poly(methyl methacrylate) Matrix*. Langmuir, 2004. **21**(1): p. 437-442.
13. Kumar, S.S., et al., *Stabilized Gold Nanoparticles by Reduction Using 3,4-Ethylenedioxythiophene-polystyrenesulfonate in Aqueous Solutions: Nanocomposite Formation, Stability, and Application in Catalysis*. Langmuir, 2007. **23**(6): p. 3401-3408.
14. Prucek, R., et al., *Polyacrylate-assisted synthesis of stable copper nanoparticles and copper(II) oxide nanocubes with high catalytic efficiency*. Journal of Materials Chemistry, 2009. **19**(44): p. 8463-8469.
15. Coulter, M.M., et al., *Preparing water-dispersed palladium nanoparticles via polyelectrolyte nanoreactors*. Chemical Science. **1**(6): p. 772-775.
16. Bronstein, L.M., et al., *Interaction of metal compounds with "double-hydrophilic" block copolymers in aqueous medium and metal colloid formation*. Inorganica Chimica Acta, 1998. **280**(1-2): p. 348-354.
17. Lee, H., et al., *Antibiofouling Polymer-Coated Superparamagnetic Iron Oxide Nanoparticles as Potential Magnetic Resonance Contrast Agents for in Vivo Cancer Imaging*. Journal of the American Chemical Society, 2006. **128**(22): p. 7383-7389.
18. Neoh, K.G. and E.T. Kang, *Functionalization of inorganic nanoparticles with polymers for stealth biomedical applications*. Polymer Chemistry, 2010. **2**(4): p. 747-759.
19. Babu, K. and R. Dhamodharan, *Grafting of Poly(methyl methacrylate) Brushes from Magnetite Nanoparticles Using a Phosphonic Acid Based Initiator by Ambient Temperature Atom Transfer Radical Polymerization (ATATRP)*. Nanoscale Research Letters, 2008. **3**(3): p. 109 - 117.

Highly stable & oppositely charged building blocks

20. Zhang, F., et al., *Preparation and characterization of polystyrene grafted magnesium hydroxide nanoparticles via surface-initiated atom transfer radical polymerization*. Journal of Polymer Research, 2008. **15**(4): p. 319-323.
21. Vestal, C.R. and Z.J. Zhang, *Atom Transfer Radical Polymerization Synthesis and Magnetic Characterization of MnFe₂O₄/Polystyrene Core/Shell Nanoparticles*. Journal of the American Chemical Society, 2002. **124**(48): p. 14312-14313.
22. von Werne, T. and T.E. Patten, *Preparation of Structurally Well-Defined Polymer-Nanoparticle Hybrids with Controlled/Living Radical Polymerizations*. Journal of the American Chemical Society, 1999. **121**(32): p. 7409-7410.
23. Chang, M.J., et al., *Surface-initiated atom transfer radical polymerization from Mg(OH)₂ nanoparticles to prepare the well-defined polymer-Mg(OH)₂ nanocomposites*. Journal of applied polymer science, 2007. **103**(6): p. 3680-3687.
24. Sun, Y., et al., *Surface initiated ATRP in the synthesis of iron oxide/polystyrene core/shell nanoparticles*. European Polymer Journal, 2007. **43**(3): p. 762-772.
25. Xu, W., et al., *Atom transfer radical polymerization of n-octyl acrylate under microwave irradiation*. European Polymer Journal, 2003. **39**(7): p. 1349-1353.
26. Barbey, R., et al., *Polymer Brushes via Surface-Initiated Controlled Radical Polymerization: Synthesis, Characterization, Properties, and Applications*. Chemical Reviews, 2009. **109**(11): p. 5437-5527.
27. Boyer, C., et al., *The design and utility of polymer-stabilized iron-oxide nanoparticles for nanomedicine applications*. NPG Asia Mater. **2**: p. 23-30.
28. Zubarev, E.R., et al., *Amphiphilic Gold Nanoparticles with V-Shaped Arms*. Journal of the American Chemical Society, 2006. **128**(15): p. 4958-4959.
29. Amici, J., et al., *Polymer grafting onto magnetite nanoparticles by "click" reaction*. Journal of Materials Science. **47**(1): p. 412-419.
30. Ranjan, R. and W.J. Brittain, *Combination of Living Radical Polymerization and Click Chemistry for Surface Modification*. Macromolecules, 2007. **40**(17): p. 6217-6223.
31. Schneider, G.g.F. and G. Decher, *From "Nano-bags" to "Micro-pouches". Understanding and Tweaking Flocculation-based Processes for the Preparation of New Nanoparticle-Composites*. Nano Letters, 2008. **8**(11): p. 3598-3604.
32. Chen, J., J.A. Heitmann, and M.A. Hubbe, *Dependency of polyelectrolyte complex stoichiometry on the order of addition. 1. Effect of salt concentration during streaming current titrations with strong poly-acid and poly-base*. Colloids and Surfaces A: Physicochemical and Engineering Aspects, 2003. **223**(1-3): p. 215-230.
33. Naderi, A., et al., *Trapped non-equilibrium states in aqueous solutions of oppositely charged polyelectrolytes and surfactants: effects of mixing protocol and salt concentration*. Colloids and Surfaces A: Physicochemical and Engineering Aspects, 2005. **253**(1-3): p. 83-93.
34. Qi, L., et al., *Influence of the Formulation Process in Electrostatic Assembly of Nanoparticles and Macromolecules in Aqueous Solution: The Mixing Pathway*. The Journal of Physical Chemistry C. **114**(30): p. 12870-12877.
35. Qi, L., et al., *Influence of the Formulation Process in Electrostatic Assembly of Nanoparticles and Macromolecules in Aqueous Solution: The Interaction Pathway*. The Journal of Physical Chemistry C. **114**(39): p. 16373-16381.
36. Destremaut, F., et al., *Microfluidics with on-line dynamic light scattering for size measurements*. Lab on a Chip, 2009. **9**(22): p. 3289-3296.
37. Qi, L., et al., *Redispersible Hybrid Nanopowders: Cerium Oxide Nanoparticle Complexes with Phosphonated-PEG Oligomers*. ACS Nano, 2008. **2**(5): p. 879-888.
38. Sehgal, A., et al., *Precipitation-Redispersion of Cerium Oxide Nanoparticles with Poly(acrylic acid): Toward Stable Dispersions*. Langmuir, 2005. **21**(20): p. 9359-9364.
39. Chanteau, B., J. Fresnais, and J.F. Berret, *Electrosteric Enhanced Stability of Functional Sub-10 nm Cerium and Iron Oxide Particles in Cell Culture Medium*. Langmuir, 2009. **25**(16): p. 9064-9070.

Highly stable & oppositely charged building blocks

40. Shetty, A.M., et al., *Multiangle Depolarized Dynamic Light Scattering of Short Functionalized Single-Walled Carbon Nanotubes*. The Journal of Physical Chemistry C, 2009. **113**(17): p. 7129-7133.
41. Trovarelli, A., et al., *The utilization of ceria in industrial catalysis*. Catalysis today, 1999. **50**(2): p. 353-367.
42. Goharshadi, E.K., et al, S. Samiee, and P. Nancarrow, *Fabrication of cerium oxide nanoparticles: Characterization and optical properties*. Journal of Colloid and Interface Science, 2011. **356**(2): p. 473-480.
43. Yakimova, M.S., et al., *Oxidation of CO on nanocrystalline ceria promoted by transition metal oxides*. Doklady Chemistry, 2009. **427**(2): p. 186-189.
44. Ji, P., et al., *Study of adsorption and degradation of acid orange 7 on the surface of CeO₂ under visible light irradiation*. Applied Catalysis B: Environmental, 2009. **85**(3-4): p. 148-154.
45. Dao, N.N., et al., *UV absorption by cerium oxide nanoparticles/epoxy composite thin films*. Advances in Natural Sciences: Nanoscience and Nanotechnology, 2011. **2**(4): p. 045013.
46. Heckert, E.G., et al., *The role of cerium redox state in the SOD mimetic activity of nanoceria*. Biomaterials, 2008. **29**(18): p. 2705-2709.
47. Asati, A., et al., *Oxidase-Like Activity of Polymer-Coated Cerium Oxide Nanoparticles*. Angewandte Chemie International Edition, 2009. **48**(13): p. 2308-2312.
48. Babu, S., et al., *Electron paramagnetic study on radical scavenging properties of ceria nanoparticles*. Chemical Physics Letters, 2007. **442**(4-6): p. 405-408.
49. Selvan, V.A.M.e.a., R.B. Anand, and M. Udayakumar, *Effects of cerium oxide nanoparticle addition in diesel and diesel-biodiesel-ethanol blends on the performance and emission characteristics of a CI engine*. Journal of Engineering and Applied Sciences, 2009. **4**: p. 1-6.
50. Tago, T., et al., *Synthesis and optical properties of SiO₂-coated CeO₂ nanoparticles*. Journal of Nanoparticle Research, 2003. **5**(1): p. 55-60.
51. Kevin, C.K., T. Druffel, and M.K. Sunkara, *Anti-reflective optical coatings incorporating nanoparticles*. Nanotechnology, 2005. **16**(7): p. S338.
52. Ansari, A.A., et al., *Sol-gel derived nanoporous cerium oxide film for application to cholesterol biosensor*. Electrochemistry Communications, 2008. **10**(9): p. 1246-1249.
53. Pelletier, D.A., et al., *Effects of Engineered Cerium Oxide Nanoparticles on Bacterial Growth and Viability*. Applied and Environmental Microbiology, 2010. **76**(24): p. 7981-7989.
54. Bai, W., et al., *Thermophoresis-assisted vapour phase synthesis of CeO₂ and Ce_xY_{1-x}O_{2-δ} nanoparticles*. Solid State Ionics, 1999. **116**(3-4): p. 225-228.
55. Mädler, L., W.J. Stark, and S.E. Pratsinis, *Flame-made ceria nanoparticles*. J. Mater. Res, 2002. **17**(6): p. 1356-1362.
56. Deshpande, A.S., et al., *Synthesis and Characterization of Stable and Crystalline Ce_{1-x}Zr_xO₂ Nanoparticle Sols*. Chemistry of Materials, 2004. **16**(13): p. 2599-2604.
57. Masui, T., et al., *Characterization of Cerium(IV) Oxide Ultrafine Particles Prepared Using Reversed Micelles*. Chemistry of Materials, 1997. **9**(10): p. 2197-2204.
58. Hwang, C.-C., et al., *Combustion synthesis of nanocrystalline ceria (CeO₂) powders by a dry route*. Materials Science and Engineering: B, 2006. **132**(3): p. 229-238.
59. Chengyun, W., et al., *A novel method to prepare nanocrystalline (7 nm) ceria*. Materials Science and Engineering: B, 1996. **39**(3): p. 160-162.
60. Gao, F., Q. Lu, and S. Komarneni, *Fast Synthesis of Cerium Oxide Nanoparticles and Nanorods*. Journal of Nanoscience and Nanotechnology, 2006. **6**(12): p. 3812-3819.
61. Hirano, M. and E. Kato, *Hydrothermal Synthesis of Nanocrystalline Cerium(IV) Oxide Powders*. Journal of the American Ceramic Society, 1999. **82**(3): p. 786-788.
62. Buettner, K.M., C.I. Rinciog, and S.E. Mylon, *Aggregation kinetics of cerium oxide nanoparticles in monovalent and divalent electrolytes*. Colloids and Surfaces A: Physicochemical and Engineering Aspects, 2010. **366**(1-3): p. 74-79.

Highly stable & oppositely charged building blocks

63. Bumajdad, A., J. Eastoe, and A. Mathew, *Cerium oxide nanoparticles prepared in self-assembled systems*. *Advances in Colloid and Interface Science*, 2009. **147-148**: p. 56-66.
64. Yu, S.-H., H. Cölfen, and A. Fischer, *High quality CeO₂ nanocrystals stabilized by a double hydrophilic block copolymer*. *Colloids and Surfaces A: Physicochemical and Engineering Aspects*, 2004. **243**(1-3): p. 49-52.
65. Izu, N., et al., *Controlled Synthesis of Monodispersed Cerium Oxide Nanoparticle Sols Applicable to Preparing Ordered Self-Assemblies*. *Bulletin of the Chemical Society of Japan*, 2008. **81**(6): p. 761-766.
66. Zgheib, N., et al., *Cerium oxide encapsulation by emulsion polymerization using hydrophilic macroRAFT agents*. *Polymer Chemistry*, 2013. **4**(3): p. 607-614.
67. Safi, M., et al., *Interactions between sub-10-nm iron and cerium oxide nanoparticles and 3T3 fibroblasts: the role of the coating and aggregation state*. *Nanotechnology*, 2010. **21**(14): p. 145103.
68. Gu, H. and M.D. Soucek, *Preparation and Characterization of Monodisperse Cerium Oxide Nanoparticles in Hydrocarbon Solvents*. *Chemistry of Materials*, 2007. **19**(5): p. 1103-1110.
69. Zhang, P., et al., *Biotransformation of Ceria Nanoparticles in Cucumber Plants*. *ACS Nano*, 2012. **6**(11): p. 9943.
70. Kartsonakis, I.A., et al., *Synthesis, Characterization, and Antibacterial Action of Hollow Ceria Nanospheres with/without a Conductive Polymer Coating*. *Journal of the American Ceramic Society*, 2008. **91**(2): p. 372-378.
71. Perez, J.M., et al., *Synthesis of Biocompatible Dextran-Coated Nanoceria with pH-Dependent Antioxidant Properties*. *Small*, 2008. **4**(5): p. 552-556.
72. Asati, A., et al., *Surface-Charge-Dependent Cell Localization and Cytotoxicity of Cerium Oxide Nanoparticles*. *ACS Nano*. **4**(9): p. 5321-5331.
73. Vicennati, P., et al., *Polyethylenimine In Medicinal Chemistry*. *Current Medicinal Chemistry*, 2008. **15**(27): p. 2826-2839.
74. Xia, T., et al., *Polyethyleneimine Coating Enhances the Cellular Uptake of Mesoporous Silica Nanoparticles and Allows Safe Delivery of siRNA and DNA Constructs*. *ACS Nano*, 2009. **3**(10): p. 3273-3286.
75. Aymonier, C., et al., *Hybrids of silver nanoparticles with amphiphilic hyperbranched macromolecules exhibiting antimicrobial properties*. *Chemical Communications*, 2002(24): p. 3018-3019.
76. Chane-Ching, J.Y., *Preparing a dispersible, sol-forming cerium (IV) composition*. 1994, Google Patents.
77. Chen, H.-I. and H.-Y. Chang, *Synthesis of nanocrystalline cerium oxide particles by the precipitation method*. *Ceramics International*, 2005. **31**(6): p. 795-802.
78. Berret, J.F., et al., *Stable oxide nanoparticle clusters obtained by complexation*. *Journal of Colloid and Interface Science*, 2006. **303**(1): p. 315-318.
79. Jiang, G., et al., *Hyaluronic acid-polyethyleneimine conjugate for target specific intracellular delivery of siRNA*. *Biopolymers*, 2008. **89**(7): p. 635-642.
80. Follain, N.g., et al., *Coupling of amines with polyglucuronic acid: Evidence for amide bond formation*. *Carbohydrate Polymers*, 2008. **74**(3): p. 333-343.
81. Adamczyk, Z., et al., *Structure of Poly(acrylic acid) in Electrolyte Solutions Determined from Simulations and Viscosity Measurements*. *The Journal of Physical Chemistry B*, 2006. **110**(45): p. 22426-22435.
82. Wang, J. and P. Somasundaran, *Reversible conformational behavior of poly(acrylic acid) LB film with changes in pH, ionic strength and time*. *Colloids and Surfaces A: Physicochemical and Engineering Aspects*, 2006. **273**(1-3): p. 63-69.
83. Dobrynin, A.V. and M. Rubinstein, *Theory of polyelectrolytes in solutions and at surfaces*. *Progress in Polymer Science*, 2005. **30**(11): p. 1049-1118.

Highly stable & oppositely charged building blocks

84. Sujana, M.G., K.K. Chattopadhyay, and S. Anand, *Characterization and optical properties of nano-ceria synthesized by surfactant-mediated precipitation technique in mixed solvent system*. Applied Surface Science, 2008. **254**(22): p. 7405-7409.
85. Karakoti, A.S., et al., *PEGylated Nanoceria as Radical Scavenger with Tunable Redox Chemistry*. Journal of the American Chemical Society, 2009. **131**(40): p. 14144-14145.
86. Francis, S., L. Varshney, and K. Tirumalesh, *Studies on radiation synthesis of polyethyleneimine/acrylamide hydrogels*. Radiation Physics and Chemistry, 2006. **75**(7): p. 747-754.
87. Deng, Y., et al., *Preparation and characterization of hyaluronan/chitosan scaffold cross-linked by 1-ethyl-3-(3-dimethylaminopropyl) carbodiimide*. Polymer International, 2007. **56**(6): p. 738-745.
88. Carrillo, A., et al., *Noncovalent Functionalization of Graphite and Carbon Nanotubes with Polymer Multilayers and Gold Nanoparticles*. Nano Letters, 2003. **3**(10): p. 1437-1440.
89. Parajuli, D.C., et al., *Synchronized Polymerization and Fabrication of Poly(acrylic acid) and Nylon Hybrid Mats in Electrospinning*. ACS Applied Materials & Interfaces, 2009. **1**(4): p. 750-757.
90. Tjipangandjara, K.F., et al., *Correlation of alumina flocculation with adsorbed polyacrylic acid conformation*. Colloids and Surfaces, 1990. **44**(0): p. 229-236.
91. Wang, H., et al., *Binding of Sodium Dodecyl Sulfate with Linear and Branched Polyethyleneimines in Aqueous Solution at Different pH Values*. Langmuir, 2006. **22**(4): p. 1526-1533.
92. Kim, K., et al., *pH Effect on Surface Potential of Polyelectrolytes-Capped Gold Nanoparticles Probed by Surface-Enhanced Raman Scattering*. Langmuir. **26**(24): p. 19163-19169.
93. Dai, J., et al., *Controlling the Permeability of Multilayered Polyelectrolyte Films through Derivatization, Cross-Linking, and Hydrolysis*. Langmuir, 2001. **17**(3): p. 931-937.
94. Li, Z., F.W. Fowler, and J.W. Lauher, *Weak Interactions Dominating the Supramolecular Self-Assembly in a Salt: A Designed Single-Crystal-to-Single-Crystal Topochemical Polymerization of a Terminal Aryldiacetylene*. Journal of the American Chemical Society, 2008. **131**(2): p. 634-643.
95. Adamczyk, Z., et al., *Characterization of poly(ethylene imine) layers on mica by the streaming potential and particle deposition methods*. Journal of Colloid and Interface Science, 2007. **313**(1): p. 86-96.
96. Sun, J. and L. Gao, *Development of a dispersion process for carbon nanotubes in ceramic matrix by heterocoagulation*. Carbon, 2003. **41**(5): p. 1063-1068.
97. Ulrich, S., A. Laguecir, and S. Stoll, *Complex formation between a nanoparticle and a weak polyelectrolyte chain: Monte Carlo simulations*. Journal of Nanoparticle Research, 2004. **6**(6): p. 595-603.
98. Ulrich, S., A. Laguecir, and S. Stoll, *Complexation of a Weak Polyelectrolyte with a Charged Nanoparticle. Solution Properties and Polyelectrolyte Stiffness Influences*. Macromolecules, 2005. **38**(21): p. 8939-8949.
99. Dubinsky, S., et al., *Thermal degradation of poly(acrylic acid) containing copper nitrate*. Polymer Degradation and Stability, 2004. **86**(1): p. 171-178.
100. Van Dyke, J.D. and K.L. Kasperski, *Thermogravimetric study of polyacrylamide with evolved gas analysis*. Journal of Polymer Science Part A: Polymer Chemistry, 1993. **31**(7): p. 1807-1823.
101. Wang, X., et al., *Control of aggregate size of polyethyleneimine-coated magnetic nanoparticles for magnetofection*. Nano Research, 2009. **2**(5): p. 365-372.
102. Stevens, M.J. and S.J. Plimpton, *The effect of added salt on polyelectrolyte structure*. The European Physical Journal B - Condensed Matter and Complex Systems, 1998. **2**(3): p. 341-345.

Highly stable & oppositely charged building blocks

103. Borisov, O.V. and E.B. Zhulina, *Effects of ionic strength and charge annealing in star-branched polyelectrolytes*. The European Physical Journal B - Condensed Matter and Complex Systems, 1998. **4**(2): p. 205-217.
104. Iijima, S., *Helical microtubules of graphitic carbon*. Nature, 1991. **354**(6348): p. 56-58.
105. Karousis, N., N. Tagmatarchis, and D. Tasis, *Current Progress on the Chemical Modification of Carbon Nanotubes*. Chemical Reviews. **110**(9): p. 5366-5397.
106. Dillon, A.C., *Carbon Nanotubes for Photoconversion and Electrical Energy Storage*. Chemical Reviews. **110**(11): p. 6856-6872.
107. Schluter, A.D., A. Hirsch, and O. Vostrowsky, *Functionalization of Carbon Nanotubes*, in *Functional Molecular Nanostructures*. 2005, Springer Berlin Heidelberg. p. 193-237.
108. Schnorr, J.M. and T.M. Swager, *Emerging Applications of Carbon Nanotubes*. Chemistry of Materials. **23**(3): p. 646-657.
109. Wang, Y., J. Wu, and F. Wei, *A treatment method to give separated multi-walled carbon nanotubes with high purity, high crystallization and a large aspect ratio*. Carbon, 2003. **41**(15): p. 2939-2948.
110. Lu, K.L., et al., *Mechanical damage of carbon nanotubes by ultrasound*. Carbon, 1996. **34**(6): p. 814-816.
111. Esumi, K., et al., *Chemical treatment of carbon nanotubes*. Carbon, 1996. **34**(2): p. 279-281.
112. Datsyuk, V., et al., *Chemical oxidation of multiwalled carbon nanotubes*. Carbon, 2008. **46**(6): p. 833-840.
113. Tasis, D., et al., *Chemistry of Carbon Nanotubes*. Chemical Reviews, 2006. **106**(3): p. 1105-1136.
114. Hu, H., et al., *Chemically Functionalized Carbon Nanotubes as Substrates for Neuronal Growth*. Nano Letters, 2004. **4**(3): p. 507-511.
115. Vaisman, L., H.D. Wagner, and G. Marom, *The role of surfactants in dispersion of carbon nanotubes*. Advances in Colloid and Interface Science, 2006. **128-130**: p. 37-46.
116. Bryning, M.B., et al., *Thermal conductivity and interfacial resistance in single-wall carbon nanotube epoxy composites*. Applied Physics Letters, 2005. **87**(16): p. 161909-161909-3.
117. Sundararajan, P.R., S. Singh, and M. Moniruzzaman, *Surfactant-Induced Crystallization of Polycarbonate*. Macromolecules, 2004. **37**(26): p. 10208-10211.
118. Ajayan, P.M., et al., *Aligned carbon nanotube arrays formed by cutting a polymer resin-nanotube composite*. Science, 1994. **265**(5176): p. 1212-1214.
119. Moniruzzaman, M. and K.I. Winey, *Polymer Nanocomposites Containing Carbon Nanotubes*. Macromolecules, 2006. **39**(16): p. 5194-5205.
120. Chen, G.-X., et al., *Controlled Functionalization of Multiwalled Carbon Nanotubes with Various Molecular-Weight Poly(L-lactic acid)*. The Journal of Physical Chemistry B, 2005. **109**(47): p. 22237-22243.
121. Lin, Y., et al., *Polymeric Carbon Nanocomposites from Carbon Nanotubes Functionalized with Matrix Polymer*. Macromolecules, 2003. **36**(19): p. 7199-7204.
122. Hill, D.E., et al., *Functionalization of Carbon Nanotubes with Polystyrene*. Macromolecules, 2002. **35**(25): p. 9466-9471.
123. Lin, Y., et al., *Functionalizing Multiple-Walled Carbon Nanotubes with Aminopolymers*. The Journal of Physical Chemistry B, 2002. **106**(6): p. 1294-1298.
124. Eitan, A., et al., *Surface Modification of Multiwalled Carbon Nanotubes: Toward the Tailoring of the Interface in Polymer Composites*. Chemistry of Materials, 2003. **15**(16): p. 3198-3201.
125. Tzong-Liu Wang, Chin-Chung Yu, and N.-F. Wang, *Preparation, Characterization, and Properties of Polyurethane-Grafted Multiwalled Carbon Nanotubes and Derived Polyurethane Nanocomposites*. Journal of Nanomaterials, 2011.
126. Bartholome, C., et al., *Electromechanical properties of nanotube-PVA composite actuator bimorphs*. Nanotechnology, 2008. **19**(32): p. 325501.

Highly stable & oppositely charged building blocks

127. Lee, S.W., et al., *Layer-by-Layer Assembly of All Carbon Nanotube Ultrathin Films for Electrochemical Applications*. Journal of the American Chemical Society, 2008. **131**(2): p. 671-679.
128. Islam, M.F., et al., *High Weight Fraction Surfactant Solubilization of Single-Wall Carbon Nanotubes in Water*. Nano Letters, 2003. **3**(2): p. 269-273.
129. Saint-Aubin, K., et al., *Dispersion and Film-Forming Properties of Poly(acrylic acid)-Stabilized Carbon Nanotubes*. Langmuir, 2009. **25**(22): p. 13206-13211.
130. Huang, W., et al., *Sonication-Assisted Functionalization and Solubilization of Carbon Nanotubes*. Nano Letters, 2002. **2**(3): p. 231-234.
131. Damian, C.M., A.M. Pandele, and H. Iovu, *Ethylenediamine functionalization effect on the thermo-mechanical properties of epoxy nanocomposites reinforced with multiwall carbon nanotubes*, UPB Sci. Bull. **72**(3).
132. Chen, S., et al., *Preparation of Poly(acrylic acid) Grafted Multiwalled Carbon Nanotubes by a Two-Step Irradiation Technique*. Macromolecules, 2005. **39**(1): p. 330-334.
133. Liu, P., *Modifications of carbon nanotubes with polymers*. European Polymer Journal, 2005. **41**(11): p. 2693-2703.
134. Damian, C.M., A.M. Pandele, and H. Iovu, *Ethylenediamine functionalization effect on the thermo-mechanical properties of epoxy nanocomposites reinforced with multiwall carbon nanotubes*, U.P.B. Sci. Bull, 2010. **72**(3): p. 163.
135. Verma, K.K., Seema, and Chhabra.S, *Synthesis and characterization of Ethylenediamine complexes of some aryltellurium trihalides*. International Journal of Chemical Sciences, 2008. **6**(1): p. 59-67.
136. Wang, J. and W. Wu, *Swelling behaviors, tensile properties and thermodynamic studies of water sorption of 2-hydroxyethyl methacrylate/epoxy methacrylate copolymeric hydrogels*. European Polymer Journal, 2005. **41**(5): p. 1143-1151.
137. Zou, H., S. Wu, and J. Shen, *Polymer/Silica Nanocomposites: Preparation, Characterization, Properties, and Applications*. Chemical Reviews, 2008. **108**(9): p. 3893-3957.
138. Rahman, I.A. and V. Padavettan, *Synthesis of Silica Nanoparticles by Sol-Gel: Size-Dependent Properties, Surface Modification, and Applications in Silica-Polymer Nanocomposites-A Review*. Journal of Nanomaterials. **2012**: p. 15.
139. StÖber, W., A. Fink, and E. Bohn, *Controlled growth of monodisperse silica spheres in the micron size range*. Journal of Colloid and Interface Science, 1968. **26**(1): p. 62-69.
140. Metin, C., et al., *Stability of aqueous silica nanoparticle dispersions*. Journal of Nanoparticle Research. **13**(2): p. 839-850.
141. Metin, C., et al., *Stability of aqueous silica nanoparticle dispersions under subsurface conditions*. Clean Technology, 2010.
142. Heikkinen, J.J., J.P. Heiskanen, and O.E.O. Hormi, *Grafting of functionalized silica particles with poly(acrylic acid)*. Polymers for Advanced Technologies, 2006. **17**(6): p. 426-429.
143. Suzuki, K., et al., *Modification of porous silica particles with poly(acrylic acid)*. Polymers for Advanced Technologies, 2000. **11**(2): p. 92-97.
144. Jiang, L., et al., *Synthesis and characterization of stimuli-responsive poly(acrylic acid) grafted silica nanoparticles*. Smart Materials and Structures, 2007. **16**(6): p. 2169.
145. McBain, S.C., et al., *Polyethyleneimine functionalized iron oxide nanoparticles as agents for DNA delivery and transfection*. Journal of Materials Chemistry, 2007. **17**(24): p. 2561-2565.
146. Parfenyuk, E., G. Kulikova, and I. Ryabinina, *DSC and spectroscopic investigation of human serum albumin adsorbed onto silica nanoparticles functionalized by amino groups*. Journal of Thermal Analysis and Calorimetry. **100**(3): p. 987-991.
147. Rosenholm, J.M., et al., *Targeting of Porous Hybrid Silica Nanoparticles to Cancer Cells*. ACS Nano, 2008. **3**(1): p. 197-206.

Highly stable & oppositely charged building blocks

148. Gude, K. and R. Narayanan, *Synthesis and Characterization of Colloidal-Supported Metal Nanoparticles as Potential Intermediate Nanocatalysts*. The Journal of Physical Chemistry C. **114**(14): p. 6356-6362.
149. Branda, F., et al., *The effect of mixing alkoxides on the StÖber particles size*. Colloids and Surfaces A: Physicochemical and Engineering Aspects, 2007. **299**(1-3): p. 252-255.
150. Rahman, I.A., M. Jafarzadeh, and C.S. Sipaut, *Synthesis of organo-functionalized nanosilica via a co-condensation modification using γ -aminopropyltriethoxysilane (APTES)*. Ceramics International, 2009. **35**(5): p. 1883-1888.

Chapter 3: Fine tuning of electrostatic complexation between the oppositely charged BBs in bulk.

Abstract

We have investigated the characteristics and properties of the “desalting transition” approach when applied to various oppositely charged BBs. We have shown for the first time the fine-tuning of the complexation between *all*-nanoparticles/tubes hybrids BBs. Confirming the universality and applicability of the desalting transition foreseen in chapter 1 to all types of *stable* colloids. The I_b value of each set was found to differ according to the features of the interacting BBs such as their weak or strong character, architecture, M_w s and nature of the functional groups along the PE backbone. Stable and finite sized non-stoichiometric ($Z \neq 1$) electrostatic complexes were obtained for all the hybrid systems. The robotic experiment has shown that the critical ionic strength I_b is indeed independent of the concentration of building blocks. It should be noted that the complete “electrostatic” screening of opposite charged components was made possible when no secondary forces such as H-bonding or hydrophobic effect were at play in the complexation. Indeed, H-bonding plays an essential role in the complexation when weak PEs were used with an interaction dependent on the proton donor-acceptor characteristics of amine and acid functional groups. H-bonds formation at high I_s was controlled by the presence and nature of inorganic nanoparticles/tubes and the protonation state of functional groups induced by the added salt. Beyond, these remarkable features and findings pushed us to transfer in the next chapter this bulk desalting concept to a substrate/solution interface and investigate the controlled growth of functional hybrid layers.

Introduction

Previous works ^[1-6] on the “desalting transition” from our consortium encouraged us to follow this complexing route to fabricate various electrostatic hybrid complexes (hybrid clusters) with versatile morphologies and properties from our novel highly saline stable hybrid building blocks (BBs) developed in the previous chapter. In a recent publication from our group, the electrostatic co-assembly between oppositely charged PAA coated ceria and PDDAC has been reported and showed potential interest^[6]. Following this work, we have for the first time generalized to *all-hybrid* BBs the concept of the desalting transition investigated in chapter 1 on pure PEs complexes. We put six systems under scrutiny namely the asymmetric couple (CeO₂-PAA_{2k}/PDDAC_{100k}) and symmetric ones (CeO₂-PAA_{2k}/CeO₂-*b*PEI_{25k}, MWCNT-*cb*PEI_{25k}/PAA_{2k}, MWCNT-*cb*PEI_{25k}/MWCNT-*c*PAA_{5k}, SiO₂-PAA_{5k}/*l*PEI_{2k} and SiO₂-PAA_{5k}/*b*PEI_{25k}). The stability of our different BBs under high ionic strength enabled the fine tuning of their electrostatic co-assembly. It should be noted that the transition was studied here on cationic and anionic hybrid materials of same type. In the future, it would be very interesting to pay more attention on the co-assembly of BBs of different nature. Some preliminary experiments will be shown in the conclusion & perspectives chapter.

Experimental section

Materials

The components were “highly stable” cationic and anionic functional CeO₂, covalent MWCNT nanocomposites (MWCNT-*cb*PEI_{25k} and MWCNT-*cPAA*_{5k}, generally referred as *MWCNT-cPEs*) and SiO₂-PAA_{5k}, all developed in chapter 2 and different PEs (PDDAC_{100k}, PAA_{2k} and *l*PEI_{2k}). Acids (HCl, HNO₃) and bases (NaOH, NH₄OH) and NH₄Cl were purchased from Sigma Aldrich and used without purification.

Methods

Desalting transition

Aqueous solutions of each individual component were prepared at pH 8 and at a concentration of 0.1 wt% except for MWCNT-*cPEs* nanocomposites, where the dispersions were prepared at C=0.01 wt%. The desalting experiments performed in chapter 1, between oppositely charged PEs of asymmetric (w/s) and symmetric systems (w/w or s/s) guided us to set the initial ionic strength (I_0) for the present systems, as the “*electrostatic*” complexation takes place between the same pairs of functional PEs. Accordingly, asymmetric systems undergo transition at a smaller ionic strength than symmetric ones. For the CeO₂-PAA_{2k}/PDDAC_{100k} (w/s) pair the initial ionic strength was set to $I_0 = 1\text{M}$, whereas for all other w/w systems (CeO₂-PAA_{2k}/CeO₂-*b*PEI_{25k}, MWCNT-*cb*PEI_{25k}/PAA_{2k}, MWCNT-*cb*PEI_{25k}/MWCNT-*cPAA*_{5k}, SiO₂-PAA_{5k}/*l*PEI_{2k} and SiO₂-PAA_{5k}/*b*PEI_{25k}) was set to $I_0 = 4\text{M}$. The mixing of oppositely charged solutions at their corresponding I_0 was then carried out at equal volume ratio ($X = V_{\text{NPs}}/V_{\text{PEs}}$), yielding clear dormant dispersions. Hydrodynamic radii (R_H) were measured immediately after each dilution step by DLS. Controlled dilution of salt via a drop-by-drop addition of DI water allowed to attain a transition zone between unaggregated and clustered state at a critical bulk transition (I_b), different for each set. The further gradual dilution ended up with a turbid solution.

Electrostatic complexation of BBs in bulk

Desalting transition by Robotic platform

This specific set of experiments was carried out in close collaboration with Rhodia Lab of Future (LOF). They are indeed specialized in high throughput screening technologies, such as milli/micro fluidics and robotic platforms, combined with data mining and online characterization tools. This enables to explore a much larger panel of parameters in formulation processes, without sacrificing time and manpower. We took advantage of a robotic platform developed in the framework of SUGHAR project to coarsely study the desalting transition as a function of the ionic strength at different concentration ranges. A picture of the robotic set-up used for the sample preparation is shown in Figure 3.1.



Figure 3.1: *Real robot configuration for the sample preparation.*

A three-step sample preparation protocol was established. In step 1, separate stock solutions of both BBs at pH ~ 7 and at $C=1\text{ wt}\%$ with $1/4\text{M}$ of NH_4Cl were prepared manually, as well as water at the same ionic strength and pH. In step 2, separate BBs solutions at different C ranging from $0.1\text{ wt}\%$ to $1\text{ wt}\%$ (10 concentrations) were prepared by diluting their respective stock solutions with water at the same I_s . The solutions were then mixed at the same concentration and equal volume to generate dormant solutions with concentration ranging from $0.1\text{ wt}\%$ to $1\text{ wt}\%$. The step 3 was performed in the robotic platform (Zinsser), where each dormant solution obtained from the step 2 was sampled and later completed with pre-calculated volumes of DI water to generate a formulation series with different I_s (M) = 1, 0.95, 0.9, 0.85, 0.8, 0.75, 0.7, 0.65, 0.6, 0.55, 0.5, 0.4, 0.3M. Finally, $10 \times 13 = 130$ formulations were obtained with different concentrations and ionic strengths I_s . During the step 3, the solutions in 1mL glass vials were brought between a camera and a black

Electrostatic complexation of BBs in bulk

background by a robotic arm to take a picture of each sample after dilution with DI water. Taking into account the robotic arm displacement time, a short period of 20 seconds was set for each sample before taking the picture. The resulting pictures helped us to construct an overall phase diagram as a function of C and I_s .

Isothermal titration Calorimetry

ITC experiments were performed on the CeO_2 -PAA_{2k}/PDDAC_{100k} system only to understand the nature of interactions. In the future, all others couples will be investigated in detail to better understand the modification of the thermodynamics in the presence of nanoparticles and/or nanotubes. Separate aqueous stock solutions of CeO_2 -PAA and PDDAC were prepared at 0.1 wt% by taking their molar charge (Z) into account. The pH was adjusted with the help of HNO_3 and NH_4OH to pH 7. ITC experiments and analysis of raw data were carried out as in chapter 1 (for more details see Isothermal Titration Calorimetry section in chapter 1).

Results & Discussions

Ceria NPs system

Asymmetric system ($\text{CeO}_2\text{-PAA}_{2k}/\text{PDDAC}_{100k}$)

Desalting transition by Robotic platform

The robotic platform helped us to determine coarsely and rapidly the impact of BBs concentration on I_b and size of the hybrid clusters (just after the mixing). The pictures taken by the robot enabled the construction of the phase diagram, where the concentration and the ionic strength range from 0.1 wt% to 1 wt% from left to right and from 0.3M to 1M from bottom to top respectively.

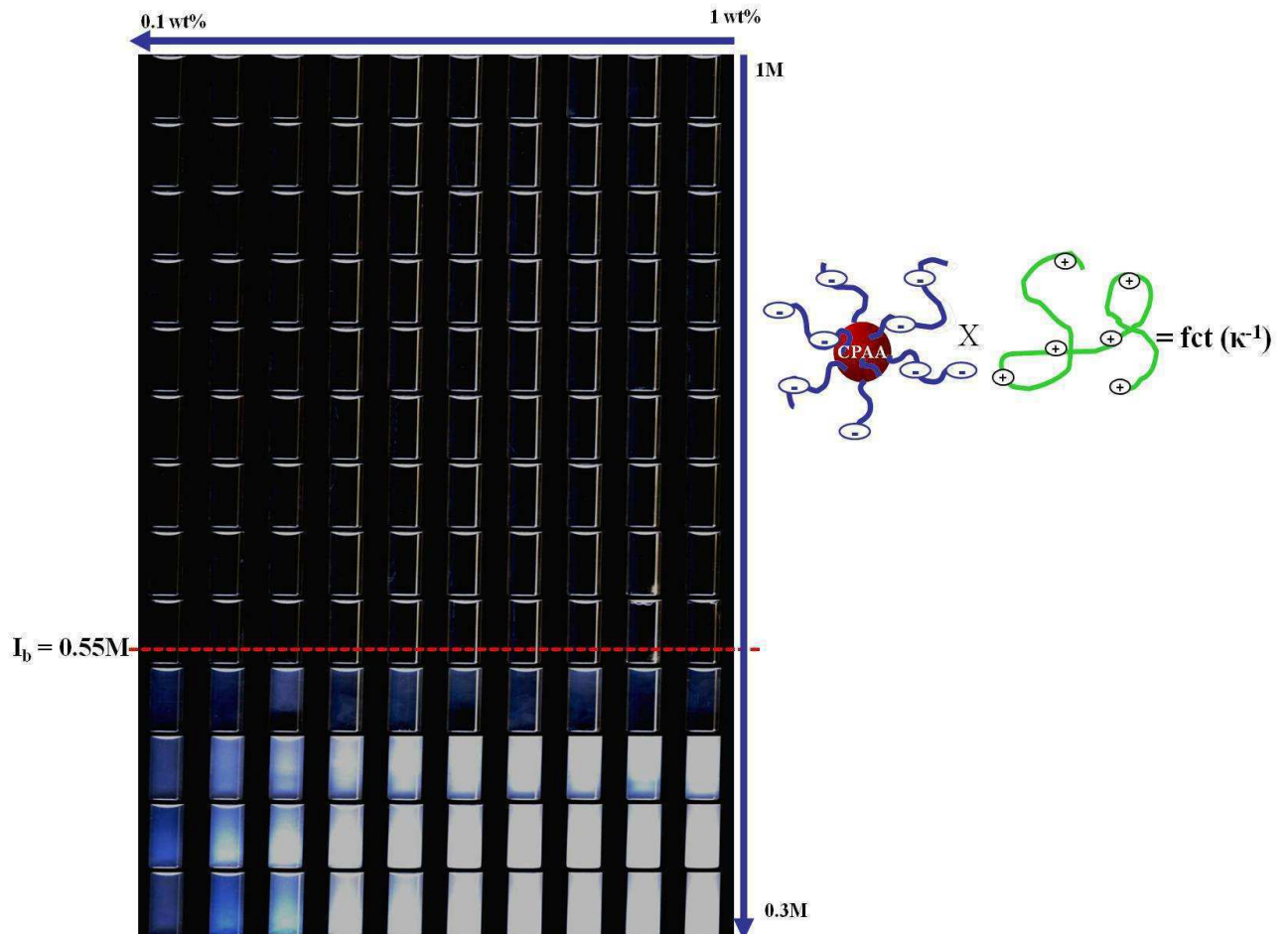


Figure 3.2: Robotic phase diagram of the asymmetric $\text{CeO}_2\text{-PAA}_{2k}/\text{PDDAC}_{100k}$ complexation. Top to bottom: I_s (M) = 1, 0.95, 0.85, 0.8, 0.75, 0.7, 0.65, 0.6, 0.55, 0.5, 0.4, 0.3. left to right: C (wt%) = 0.1, 0.2, 0.3, 0.4, 0.5, 0.6, 0.7, 0.8, 0.9, 1.

Electrostatic complexation of BBs in bulk

This phase diagram clearly indicates that the transition occurred between 0.6M and 0.55M for all the concentration used, suggesting that I_b is indeed independent of the building-blocks concentration; a result not obvious when we first planned the experiment. There is however an increased turbidity with the C below I_b indicating that initial concentration has a great impact on the size of the complexes. Indeed, the probability of interaction of oppositely charged BBs scales with the solution concentration. It should be noted that at longer time however, all the samples below I_b have roughly the same size (or have precipitated) showing that the complexation is kinetically controlled.

A systematic investigation of the sizes of all the aggregates generated in the 130 samples was tedious and time consuming. We therefore decided to proceed with the investigation at $C = 0.1$ wt%, in order to save time, reduce the consumption of our BBs solutions and slow down the complexation kinetics avoiding a macroscopic precipitation (if any) at short times. A manual desalting transition was performed at $C = 0.1$ wt% and shown in the next section.

Manual desalting transition

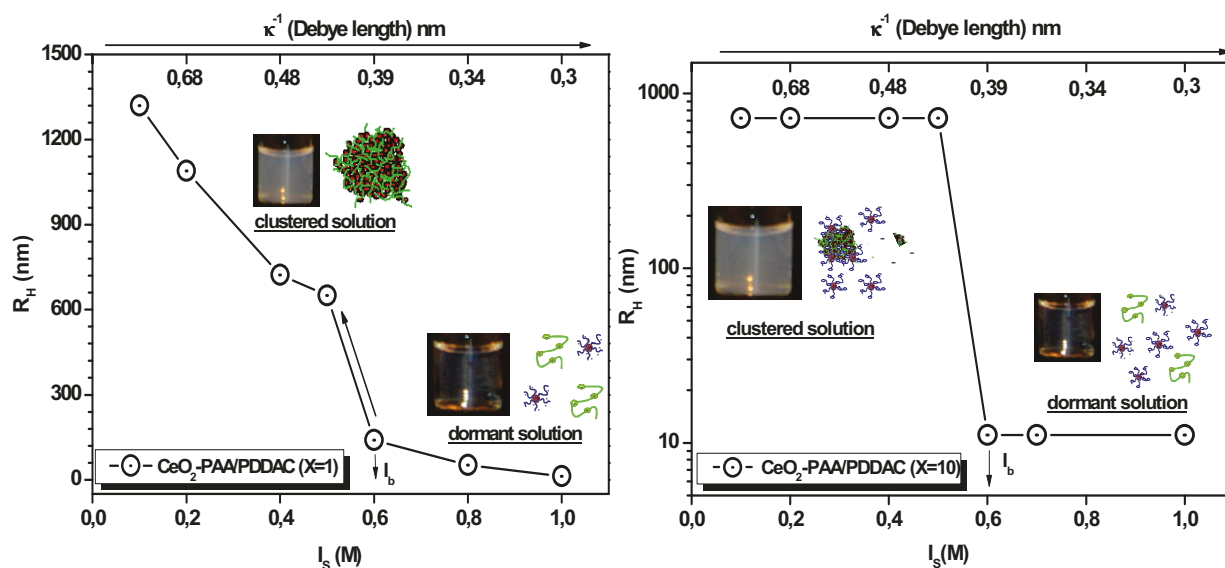


Figure 3.3: Hydrodynamic radius (R_H) as a function of the bulk ionic strength for the CeO_2 -PAA_{2k}/PDDAC_{100k} [(left $X = 1$) and (right $X = 10$)].

Electrostatic complexation of BBs in bulk

The separate stock solutions prepared at $C = 0.1$ wt% were mixed at equal X and $Z \neq 1$. [For weak PEs, as the degree of ionization depends on pH, the effective charges i.e. charges borne by pH, are not equal to structural charges, and therefore $Z = \frac{\text{anionic}}{\text{cationic}} \neq 1$, which is true for all the systems studied here]. As evidenced in the Figure 3.3, dilution triggered the co-assembly and the I_b value for the $\text{CeO}_2\text{-PAA}_{2k}/\text{PDDAC}_{100k}$ system was found to be 0.6M, which is in close agreement with the robotic experiment. This I_b value is slightly higher than the value found for pure $\text{PAA}_{2k}/\text{PDDAC}_{100k}$ system^[3], where the transition indeed occurred at 0.54M. For the present case, the shift of I_b to higher salt concentration indicates that the “electrostatic” interaction between the PAA present on the ceria NPs and PDDAC is stronger than in the PAA/PDDAC system; a result in agreement with the report by Etrych^[7], showing that I_b value is shifted to higher concentration of salt when the electrostatic interaction is stronger.

The stronger interaction for the system $\text{CeO}_2\text{-PAA}_{2k}/\text{PDDAC}$ is likely due to the presence of ceria NPs, which are known to slightly lower the pKa of PAA chains from pH 4.3 to 3.3 (see in chapter 2, Figure 2.14) through the formation of heterometallic coordination bonds. The addition of 1M NH_4Cl to $\text{CeO}_2\text{-PAA}$ immediately decreases the pH of PAA corona chains from pH 8 to 5.5, which is not the case for *free* PAA, where the decrease is considerably less (from pH 8 to 7.2 at 1M). As a result, the corona PAA chains at pH=5.5 are relatively less protonated (or neutral)^[8] (meaning that ionized H^+ recombined to COO^- to form again COOH) than the *free* PAA chains at pH 7.2, where an excess of COO^- groups is present. Indeed, recently it has been documented that the electrostatic interaction between PAA and PDDAC is found to be stronger when PAA is protonated, because protonated PAA cannot engage H-bonding with water^[9]. In agreement with the previous statement, the protonated PAA chains present on the ceria at pH 5.5 undergo a stronger electrostatic interaction with PDDAC shifting then the I_b further up.

On the same line, the sizes of the “electrostatic hybrid clusters” were larger than the corresponding organic complexes of pure PEs, due to the presence of ceria NPs. At 1M of salt, where the interaction is completely screened off, the size measured was around 10 nm, corresponding to the R_H of the PAA stabilized ceria NPs. Slow manual dilution with DI water generated larger (> 1000 nm) and polydispersed aggregates. The hybrid complexes were very stable and the complexation *irreversible* throughout the course of the study when the salt was *reset* to I_0 , due to the presence of the *dense* inorganic materials, a statement valid for all other

Electrostatic complexation of BBs in bulk

hybrid systems studied except for the $\text{SiO}_2\text{-PAA}_{5k}/\ell\text{PEI}_{2k}$, where the complexation is *reversible* (vide infra).

In order to see the influence of the volume fraction X , a dormant solution was prepared at $X=10$ ($V_{\text{CeO}_2\text{-PAA}}/V_{\text{PDDAC}}$), where an excess of PAA coated NPs is present. The determined I_b was in close similarity with the system of equal volume ratio ($X=1$), suggesting that X does not have a significant influence on I_b as well. The aggregates were however in this case of finite (and smaller) sizes indicating the formation of non-stoichiometric complexes stabilized by an excess of anionic charges, due to the lack of oppositely charged PDDAC chains. The manual and robotic desalting transition experiments have shown that I_b was independent of the concentration and the volume ratio; those two parameters have on the other side a great impact on the size and stability of the co-assembled hybrid clusters.

Isothermal Titration Calorimetry

We have measured the complexation enthalpy between PAA coated nanoceria NPs ($\text{CeO}_2\text{-PAA}_{2k}$) and PDDAC chains at $\text{pH} \sim 7$. As in chapter 1, ITC experiments were carried out in two ways: $\text{CeO}_2\text{-PAA}_{2k}$ was injected into PDDAC (type I), or PDDAC was injected into $\text{CeO}_2\text{-PAA}_{2k}$ (type II). Figure 3.4 & Figure 3.5 show that both type of experiments were associated with endothermic processes, in line with the strong electrostatic interaction at play in the system due to the presence of ceria NPs; suggesting a complexation driven by entropy through the release of counter-ions (see Table 3. 4). Some differences do exist however with the pure PEs (PDDAC/PAA) system investigated in chapter 1. Indeed, secondary endothermic and exothermic peaks are showing up in the hybrid asymmetric system for type I and II experiments respectively.

At the beginning of type I experiments, individual PDDAC chains decorated with oppositely charged ceria NPs were formed. In a second stage, the large secondary endothermic peak clearly seen in Figure 3.4 might be due to the energetic cost associated with the formation/reorganisation of those PDDAC unimers into larger non-stoichiometric structures; a feature not observed in the pure PEs system (PAA/PDDAC) and likely due to the reduced number of conformation of NPs. As mentioned in chapter 1, the ITC data were fitted with the MNIS model and the peaks not associated with a direct electrostatic complexation were not taken into account.

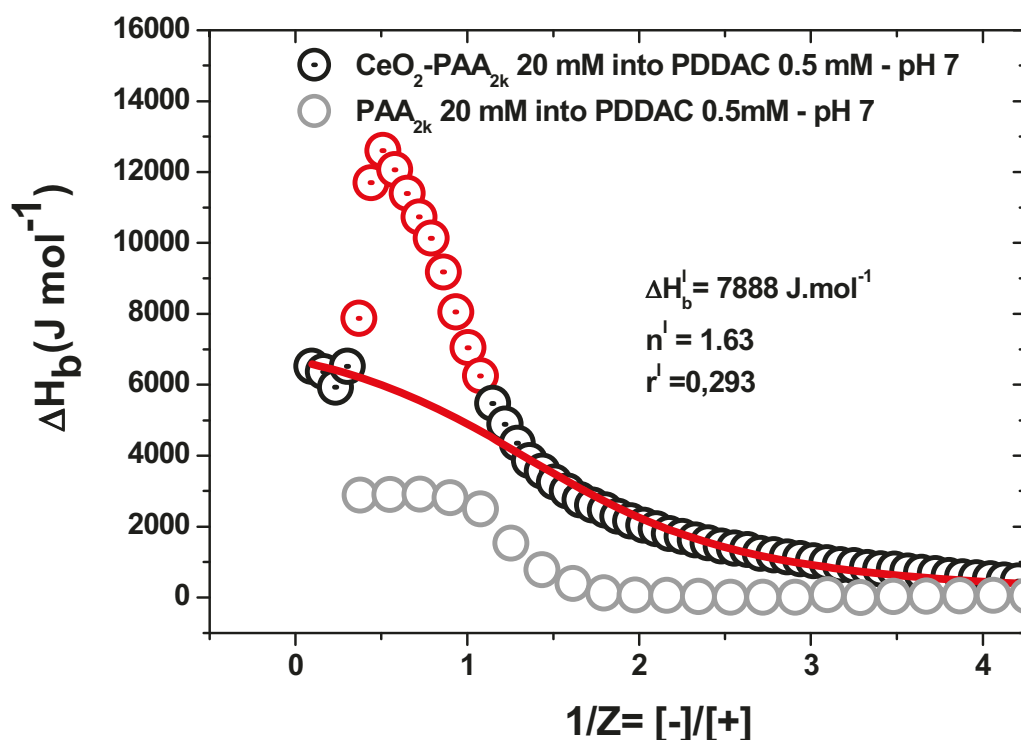


Figure 3.4: Type I ITC binding isotherms at pH=7 resulting from the addition of a 20mM CeO₂-PAA_{2k} solution into a 0.5 mM PDDAC solution. Red lines represent the MNIS fit to the data performed off the peaks (see chapter 1). : Type I ITC binding isotherm for the pure PEs (PAA into PDDAC) complexation is also shown for comparison (see chapter 1).

The different thermodynamics parameters retrieved from the fits are gathered in Table 3.5. The final complexes of type I have a stoichiometry n much smaller than 1 (0.61) suggesting an anionically stabilized structures as in the case of pure PEs system (PAA/PDDAC).

In the case of type II experiments, the large PDDAC chains can easily wrap many NPs through electrostatic interaction and create large nanogels where NPs play the role of physical cross-linking point. In a second stage, the presence of an exothermic peak (not seen in the pure PEs system as well) is rather puzzling but we can imagine that it is associated with the shrinkage of the gel occurring while adding more PDDAC chains. Here again the generated complexes are not stoichiometric and anionically charged ($n \sim 0.7$). More work is necessary however to better catch the exact unfolding of the different complexation stages.

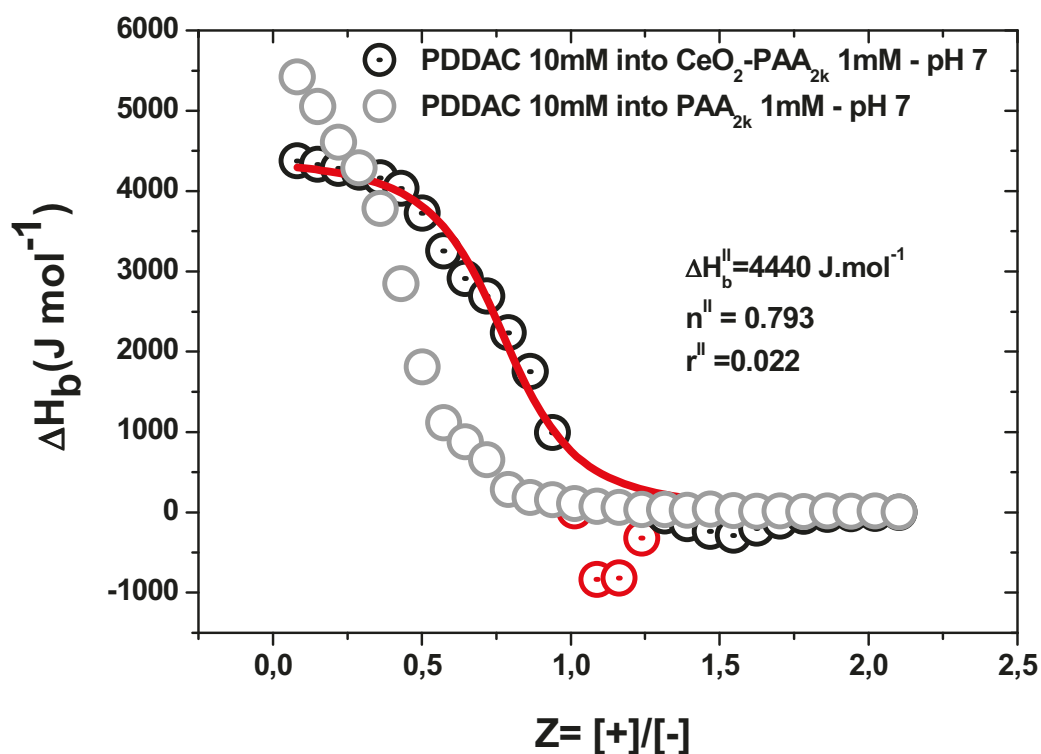


Figure 3.5: Type II ITC binding isotherms at pH=7 resulting from the addition of a 10mM PDDAC solution into 1mM CeO₂-PAA_{2k} solution. Red lines represent the MNIS fit to the data performed off the peaks (see chapter 1). Type II ITC binding isotherm for the pure PEs (PDDAC into PAA) complexation is also shown for comparison (see chapter 1).

The order of mixing does matter as well and the generated complexes although both anionically stabilized have different stoichiometry. Furthermore, as seen in Table 3.6, the different calculated contributions (MNIS model) to the complexation free energy are highlighting as expected an entropy driven co-assembly process.

Type	$n=[+]/[-]$	$K_b (M^{-1})$	$\Delta G (kJ.mol^{-1})$	$\Delta H (kJ.mol^{-1})$	$-T.\Delta S (J.mol^{-1})$
I	$1/1.63=0.61$	7×10^3	-21.5	+7.9	-29.4
II	0.79	4.5×10^4	-26.1	+4.4	-30.5

Table 3.7: Thermodynamic parameters for the complexation of CeO₂-PAA_{2k}/PDDAC.

Symmetric system (CeO₂-PAA_{2k}/CeO₂-bPEI_{25k} NPs)

Figure 3.6 shows the desalting transition between oppositely charged ceria NPs. Mixing an equal volume of oppositely charged ceria dispersions at pH 8 and at 4M yielded a clear non-reactive dormant solution.

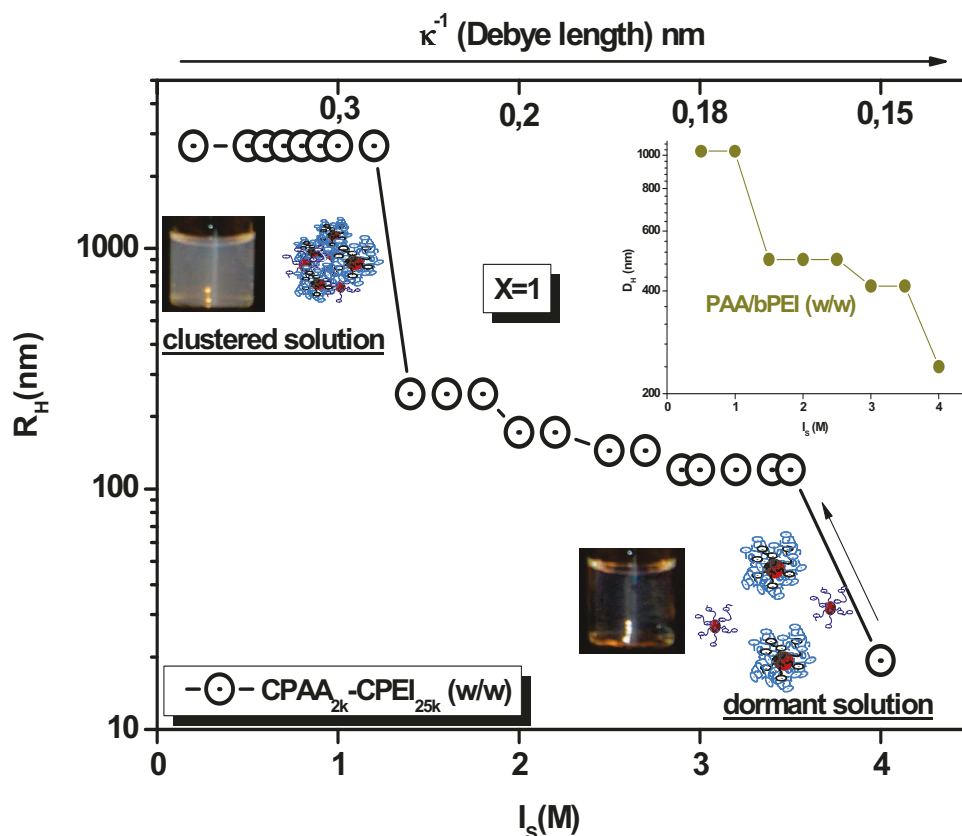


Figure 3.6: Hydrodynamic radii (R_H) of oppositely charged ceria NPs as a function of the ionic strength I_s (NH_4Cl). (Insert: desalting transition between PAA_{2k} and bPEI_{25k}).

The “electrostatic” complexation was then triggered by a step-dilution with DI water. The desalting transition trend observed here is in close similarity with the transition of PAA_{2k}/bPEI_{25k} system (see desalting transition of PEs in chapter 1, Figure 1.4), as the corona of oppositely charged ceria NPs were constructed by the same PEs pair. As anticipated, the transition proceeded via two stages at 3.5M and 1.5M corresponding to ion-pair and large aggregate formation respectively. As mentioned in chapter 1, the peculiar architecture of bPEI delayed the dilution by locally shifting the I_b to lower concentration of salt^[10].

Electrostatic complexation of BBs in bulk

A closer look to the data shows however that the interaction of the NPs/NPs system at 4M differs from the pure PAA/*b*PEI PEs system where the overall interaction cannot be completely turned off; the measured R_H in the dormant is indeed larger than the individual PEs R_H even at high ionic strength likely due to the presence of ionic H-bonding interactions between non-protonated nitrogen atoms of *b*PEI (pH 7) and electronegative oxygen atoms of fully ionized carboxylate moieties in PAA (pH 7).

In the NPs/NPs system, the measured R_H at 4M corresponds to the individual CeO_2 -*b*PEI_{25k} and CeO_2 -PAA_{2k} NPs (two distinct size distribution curves not shown here), indicating that the interaction between oppositely charged NPs can be completely switched off. This observation suggests that at 4M the influence of H-bonding interaction is somehow suppressed by the presence of ceria NPs. As pointed out in chapter 2, ceria NPs are known to shift the pKa of *b*PEI to higher pH values (chapter 2, Figure 2.14). As a result, the amine groups of *b*PEI are protonated even at high pHs. The CeO_2 -*b*PEI solution was here prepared at pH-8, where the $\zeta = +25\text{mV}$. The addition of 4M of salt further enhanced the protonation of amines as indicated by a rapid decrease in pH not seen for free *b*PEI_{25k} chains.

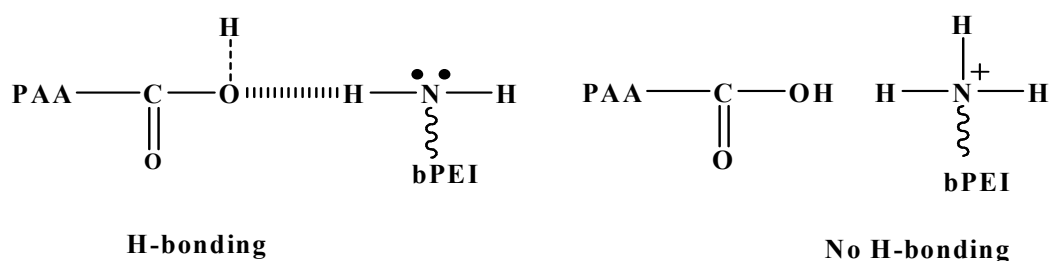


Figure 3.7: Schematic representation of hydrogen bonding between PAA and *b*PEI.

The PAA corona chains of CeO_2 -PAA_{2k} NPs are known to exist at high salt content in the protonated form as explained previously. The exact role of ceria NPs behind these drifts in pH remains poorly understood. When these two salted solutions are mixed, although the protonated amines are ready to donate protons, the protonated acid functional groups (COOH) do not have much free electronegative oxygen atoms anymore to accept those protons. The H-bonding interactions are therefore not favored by the poor acceptance ability of CeO_2 -PAA_{2k} at high Is. In other words, when both amines and acids are protonated, H-

Electrostatic complexation of BBs in bulk

bonding interaction highly depends on the proton donor-acceptor ability, as depicted in the Figure 3.7.

Furthermore, CPEI_{25k} NPs possess only 3 chains per particle as determined in chapter II via TGA experiments (Figure 2.16), reducing even further the possibility of H-bonding interactions due to a lower concentration of primary and secondary amines. It should be noted in addition that since both PEs are present on NPs surface, their conformations (less degree of freedom) are then providing an unfavorable environment for H-bondings formation. The measured size at sufficiently high ionic strength gives then an idea of the H-bonding interaction at play in the mixture.

During the dilution step, the protonation state can change as the salt concentration decreases. Co-assembly can then be driven either by the H-bonding or electrostatic or by both interactions. In the present system it is not clear what type of interaction(s) is (are) taking place between PAA and *b*PEI/*l*PEI chains upon dilution. Therefore it is recommended in the future to perform bulk complexation and ITC in the presence of urea, a known H-bond breaking agent, to sort out the different forces at play in a w/w symmetric system.

A rather constant value for R_H below $I_b \sim 1.5M$ indicates that the sizes of non-stoichiometric complexes were stabilized either by excess cationic particle ($Z < 1$) or by excess anionic particles ($Z > 1$) as the desalting transition for mixed NPs/NPs occurred at $Z \neq 1$. The onset of this desalting transition at a given model substrate/solution interface together with the layer-by-layer assembly of ceria NPs BBs to generated hybrid functional surfaces will be discussed in the next chapter.

Carbon nanotubes systems

Desalting transition between MWCNTPEI_{25k} and PAA_{2k}

Unlike MWCNT- *w*PEs and acid/aminated tubes, the stability of covalent MWCNTs-composites (MWCNT-*c*PEs) under high I_s allows the fine tuning of the interaction.

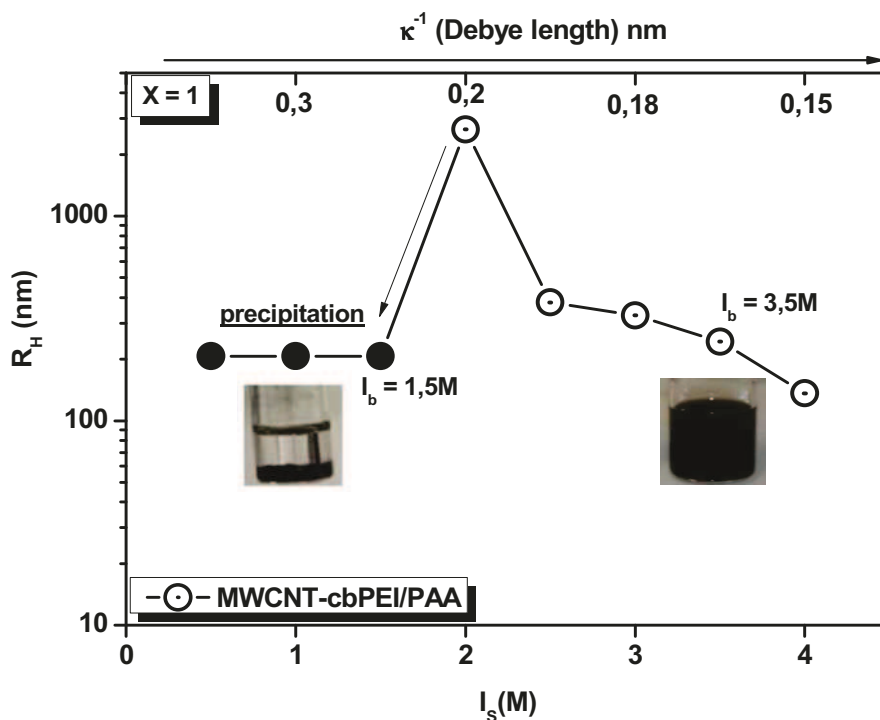


Figure 3. 8: Hydrodynamic diameter (R_H) as a function of ionic strength for the electrostatic co-assembly between MWCNTPEI_{25k} and PAA_{2k}. The closed circles correspond to precipitation, induced by the second critical bulk desalting transition (I_b).

The mixing of oppositely charged PEs grafted NTC ($X = 1$) at 4M yielded clear solutions. In Figure 3. 8 the value of R_H at 4M corresponds to individual MWCNT-*cb*PEI_{25k} suggesting the absence of H-bonding interactions between the protonated amine groups of *b*PEI and the protonated acid groups of PAA (PAA pH decreased from 7 to ~ 4.9 after the addition of 4M of NH_4Cl), together with a reduced number of conformations of *b*PEI chains as explained previously.

In agreement with the PAA_{2k}/*b*PEI_{25k} PEs pair, the step-dilution of the current system triggered a first transition at 3.5M and a second one at 1.5M as depicted in the Figure 3. 8. Unlike ceria NPs system, the precipitation of visible black fractal clusters at 1.5M does not necessarily mean the formation of stoichiometric complexes ($Z = 1$). The macroscopic aggregation is indeed induced by the high aspect ratio morphology of the MWCNTs increasing the probability of interaction at a given concentration.

Desalting transition between oppositely charged MWCNTs

Figure 3.9 shows the desalting transition between oppositely charged MWCNTs. Mixing equal volumes of oppositely charged tubes at 4M yielded a “visually clear” dormant dispersion. The value of R_H at 4M is however slightly larger than for both individual tubes, indicating the formation of “small aggregates”. The interaction between oppositely charged PEs grafted NTC cannot then be completely screened off due to H-bonding/acid-base interactions between residual $-\text{COOH}$ and $-\text{NH}_2$ groups of their parent material.

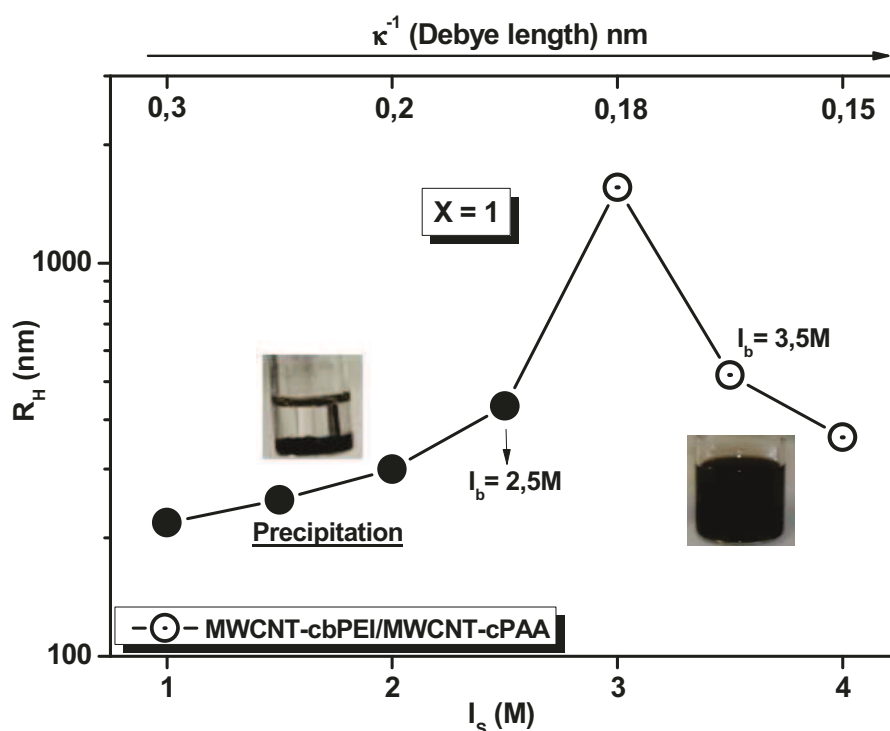


Figure 3.9: Desalting transition between oppositely charged MWCNT-cPEs.

The interaction of PAA_{5k} corona of higher Mw with $b\text{PEI}_{25k}$ shifted the I_b to higher concentrations of salt (2.5M), in agreement with Etrych *et al.*^[7]. The size of the aggregates just above I_b is smaller (~ 1560) than in the previous system (2650) where shorter PAA_{2k} chains were able to diffuse more easily and fully complex with oppositely charged $b\text{PEI}$ units. Whereas in the current system both interacting tubes being (semi) rigid, the complexation highly depends on the tubes orientation. As in the previous system, the drop in R_H observed below 3M suggests the formation and precipitation of huge aggregates influenced by the high nanotubes aspect ratio. The layer-by-layer self assembly and desalting transition of this NTC system at a model interface will be investigated in the chapter 4.

Silica NPs systems

Desalting transition between $\text{SiO}_2\text{-PAA}_{5k}$ and ℓPEI_{2k}

Figure 3.10 represents the co-assembly of stable anionic silica BBs with cationic ℓPEI as a function of the ionic strength. The value of R_H at 4M corresponds well to individual anionic silica, indicating the absence of H-bonding interactions as $-\text{NH}_2$ groups (prone to form H-bonding with $-\text{COOH}$ groups rather than with $-\text{NH}$ groups) are much less in ℓPEI .

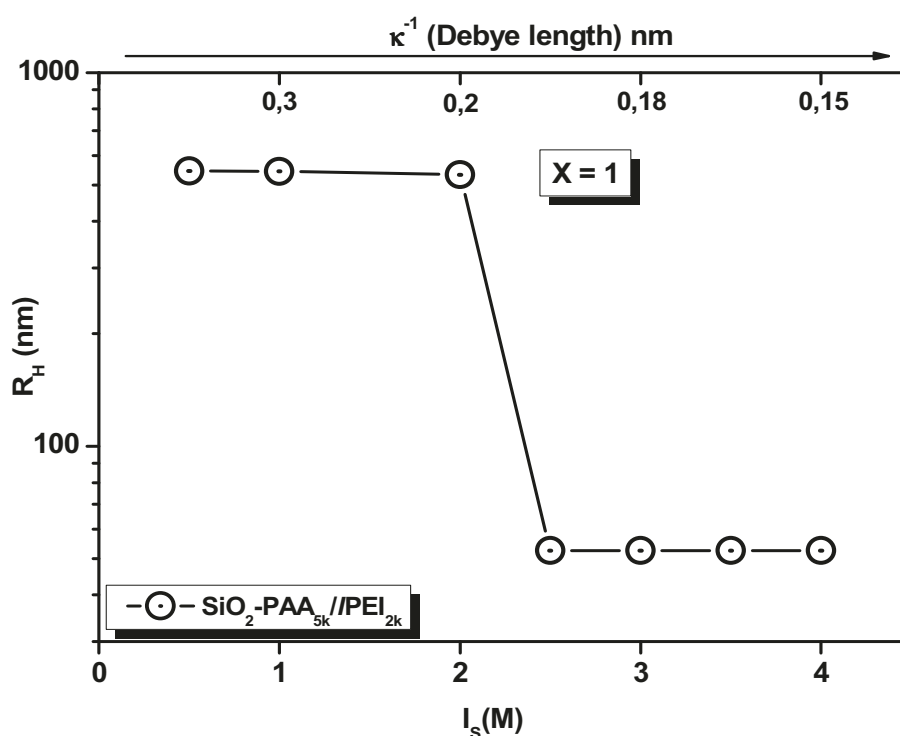


Figure 3.10: Ionic strength dependence of the hydrodynamic diameter for a dispersion containing $\text{SiO}_2\text{-PAA}_{5k}$ and oppositely charged ℓPEI_{2k} .

The critical I_b value for the present system was observed at 2.5M, which is exactly the same as for the $\text{PAA}_{2k}/\ell\text{PEI}_{2k}$ pair^[3]. But for the $\text{SiO}_2\text{-PAA}_{5k}/\ell\text{PEI}_{2k}$ pair, in agreement with Etrych *et al.*^[7], it was expected to notice a slightly higher shift in I_b , when PAA_{2k} was replaced by PAA_{5k} .

The absence suggests that the shift in I_b value not only depends on the increase in Mw, but also on the nature (number and ionization state) of the functional/complementary groups especially when weak PEs like ℓPEI are used. As mentioned earlier, the COO^- of SiPAA_{5k} is known to interact preferably/strongly with $-\text{NH}_2$ rather than with $-\text{NH}$. Due to the

Electrostatic complexation of BBs in bulk

lack of $-\text{NH}_2$ groups and the weak cationic nature of $-\text{NH}$ groups in ℓPEI at a given pH 7, significant shift in I_b was not observed by the very weak interaction between SiPAA_{5k} and ℓPEI .

Furthermore, it has been shown in chapter 1 that high Mw PEs generally results in large size complexes. Whereas, the smaller size generated by the electrostatic complexes of $\text{SiPAA}_{5k}/\ell\text{PEI}_{2k}$ (~ 550 nm) compared to the $\text{PAA}_{2k}/\ell\text{PEI}_{2k}$ PEs system (~ 1000 nm) is due to a lower grafting density of PAA_{5k} chains to aminated silica, a characteristic of the “grafting to” approach together with a weaker electrostatic interaction generated by the weak nature of cationic ℓPEI chains. This weaker interaction is likely responsible for the *reversible* nature of those complexes where full dissociation is effective when the anionic strength is reset back to 4M. Fabrication of functional surfaces from this specific BBs pair throughout the desalting transition and LbL approach will be discussed in the forthcoming chapter.

Desalting transition between $\text{SiO}_2\text{-PAA}_{5k}$ and $b\text{PEI}_{25k}$

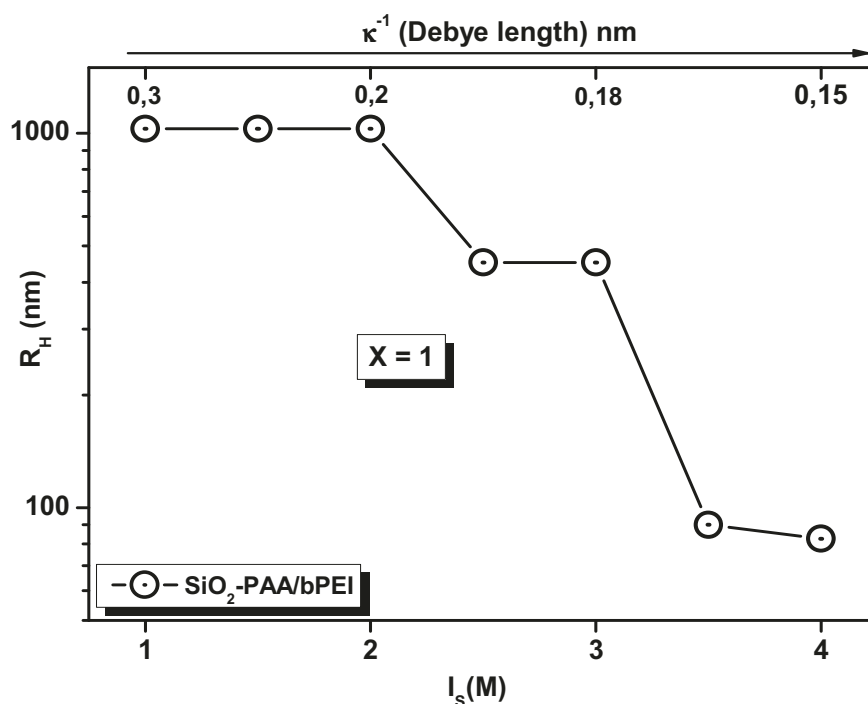


Figure 3.11: Hydrodynamic radius (R_H) as a function of ionic strength for $\text{SiO}_2\text{-PAA}_{5k}/b\text{PEI}_{25k}$.

As shown in the Figure 3.11, when ℓPEI chains are replaced by branched $b\text{PEI}_{25k}$ ones, the critical I_b value shifts to a higher salt concentration of 3.5M due to the interaction

Electrostatic complexation of BBs in bulk

of $-\text{NH}_2$ groups of *b*PEI with $-\text{COO}^-$ groups of $\text{PAA}_{5\text{k}}$ through H-bonding and electrostatic interaction what leads to the formation of slightly larger size ion-pair complexes. The second transition at 2.5M involves the interaction between the acid groups of PAA with the $-\text{NH}$ groups of *b*PEI together with the ion-pair complexes aggregation through bridging^[11]. This desalting transition is in close similarity with oppositely charged MWCNT-cPEs (MWCNT-c*b*PEI_{25k} and MWCNT-cPAA_{5k}) as the interacting PEs pair is the same. Higher *b*PEI_{25k} Mws together with larger anionic silica NPs generated larger complexes with R_{H} values around ~1000 nm twice the size of the SiO_2 -PAA_{5k}/*l*PEI_{2k} pair.

Conclusions

In this chapter, we have investigated the features of the “desalting transition” process when applied to various oppositely charged BBs. We have shown for the first time that it was possible to fine-tune the complexation between *all*-nanoparticles/tubes hybrids BBs as illustrated in Figure 3.12. Confirming the universality and applicability of the desalting transition foreseen in chapter 1 to all types of *stable* colloids.

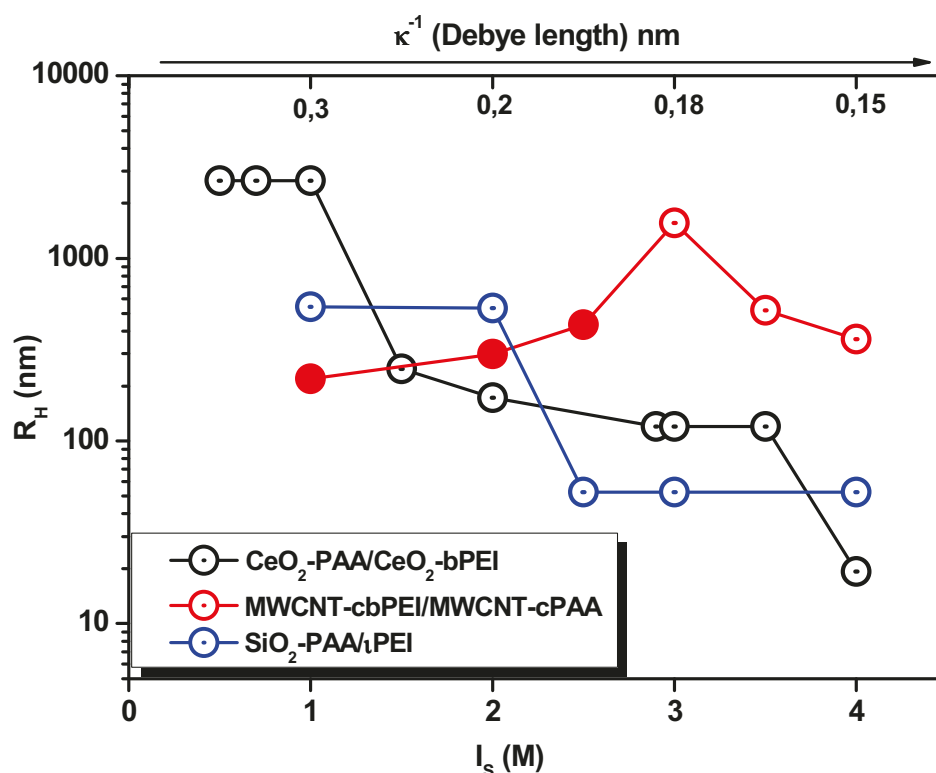


Figure 3.12: Desalting transition between oppositely charged *all*-nanoparticles/tubes BBs: CeO₂ and MWCNTs systems and the co-assembly of SiO₂-PAA/lPEI.

The I_b value of each set was found to differ according to the features of the interacting BBs such as their weak or strong character, architecture, Mws and nature of the functional groups along the PE backbone. Stable and finite sized non-stoichiometric ($Z \neq 1$) electrostatic complexes were obtained for all the hybrid systems. The robotic experiment has shown that the critical ionic strength I_b is indeed independent of the concentration of building blocks. It should be noted that the complete “electrostatic” screening of opposite charged components was made possible when no secondary forces such as H-bonding or hydrophobic effect were at play in the complexation. Indeed, our experiments showed that H-bonding plays an

Electrostatic complexation of BBs in bulk

essential role in the complexation when weak PEs were used with an interaction dependent on the proton donor-acceptor characteristics of amine and acid functional groups. H-bonds formation at high I_s were controlled by the presence and nature of inorganic nanoparticles/tubes and the protonation state of functional groups induced by the added salt.

In the asymmetric system, the CeO₂-PAA NPs in the presence of 1M of NH₄Cl are forbidden to engage hydrogen bonding with water, thereby allowing the NPs to interact strongly with PDDAC chains via electrostatic interaction during dilution as suggested by a slightly higher I_b value.

“Real” dormant solutions at I_0 were only obtained for symmetric systems of oppositely charged ceria NPs, MWCNT-cbPEI_{25k}/PAA_{2k} and SiO₂-PAA_{5k}/ℓPEI_{2k}, where H-bonding interactions were not favored by protonated PAA and PEI chains. In the last pair, the lack of –NH₂ groups not only banned the H-bonding interactions at 4M but generated relatively small and finite sized *reversible* hybrid complexes due to the weak interacting nature of –NH in ℓPEI_{2k}. In case of oppositely charged covalent MWCNT-cPEs nanocomposites and SiO₂-PAA_{5k}/bPEI_{25k}, H-bonding interaction even at I_0 was triggered by a large number of repeating units in both weak PEs, although they were rigid and protonated. This attribute put forward that H-bonding formation not only depends on the protonation states of the complementary functional groups but also on the Mw of the interacting PEs.

All these interesting findings pushed us to transfer this bulk desalting transition concept to a substrate/solution interface in order to generate functional hybrid surfaces with unique properties and applications.

Summary of the different I_b

Oppositely charged components	Transition I	Transition II	Presence of H-bonding at I_0
CeO ₂ -PAA _{2k} /PDDAC _{100k}	0.6M	---	No
CeO ₂ -PAA _{2k} /CeO ₂ -bPEI _{25k}	3.5M	1.5M	No
MWCNT-cbPEI _{25k} /PAA _{2k}	3.5M	1.5M	No
MWCNT-cbPEI _{25k} /MWCNT-cPAA _{5k}	3.5M	2.5M	yes
SiO ₂ -PAA _{5k} /ℓPEI _{2k}	2.5M	----	No
SiO ₂ -PAA _{5k} /bPEI _{25k}	3.5M	2.5M	yes

References

1. Fresnais, J., J.F. Berret, B. Frka-Petescic, O. Sandre, and R. Perzynski, *Electrostatic Co-Assembly of Iron Oxide Nanoparticles and Polymers: Towards the Generation of Highly Persistent Superparamagnetic Nanorods*. *Advanced Materials*, 2008. **20**(20): p. 3877-3881.
2. Fresnais, J., C. Lavelle, and J.F. Berret, *Nanoparticle Aggregation Controlled by Desalting Kinetics*. *The Journal of Physical Chemistry C*, 2009. **113**(37): p. 16371-16379.
3. Yan, M., J. Fresnais, S. Sekar, J.P. Chapel, and J.F. Berret, *Magnetic Nanowires Generated via the Waterborne Desalting Transition Pathway*. *ACS Applied Materials & Interfaces*, 2011. **3**(4): p. 1049-1054.
4. Yan, M., L. Chevy, and J.F. Berret, *Fabrication of Magnetic Clusters and Rods using Electrostatic Co-assembly*, in *Progress in Colloid and Interface Science*. 2010. p. 35-39.
5. Berret, J.F., *Controlling electrostatic co-assembly using ion-containing copolymers: From surfactants to nanoparticles*. *Advances in Colloid and Interface Science*. **167**(1-2): p. 38-48.
6. Qi, L., J.r. Fresnais, J.-F.o. Berret, J.-C. Castaing, F. Destremaut, J.-B. Salmon, F. Cousin, and J.-P. Chapel, *Influence of the Formulation Process in Electrostatic Assembly of Nanoparticles and Macromolecules in Aqueous Solution: The Interaction Pathway*. *The Journal of Physical Chemistry C*, 2010. **114**(39): p. 16373-16381.
7. Etrych, T., L. Leclercq, M. Boustta, and M. Vert, *Polyelectrolyte complex formation and stability when mixing polyanions and polycations in salted media: A model study related to the case of body fluids*. *European Journal of Pharmaceutical Sciences*, 2005. **25**(2-3): p. 281-288.
8. Grunlan, J.C., L. Liu, and O. Regev, *Weak polyelectrolyte control of carbon nanotube dispersion in water*. *Journal of Colloid and Interface Science*, 2008. **317**(1): p. 346-349.
9. Alonso, T., J. Irigoyen, J.J. Iturri, I.L. Iarena, and S.E. Moya, *Study of the multilayer assembly and complex formation of poly(diallyldimethylammonium chloride) (PDADMAC) and poly(acrylic acid) (PAA) as a function of pH*. *Soft Matter*, 2012. **9**(6): p. 1920-1928.
10. Laugel, N., C. Betscha, M. Winterhalter, J.-C. Voegel, P. Schaaf, and V. Ball, *Relationship between the Growth Regime of Polyelectrolyte Multilayers and the Polyanion/Polycation Complexation Enthalpy*. *The Journal of Physical Chemistry B*, 2006. **110**(39): p. 19443-19449.
11. Maurstad, G., S. Kitamura, and B.T. Stokke, *Isothermal titration calorimetry study of the polyelectrolyte complexation of xanthan and chitosan samples of different degree of polymerization*. *Biopolymers*, 2011. **97**(1): p. 1-10.

PART II

Chapter 4: Growth of hybrid layers at a solution/substrate interface

Abstract

We report in this chapter the growth of hybrid layers made from the electrostatic complexation of different oppositely charged BBs developed in chapter 2. In a first part, the electrostatic Layer-by-Layer (ELbL) sequential adsorption method is taken as a benchmark and used to build layers with different NPs, PEs and CNTs. In a second part, we transfer the *bulk* desalting transition concept to a solution/substrate interface and put forward a new assembly method coined hereafter Surface grown Layer (SgL). The growth is controlled here at the onset of the bulk desalting transition by fine-tuning the ionic strength (I_s) of the dispersions through suitable experimental conditions.

The influence of some key parameters on LbL and SgL processes such as pH, salt concentration, PEs nature, substrate physical-chemistry and charge ratio Z is put under scrutiny through a careful monitoring of both type of growth via Quartz Crystal Microbalance (QCM) experiments. Adsorbed amounts, growth regimes, volume fraction of the inorganic BBs, compactness and stability of the layers are some of the key features investigated in details.

The simple and novel SgL approach is shown here to be a very versatile method able to generate in one-step thick hybrid layers. The complementary use of both SgL and LbL growth methods together with very stable BBs opens the pathways to generate smart functional surfaces with varying morphology, properties and applications.

Introduction

Over the past two decades, an extensive body of work has been devoted to the development of versatile functional surfaces, one of the final goals of the modern chemistry, biology and physics. The fabrication of such functional surfaces at nanometer level has enabled their applications in a wide range of fields^[1-5]. In particular, the electrostatic complexation of oppositely charged inorganic nanomaterials and PEs at an interface have recently attracted an increasing interest since as a promising pathway to generate versatile hybrid functional films by combining the advantageous properties of both organic and inorganic worlds^[6]. Now-a-days inorganic nanomaterials are not only restricted to monodisperse spherical colloids but include tubes, rods, wires, belts, disks etc^[6-8]. Their unique physical features and specific properties including high refractive index, electrical conductivity, reactivity, sensitivity to magnetic field provide unusual and remarkable attributes to the films with numerous promising applications in many scientific and technological fields^[9].

In terms of industrial applications, several manufacturers are highly demanding the designing of “*thick*” functional coatings ($> 1 \mu\text{m}$) to increase the durability of substrates. In some cases, a *critical thickness* is necessary to enable some specific applications^[3]. Despite, there are still some key limitations to generate such *thick* hybrid functional surfaces. A variety of deposition techniques such as electrochemical and chemical vapor deposition (CVD) are available. Those processes are not simple and cost effective. On the other hand, the conventional and very popular Layer by Layer (LbL) method is an eco-friendly and inexpensive technique, originally discovered by Iler *et al.*,^[10] in the sixties to generate *all-nanoparticle* multilayers, then rediscovered and brought to fame by Decher *et al.*,^[11] in the nineties. Initially implemented on oppositely charged PEs, it was later on extended to all types of inorganic materials such as nanoparticles, nanowires and nanotubes etc... Now-a-days, the LbL process is an efficient platform to develop organic/inorganic tunable functional coatings^[12], colloids or capsules^[13, 14] via the sequential deposition/adsorption of oppositely charged components driven by various forces such as electrostatic interaction, hydrogen and covalent bonding, van der Waals and hydrophobic interactions^[15-18]. Of which the electrostatic LbL (ELbL) is the most used and documented approach with a growth mechanism driven by the overcharging of complementary charged functional groups.

Fabrication of functional surfaces

There are various techniques, more or less complicated to implement, available to develop ELbL functional surfaces such as simple dipping, spinning, spray assisted and roll-to-roll process^[19-21]. The final functionality of ELbL films can readily be altered, modified or varied through the number of deposited layers and the nature of the adsorbed components. Indeed, the thickness depends on various factors such as the charge density, concentration of species and assembly conditions such as pH and ionic strength^[22, 23]. Among them, the ionic strength plays a central role in the multilayer fabrication. Recently, it has been reported that 5M of NaCl disassembled the polyelectrolyte multilayer (PEMs) constructed from the strong PSS/PDDAC pair^[24], indicating that high concentration of salt can easily change the structure and physico-chemical properties of PEC multilayers.

ELbL method has several advantages including its simplicity and applicability to almost all kinds of inorganic materials, a fine control over the thickness at nano level and plethora of applications in many fields such as optoelectronic devices, drug delivery, biology, biosensors and functional coatings include hydrophilic and hydrophobic coatings, anti-reflection, anti-corrosive and conductive surfaces. It possesses however some drawbacks^[25] in the fabrication of thick functional layers:

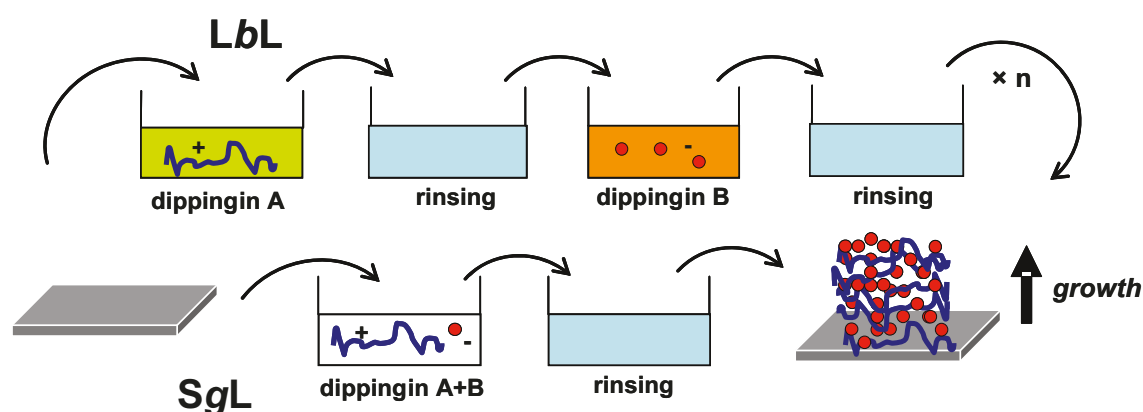


Figure 4. 1: Schematic representation of Layer-by-Layer (LbL) and Surface grown Layers (SgL).

- It is a time consuming and sometime tedious process as it involves numerous dipping and rinsing steps to attain several tens of nm thickness.

- The typical ELbL method proceeds through several rinsing stages between each adsorption step. During this rinsing stage large amounts of components are wasted which then reduce their contribution in the final multilayer formation.
- Alternative approaches as spray, spin assisted and Roll-to-Roll are cost effective to carry out.

Can we generate hybrids functional layers by the electrostatic complexation of oppositely charged inorganic/organic (BBs) via another approach?

In the previous chapter we have shown that the “electrostatic” interaction between oppositely charged building blocks (BBs) can be efficiently controlled and tuned as a function of the solution ionic strength I_s . In the current chapter we would like to take advantages of these interesting features and investigate the possibility to transfer the *bulk desalting transition concept* to a substrate/solution interface in order to generate the functional hybrid surfaces in one step. This new approach is coined as Surface *grown Layer* or SgL and should be thought as a different but complementary to the classical ELbL approach. The latter will be taken in the current chapter as benchmark as it shares with SgL the same entropy driven complexing force through the multistep “electrostatic” sequential adsorption of BBs.

In the following, we will first study the LbL growth between different BBs developed in chapter 2. In a second step we will investigate how to trigger in a single step at a fluid/solid interface the spontaneous growth of a hybrid layer through fine-tuning of the electrostatic interaction between oppositely charged components. Before going into more details, the key ingredients of the SgL approach will be briefly described.

Surface Grown Hybrid Functional Layers (SgL) approach

The “electrostatic” complexation between any *stable* oppositely charged (A & B) BBs can be controlled at a solution/substrate interface as a function of the ionic strength with a strategy based on the transposition of the “desalting transition concept” at a surface possessing an initial affinity with one of the components. As mentioned in chapter 1 & 3, every dormant solution possesses a critical lower and upper boundary denoted as I_b and I_0 respectively. When the ionic strength of the complex solution is lower than I_b ($I_s < I_b$), co-

Fabrication of functional surfaces

assembly between oppositely charged species takes place in the bulk and form large electrostatic hybrid aggregates that eventually precipitate at the surface. When $I = I_0$, due to the dormant nature of the solution no complexation occurs in the bulk while one of the components having certain affinity with the surface might adsorb via van der Waals, hydrophobic or hydrogen bonding interactions. When I_s lies between I_b and I_0 ($I_b < I_s < I_0$), the solution close to the interface turns reactive and triggers the spontaneous growth of a hybrid layer. The driving force is mainly electrostatic and the growth kinetics can in principle be tuned via different parameters. The growth process involves only one dipping and rinsing stage to achieve the desired thickness which in turn can be readily altered by tuning I_s and /or the deposition time.

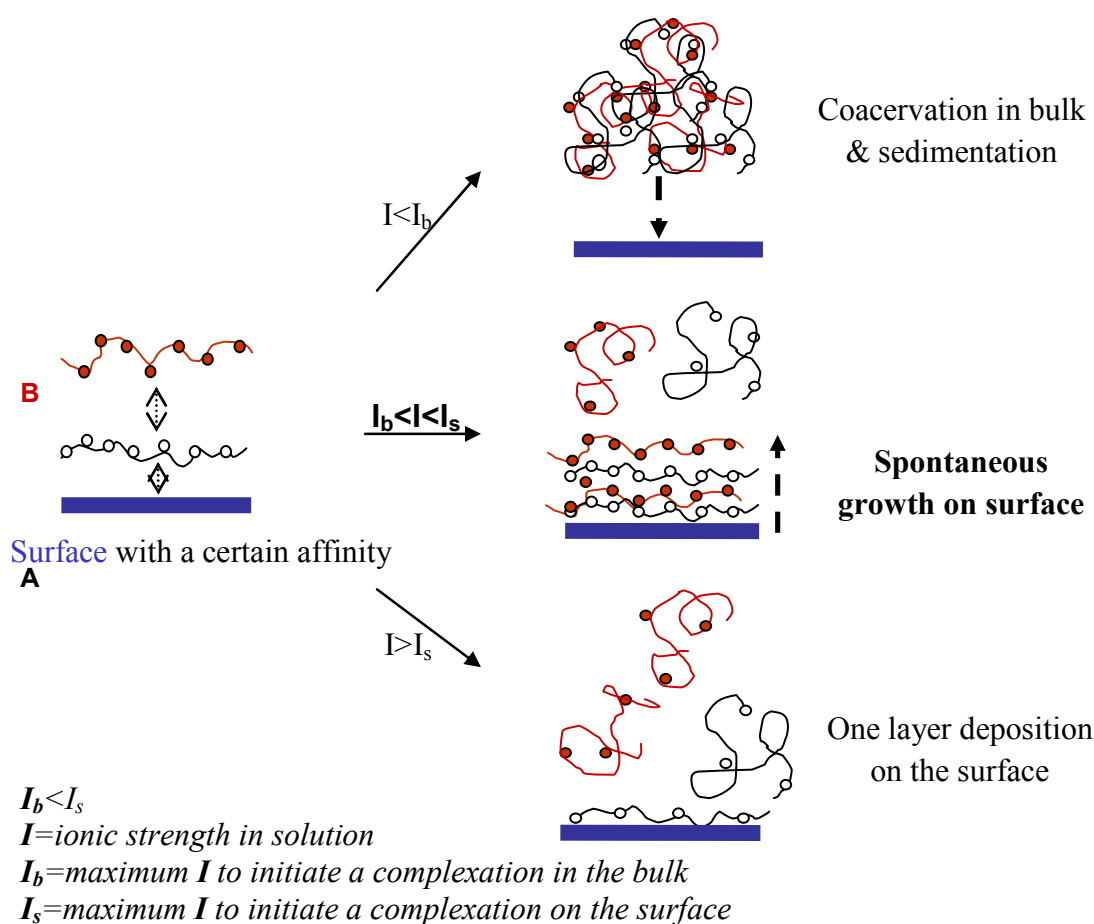


Figure 4. 2 : Illustration of the co-assembly between oppositely charged colloids and/or polymers in the presence of surface as a function of I_s (from Ling Qi p.H.D thesis).

Experimental section

Materials

The components were the cationic and anionic hybrid building blocks (BBs) developed in chapter 2: PAA and *b*PEI functionalized ceria ($\text{CeO}_2\text{-PAA}_{2k}$ & $\text{CeO}_2\text{-}b\text{PEI}_{25k}$); covalent ($\text{MWCNT-c}b\text{PEI}_{25k}$ and MWCNT-cPAA_{5k}), non-covalent (MWCNT-wPEI and MWCNT-wPAA) and short ligands tethered (MWCNT-COOH and MWCNT-NH_2) MWCNTs; $\text{SiO}_2\text{-PAA}_{2k}$ NPs. Together with cationic PDDAC, *l*PEI, *b*PEI and anionic PAA, PSS PEs. Polystyrene (PS) ~ 250 kg/mol, octadecyltrimethoxysilane (TMOS) were purchased from Sigma Aldrich. Bare cerium oxide nanoparticles (CNPs) were kindly provided by Rhodia Company. Solvents such as toluene, acids (HNO_3 , HCl), bases (NH_4OH , NaOH) and salts (NH_4Cl , NaNO_3) were used as such without further purification.

Methods

Quartz Crystal Microbalance (QCM) experiments

Layer *by* layer and Surface *grown* Layer adsorption processes were monitored using a QCM with dissipation, QCM-D (*Q-Sense E4 instrument, AB, Sweden*) with modified silica-coated quartz crystals. In a typical experiment the voltage impulse applied across the gold electrodes excites the crystal at its fundamental resonance frequency (f_0) and then a free decay of signal is followed. Two parameters are thus measured: a resonance frequency and dissipation *D* obtained from the decay. Up to 13 harmonics are followed, but here we will present the results for the fifth overtone only.

Any material adsorbing (/desorbing) onto the crystal surface induces a decrease (/increase) of the resonance frequency ($\Delta f = f - f_0$). If the adsorbed mass is evenly distributed, rigidly attached and small compared to the mass of the crystal, Δf is directly related to the adsorbed mass per unit area ($\text{mg}\cdot\text{m}^{-2}$), Δm by the Sauerbrey equation^[26]:

$$\Delta m = -C \frac{\Delta f}{n} \quad (1)$$

Where *C* is the Sauerbrey constant ($0.177 \text{ mg}\cdot\text{s}\cdot\text{m}^{-2}$ for a 5 MHz quartz sensor) and *n* is the overtone number. This equation was originally derived assuming rigidly attached layers in the gas phase that have the same shear modulus and density as quartz^[27]. The QCM-D is

Fabrication of functional surfaces

sensitive to changes in density and viscosity of the surrounding medium, the addition of a viscous film containing associated liquid requires the use of viscoelastic modeling to obtain explicit Δm values for the adsorbed film. An indication of frictional losses due to viscoelastic properties of the adsorbed layer is provided by changes in dissipation

$$\Delta D = \frac{E_{dissipated}}{2\pi E_{stored}} \quad (2)$$

where E_{stored} is the energy stored in the sensor crystal and $E_{dissipated}$ is the energy dissipated by the viscous nature of the surrounding medium. High dissipation values reflect a thick and loosely adsorbed layer, while a thin and rigid layer vibrates with the crystal, indicating a low dissipation factor. For adsorbed films where the dissipation D is less than 2×10^{-6} the Sauerbrey ^[28] relation holds. For larger dissipation where the adsorbed mass shows strong frequency dependence, the Voigt model can be used to determine the hydrodynamic mass of the adsorbed layers.

Sensor preparation:

Silica-coated quartz sensors were cleaned with ethanol, ultra sonication and UVO treatment before silanization using a 2%/w octadecyltrimethoxysilane solution in toluene. The sensors were then covered with a 200 nm PS layer via spin-coating (2.8% PS solution in toluene at 2500 RPM) and thermally annealed before use (95 °C for 2 hours) giving rise to a smooth hydrophobic surface. In a third step, sensors were dipped into a bare nanoceria solution (0.1 wt %) containing 0.1 M NaNO₃ during 1 hour enabling the formation of a well-packed *cationic* nanoceria monolayer on top of the PS ^[29]. The initial charge on the sensor can then be tuned via the adsorption of a PE monolayer either anionic (PSS at 0.1 wt%, 10⁻²M NH₄Cl) or cationic (PDDAC or PAH at 0.1 wt%, 10⁻²M NH₄Cl). *This pre-functionalization step is crucial as it enables to reuse and recycle to infinity the sensors after each QCM experiment by a simple toluene cleaning that dissolves the underlying PS film and subsequently removes any adsorbed layer easily* (Figure 4. 3).

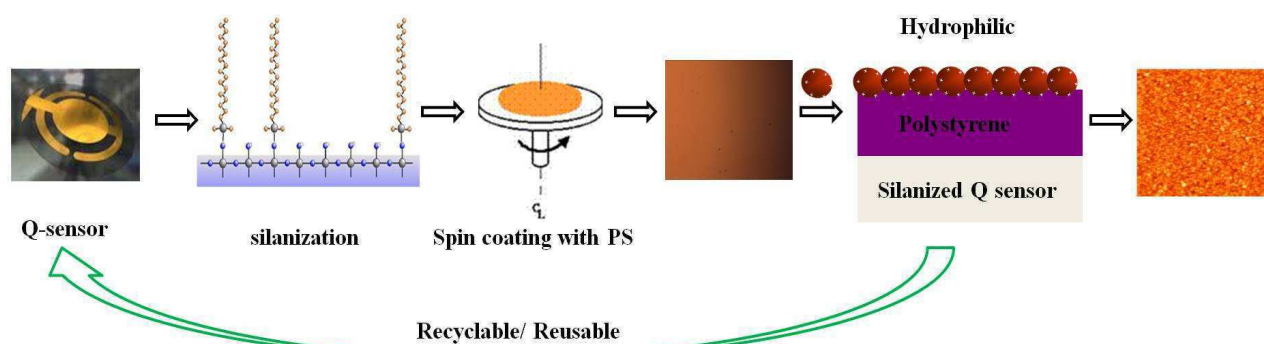


Figure 4. 3: Schematic representation of the preparation of the reusable QCM sensors.

Layer-by-Layer self assembly (LbL)

Separate solutions of cationic and anionic hybrid building blocks formulated in chapter 2, cationic (*b*PEI, *l*PEI, PDDAC) and anionic (PAA) PEs were prepared 0.1 wt% with 10^{-2} M NH_4Cl in water. The LbL sequential adsorption was carried out on the modified Q-sensors within a QCM cell for the following sets of BBs: CeO_2 -PAA/PDDAC, CeO_2 -PAA/ CeO_2 -*b*PEI, MWCNT-*cb*PEI/PAA, MWCNT-*w*PEI/MWCNT-*w*PAA, MWCNT-*cb*PEI/MWCNT-*c*PAA and SiO_2 -PAA/*l*PEI. The deposition cycle was repeated until 12 bilayers for each pair. The QCM cell was rinsed between 2 deposition cycles using DI water at the same ionic strength. The growth of the multilayer was monitored following Δf (more details in “chapter 0”) after each deposition cycle. The multilayers were then gently dried under nitrogen and the morphologies characterized in certain cases by AFM in air (Dimension ICON from Bruker AXS operating in tapping mode).

Self assembly of MWCNT-COOH and MWCNT-NH₂:

It was not possible to carry out LbL assembly of acid and amine terminated MWCNTs inside the QCM cell (see results & discussions). Sequential adsorption was then performed outside the QCM cell^[30]. In short, acid and amine functionalized MWCNT suspensions were prepared independently at a concentration of 0.025 wt% by dispersing a calculated amount of CNT powders into DI water at pH 2.5 (adjusted with HCl). Both suspensions were then subjected to ultrasonication for 15 min to obtain stable dispersions. The assembly was carried

Fabrication of functional surfaces

out on glass substrates in order to monitor the growth of the layers via UV-Visible absorption spectroscopy. Glass substrates were cleaned with ethanol, water and subjected to UVO treatment for 20 mins and then immersed into a MWCNT-NH₂ dispersion for 30 mins, followed by three rinsing steps with DI water at pH 2.5 at an interval of 3, 2 and 2 mins to remove unadsorbed aminated tubes. In a second step, the substrate was dipped into a MWCNT-COOH dispersion resulting in the formation of a MWCNT bilayer. This operation was repeated 8 times to obtain 8 bilayers on both side of the glass substrate. Cross-linking was then established between acid and amine tubes by heating the films up to 150°C for 2 hrs (formation of amide bonds) to give some mechanical integrity to the multilayer. The resulting films were then characterized by AFM in air. Furthermore, it should be noted that *LbL* approach has not been efficiently performed for PEs wrapped MWCNTs as free PEs chains present in the solution quickly diffused and adsorbed on the surface (highest diffusion coefficient) hindering any further adsorption of the like charge wrapped CNT tubes.

Surface grown hybrid functional layers (SgL)

To investigate the features of this new approach, different asymmetric (CeO₂-PAA_{2k}/PDDAC_{100k}) and symmetric (CeO₂-PAA_{2k}/CeO₂-bPEI_{25k}, MWCNT-cbPEI_{25k}/PAA_{2k}, and SiO₂-PAA_{5k}/lPEI_{2k} BBs) systems were put under scrutiny and compared with the conventional *LbL* sequential assembly. Both types of growth were monitored by QCM on a functional polystyrene covered Q-sensor. Dormant solutions at a desired concentration were prepared at 1M and 4 M NH₄Cl for asymmetric (w/s) and symmetric systems (w/w) respectively. The growth of the hybrid layers at the solution/substrate interface was triggered by a controlled drop-by-drop addition of DI water into the dormant solution to reach a given ionic strength. All the different solutions were allowed to flow into the QCM cell for 5 min with the help of a peristaltic pump (rate = 0.2 ml / min) and then stopped. For certain experiments (will be discussed later) the sample solutions were allowed to flow continuously into the cell (*dynamic* experiments). A small magnetic stirrer was used to ensure a good homogenization of the solutions prior to the injection. The grown layers were characterized by AFM and contact angles measurements as well. It should be noted that SgL strategy cannot be applied to acid/amine terminated and PEs wrapped MWCNTs as they are not stable under high ionic strength (see chapter 3).

Results & Discussions

Layer-by-Layer self assembly

Ceria NPs

NPs/PEs (CeO₂-PAA_{2k}/PDDAC_{100k}) system

The CeO₂-PAA_{2k}/PDDAC_{100k} multilayer growth was performed at pH 8 (where PAA chains are almost fully ionized) and at two different ionic strengths I_s (0.01M and at 0.6M) on the ceria modified Q-sensor and monitored as a function of number of layers by measuring the frequency shift (-ΔF).

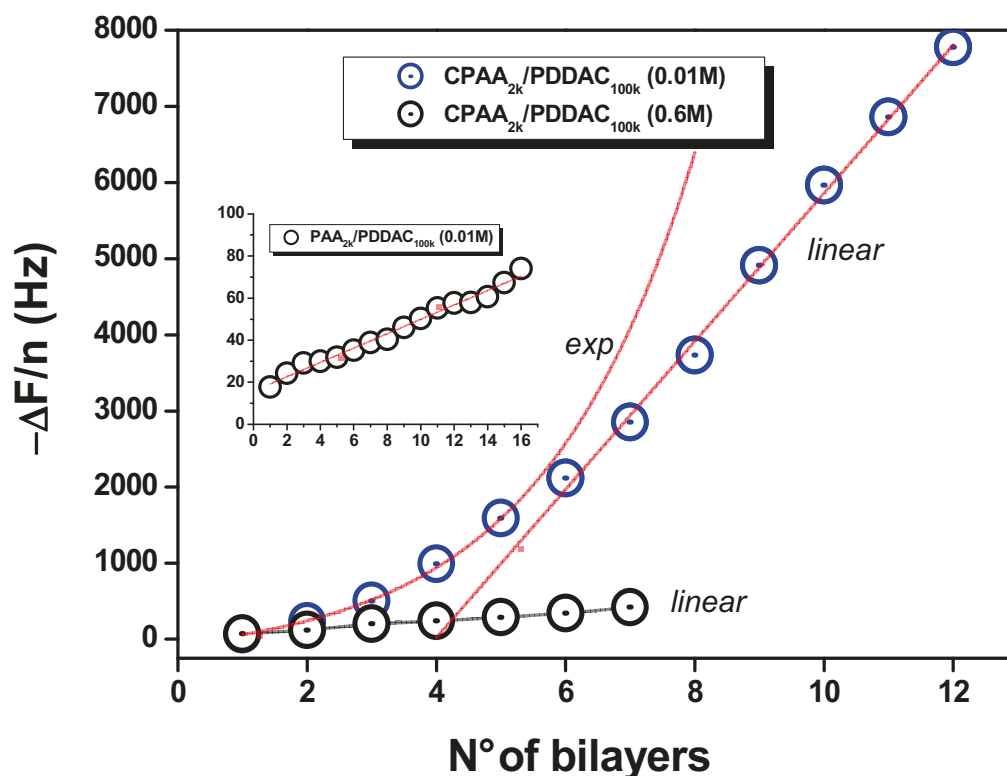


Figure 4. 4: Cumulative frequency shift (-ΔF/n) as a function of the number of layers for the LbL assembly of (CeO₂-PAA_{2k}/PDDAC_{100k})₁₂ NPs/PEs system at low (0.01M) and high (0.6M) ionic strength. The insert is showing the assembly of pure PAA_{2k}/PDDAC_{100k} PEs. Continuous lines are linear and exponential fit to the data.

Fabrication of functional surfaces

As can be seen in Figure 4. 4, there is a neat increment of the adsorbed mass with the bilayers number giving evidences of a progressive uptake of each component. Furthermore, the ionic strength has a great influence on both the nature of the growth and on the final adsorbed mass (and thickness). Since the charge of PDDAC is not pH and salt dependent, the LbL assembly of this specific pair is likely mainly ruled by the weak PAA chains.

At low ionic strength and for NPs/PEs and PEs/PEs systems the steady state growth regime is found to be linear even though the measured complexation enthalpy was endothermic in this system (see chapter 1&3)^[37]. The pseudo non-linear (“exponential”) growth regime however seen at the very beginning of the growth (up to 4 bilayers) and noticed by several authors in different systems might be attributed either to the unevenness of the surface by a low coverage or a higher affinity with the substrate. Indeed, the first layers largely depend on the substrate physico-chemical properties such the density and availability of the surface charges. After several depositions, the growth becomes independent of substrate properties and only depends on the interaction between the BBs (CPAA (/PAA) and PDDAC)^[34]. In the case of pure PE chains, the growth was linear as successive steps deposited a regular and even amount of material which then leading to a full coverage of the substrate.

Furthermore, at low ionic strength the adsorbed mass was much higher than at 0.6M. Indeed, here the PEs charge neutralization by the salt counterions of salt (extrinsic compensation or hydration) is low^[35]. Especially CPAA (/PAA) BBs, whose charge density largely depends on the pH and salt, were only weakly “extrinsically” compensated by small quantity of salt. Both CPAA (/PAA) and PDDAC chains are both fully ionized. As a result, when the first CPAA (/PAA) solution was injected into the QCM cell, part of the charges on the polyanion backbone was compensated by the positive surface present on the Q-sensor surface charge as indicated by a relatively large frequency shift (-20 Hz). The rest of the anionic charges lead to the reversal of the surface charge. In the following successive steps, PDDAC chains formed “intrinsic” electrostatic complexes (polymer-polymer interaction) with the formerly deposited CPAA (/PAA) chains via neutralizing of their negative charges; excess positive charges fuelled then the further growth of the hybrid layer as reported by Dubas *et al.*^[35]. The weak charge screening effect present at 0.01M governed then the sequential deposition of a multilayer via the charge overcompensation. For all assemblies investigated here, the dissipation was less than 2.10^{-6} (per bilayer) allowing the use of the Sauerbrey relationship to compute the adsorbed mass. After 24 deposition steps (12 bilayers),

Fabrication of functional surfaces

adsorbed masses Δm were around 1370 mg/m^2 and 10 mg/m^2 for CPAA/PDDAC and PAA/PDDAC pairs respectively. The adsorbed mass is much greater for the CPAA/PDDAC pair due to the presence of quite dense (6.5 g/cm^3) ceria NPs.

In the case of 0.6 M, the higher ionic strength enhanced the extrinsic compensation of the PE backbones leading to more coiled and looped chains^[35]. Consequently, the charge density borne by the CeO_2 -PAA NPs was weak and provided reduced accessibility to the next absorbing PDDAC chains, reducing the sequential uptake of the materials by one order of magnitude as clearly seen in Figure 4. 4; a result not completely surprising for a system interacting solely via electrostatic interaction (see chapter 1 & 3).

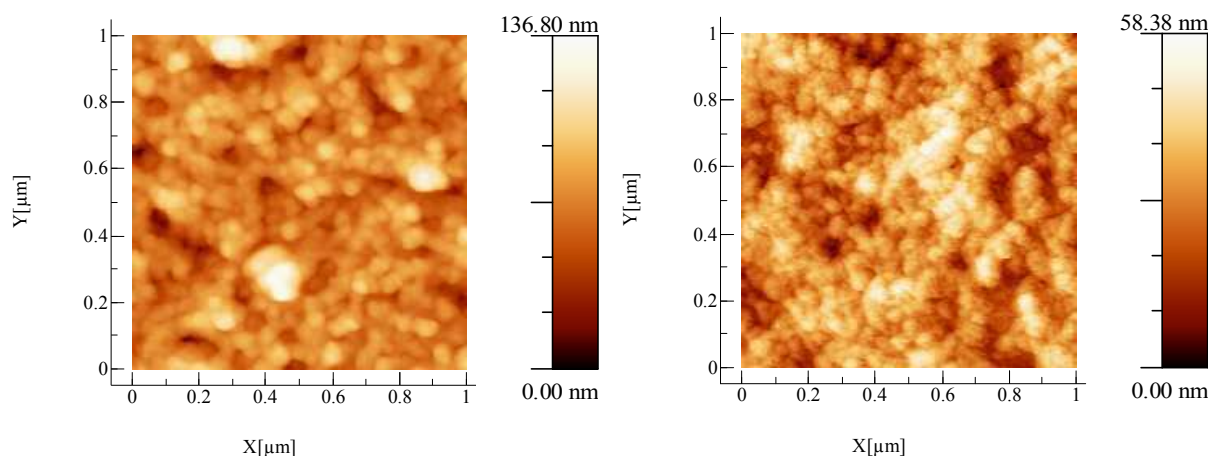


Figure 4. 5: AFM topography images of the $(\text{CeO}_2\text{-PAA/PDDAC})$ LbL assembly at low 0.01M (left) and high 0.6M (right) ionic strength.

Figure 4. 5 shows AFM morphological images of the LbL multilayer fabricated at low 0.01M and high 0.6M ionic strength. In agreement with literature reports, the thickness of the multilayer built at 0.01M is greater than the one made at 0.6M due to the deposition of a larger amounts of materials via a relatively strong interaction between BBs. The strong repulsive forces acting between some of the NPs gave rise to rougher surfaces ($R_{\text{RMS}} \sim 16 \text{ nm}$) as can be seen on the left of Figure 4. 5. Whereas at high I_s the coiled nature of the PEs chains generated a smoother ($R_{\text{RMS}} \sim 9 \text{ nm}$) and more closely packed structures^[22].

Fabrication of functional surfaces

In order to investigate the hybrid structure in its depth, we have worked out a cross-sectional view of the multilayer. For that purpose a *LbL* multilayer of the $(\text{CeO}_2\text{-PAA/PDDAC})_{12}$ system was assembled on a sheet of a smooth and flexible PET surface previously functionalized with bare ceria NPs with the same conditions as in the QCM cell. In a second step, the overall assembly was embedded in an epoxy resin prior to perform an ultramicrotomic cut perpendicularly to the hybrid layer as illustrated in Figure 4. 6. The thickness of this rather compact layer of NPs was evaluated on the AFM images to ~ 350 nm. Considering that the effective layer density reads:

$$\rho_{eff} \equiv \frac{\Delta m}{t} = \rho_{NPs} \varphi_{NPs} + (1 - \varphi_{NPs}) \rho_{PEs} \quad (3)$$

The volume fraction φ_{NPs} of the functional ceria NPs can then be estimated to 0.5, a relatively high value made possible by a controlled *LbL* process.

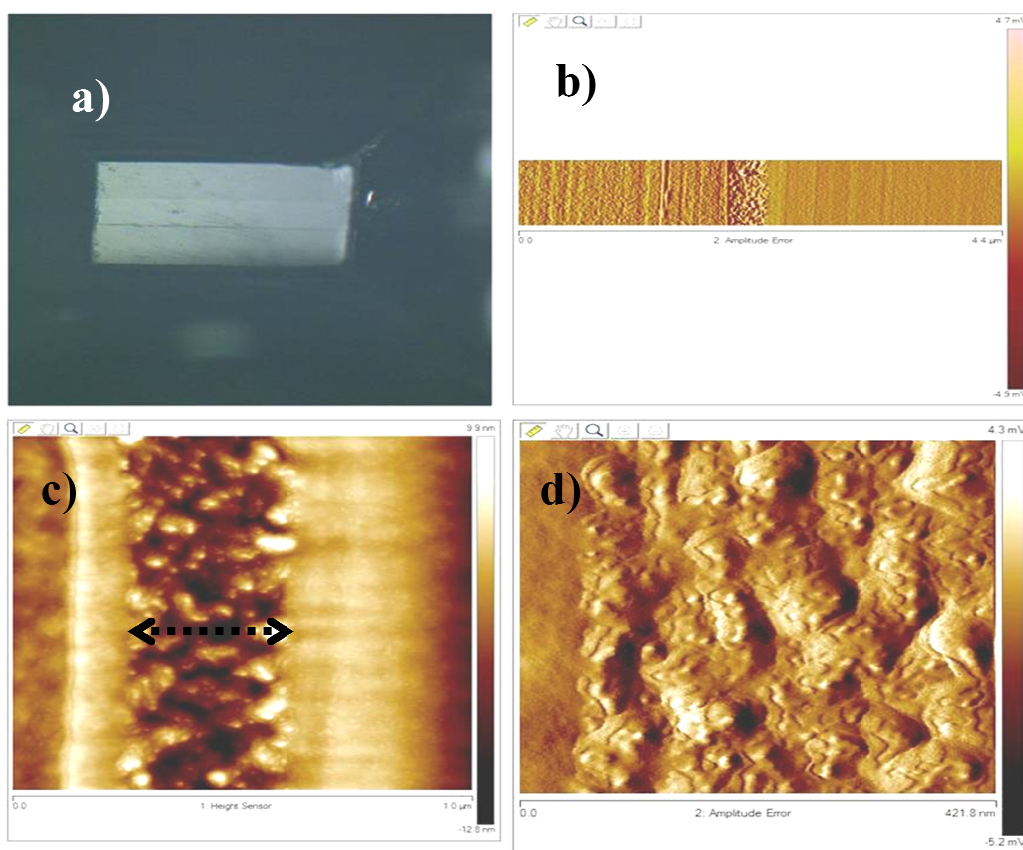


Figure 4. 6: Optical cross-sectional view of a $(\text{CeO}_2\text{-PAA/PDDAC})_{12}$ multilayer assembly deposited on a PET surface and embedded in an epoxy matrix after a microtomic cut (a). AFM cross sectional images of the hybrid layer with increasing magnification from (b) to (d).

NPs/NPs (CeO_2 -PAA_{2k}/ CeO_2 -bPEI_{25k})₁₂ system

As already mentioned, LbL is a viable route to fabricate smart surfaces by fine tuning the assembly conditions such as pH, salt and the type of components. Here we use the LbL approach to develop an *all*-NPs functional coating through the co-assembly of oppositely charged ceria NPs with the hope of a high NPs loading in the final nanocomposite layer.

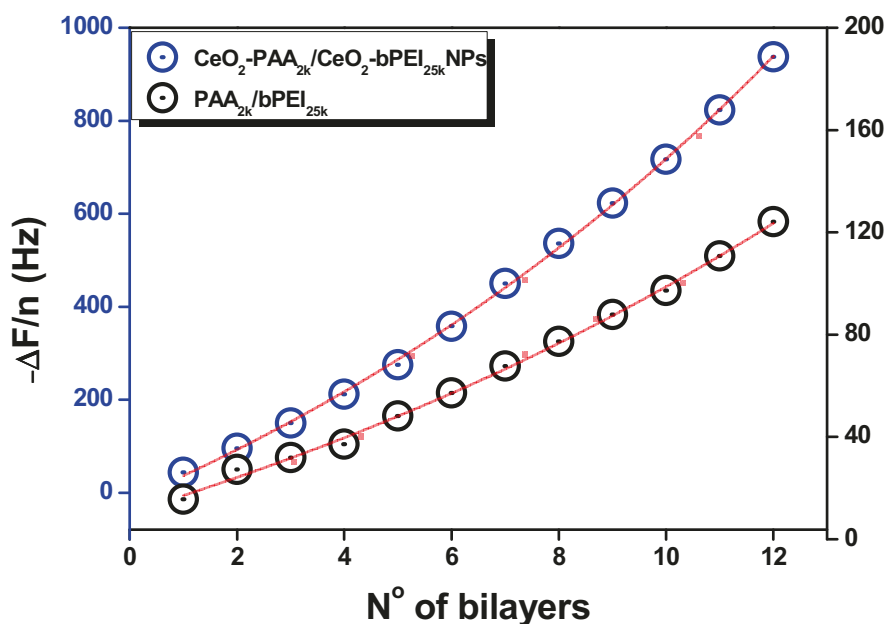


Figure 4. 7: Cumulative frequency shift ($-\Delta F/n$) as a function of the number of layers for the LbL of oppositely charged PEs ($PAA_{2k} / bPEI_{25k}$)₁₂ and NPs (CeO_2 -PAA_{2k} / CeO_2 -bPEI_{25k})₁₂ as monitored by QCM. The deposition was made at pH 8 and pH 7 (0.01M NH_4Cl) for anionic and cationic building-block respectively. Y scales are different for PEs and NPs to highlights the exponential growth in both cases. Continuous lines are exponential fits to the data.

A large body of work has been devoted to the LbL assembly of weak PEs due to an easy control of the charge density along the PEs backbone with the pH of the solution enabling the fine tuning of the thickness and some related properties^[31]. The growth is generally exponential at the beginning and turns linear after the initial deposited bilayer scaffold (~ 10 -15)^[32]. Figure 4. 7 shows the sequential deposition of both oppositely charged NPs and free PEs building blocks ($PAA_{2k}/bPEI_{25k}$) at pH 8/7. Both LbL assemblies indeed showed a weak exponential regime at least up to 12 bilayers. This exponential growth is a

Fabrication of functional surfaces

peculiar characteristic of the branched architecture of PEs as recently reported by Choi *et al.*^[36].

The globular and compact conformation of *b*P EI chains allows only their outer shell to interact with PAA chains. As a result the counterions which are trapped inside the compact structure lead to a large mismatch in ionic pairing. Those trapped effective charges triggers the high mobility and faster diffusion of PEs which then facilitates the exponential growth^[36]. In addition to the conformation, the length and number of branches and charge density modulated by pH and salt also play a role. In agreement with Laugel *et al.*^[37], the weak interaction between the fully ionized $-\text{COOH}$ of PAA and moderately protonated $-\text{NH}_2$ of *b*P EI at the given pH combination (8/7) also facilitates the exponential growth. The diffusion dependent exponential growth is certainly only valid for free PEs assembly but not for all-NPs assembly, where charged macromolecules are tethered to large and rigid NPs and cannot therefore diffuse freely.

In such case, this observed exponential regime might be a signature of the rearrangements of the electrostatic complexes formed between oppositely charged ceria NPs in the multilayer as mentioned by Schonhoff *et al.*^[34]. The protonation/deprotonation at a given pH of COOH of PAA by $-\text{NH}_2$ groups of *b*P EI or vice versa, the presence of different types of amines and a lower number of *b*P EI chains on the cationic ceria, might be the key factors. More work is likely needed to catch the full mechanism at play here behind this exponential growth.

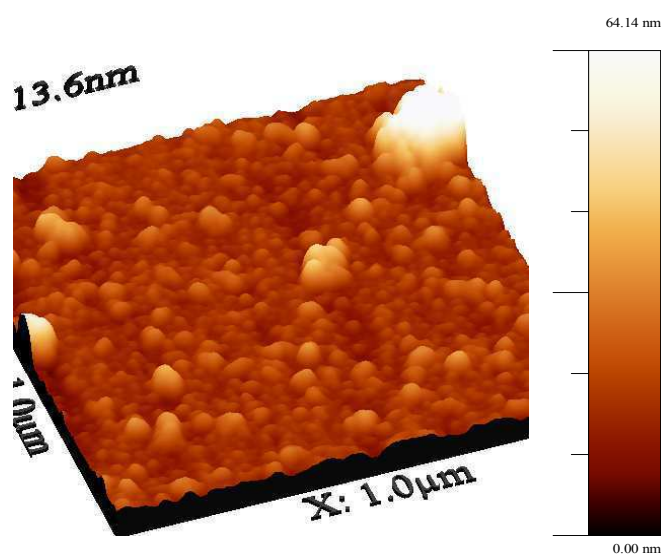


Figure 4. 8 : 3D AFM image of LbL multilayer (12 bilayers) made from oppositely charged ceria NPs.

Fabrication of functional surfaces

For both the NPs and PEs assemblies, dissipation was less than 2.10^{-6} (per bilayer) enabling the use of Sauerbrey relationship to compute adsorbed masses of 170 mg/m^2 and 23 mg/m^2 for *all*-NPs and pure PEs respectively. The “nano clustered” layer has a thickness of about 80 nm as measured directly by AFM. The thickness is relatively low for *all*-NPs assembly^[38, 39] due to the rigidity and electrostatic exclusion of NPs originating from the charge density of CPAA and CPEI at their respective pH of 8 and 7, as reported recently by Yang *et al.*^[31]. Here also we can estimate a NPs volume fraction φ_{NPS} of 0.2, a relatively lower value as compared with the less rigid NPs/PE_S assembly as seen in Figure 4. 8 suggests rather loosely packed multilayer.

As mentioned in chapter 1, the mechanism underlying the complexation mediated between weak PEs can indeed be very complicated to grasp and sort out the forces at play even more. We have just seen that the adsorbed amount is quite small at pH where both PEs are supposed to be charged and interacting through electrostatic forces. We have briefly investigated the LbL assembly of pure PAA/*b*PEI PEs at 2 different pH in order to find more suitable conditions if any.

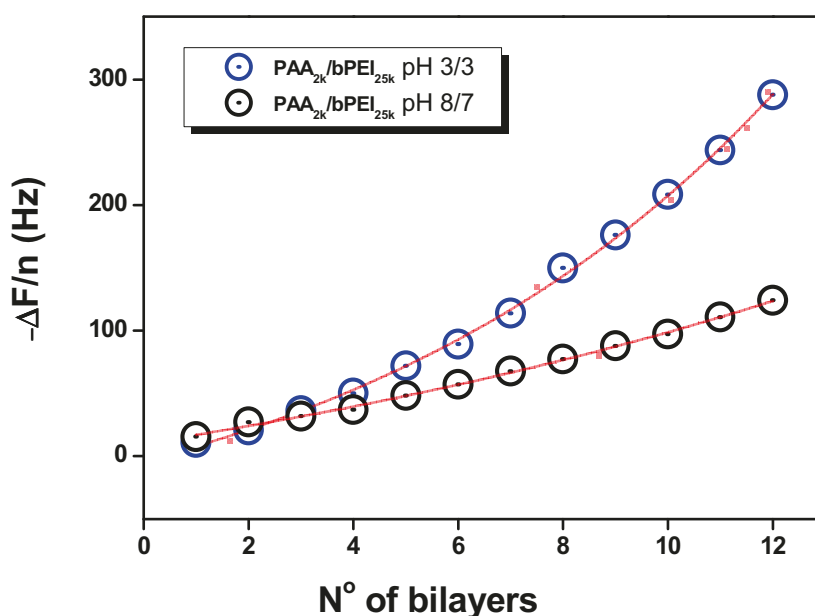


Figure 4. 9 : Cumulative frequency shift ($-\Delta F/n$) as a function of the number of layers for the LbL of oppositely charged PEs ($PAA_{2k} / bPEI_{25k}$) at $pH=8/7$ and $pH=3/3$ as monitored by QCM. Continuous lines are exponential fits to the data.

Fabrication of functional surfaces

Figure 4. 9 shows the LbL assembly of PAA/*b*PEI was carried out at pH 7/8 where both groups are partially charged and pH 3/3 where *b*PEI is fully protonated, while PAA segments are not charged. The adsorbed amount at pH 3/3 is almost 3 times higher than the one for pH 8/7 with a much steeper exponential growth. This dramatic increase is due to the intrinsic coiled conformation of PAA at that pH and the local titration between –COOH groups of PAA and –NH₂ groups of *b*PEI. The fully ionized *b*PEI requires more PAA chains for charge overcompensation which then lead to increase the adsorbed amount and consequently the final thickness. A feature that will be seen further down in the case of CNTs assembly as well.

Those multilayer film can be used for example to fabricate functional coatings to protect especially metals from corrosion or in UV sensing materials, since ceria NPs possess the special property to scavenge free radicals and a high sensitivity to UV rays^[40, 41]. Some preliminary experiments on the application aspects will be shown in chapter 5.

Carbon NTs system

MWCNT-COOH/MWCNT-NH₂ system

Multilayered MWCNTs thin films were generated via the sequential deposition of acid and amine functionalized MWCNTs following the protocol defined in the experimental section. The presence of ionisable/protonable groups on the CNTs suggests that final thicknesses might be tuned. Lee *et al.*^[30], reported that relatively thick assembled MWCNTs films were obtained when the ionization degree of MWCNT-COOH (or the solution pH) is low in agreement with what we found for the PAA/*b*PEI PEs system (Figure 4. 9). In our opinion, the effect is here provided initially by a weaker repulsion between the carboxylated CNTs and some H-bonding interactions with the substrate increasing the first adsorbed layer amount on the surface. In subsequent adsorptions, highly protonated aminated CNTs at low pH will strongly interact with COOH groups via acid-base interactions giving rise to larger adsorbed amounts (amines are titrating acid groups). In the present experiment, the pH was fixed to 2.5 for both acid and amine CNTs. Although QCM is the well known platform to monitor the growth of multilayers, it was not possible to carry out the growth of those somehow weakly functional CNTs. They indeed adsorb preferentially onto the plastic tubings

Fabrication of functional surfaces

via hydrophobic interactions before reaching the cell as clearly indicated by an intense black color

Figure 4. 10a on their inner surface; a thorough rinsing was unable to remove the layer. Successive injections of oppositely charged MWCNTs performed an LbL assembly on the tubing itself rather than in the cell.

The assembly was then carried out on a glass slide inside a petri dish as mentioned in the *preparation of thin films* substrate by alternatively dipping it into aminated and acid MWCNTs dispersions for 20 min. We have cycled this step 16 times generating a glass slide with 8 bilayers on each side.

The resulting thin film were very fragile and “visually” inhomogeneous due to the removal of some black materials from the substrate during the rinsing stage, as depicted in Figure 4. 10b. In order to give some mechanical integrity to the CNTs film, amides bonds were created by heating up to 150°C for 2 hrs^[42]. As seen in Figure 4. 10c the thermal treatment tightened the network via interconnectivity and reinforced the film against capillary force induced by water.

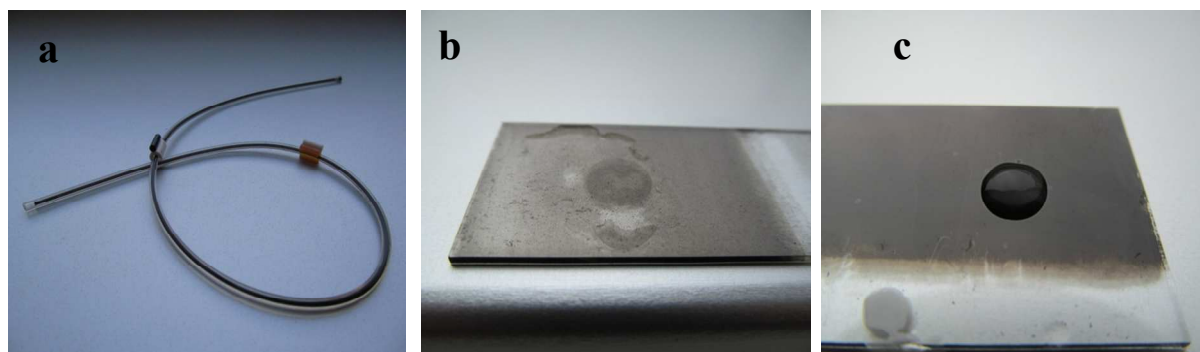


Figure 4. 10 a) QCM tubings with a thick black coating due to the alternate adsorption of functionalized MWCNTs. b) Removal of materials from the glass substrate during the rinsing stage before cross-linking. c) Reinforced CNTs film via the formation of amide bonds.

Fabrication of functional surfaces

Each “cross linked” multilayer was then subjected to UV-Vis spectroscopy. Figure 4.11 shown below gives a direct evidence of the multilayer growth with an absorbance (550 nm) increasing linearly with the bilayers number. This linear regime confirms that each deposition step deposits the same amount of oppositely charged short ligands tethered MWCNTs in the matrix, as reported by Olek et al^[42, 43].

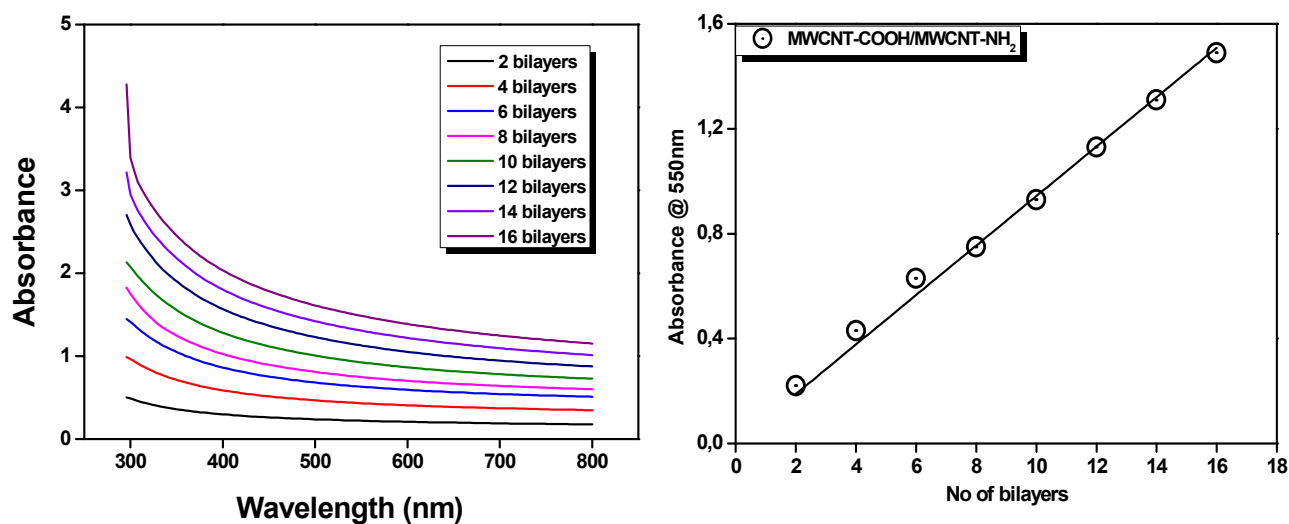


Figure 4. 11: UV-Vis absorption spectra of a glass substrate in the course of the LbL of MWCNT-COOH/MWCNT-NH₂ (left). Absorption of LbL thin films at 550 nm Vs the number of bilayers (right).

AFM characterizations performed on a bilayer revealed that the tubes were randomly oriented on the substrate and percolated due to efficient acid-base interactions. The small “white bumps” visible on the images are impurities such as inorganic catalyst NPs. The measured roughness first increased from 1 (13.1 nm) to 4 (26.7) bilayers before decreasing and stabilizing around 8 bilayers (18) suggesting a densification of the multilayer with the thickness.

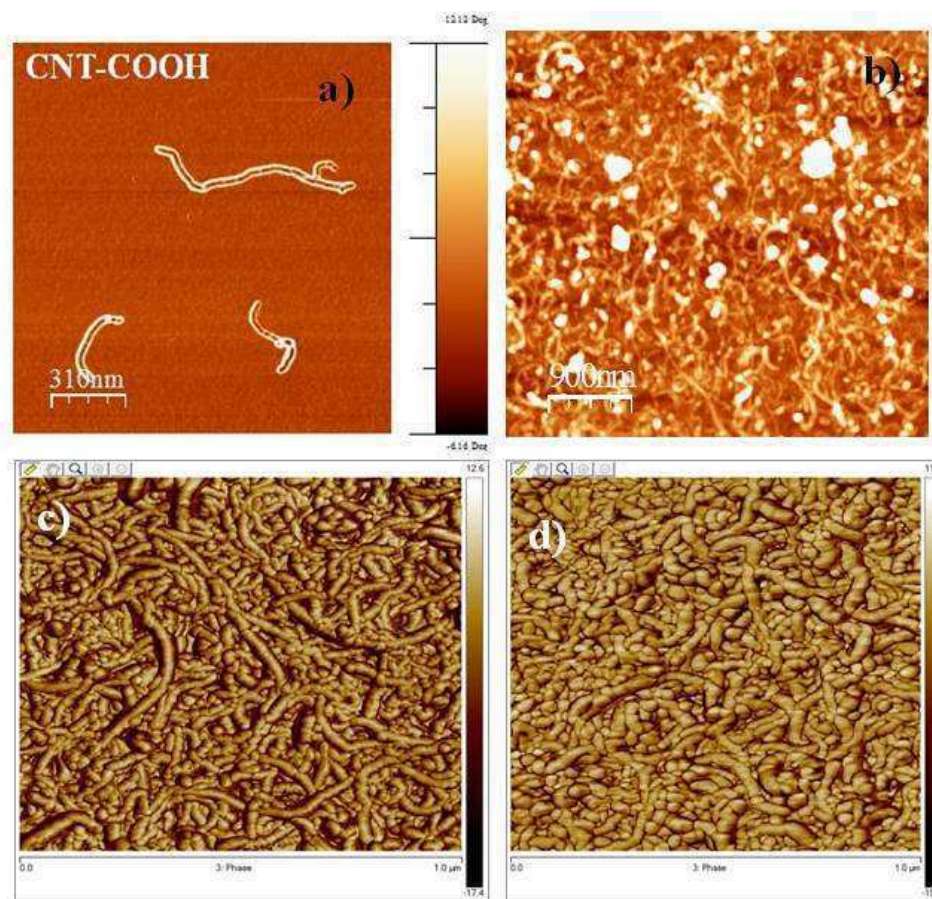


Figure 4.12: AFM images of (a) individual MWCNT-COOH (b) percolated $(MWCNTCOOH/MWCNTNH_2)_1$ (c) 4 and (d) 8 LbL bilayers on a silicon wafer surface.

The generation of CNTs multilayer on the CeO_2 coated PET substrates resulted in “thin transparent conductive” film and will be discussed in detail in chapter 5.

MWCNT-wPEI/MWCNT-wPAA system

The LbL assembly of PEs wrapped CNTs was carried out on the MWCNT-wPEI_{21k} and MWCNT-wPAA_{31k} system at pH 5 inside a QCM cell as explained in the experimental section. Figure 4. 13 gives direct evidence that it is not possible to growth the film beyond the fifth bilayers due to desorption of some of the PEs chains wrapped around the CNTs and their subsequent adsorption onto the oppositely charged sensor surface. Indeed, with time the weakly adsorbed PEs via hydrophobic forces started to desorb from both CNTs surface as mentioned in chapter 2 and triggered the re-formation of CNTs bundles via van der Waals attraction and their precipitation.

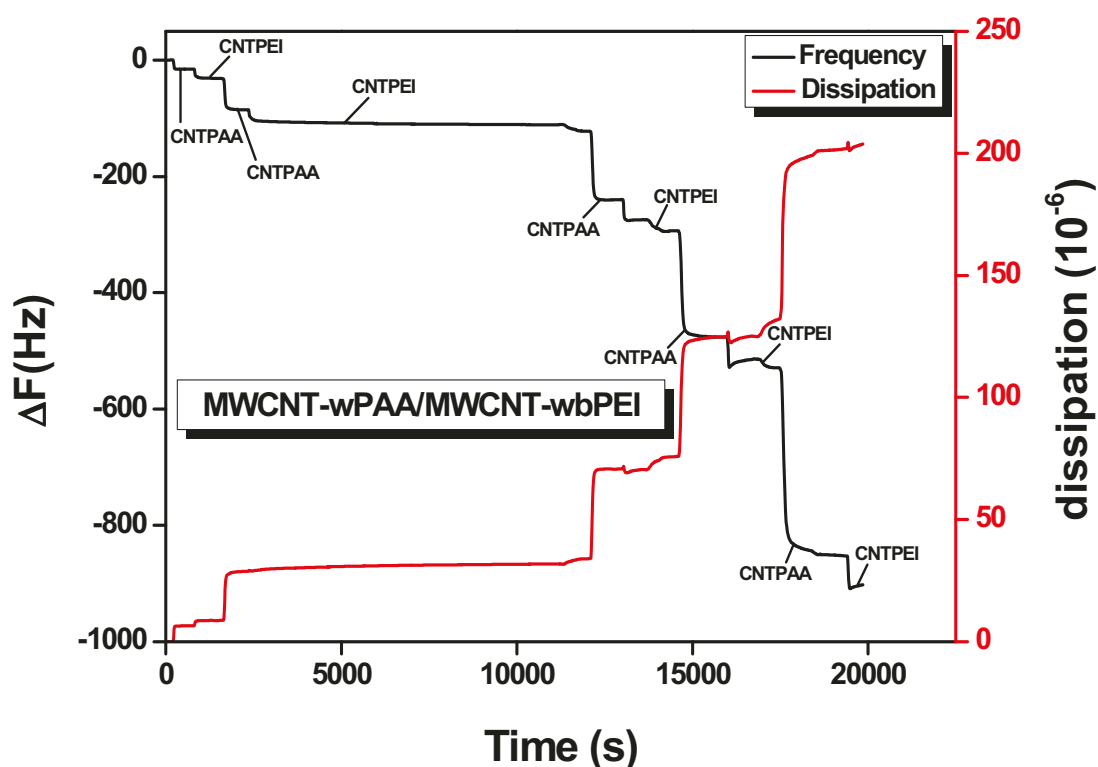


Figure 4. 13: *LbL growth of oppositely charged MWCNT-wPAA/MWCNT-wPEI monitored by QCM.*

It is then essential to minimize or remove those free PEs to enable the efficient growth of a CNTs nanocomposite only. Centrifugation or dialysis (equilibrium shifted) will unfortunately enhance the PEs desorption leading to CNTs aggregation. Covalently tethered MWCNT-PEs nanocomposites where free PEs chains can be gently removed can fortunately enable the growth of a multilayer with a desired number of bilayers depositions.

MWCNT-cbPEI_{25k}/PAA_{2k} and MWCNT-cbPEI_{25k}/MWCNT-cPAA_{5k} systems

Figure 4. 14 shows the *LbL* assembly of covalently grafted MWCNT-cbPEI_{25k}/PAA_{2k}^[44] and MWCNT-cbPEI_{25k}/MWCNT-cPAA_{5k}^[45] nanocomposites. The features of the films can be tailored as a function of pH and salt because the CNTs corona is made out from pH (and salt) responsive weak PEs. As described in the experimental section, and in order to have a starting anionic substrate, a bare ceria NPs modified Q-sensor was immersed into a 0.1 wt% PSS solution for 1 hr at RT. For the three systems investigated, the

multilayer growth is weakly exponential likely for the same reasons as in the case of oppositely charged ceria NPs.

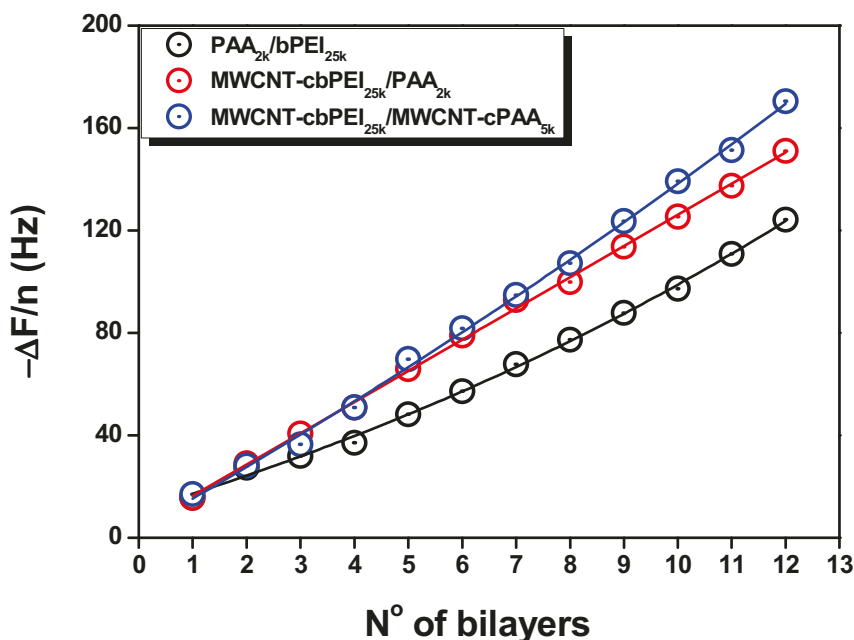


Figure 4. 14 : Cumulative frequency shift ($-\Delta F/n$) as a function of the number of layers for the LbL multilayer growth of $bPEI/PAA_{2k}$, $MWCNT-cbPEI/PAA$ and $MWCNT-cPAA/MWCNT-cbPEI$ pair performed at pH 7/7.

The adsorbed mass calculated using the Sauerbrey expression was about 27 mg/m^2 and 30 mg/m^2 for the $MWCNTbPEI_{25k}/PAA_{2k}$ and oppositely charged tubes. The Δm of “all-MWCNT” assembly is slightly higher than the $MWCNTbPEI_{25k}/PAA_{2k}$. This might be due to the acid-base interaction between the residual $-\text{COOH}$ and $-\text{NH}_2$ groups of parent material in addition to the interaction between the $bPEI_{25k}$ and PAA_{5k} . In overall the adsorbed mass and the thickness is very low for all the MWCNTs pairs investigated in comparison with the ceria NPs system. This behaviour depends certainly on the elongated nature of the CNTs and the choice of orientation of the oppositely charged CNTs to intimate with others, as reported recently by Paloniemi *et al.*,^[45] and of course on the pH at which deposition occurs as seen previously suggesting once again that a purely electrostatic assembly will not produce thick and dense films. A feature that we will be investigated in near future.

Fabrication of functional surfaces

In agreement with Liao et al^[44], these LbL films are expected to exhibit superhydrophobic behaviour if they are dense enough. These thin MWCNTs films are promising candidates for self cleaning applications.

Silica NPs system

SiO₂-PAA_{5k}/ℓPEI_{2k} system

The LbL assembly of the SiO₂-PAA/ℓPEI pair was initially carried out at pH 7/7, where anionic silica is fully charged, but showed a very weak growth due to the similar reasons as mentioned previously and additionally to a very weak protonation state of ℓPEI (secondary amines) as this pH. The assembly was then carried out at pH 3/3 and at 0.01M NH₄Cl on a PSS modified Q-sensor.

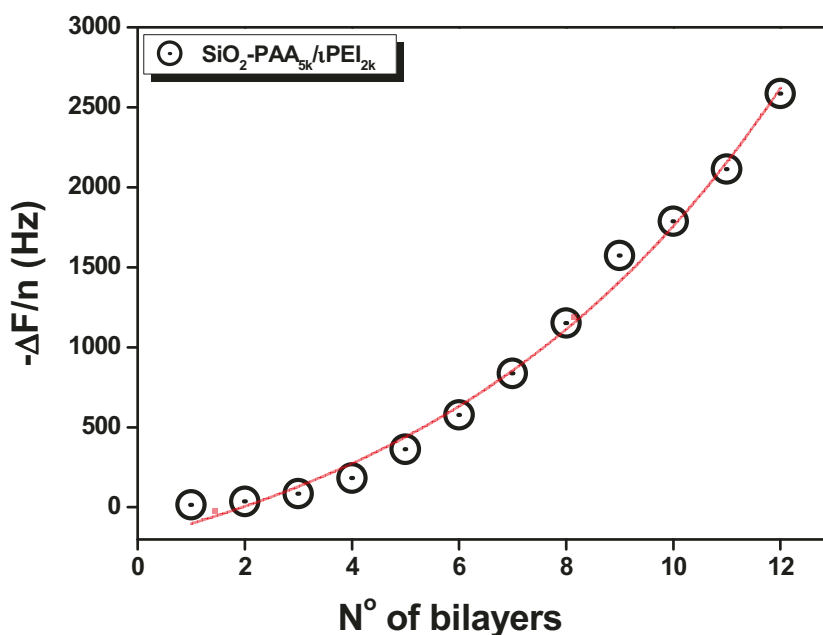


Figure 4.15 Cumulative frequency shift ($-\Delta F/n$) as a function of the number of layers for the LbL exponential growth of SiO₂-PAA/ℓPEI system at pH 3/3.

Fabrication of functional surfaces

The exponential growth observed here *LbL* assembled multilayer is due to acid-base interactions between weakly ionized $-\text{COOH}$ groups of PAA and the high protonation state of $-\text{NH}$ groups of ℓPEI ; and not directly related to electrostatic interactions that are rather weak at this pH. Furthermore, the swollen multilayers, a characteristic feature of the weak interactions as reported by Choi *et al.*^[36], allowed the diffusion of PEs into the multilayers, facilitating the exponential regime.

The Δm for the present system was found around 460 mg/m^2 deduced from the Sauerbrey relation with a thickness of 270 nm. The steep growth (Δm) and quite important thickness of the multilayer at a given pH condition is mainly caused by the formation of clustered silica particles via the intermolecular H-bonding interactions between the SiPAA_{5k} (PAA at this pH is known to promote the H-bonding). The silica NPs volume fraction within this layered structure is estimated to 0.64, higher than what was found for the ceria NPs/PEs system; a result due to the low pH condition of the assembly. The overall *LbL* assembly of *all* silica NPs (NP-PAA/NP-PEI) will be performed in near future as it is expected to bring potential applications in self-cleaning and anti-fogging systems (superhydrophobicity & superhydrophilicity).

Surface grown hybrid functional Layers (SgL)

Ceria NPs system

NPs/PEs (CeO₂-PAA_{2k}/PDDAC_{100k}) system

The dormant CeO₂-PAA/PDDAC solution was prepared by mixing in one shot 0.1 wt% of both stock solutions at 1M NH₄Cl (added to the dispersions after the pH adjustment to 8) followed by a stirring at RT for 5 min to ensure a good homogenization. An estimation of the charge ratio Z under an equal volume of mixing ($X = V_{np}/V_{pol} = 1$) shown below gave a value ~ 1 .

$$Z = \frac{d_{NP} M_w^{pol} X}{n_{pol} M_w^{NP}} \quad (4)$$

Where Z = charge ratio, d_{NP} = the nanoparticles density, M_w^{pol} = PEs M_w , X = volume ratio, n_{pol} = PEs repeating units and M_w^{NP} = nanoparticles M_w . It should be noted that to avoid vibration, no stirring was performed during the injection into the QCM cell, whereas it was carried out during each dilution step. The sample solution was allowed to flow into the cell for 5 min with the help of a peristaltic pump and stopped afterwards.

Figure 4.16 shows the QCM growth of a hybrid layer via the SgL approach as a function of the ionic strength. The insert highlights the adsorption as a monolayer of one of the component present in the dormant solution when first in contact with the substrate. The CPAA most likely adsorb as individual NPs giving with an estimated amount of (2.5 mg/m² or 20 Hz) lower than a dense monolayer of bare ceria NPs (15 mg/m² or 90 Hz) suggesting weak interactions between the PAA corona chains and the Q sensor substrate at this high ionic strength. The dormant solution was then diluted with a drop-by-drop addition of DI water to reach $I_b \sim 0.6M$, the critical bulk ionic strength for this specific pair (determined from DLS experiments in chapter 3). The injection of this reactive solution into the QCM cell deposited of 10.6 mg/m² of a hybrid layer, a value 5 times higher than individual CPAA NPs. The decrease of the ionic strength (or the increase of the Debye screening length) via dilution triggered the formation of small “electrostatic” complexes (or clusters) at the interface and the subsequent growth of the layer.

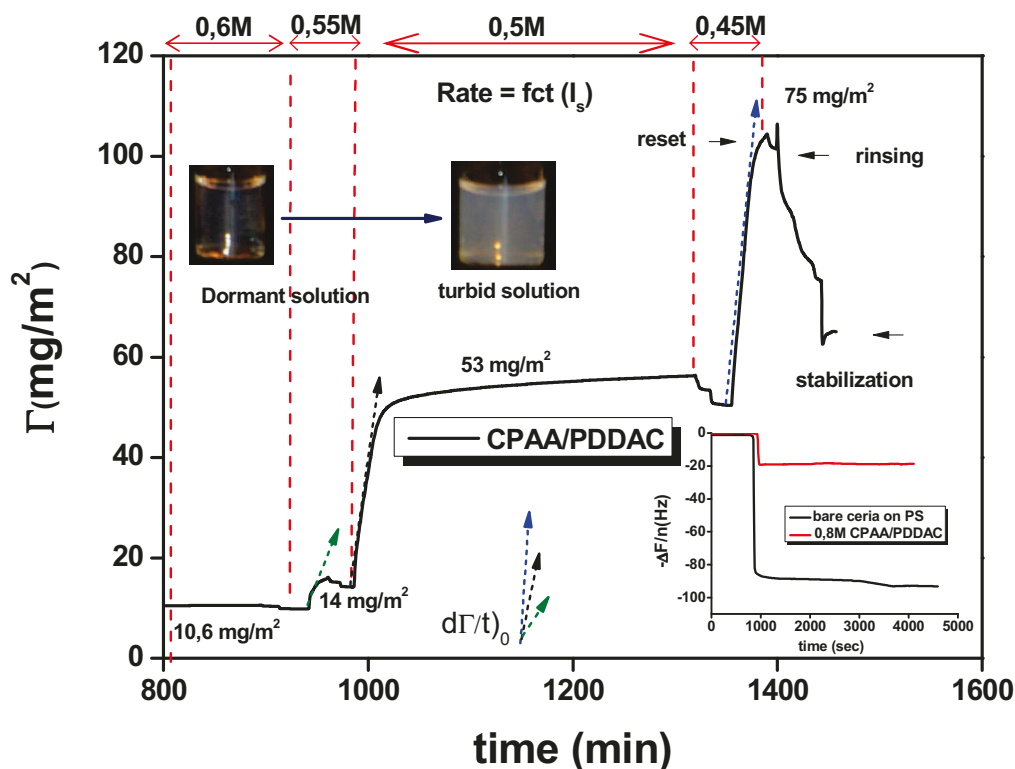


Figure 4.16 : SgL growth (deposited amount) of the CeO_2 -PAA_{2k}/PDDAC pair onto a bare ceria modified sensor as a function of different salt concentrations monitored by QCM. Insert shows the adsorbed amount of both CPAA NPs present in the dormant solution and bare ceria NPs.

As can be seen in Figure 4.16, decreasing I_s will increase the growth rate ($\frac{d\Gamma}{dt}$) at the onset of the complexation (where adsorption is controlled by BBs diffusion); giving the possibility to tune the final adsorbed amount easily (where adsorption is controlled by BBs reaction). Adding back 1M (“reset”) to the solution stopped the growth by setting off the driving force with no desorption or disassembly visible during the time frame of the experiment. The drop observed at the end corresponds likely to loosely bound materials being removed and/or compaction of the layer during the DI rinsing stage; the signal reaching a stable value afterwards.

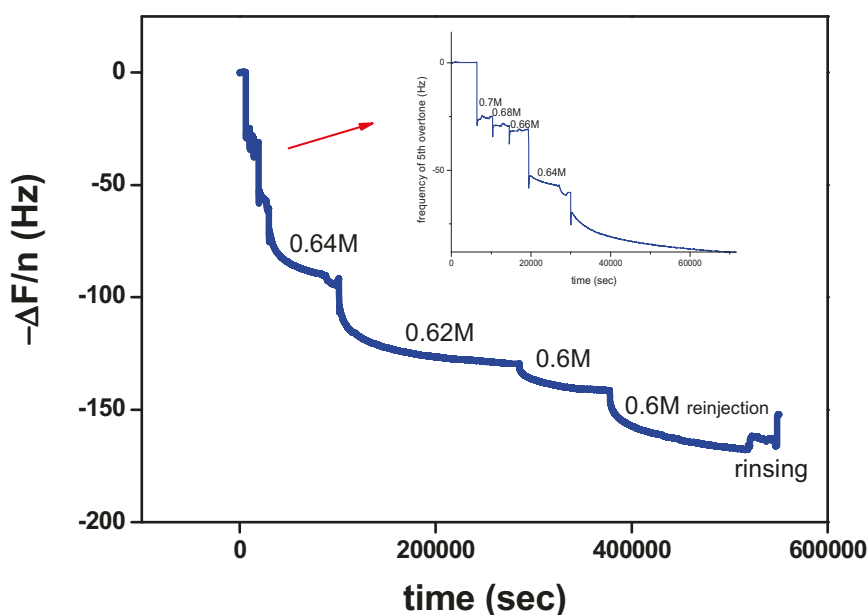


Figure 4. 17 : *SgL growth of the CeO_2 -PAA_{2k}/PDDAC pair onto a bare ceria modified sensor just above the critical bulk concentration I_b monitored by QCM.*

At an ionic strength just below I_b where the bulk solution is still dormant, the presence of the surface initiates a growth as can be seen in Figure 4. 17. At 0.7M the monolayer of negatively charged CeO_2 -PAA adsorbs onto the bare cationic ceria monolayer. A further dilution to 0.68M and 0.66M results in very slight adsorption (only 4 and 2 Hz shift). The genuine growth seems to start at 0.64M. Between 0.64 M and 0.6M the system *awakes* close to the interface while still dormant in the bulk. Above 0.6 M, the small clusters are being formed in the bulk and further adsorbed on the surface. Initiation of the bulk complexation depends strongly on different parameters such as the dilution pathway, the time scale of the experiment and the concentration of BBs. At the end of the experiment the QCM cell was rinsed with solution of increasing salt concentration (from 0.6 back to 0.7M) to switch off the interaction and stop the film growth. The final rinsing step with pure water compactified the layer (with expulsion of water). The thicknesses produced in this regime are somehow rather thin.

The ionic strength in the SgL process enables then the efficient control of the growth of a hybrid layer at the liquid/substrate. In the following, we have studied the influence of others factors as the substrate nature, flow rate and charge ratio Z on the growth. We have set

Fabrication of functional surfaces

the ionic strength at the onset of the bulk transition [I_0 (1M) $> I_s$ (termed here “excited” solution) (0.62M) $> I_b$ (0.6M)] in order to lies between a monolayer and larger aggregates.

Assembly at different Z

“Excited” solutions at different charge ratios (Z) were prepared by tuning the volume ratio (X) of dormant solutions followed by a dilution with DI water to down $I_s \sim 0.62M$. Figure 4.18 shows that charge ratio as well is an important parameter to control the final adsorbed amount. The surface growth at $Z=1$ ($X=1$, $\Delta F=-78$ Hz) generates the largest adsorbed amount with a growth that does not level off completely in agreement with the growth close to the stoichiometry of (indefinitely) large aggregates (see Figure 3.3 in chapter 3) in the bulk via a continuous compensation of charges. Away from stoichiometry and again in agreement with the bulk behaviour, the adsorbed amount was smaller when an excess of either anionic CPAA ($Z=10$, $\Delta F=-33$ Hz) or cationic PDDAC ($Z=0.1$, $\Delta F=-55$ Hz) charges were present.

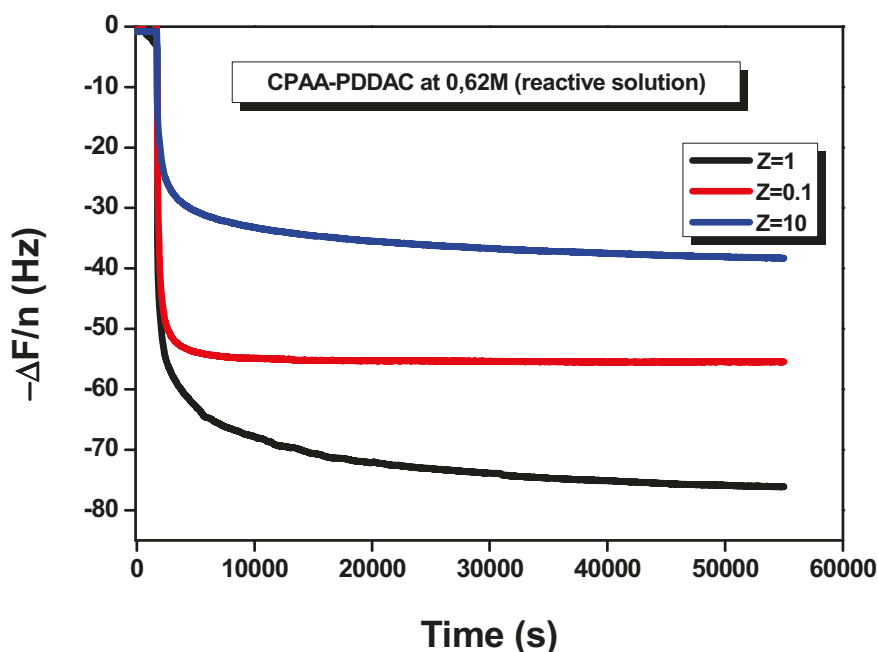


Figure 4.18: SgL growth of an (CeO_2 - PAA_{2k} /PDDAC) excited solution ($I_s=0.62M$) at different charge ratio (Z) monitored by QCM.

Fabrication of functional surfaces

Here we form small non-stoichiometric hybrid clusters with finite sizes and neat anionic or cationic charges. For $Z = 0.1$, the assembly was carried out on a PSS modified substrate as PDDAC was present in large excess. The amount was ($\sim 10 \text{ mg/m}^2$) slightly higher than in the case of $Z = 10$ ($\sim 6.6 \text{ mg/m}^2$) likely due to the large and flexible PDDAC chains wrapping the few CPAA NPs available. At $Z=10$, the adsorbed amount although smaller $\sim (6.6 \text{ mg/m}^2)$ was still larger than in the case of pure CPAA NPs.

To obtain thicker layer, the growth should then be performed at $Z \sim 1$ to continuously fuel the complexation. Furthermore, scratches made on the substrates were necessary to retrieve the different layer thicknesses through AFM measurements. Q-sensor being quite fragile and expensive, SgL was performed in the same conditions on top of silicon wafer substrates.

Out of four bare ceria covered silicon wafers, two were dipped into excited solutions horizontally and the two others were kept vertically. After 2 hrs, one set of substrates were taken out followed by the second set after 21 hrs.

The wet surfaces were dried under nitrogen flow and scratched with a thin needle, subsequently analysed by AFM as shown in Figure 4.19 and compared with the morphology of bare ceria on mica and SgL film fabricated at $Z \sim 1$ inside the QCM cell.

The measured thicknesses of all the hybrid films were between 200 and 219 nm. This indicates that the thicknesses of the vertically coated films were comparable with the horizontal ones, but the roughness of horizontal films was slightly higher than the vertical ones. Out of this measured 219 nm, 200 nm corresponded to the thickness of the PS coated substrate (from spectroscopy ellipsometry by applying a Cauchy model) and the remaining 19 nm was attributed to the thickness of the hybrid grown layers. Beyond, AFM images suggest that SgL produced quite “thin” homogeneous smooth hybrid films.

The thickness of the SgL hybrid layers are however lower than expected. This pushed us to find out optimum experimental conditions in order to enhance the adsorption amount. During some of the SgL experiments, it was indeed noticed that re-injection stimulated the adsorption. This feature, decided us to perform SgL experiments under dynamic conditions through a continuous injection of the solution.

Fabrication of functional surfaces

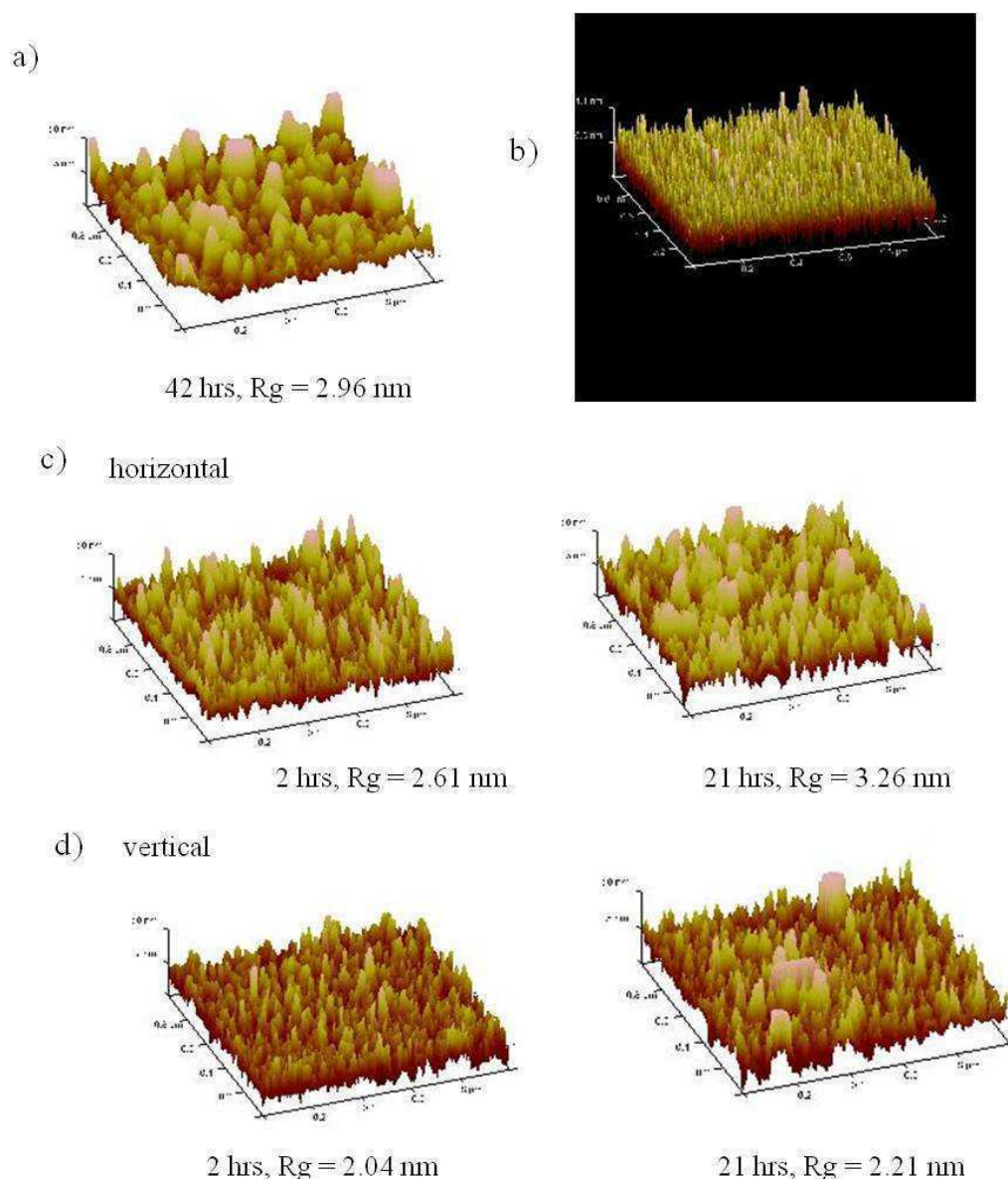


Figure 4.19 : 3D AFM analysis of a) as grown layers from excited solution on *Q*-sensor. b) bare ceria NPs on mica. Hybrid layers grown from excited solutions onto silicon wafers c) horizontal 2 hrs (left) and 21 hrs (right), d) vertical 2 hrs (left) and 21 hrs (right).

This approach is however solution-intensive, and in order to reduce or recycle the solution, we have designed a circular set-up where solution flows continuously in a closed circuit. “Circular” and “static” conditions were compared in the next paragraph.

Impact of substrates and experimental conditions

Figure 4. 20 shows the adsorption ($I_s \sim 0.62M$) at $Z \sim 1$ on bare ceria modified Q-sensor substrate with *dynamic* or *static* conditions. A spontaneous and higher adsorption amount more than three times greater was observed for the “circular” experiments in comparison with the static one. Shearing helps reorganizing the materials at interface and provides more spaces for the forthcoming components or clusters. Under the same time frame, the thickness obtained is definitely much higher than in static conditions. SgL performed in dynamic conditions is then a promising route to fabricate relatively thicker films.

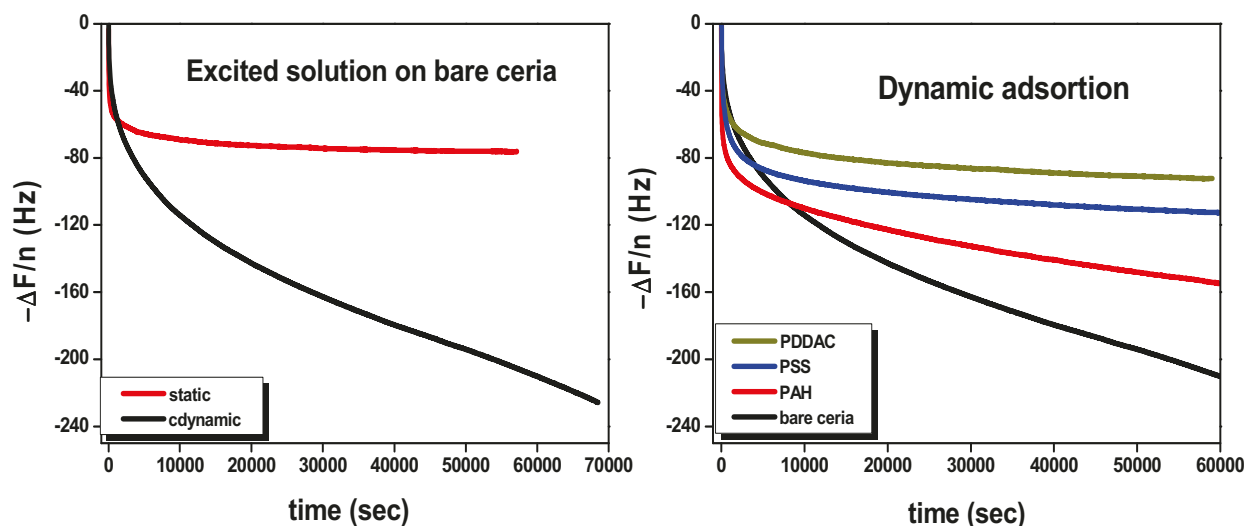


Figure 4. 20: SgL growth of CeO_2 -PAA/PDDAC ($0.62M$, $Z \sim 1$ system) on bare ceria coated Q-sensor in static and dynamic conditions (left) and as a function of the substrate nature (right).

Furthermore the influence of various substrates such as cationic/anionic PEs and NPs modified Q-sensor on the dynamic SgL growth was investigated at charge stoichiometry (Figure 4. 20 right). The adsorbed amount follows the series: bare ceria > PAH > PSS > PDDAC. As can be seen, a sharp increase in the adsorption rate and adsorbed amount was obtained for the bare (cationic) ceria covered substrate. It is not clear at the moment why we have such differences. We can imagine that beyond the sole electrostatic interaction strong coordination interactions (see chapter 2) between PAA chains and ceria NPs might have enhanced the initial adsorption. In the case of PAH, acid-base interactions between $-NH_2$

Fabrication of functional surfaces

groups of PAH and $-\text{COOH}$ groups of CPAA are certainly responsible of the highest amount obtained for a PEs. At the lower bound we have the PDDAC interacting solely through electrostatic interaction with oppositely charged NPs. The slightly higher value obtained for PSS is likely due to the extra hydrophobic interaction at play between PSS and PDDAC chains (see chapter 1). Furthermore, no noticeable changes were observed by changing the flow rate (and thus the shear rate as well) from 0.2 to 0.4ml/min.

We have then investigated the SgL approach at different ionic strength using this time dynamic conditions with optimized experimental conditions on bare ceria NPs covered Q-sensor. As expected, with *continuous* shearing, the adsorbed amount at 0.6M for instance ($\Gamma_{40\text{hrs}} \sim 83 \text{ mg/m}^2$) is almost 8 times greater than the one found out in the *static* conditions ($\Gamma_{16\text{hrs}} \sim 10.6 \text{ mg/m}^2$). The growth was stopped on demand as well by resetting the ionic strength back to 1M. It should be noted that the hybrid layer seems to grow indefinitely under such dynamic conditions.

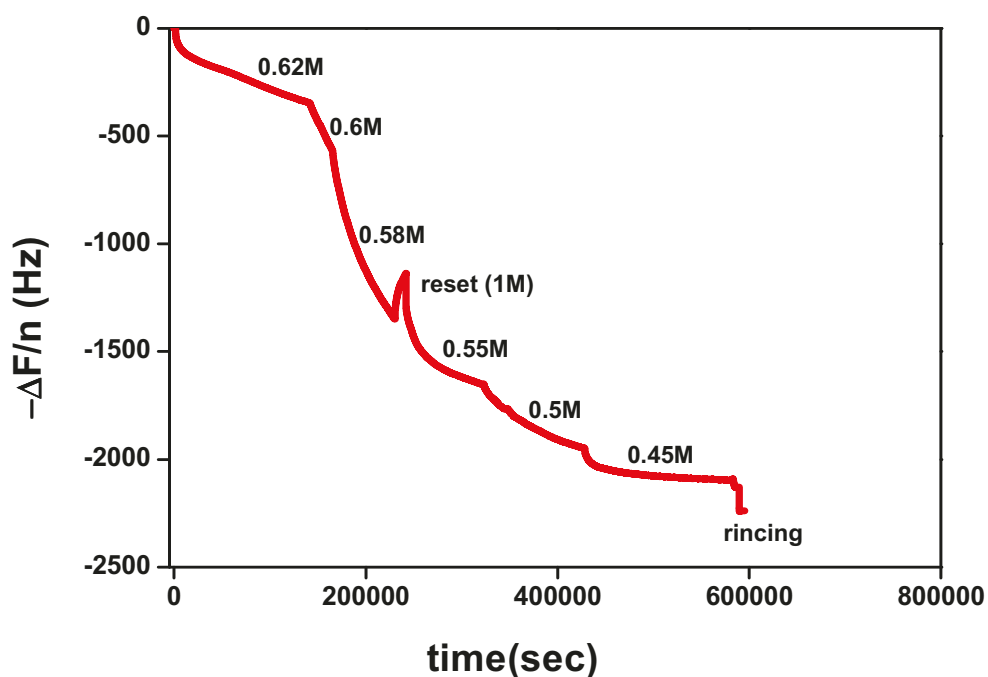


Figure 4. 21: SgL growth of the $\text{CeO}_2\text{-PAA}_{2k}/\text{PDDAC}$ pair onto a bare ceria modified sensor as a function of different salt concentrations monitored by QCM in dynamic conditions.

Fabrication of functional surfaces

As one can see, the SgL approach is an interesting approach to obtain in 1 step relatively thick hybrid layers and can be a very good complementary technique to the conventional LbL sequential adsorption method. This approach can be used for example to growth “thick” hybrid anti-corrosion layers on alumina substrates. Suitable conditions to obtain such functional layers will be discussed in chapter 5.

NPs/NPs (CeO_2 -PAA_{2k}/ CeO_2 -bPEI_{25k}) system

After showing some proofs of concept on the NPs/PEs system, we have investigated the SgL growth on *all*-NPs system (Figure 4. 22). A complete screening of the “electrostatic” interaction in the bulk was obtained for this specific pair of BBs at the initial ionic strength of 4M (see chapter 3). Close to the interface the H-bonding interactions left over were likely responsible for the small measured adsorption beyond the sole adsorption of individual BBs. When the ionic strength was brought down to 3.5M, an increment in the adsorption amount of 16.6 mg/m² was noticed.

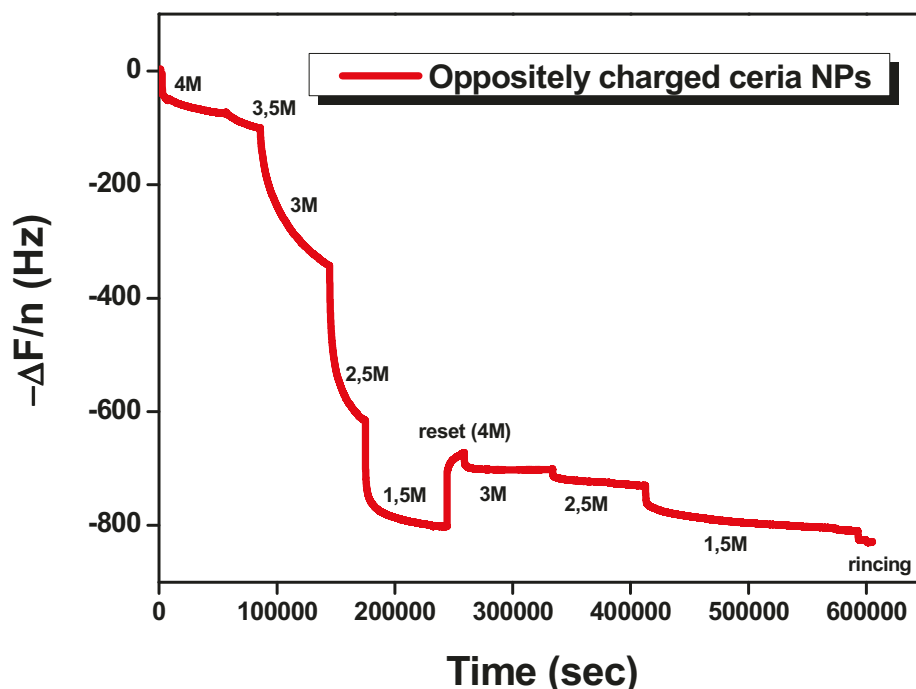


Figure 4. 22: SgL growth of the CeO_2 -PAA_{2k}/ CeO_2 -bPEI_{25k} pair onto a bare ceria modified sensor as a function of different salt concentrations monitored by QCM in dynamic conditions.

Fabrication of functional surfaces

Lowering further the ionic strength (3M, 2.5M and 1.5M), and increasing consequently the Debye screening length caused a larger and spontaneous adsorption with time without reaching a plateau. When the ionic strength was *reset* back to 4M, the growth stopped as expected giving rise to a constant signal (plateau) suggesting a high stability of the NPs/NPs co-assembled layers.

It should be noted that the overshoot observed during the reset point is likely attributed to the swelling (loosening) of the assembled film under high ionic strength and the removal of loosely bound aggregates. A second stage of growth was then initiated up to the final “annealing” rinsing step. At low ionic strength and long adsorption time however, we have the formation of very large aggregates that can precipitate onto the surface as shown in Figure 4.23.

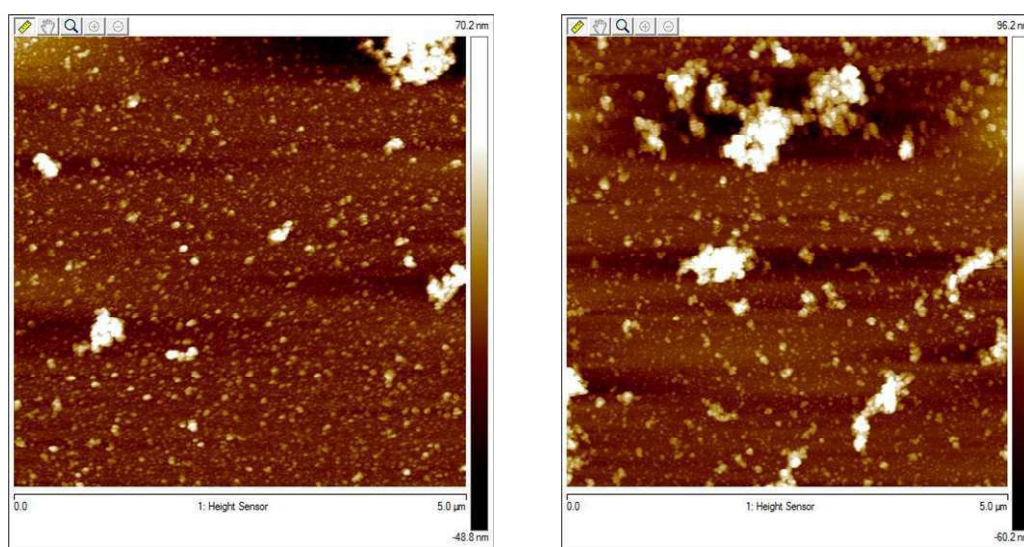


Figure 4.23: AFM analysis of the surface morphology of hybrid layers made from oppositely charged ceria NPs deposited by SgL during 48 hours onto silicon wafer substrates 2.5M (left) and at 1.5M (right).

Carbon nanotubes system

NTCs/PEs (MWCNT-cbPEI_{25k}/PAA_{2k}) system

Salt triggered co-assembly was carried out on the PSS modified sensor between oppositely charged cationic *b*PEI functionalized MWCNTs and short PAA chains. At $I_0 = 4M$, a weak plateau due to the complete screening effect of salt, corresponding to the monolayer adsorption of cationic MWCNTs was observed. As mentioned in the previous experiments, the further successive dilutions (from 3.5M to 2M), triggered the growth at the surface via the spontaneous co-assembly of oppositely charged BBs with increasing screening lengths.

In agreement with the bulk desalting transition (I_b), a slightly higher growth was obtained at 2M reaching quickly a plateau (diffusion controlled adsorption), indicative of the formation of CNT clusters at the surface ($R_H \sim 1200$ nm found in the bulk). 2M dispersion kept outside the QCM cell without stirring precipitated eventually with time (large visible black aggregates)

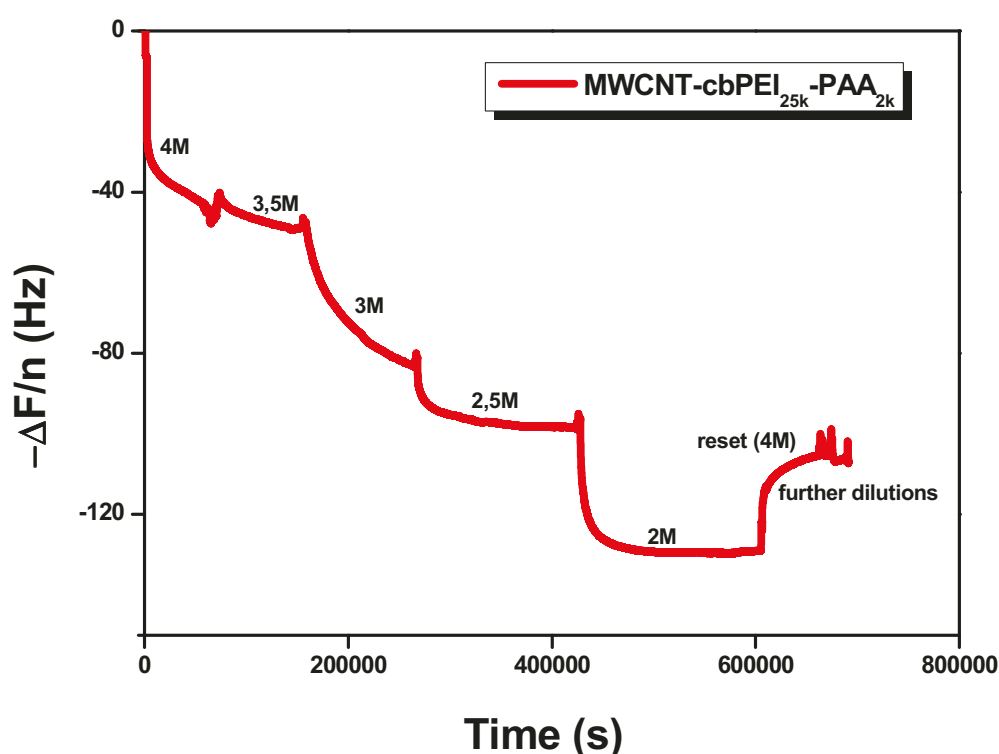


Figure 4. 24: *SgL growth of the MWCNT-cbPEI/PAA_{2k} pair on PSS modified sensor as a function of different salt concentrations monitored by QCM in dynamic conditions.*

Fabrication of functional surfaces

When the 2M dispersion was *reset* back to 4M, the precipitated black materials never dispersed back into the dispersion (on the experiment time scale) suggesting a high stability of the co-assembled structures. The overshoot observed at the *reset* point is certainly caused by the swelling and the removal of loosely bond clusters. The presence of a plateau further indicated the stability of the carbon nanotubes hybrid films.

Furthermore, although the separate stock solutions of *b*PEI and PAA covalently functionalized MWCNTs are highly stable under 4M of NH_4Cl , their mixture under stirring even for 5 min yielded an aggregated dispersion. A result not completely unexpected as we have noticed that CNTs under shearing are subjected easily to aggregation, especially in the presence of impurities as the ones found in our MWCNT. Furthermore, the ion-pair formation via H-bonding interactions between residual $-\text{COOH}$ and $-\text{NH}_2$ groups of their parent material might have lead to aggregation as well. In the future, the SgL growth of oppositely charged CNTs should be performed at different pHs with “pure” CNTs to better understand what is driving here the complexation at an interface.

Silica NPs system

NPs/PEs ($\text{SiO}_2\text{-PAA}_{5k}/\ell\text{PEI}_{2k}$) system

In order to investigate SgL assembly when one of the BBs is highly charged (SiPAA_{5k} is almost fully ionized at neutral pH) and to be consistent with the bulk desalting transition experiment performed in chapter 3, the co-assembly between $\text{SiO}_2\text{-PAA}_{5k}/\ell\text{PEI}$ as a function of I_s was carried out at pH 7 on bare ceria NPs modified sensor. At 4M, a slight decrease in ΔF (or increase in adsorption) was indicative of the adsorption of a SiPAA_{5k} NPs monolayer. A further dilution down to 2.3M has not however shown any efficient growth due to a weak “electrostatic” interaction between weakly protonated $-\text{NH}$ groups of ℓPEI and $-\text{COOH}$ groups of the PAA corona. In agreement with the bulk desalting transition, when I_s was lowered below the critical bulk I_b , spontaneous growth at the interface was triggered via weak inter-molecular H-bonding interactions between anionic silica NPs and cationic ℓPEI PEs. A pretty large increase in ΔF during the rinsing step performed at 1.7M suggested likely the partial desorption of some loosely bound materials from the interface. By resetting the ionic strength back to 4M, this specific system completely dissolved due to weaker

interactions between $\text{SiO}_2\text{-PAA}_5$ and linear PEI chains bearing very few primary amine groups.

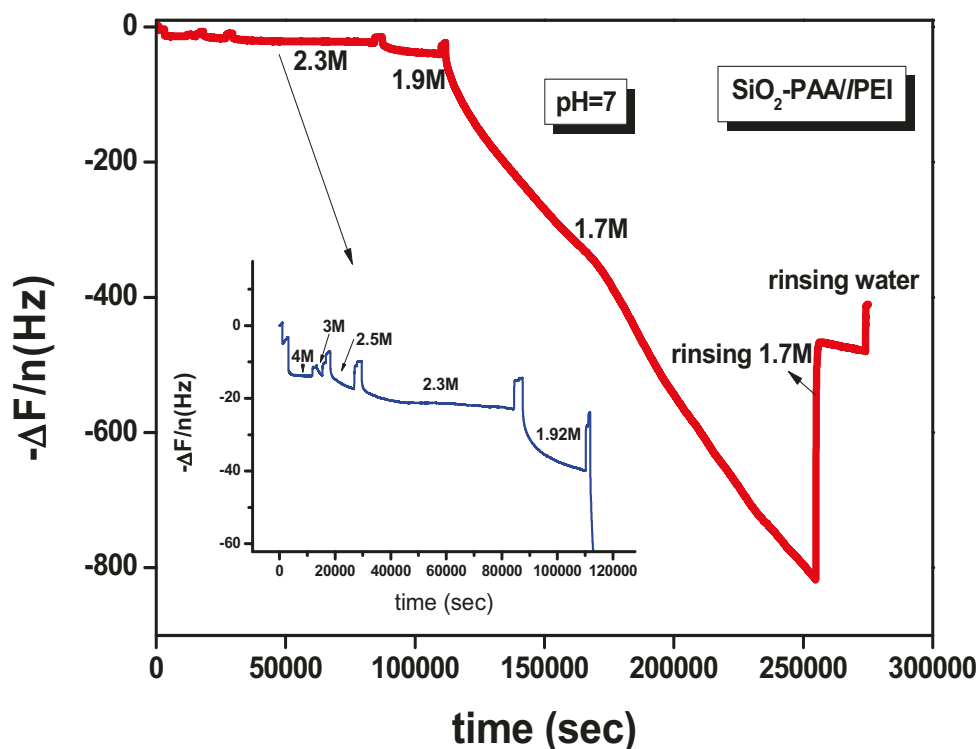


Figure 4.25: *SgL growth of the $\text{SiO}_2\text{-PAA}/\ell\text{PEI}$ sensor as a function of different salt concentrations monitored by QCM in dynamic conditions. Inset is showing a zoom of the region between 4 down to 2.3 M.*

The same experiment was then performed again at a lower pH where the ℓPEI chains are fully charged (secondary amines). The large frequency shift observed in the dormant solution at 4M indicates that anionic silica NPs likely did interact with ℓPEI chains via hydrogen-bonding. Furthermore, free PAA chains are normally protonated at pH 3 below their pKa. Here the presence of SiO_2 NPs shifted likely their pKa from 4.5 down to 3 as shown in chapter 2 via zeta potential measurements. Consequently, anionic silica NPs are slightly negatively charged triggering then some electrostatic complexation with fully protonated ℓPEI chains. The adsorbed amount was indeed found to increase (Figure 4. 26) with the Debye length (decrease of the ionic strength).

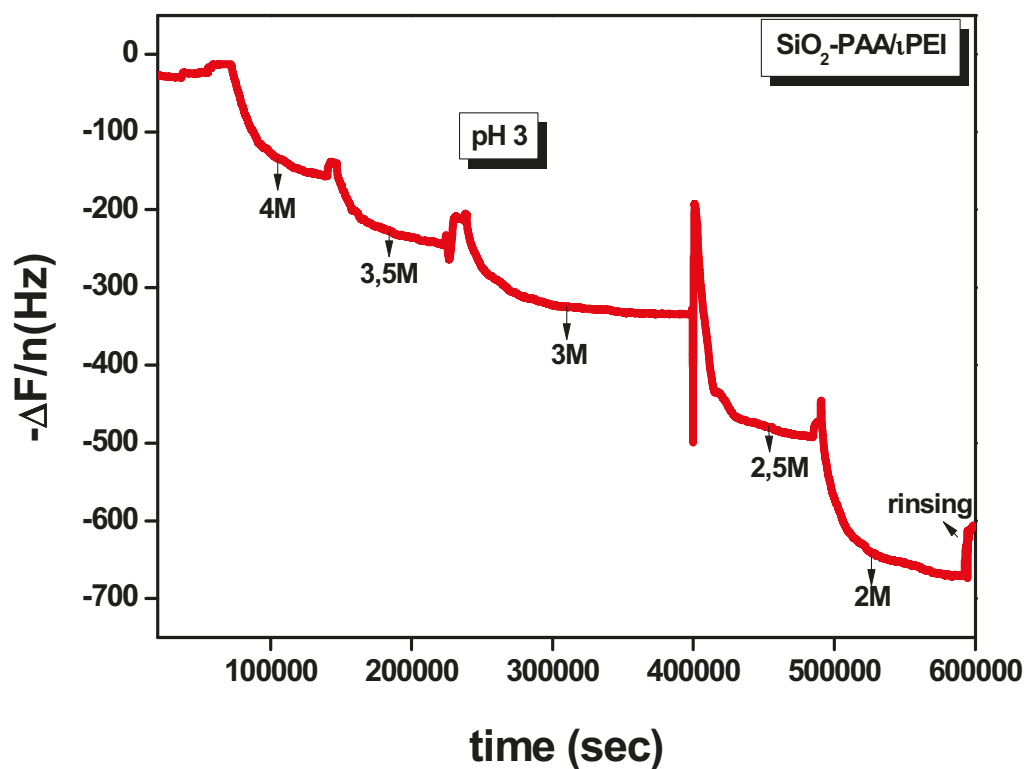


Figure 4. 26: *SgL growth of the SiO₂-PAA/lPEI sensor as a function of different salt concentrations monitored by QCM in dynamic conditions performed at pH=3.*

Conclusions

We have investigated in details in this chapter the growth of hybrid multilayers at a solution/substrate interface made from the complexation of the different oppositely charged pair of BBs developed in chapter 2: CeO₂ and SiO₂ NPs, MWCNTs and weak and strong PEs. Two complementary assembling approaches have been put under scrutiny by a careful monitoring of the growth via QCM experiments performed on bare CeO₂ NP functionalized Q-sensors.

In a first part, the classical “electrostatic” Layer-*by*-Layer (EL*bl*L) sequential adsorption method mostly used in the literature to growth *all*-organic PEs layer was taken here as a benchmark and helped us to generate organic/inorganic thin coatings. Beyond the nature and shape of the inorganic BBs, different key processing parameters were investigated such as pH and ionic strength of the solution and PEs nature. The different growth regimes (exponential vs. linear growth), final adsorbed amounts and volume fractions of inorganic material were shown to depend on the strength of the intermolecular interaction (ionic strength), the nature of functional groups, architecture of the PEs and most critically on the pH (ionisation/protonation state) at which the different sequential adsorptions are performed. Counter intuitively, the assembly pH should be set at a value where at least one of the two interacting “weak” BBs is not charged in order to promote acid-basic interactions more efficient to growth thicker multilayers than the sole electrostatic interaction.

In a second part, we have transferred the *bulk* desalting transition concept to a solution/substrate interface and put forward a new assembly method called Surface grown Layers (SgL). The growth is here triggered at the onset of the bulk transition by fine-tuning the ionic strength (I_s) of the dispersions and through suitable experimental conditions (static vs. dynamic growth). The growth can be stopped by setting back to higher salt concentration and further resumed by a new dilution step. Different key parameters specific to the SgL growth such as charge ratio, physical-chemistry of the bare substrate and nature of the PEs were investigated specifically on the CeO₂-PAA_{2k}/PDDAC system. Below the critical bulk ionic strength I_b , the initial growth rate of the layer was shown to depend on the value of I_s . Relatively “thick” hybrid layers can be fabricated from a reactive solution prepared at charge stoichiometry. Furthermore, thicker films can be developed in *dynamic* conditions where shear forces at play favour a higher (formation and further) adsorption of the complexes.

Fabrication of functional surfaces

Finally, in most situations studied here, the as grown multilayers are very stable and do not disassemble in high ionic strength solution as pure PEs multilayers made via *LbL* do.

These preliminary studies that will be more deeply investigated in the future are quite encouraging and show that the simple and novel SgL approach is a very versatile method able to generate in one-step thick hybrid layers. The complementary use of both SgL and *LbL* growth methods together with very stable BBs opens pathways to generate smart functional surfaces with varying morphology, properties and applications.

References

1. Liu, J., Q. Wang, and X. Fan, *Layer-by-layer self-assembly of TiO₂ sol on wool to improve its anti-ultraviolet and anti-ageing properties*. Journal of Sol-Gel Science and Technology. **62**(3): p. 338-343.
2. Yang, M., Y. Yang, H. Yang, G. Shen, and R. Yu, *Layer-by-layer self-assembled multilayer films of carbon nanotubes and platinum nanoparticles with polyelectrolyte for the fabrication of biosensors*. Biomaterials, 2006. **27**(2): p. 246-255.
3. Cebeci, F.C., Z. Wu, L. Zhai, R.E. Cohen, and M.F. Rubner, *Nanoporosity-Driven Superhydrophilicity: A Means to Create Multifunctional Antifogging Coatings*. Langmuir, 2006. **22**(6): p. 2856-2862.
4. Wood, K.C., J.Q. Boedicker, D.M. Lynn, and P.T. Hammond, *Tunable Drug Release from Hydrolytically Degradable Layer-by-Layer Thin Films*. Langmuir, 2005. **21**(4): p. 1603-1609.
5. Manna, U., S. Bharani, and S. Patil, *Layer-by-Layer Self-Assembly of Modified Hyaluronic Acid/Chitosan Based on Hydrogen Bonding*. Biomacromolecules, 2009. **10**(9): p. 2632-2639.
6. Srivastava, S. and N.A. Kotov, *Composite Layer-by-Layer (LBL) Assembly with Inorganic Nanoparticles and Nanowires*. Accounts of Chemical Research, 2008. **41**(12): p. 1831-1841.
7. Vial, S.p., I. Pastoriza-Santos, J. PÃ©rez-Juste, and L.M. Liz-MarzÃ¡n, *Plasmon Coupling in Layer-by-Layer Assembled Gold Nanorod Films*. Langmuir, 2007. **23**(8): p. 4606-4611.
8. Wang, Y., Z. Tang, P. Podsiadlo, Y. Elkasabi, J. Lahann, and N.A. Kotov, *Mirror-Like Photoconductive Layer-by-Layer Thin Films of Te Nanowires: The Fusion of Semiconductor, Metal, and Insulator Properties*. Advanced Materials, 2006. **18**(4): p. 518-522.
9. Podsiadlo, P., S. Paternel, J.-M. Rouillard, Z. Zhang, J. Lee, J.-W. Lee, E. Gulari, and N.A. Kotov, *Layer-by-Layer Assembly of Nacre-like Nanostructured Composites with Antimicrobial Properties*. Langmuir, 2005. **21**(25): p. 11915-11921.
10. Iler, R.K., *Multilayers of colloidal particles*. Journal of Colloid and Interface Science, 1966. **21**(6): p. 569-594.
11. Decher, G., *Fuzzy Nanoassemblies: Toward Layered Polymeric Multicomposites*. Science, 1997. **277**(5330): p. 1232-1237.
12. Nakashima, T., J. Zhu, M. Qin, S. Ho, and N.A. Kotov, *Polyelectrolyte and carbon nanotube multilayers made from ionic liquid solutions*. Nanoscale. **2**(10): p. 2084-2090.
13. Caruso, F., R.A. Caruso, and H. Mohwald, *Nanoengineering of Inorganic and Hybrid Hollow Spheres by Colloidal Templating*. Science, 1998. **282**(5391): p. 1111-1114.
14. Wang, D., A.L. Rogach, and F. Caruso, *Semiconductor Quantum Dot-Labeled Microsphere Bioconjugates Prepared by Stepwise Self-Assembly*. Nano Letters, 2002. **2**(8): p. 857-861.
15. He, J.-A., R. Valluzzi, K. Yang, T. Dolukhanyan, C. Sung, J. Kumar, S.K. Tripathy, L. Samuelson, L. Balogh, and D.A. Tomalia, *Electrostatic Multilayer Deposition of a Gold-Dendrimer Nanocomposite*. Chemistry of Materials, 1999. **11**(11): p. 3268-3274.
16. Lee, D., M.F. Rubner, and R.E. Cohen, *Formation of Nanoparticle-Loaded Microcapsules Based on Hydrogen-Bonded Multilayers*. Chemistry of Materials, 2005. **17**(5): p. 1099-1105.
17. Bergbreiter, D.E. and K.-S. Liao, *Covalent layer-by-layer assembly-an effective, forgiving way to construct functional robust ultrathin films and nanocomposites*. Soft Matter, 2009. **5**(1): p. 23-28.
18. Kotov, N.A., *Layer-by-layer self-assembly: The contribution of hydrophobic interactions*. Nanostructured Materials, 1999. **12**(5): p. 789-796.
19. Jiang, C., S. Markutsya, and V.V. Tsukruk, *Collective and Individual Plasmon Resonances in Nanoparticle Films Obtained by Spin-Assisted Layer-by-Layer Assembly*. Langmuir, 2003. **20**(3): p. 882-890.
20. Nogueira, G.M., D. Banerjee, R.E. Cohen, and M.F. Rubner, *Spray-Layer-by-Layer Assembly Can More Rapidly Produce Optical-Quality Multistack Heterostructures*. Langmuir. **27**(12): p. 7860-7867.

Fabrication of functional surfaces

21. Fujimoto, K., S. Fujita, B. Ding, and S. Shiratori, *Fabrication of layer-by-layer self-assembly films using roll-to-roll process*. Japanese journal of applied physics, 2005. **44**: p. L126-L128.
22. Elzbieciak, M., M. Kolasinska, and P. Warszynski, *Characteristics of polyelectrolyte multilayers: The effect of polyion charge on thickness and wetting properties*. Colloids and Surfaces A: Physicochemical and Engineering Aspects, 2008. **321**(1-3): p. 258-261.
23. Boddohi, S., C.E. Killingsworth, and M.J. Kipper, *Polyelectrolyte Multilayer Assembly as a Function of pH and Ionic Strength Using the Polysaccharides Chitosan and Heparin*. Biomacromolecules, 2008. **9**(7): p. 2021-2028.
24. Han, L., Z. Mao, H. Wuliyasu, J. Wu, X. Gong, Y. Yang, and C. Gao, *Modulating the Structure and Properties of Poly(sodium 4-styrenesulfonate)/Poly(diallyldimethylammonium chloride) Multilayers with Concentrated Salt Solutions*. Langmuir. **28**(1): p. 193-199.
25. Shim, B.S., P. Podsiadlo, D.G. Lilly, A. Agarwal, J. Lee, Z. Tang, S. Ho, P. Ingle, D. Paterson, W. Lu, and N.A. Kotov, *Nanostructured Thin Films Made by Dewetting Method of Layer-By-Layer Assembly*. Nano Letters, 2007. **7**(11): p. 3266-3273.
26. Alonso, T., J. Irigoyen, J.J. Iturri, I.L. Iarena, and S.E. Moya, *Study of the multilayer assembly and complex formation of poly(diallyldimethylammonium chloride) (PDADMAC) and poly(acrylic acid) (PAA) as a function of pH*. Soft Matter, 2013. **9**(6): p. 1920-1928.
27. Rodahl, M., F. Hook, A. Krozer, P. Brzezinski, and B. Kasemo, *Quartz crystal microbalance setup for frequency and Q-factor measurements in gaseous and liquid environments*. Review of Scientific Instruments, 1995. **66**(7): p. 3924-3930.
28. Vogt, B.D., C.L. Soles, H.-J. Lee, E.K. Lin, and W.-I. Wu, *Moisture Absorption and Absorption Kinetics in Polyelectrolyte Films: Influence of Film Thickness*. Langmuir, 2004. **20**(4): p. 1453-1458.
29. Chapel, J., M. Morvan, A. Rao, and Z. Zong, *Surface modified substrate for article e.g. polyolefin sheet used for vehicle component has layer of nanoscale inorganic oxide particles dispersed on hydrophobic surface of substrate*. 2007, WO2007 126925-A2; WO2007 126925-A3; US2008 124467-A1 - (Rhodia Inc., USA – CNRS).
30. Lee, S.W., B.-S. Kim, S. Chen, Y. Shao-Horn, and P.T. Hammond, *Layer-by-Layer Assembly of All Carbon Nanotube Ultrathin Films for Electrochemical Applications*. Journal of the American Chemical Society, 2008. **131**(2): p. 671-679.
31. Yang, Y.-H., M. Haile, Y.T. Park, F.A. Malek, and J.C. Grunlan, *Super Gas Barrier of All-Polymer Multilayer Thin Films*. Macromolecules, 2011. **44**(6): p. 1450-1459.
32. Porcel, C., P. Lavallo, G. Decher, B. Senger, J.C. Voegel, and P. Schaaf, *Influence of the Polyelectrolyte Molecular Weight on Exponentially Growing Multilayer Films in the Linear Regime*. Langmuir, 2007. **23**(4): p. 1898-1904.
33. Podsiadlo, P., M. Michel, J. Lee, E. Verploegen, N. Wong Shi Kam, V. Ball, J. Lee, Y. Qi, A.J. Hart, P.T. Hammond, and N.A. Kotov, *Exponential Growth of LBL Films with Incorporated Inorganic Sheets*. Nano Letters, 2008. **8**(6): p. 1762-1770.
34. Schonhoff, M., *Layered polyelectrolyte complexes: physics of formation and molecular properties*. Journal of Physics: Condensed Matter, 2003. **15**(49): p. R1781.
35. Dubas, S.T. and J.B. Schlenoff, *Polyelectrolyte Multilayers Containing a Weak Polyacid: Construction and Deconstruction*. Macromolecules, 2001. **34**(11): p. 3736-3740.
36. Choi, I., R. Suntivich, F.A. Plamper, C.V. Synatschke, A.H.E. Müller, and V.V. Tsukruk, *pH-Controlled Exponential and Linear Growing Modes of Layer-by-Layer Assemblies of Star Polyelectrolytes*. Journal of the American Chemical Society, 2011. **133**(24): p. 9592-9606.
37. Laugel, N., C. Betscha, M. Winterhalter, J.-C. Voegel, P. Schaaf, and V. Ball, *Relationship between the Growth Regime of Polyelectrolyte Multilayers and the Polyanion/Polycation Complexation Enthalpy*. The Journal of Physical Chemistry B, 2006. **110**(39): p. 19443-19449.
38. DeRocher, J.P., P. Mao, J.Y. Kim, J. Han, M.F. Rubner, and R.E. Cohen, *Layer-by-Layer Deposition of All-Nanoparticle Multilayers in Confined Geometries*. ACS Applied Materials & Interfaces. **4**(1): p. 391-396.

Fabrication of functional surfaces

39. Lee, D., M.F. Rubner, and R.E. Cohen, *All-Nanoparticle Thin-Film Coatings*. Nano Letters, 2006. **6**(10): p. 2305-2312.
40. Ji, P., J. Zhang, F. Chen, and M. Anpo, *Study of adsorption and degradation of acid orange 7 on the surface of CeO₂ under visible light irradiation*. Applied Catalysis B: Environmental, 2009. **85**(3-4): p. 148-154.
41. Babu, S., A. Velez, K. Wozniak, J. Szydłowska, and S. Seal, *Electron paramagnetic study on radical scavenging properties of ceria nanoparticles*. Chemical Physics Letters, 2007. **442**(4-6): p. 405-408.
42. Olek, M., J. Ostrander, S. Jurga, H. M \ddot{a} hwald, N. Kotov, K. Kempa, and M. Giersig, *Layer-by-Layer Assembled Composites from Multiwall Carbon Nanotubes with Different Morphologies*. Nano Letters, 2004. **4**(10): p. 1889-1895.
43. Mamedov, A.A., N.A. Kotov, M. Prato, D.M. Guldi, J.P. Wicksted, and A. Hirsch, *Molecular design of strong single-wall carbon nanotube/polyelectrolyte multilayer composites*. Nat Mater, 2002. **1**(3): p. 190-194.
44. Liao, K.-S., A. Wan, J.D. Batteas, and D.E. Bergbreiter, *Superhydrophobic Surfaces Formed Using Layer-by-Layer Self-Assembly with Aminated Multiwall Carbon Nanotubes*. Langmuir, 2008. **24**(8): p. 4245-4253.
45. Paloniemi, H., M. Lukkarinen, T. \ddot{A} ritalo, S. Areva, J. Leiro, M. Heinonen, K. Haapakka, and J. Lukkari, *Layer-by-Layer Electrostatic Self-Assembly of Single-Wall Carbon Nanotube Polyelectrolytes*. Langmuir, 2005. **22**(1): p. 74-83.

PART - III

Chapter 5: Toward Applications

Abstract

We highlight through preliminary experiments the combined potential of *LbL* and *SgL* growth methods to impart functionality onto representative and well encountered substrates nowadays in various applications. Aluminium, polymer and glass substrates were tentatively turned anti-corrosive, conductive and superhydrophilic/phobic respectively. Superhydrophilic/phobic glass surfaces (silicon wafer) were generated from oppositely charged nanoceria particles through *SgL* approach. Aluminum surfaces were turned anti-corrosive with the help of NH_4Cl salt which enhance ceria NPs adsorption and their ability to form a protective layer. Finally, transparent and conductive layers were developed onto polymer (PET) surfaces through the *LbL* assembly of short ligands functionalized MWCNTs.

Introduction

Recent developments in the surface science and coating technology offer plethora of applications in numerous fields ^[1-3]. Especially, multifunctional surface coatings provide unique surface properties such as corrosion inhibition, electrical (conductivity) and enhanced wettability and adhesion (antireflective coatings) to the substrates ^[4-7]. Automobile industries demand superhydrophobic surfaces to improve the self cleaning property of the glass windows. Similarly several metal industries require anti-corrosive coatings to protect as well as recover the metal at the end of device life. However, the fabrication of such functional coatings often involves the conditions and materials that are harmful to the environment. For instance anti-corrosive inorganic coatings based on the sol-gel technique require organic solvents and high processing temperature^[8]. The use of organic solvents increases the amount of volatile organic compounds (VOC) in the atmosphere which is not only harmful to the environment also injurious to health^[8]. This forced the industries to highly demand for the atmospheric condition and environmentally friendly water-borne coatings. Recent research works show that the hybrid organic-inorganic sol-gel functional coatings received tremendous interest as it does not require any harmful conditions^[9]. Furthermore the organic polymers increase the flexibility while inorganic nanoparticles enhance the adhesion with the surface via specific chemical and/or physical interactions.

Hybrid functional coatings can be developed on the desired substrates by conventional LbL approach^[10], where the oppositely charged organic macromolecules and inorganic NPs are alternatively deposited. But in some cases the high performance of surface modification depends on the coating thickness. Some reports are showing that the anti-corrosive performance significantly increases when the film thickness increases^[11, 12]. Cebeci *et al.* showed that the functional coating requires critical thickness to exhibit antifogging property^[6]. Although the critical thickness can be attained by LbL approach, it involves numerous deposition steps which are time consuming and tedious sometimes as mentioned in the chapter 4. Whereas the water-borne SgL (Surface grown hybrid functional layers) approach discussed in chapter 4, based on the salt triggered co-assembly of oppositely charged components could be a promising way to generate relatively thick hybrid functional coatings on substrates in a single step. Encouraging results seen in the previous chapter pushed us to investigate some applications. Preliminary experiments were performed on aluminium, polyethyleneterephthalate (PET) and silicon wafers substrates either via LbL or

Applications

SgL to impart anti-corrosive, conductive and wetting functionalities respectively from ceria NPs and MWCNTs.

As mentioned in introduction, this PhD work is made in the framework of the SUGHAR project gathering 2 academic laboratories and 2 industrials partners, Rhodia and ALCAN. The latter is the aluminium manufacturer and interested in anti-corrosive coatings. Corrosion is indeed one of the most important environmental impacts in our modern society that have to be prevented. In recent years, large body of works have been performed for the corrosion protection of metal substrates. Several industries have developed various coating methods to protect the metal from corrosion but failed to protect them efficiently^[8]. This is due to the fact that the anti-corrosive coatings depends on various factors such as the type and properties of substrate, pre-treatment of the substrate, incomplete understanding of physicochemical interactions between the coating materials and substrates, coating thickness and impact of external parameters such as types of solvents, pH and salt.

Furthermore, aluminium and its alloys are being increasingly used in the automobile and aerospace industries because of its high tensile strength and high strength to weight ratio. But the low corrosion resistance limits their applications. Inorganic salts of chromium have been widely used in the corrosion resistance because of their ability to passivate aluminium alloys^[13]. But chromates based coatings were banned for environmental reasons due to their high toxicity and carcinogenic effects^[14]. Further attempts have shown that cerium salts/NPs are the better alternatives to chromates. Hydrated cerium(III)oxide film fairly prevented the zinc electrode from corrosion^[15]. Hamdy *et al.*, showed that the ceria solution prepared by sol-gel method improved the corrosion resistance of aluminium alloy against 3.5% NaCl. The XRD analysis showed that the cerium was present as a very thin film^[16]. In the same vein, Schem^[17] and Yue *et al.*,^[18] have protected aluminium alloy using ceria based sol-gel coatings. But all these reports imply that in addition to the corrosion inhibitive property of ceria, a “thicker” coating is necessary for prolonged performance. Inspired from the previous works, the long term goal is here to generate relatively thick hybrid functional layers from either CeO₂-PAA/PDDAC and oppositely charged ceria NPs (CeO₂-PAA/CeO₂-bPEI) systems using the SgL. In a first step, we used LbL as a benchmark and started preliminary experiments dealing with the adsorption of anionic ceria on pre-treated alumina surface was performed and will be discussed in the forthcoming sections.

Applications

On a different perspective, on the basis of their unique electronic and thermal conducting properties, CNTs are good candidates to generate transparent conductive thin films and electrodes. In recent years, transparent conductive films have attracted tremendous interest because of their versatile applications in photovoltaic devices, displays, video recorders, organic light emitting devices (OLEDs), and organic solar cells^[19-22]. In order to fabricate such transparent and conductive film, the CNTs must be finely dispersed in the solvent media which can be achieved by surface modifications, otherwise forms bundles at the surface due to strong van der Waals attraction. In addition, the film fabrication require careful control on variety of factors such as the balance between the transparency and sheet resistance, controlled assembly and high loading of nanotubes and uniform coatings on the substrate.

In 2005, Zhang *et al.*, produced transparent MWCNTs thin films on PET surface and had an efficiency of ~2%^[23]. Yu *et al.*, prepared transparent thin films by LbL using oxidized SWCNTs. The resultant film worked both as acoustic actuators and sensors^[24]. In the same line, Lee *et al.*, fabricated all-MWCNTs ultrathin multilayer films on a glass substrate via LbL using oxidized and aminated MWCNTs. The self-assembled thin film showed higher electronic conductivity after cross-linking by heat treatment^[25]. In a similar way, transparent multilayer thin film fabrication was successfully carried out between ester modified MWCNTs and PAH by LbL assembly. The fabricated film showed the resistivity of 10k Ω with 70% transparency^[26]. As a first step toward conductive films from SgL approach, we have investigated the LbL assembly short ligands functionalized (MWCNT-COOH and MWCNT-NH₂) and wrapped (MWCNT-wbPEI/MWCNT-wPAA) CNT systems, on a hydrophobic and non reactive PET surface. In the near future, we plan to perform SgL assemblies of covalently functionalised MWCNTs (MWCNT-cbPEI/PAA and MWCNT-cbPEI/MWCNT-cPAA) on PET substrates as well to compare both approaches.

Wettability has recently attracted much attention. Depending upon the appropriate texturing and surface energy of the substrates, characteristics of wetting ranges from superhydrophilic to superhydrophobic. Superhydrophilic coatings with anti-fogging properties are highly used in daily life that include swimming goggles, eye glasses and in periscopes etc^[27]. Large numbers of research groups across the world are now working on the fabrication of such superhydrophilic substrates. Lai *et al.*^[28], fabricated TiO₂-based nanobelt thin film via elctrophoretic deposition method. The as-prepared film after annealing at 500°C, exhibited a transparent superhydrophilic coating with rapid water spreading and anti-

Applications

fogging feature. Zhang *et al.*, prepared anti-reflection and anti-fogging superhydrophilic coatings via LbL deposition of SiO₂ NPs and PDDAC^[27]. Li *et al.*,^[29] fabricated raspberry and mulberry like hierarchically structured coating using two different sizes of SiO₂ NPs via LbL assembly. Such hierarchically structured coatings presented superhydrophilic and anti-fogging properties.

Finally, self cleaning superhydrophobic surfaces show great importance in our day-to-day life. Silica nanoparticles (SiO₂ NPs) were extensively used in this aspect due to its cheap cost. Ling *et al.*, prepared transparent superhydrophobic film with a contact angle (> 150°) via dip coating method by simply dipping the APTES modified glass substrate into the SiO₂ NPs solution followed by chemical vapour deposition of fluorosilane compound^[30]. Zhai *et al.*,^[31] mimicked the lotus-leaf texture by developing a honeycomb (porous) PAH/PAA PEs multilayer, overcoated with SiO₂ NPs followed by semifluorinated silane treatment. Shiratori *et al.*, fabricated PE multilayer containing SiO₂ NPs. The film was heated to high temperature to remove the PEs and to create rough texture that exhibit the superhydrophobic behaviour^[32]. Recently, it has been disclosed that cerium based materials offer both corrosive resistance and superhydrophobic character to the substrates^[33]. Based on these observations, we have developed superhydrophilic/phobic surface from the SgL assembled oppositely charged ceria nanoparticles primarily on silicon wafers but later this can be extended on various metal alloys substrates.

Experimental section

Materials

Substrates

Aluminium alloy substrates were received from ALCAN in a form of refined spool (4N) (already degreased with alkaline washing and further annealed). This type of aluminium foil has very few contaminants or impurities such as carbon, calcium and magnesium oxide. Its surface was laminated and ridges were therefore present on the surface as represented in Figure 5.5a. Other substrates were Poly (ethylene terephthalate) PET and polypropylene sheets (250 μm) and silicon wafers.

Functional BBs

Developed hybrid BBs from chapter 2 were used such as: PAA and *b*PEI functionalized ceria NPs (CeO_2 -PAA and CeO_2 -*b*PEI), short ligands functionalized (MWCNTCOOH and MWCNTNH₂) and wrapped MWCNTs (MWCNT-wPAA and MWCNT-wPEI). PAA Mw \sim 2000 g/mol, and 1H,1H,2H,2H-perfluorooctyltriethoxysilane was purchased from Sigma Aldrich.

Acids, bases and salts

KOH, HCl, HNO₃ and salts such as NH₄Cl, NaNO₃ were received and used without further purification.

Methods

Ceria system

Wetting properties

Pre-treatment of silicon wafer - Silicon wafers were sonicated with ethanol and water for 10 min each and dried with N₂ and then placed under UVO lamp for 20 min.

Applications

Preparation of hybrid films - Dormant solution of (CeO₂-PAA/CeO₂-bPEI) was prepared by mixing an equal volume of individual components prepared separately at 0.05 wt% and 4M of NH₄Cl. DI water was then added drop-by-drop under continuous stirring to obtain an “excited” 2.5M solution into which UV-treated wafers were immersed horizontally for 2 hrs. Substrate with a deposited SgL film were then rinsed with water and dried under N₂. Water contact angles were measured with a Tracker Drop tensiometer (Teclis, France) equipped with a CCD camera via a sessile drop method coupled with a drop shape analyzer. Advancing contact angle as the “static” value was obtained immediately after the drop deposition whereas the receding contact angle was determined as the drop evaporate until reaching a plateau, the signature of the *natural* receding contact angle. In order to maximize the hydrophobicity of the hybrid substrates, they were subsequently functionalized by chemical vapour deposition of 1H,1H,2H,2H-perfluorooctyltriethoxysilane for 3 hrs followed by heating at 95°C for 2 hrs and then re-subjected to contact angle measurements.

Anti-corrosive properties

Different types of surface pre-treatments of aluminium alloy- In common, all metal surfaces contain many impurities such as oxides, dust, grease, oil and salts. Those impurities must be removed by pre-treatments to significantly enhance the adhesion with coating materials. Pre-treatment procedures help in general to increase the surface area of substrate. In addition, they strengthen the interfacial interaction between the coating materials and metal surface. In agreement with Hamdy *et al.*,^[16], three different types of pre-treatment were therefore performed on aluminium substrates as listed below to tune and improve the adhesion with anionic ceria NPs.

Type I: As received aluminium alloys were degreased via sonication in acetone for 15 min followed by a washing step with DI water and finally dried under N₂ (hereafter termed as “degreased”).

Type II: “degreased” substrates were subjected to an etching solution of 0.01M KOH for 10 min followed by a thorough rinsing with DI water.

Type III: “degreased” substrates were boiled with DI water for 1 hr to thicken their oxide layer.

Applications

Coating of pre-treated aluminium substrate with different components – All three pre-treated substrate types were dipped for 2 days at room temperature into different separate solutions containing pure DI water, 0.1M NH_4Cl , 0.3 wt% PAA, 0.1 wt% CeO_2 -PAA and 0.1 wt% CeO_2 -PAA + 0.1M NH_4Cl . Due to lack of time, only interfacial interactions with aluminium type I substrates were investigated deeply (optical images of type II & III substrates were shown in appendix). In a separate experiment, a “degreased” type I substrate was immersed into a 0.1 wt% (CeO_2 -PAA+0.1M NaNO_3) solution to study the influence of the salt nature in the corrosion resistance. After 2 days, all substrates were removed, rinsed with DI water and dried under a nitrogen flow before performing AFM characterizations.

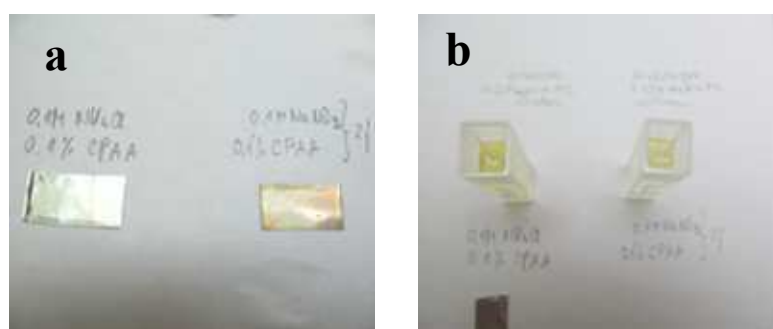


Figure 5.1: Optical images of CeO_2 -PAA NPs type I aluminium substrates (a) after immersion in a solution containing either NH_4Cl or NaNO_3 salt (b).

As can be seen in Figure 5.1a, after removal of the aluminium substrate, the 0.1 wt% CeO_2 -PAA_{2k} solution prepared with 0.1M NH_4Cl remained transparent with an intense yellow colour, whereas a slight yellow colour was noticed in the case of 0.1M NaNO_3 solution. Furthermore, the Al substrate treated with CeO_2 -PAA_{2k}+ NH_4Cl formed a thin homogeneous yellowish layer. In the case of the NaNO_3 treatment, brownish settlement was produced at the surface of the substrate, as seen in Figure 5.1b. Both solutions were characterized by UV-Vis spectroscopy before and after being in contact with Al substrates. Results are discussed further down. A comparison was made between AFM images of the Al substrates prepared from 0.1 wt% CeO_2 -PAA+0.1M NH_4Cl and 0.1 wt% CeO_2 -PAA+0.1M NaNO_3 . In addition, zeta potential measurements were carried out on the “degreased” aluminium substrate close to neutral pH with 10mM NaNO_3 (experiment performed with 10mM NaCl is shown in appendix) to better understand the interaction(s) taking place with the coating material. Finally, a general method to determine the amount of ceria NPs from any composite layer was put forward at the end.

Carbon nanotubes system

Cleaning of PET substrate

In order to achieve transparent and flexible conductive surfaces, a PET sheet was chosen and subsequently cleaned with water to remove any dust. Unfortunately, as many polymer, PET is a hydrophobic and non reactive substrate. In order to introduce stable cationic charges on its surface, it was dipped (vertically) into a 1 wt% bare CeO₂ NPs solution (pH ~ 1.5) for 10 min followed by a rinsing with a nitric acid solution at pH ~ 1.5 to remove loosely bound NPs. Very small water contact angles were measured on the modified PET ($\theta_a < 20^\circ$) suggesting the presence of hydrophilic CeO₂ NPs.

Layer-by-Layer self assembly on PET substrate

The positively charged CeO₂ modified PET substrate was immersed into a negatively charged MWCNT-COOH (0.03 wt% pH ~ 3) dispersion for 20 min rinsed with water (same pH) and dried under nitrogen. The substrate was then immersed into oppositely charged MWCNT-NH₂ (0.03 wt% pH ~ 3) dispersion for 20 min, rinsed and dried. This step was repeated to get 3 bilayers. In a similar way the LbL assembly of wrapped CNTs was carried out for the (MWCNT-wPAA/MWCNT-wPEI)₃ pair on a PET substrate (3 indicates the number of bilayers).

Conductivity measurements

To fabricate a conductive surface, the adsorbed conductive materials must reach percolation or in other words they must create a connectivity network on the substrate to conduct the electrons. MWCNTs better fit for this criterion, because of their low percolation threshold induced by their high aspect ratio. Equation 1 shows the relation between the percolation threshold and aspect ratio.

$$p_c \approx \frac{\frac{\pi L}{d^3}}{\pi + 4 \frac{L}{d} + \left(\frac{L}{d}\right)^2 (\sin(\gamma))} \quad (1)$$

where p = percolation threshold, L/d = aspect ratio, γ = angle between 2 tubes.

Applications

Resistivity was measured on the LbL modified transparent PET films as a function of number of bilayers by the following protocol. Two parallel slabs of silver lacquer (1mm width 5 mm length (L)) were applied on the PET film surface separated by a distance (D) of 5mm as shown in Figure 5. 2. The silver lacquer was allowed to dry for 1day. The resistivity was then measured by applying a DC voltage between the two electrodes. The upper limit of the device is 100mW.

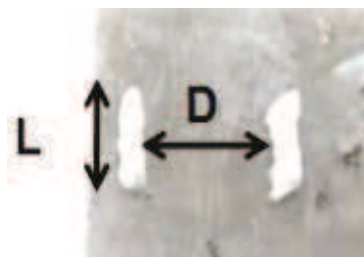


Figure 5. 2: Deposition of two parallel slab of silver lacquer on a PET substrate previously covered with a (MWCNT-PAA/MWCNT-wPEI)₃ multilayer.

The 2-point conductivity was determined from resistivity by the following equation 2,

$$\rho = R \frac{L}{D} \quad \sigma = \frac{1}{\rho} \quad (2)$$

Where σ = conductivity and ρ = sheet resistivity ($\Omega.\square$)

Results & discussions

Ceria system

Wetting properties

The hybrid layers fabricated from oppositely charged nanoparticles based on the SgL approach exhibited superhydrophilic behaviour ($\theta_a < 5^\circ$) with a fast spreading of water droplets due to the combined effect of hydrophilic BBs (wetting) and high porosity (wicking) of the SgL layer^[6]. Deposited on transparent surfaces this functional layer can generate an anti-fogging behaviour where generated fog droplets for example do not retain their shape for very long and flatten out into the surface in fractions of a second^[34]. The use of CeO₂ NPs instead of regular SiO₂ NPs can offer beyond the sole antifogging (or fouling) property some anti-UV action, very useful for plastic surfaces known to degrade quickly under UV light.

Opposite to superhydrophilicity, superhydrophobicity is sought in many high-tech applications as well. Prior to a silane treatment, this superhydrophilic layer was subjected to calcination at 500°C for 2h to burn out all the organic content and inducing thereby a rougher inorganic surface. The layer was then modified with perfluorooctyltriethoxysilane vapours for 3 hrs followed by 2h heating at 95°C to chemically tether fluorosilanes onto the CeO₂ NPs surface (and remove unreacted ones). The layer turned out much more hydrophobic with contact angles (θ_a) between 135° and 138°^[31] beyond the chemical low energy efficiency of perfluorosilane (a self-assembled monolayer of such type of silanes gives a $\theta_a \sim 110^\circ$). Superhydrophobicity with $\theta_a > 150^\circ$ and low contact hysteresis (Cassie state) is however not completely reached here likely because one needs a second length scale roughness beyond the one given by the CeO₂ NP clusters. In the near future, we will add in the *dormant solution* a third component, stable SiO₂ NPs with diameter above 100 nm to attain a complete superhydrophobic behaviour.

These very preliminary experiments are encouraging and show that SgL approach can be an easy and efficient method to control wetting and derivatives properties of substrates through surface chemistry and texturation.

Anti-corrosive properties

Zeta potential of aluminium substrate

Figure 5. 3 shows streaming potential measurements carried out on “degreased” aluminium substrates at pH 6 with 10mM NaNO₃. The final zeta potential obtained from the slope (see chapter 0) is an average of three values. The points on the slope however were varying throughout the time scale of the experiment (1 hr). This Suggests that the added NaNO₃ salt might have interacted with the Al substrate through the formation of aluminium nitrate salts.

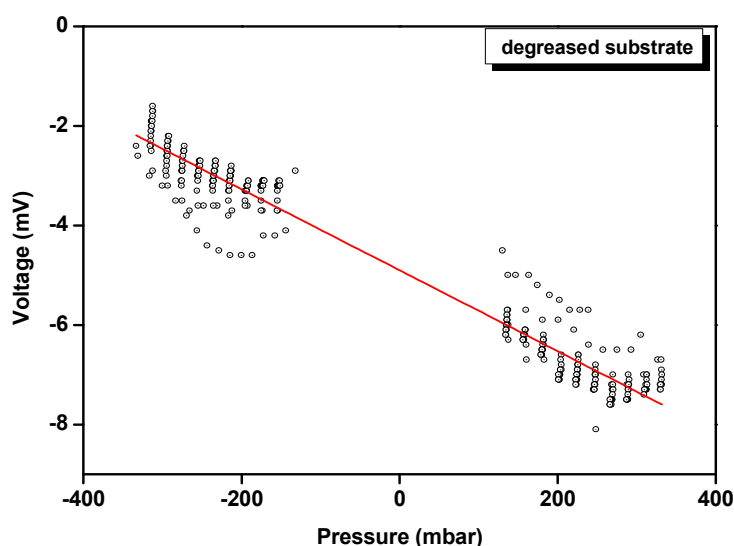


Figure 5. 3: *Generated potential difference ΔV as a function of the mechanical pressure difference ΔP driving the liquid flow on a degreased substrate at pH 6 with 10mM NaNO₃.*

The negative zeta potential $\zeta \sim -12.8 \pm 2$ mV found at pH 6/10mM NaNO₃ is indicative of the presence of hydroxyl ions (OH⁻) on the metallic surface (OH⁻ ion formation takes place spontaneously when Al substrate is in contact with H₂O). The drop of the potential with pH ($\zeta \sim -6.7$ mV at pH 3 for example) indicates a slight protonation of OH⁻ ions.

Corrosion resistivity via material coatings

Figure 5.4 shows optical images of type I substrates after interaction with different solutions. Picture a) shows the result of a water treatment for 2 days that deposited a “white thick flaky” layer on the degreased substrate while leaving the solution opaque, indicating the formation and deposition of aluminium hydroxide.

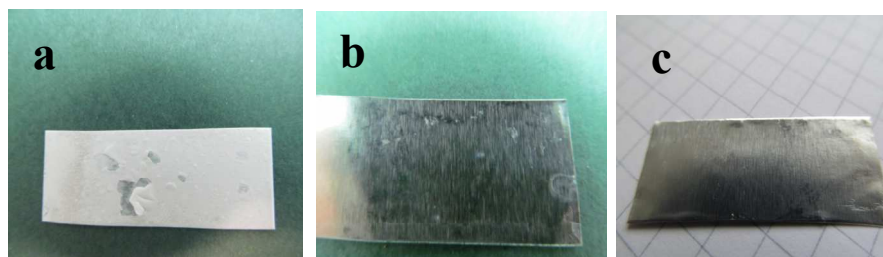


Figure 5.4: Optical images of degreased Al substrates after immersion in a) water, b) 0.1M NH_4Cl solution, and c) 0.1 % PAA solution (pH 3)

“White pitted corrosion” (b) was observed with a 0.1M NH_4Cl solution treatment, as chloride ions are well known to be aggressive towards aluminium alloys (“pitting” refers to extreme localized corrosion or blistering that creates small holes on the metal)^[8]. Due to a good adhesion and film forming property via H-bonding interaction between the COOH of PAA and -OH of Al substrate, a smooth and fine (fewer pits) surface was observed with a 0.3% PAA solution as depicted in the picture (c) of Figure 5.4.

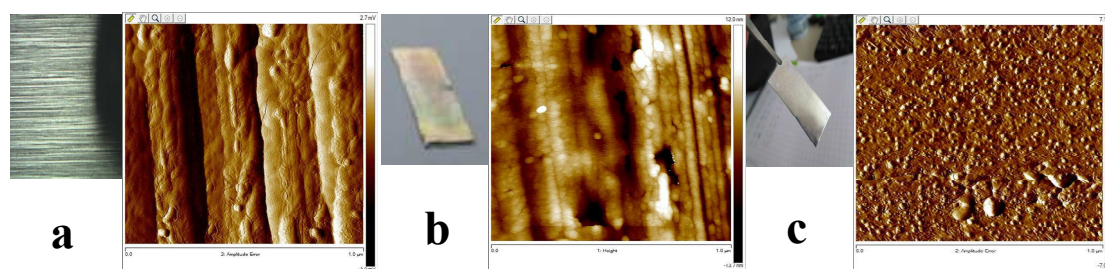


Figure 5. 5: AFM images of as-received Al alloy foil (a), type I degreased substrate with $\text{CeO}_2\text{-PAA}_{2k}$ layer (b) and $\text{CeO}_2\text{-PAA}_{2k}$ layer in the presence of NH_4Cl [0.1M].

Applications

Figure 5. 5b shows an optical image of the Al substrate immersed into a 0.1 wt% CeO₂-PAA_{2k} (pH ~ 7.8, ζ = -35mV) solution, giving rise to an iridescent layer. The reason behind this is not known at this stage. Furthermore, AFM analyses performed have shown that the CeO₂ NPs did not adsorb on the Al surface likely due to the repulsion between both negatively charged material at that pH (substrate and NPs).

Figure 5. 5c represents the same Al substrate immersed into a 0.1 wt% CeO₂-PAA_{2k} solution with 0.1M NH₄Cl (pH ~ 6.8). The smooth and homogeneous yellowish layer obtained without any visible pits suggests the presence of Ce⁴⁺ ions (a species well known to protect Al alloy from corrosion). This observation is rather unexpected, because chloride salts are known to enhance the “pitting corrosion” at metallic surfaces. Here, chloride salts (NH₄Cl) help the adsorption of CeO₂-PAA_{2k} NPs and do not seem to damage the Al surface at all as shown in Figure 5. 5c. This suggests that the coating with 0.1 wt% CeO₂-PAA+0.1M NH₄Cl might provide some “good corrosion resistance” to aluminium substrates. Electrochemical studies must of course be performed to confirm the corrosion inhibition activity.

The exact role of salt is uncertain but a possible mechanism is as follows. First of all, the presence of 0.1 M of salt decreases both the inter NPs and NPs/substrate electrostatic repulsion via the decrease of the Debye screening length favouring then a denser NP adsorption. Furthermore, in agreement with many literature reports dealing with aluminium alloy, anode dissolution and cathode depolarization (oxygen reduction) by water and dissolved oxygen occur as follows^[18].

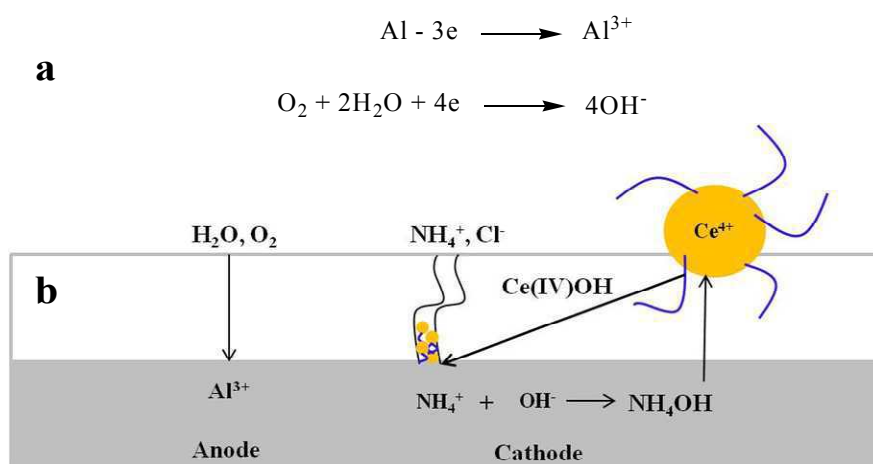


Figure 5. 6: a) Anodic oxidation and cathodic reduction of metal substrate and b) schematic representation of mechanism behind corrosion inhibition.

Applications

Figure 5. 6 suggests that hydroxyl ions (OH^-) produced by the cathodic reaction are likely neutralized by the electrolyte NH_4^+ cations (NH_4^+Cl^-)^[8]. As a result, alkalinity increases due to the formation of NH_4OH (weak base). This local pH increase is known to induce the interaction between $-\text{OH}$ ions at the Al-substrate and oxygen atoms of nano ceria likely via H-bonding. This specific interaction contributes to the formation of insoluble cerium (IV) hydroxide (Ce^{4+}) (insolubility in water is the main feature of cerium IV hydroxide) which precipitates and subsequently deactivate cathodic sites preventing then the corrosion rate as reported by Schem *et al.*,^[17]. It is important to note here that the cathodic Ce^{4+} hydroxide is mainly responsible for the corrosion inhibition of aluminium alloys. Whereas there are some reports where Ce^{3+} ions performed the anticorrosive action.

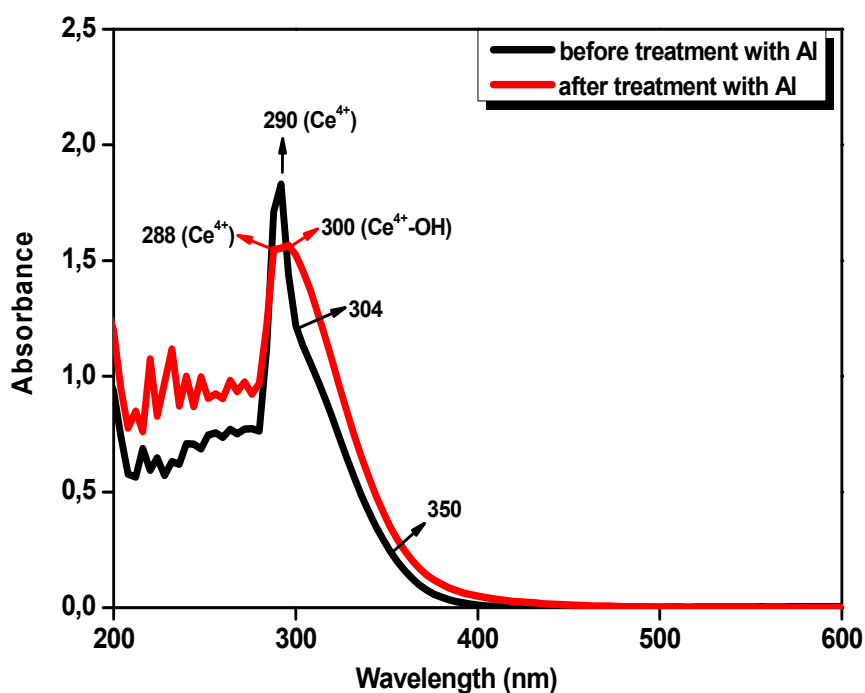


Figure 5.7: UV-Vis spectra of $\text{CeO}_2\text{-PAA}_{2k}$ dispersion containing 0.1 M NH_4Cl before (black) and after (red) immersion of an Al substrate.

The solution which was in contact with the Al-substrate appeared as intense yellow due to the auxochromic effect of $-\text{OH}^-$ ions. To cross check this point, after removal of the substrate, the solution was subjected to UV-Vis and compared with the as-prepared salted $\text{CeO}_2\text{-PAA}_{2k}$ solution. The peaks present at 290 nm in Figure 5.7 are attributed to Ce^{4+} state^[35]. For the pristine dispersion, a secondary peak (band) with a lower intensity between

Applications

304 nm and 350 nm corresponds probably to charge transfer between Ce^{4+} and H_2O . Whereas in the case of the NPs dispersion that has been in contact with the Al substrate, an increase in intensity of the secondary peak suggests rather a charge transfer between Ce^{4+} ions and auxochromic $-\text{OH}$ ions (produced from Al substrate by the added salt) through H-bonding.

This UV-Vis experiment evidenced that Ce(IV) hydroxide was formed at high pH when in contact with Al substrate acting then as a cathodic inhibitor. Cathodically produced $-\text{OH}$ at Al substrates together with added salt in the presence of ceria NPs play an important role in the corrosion resistance of aluminium alloy. Electrochemical studies of the anti-corrosive action of ceria NPs have to be undertaken in the future to get a better understanding of the exact mechanism at play here.

Furthermore, the PAA chains wrapping the bare CeO_2 NPs might have desorbed due to the local pH increase followed by a re-adsorption on uncovered Al spots due to their tendency to form H-bonding with metal surfaces. Decreasing then the porosity of the layers and preventing the oxygen diffusion to the metal surface.

The AFM image in Figure 5. 5c shows that the NPs distribution is not completely homogeneous. The homogeneity depends on the inherent defect sites and microstructure of the substrate. But as reported in the literature, smoothness and homogeneity can be enhanced via etching followed by an oxide thickening of the substrate^[16].

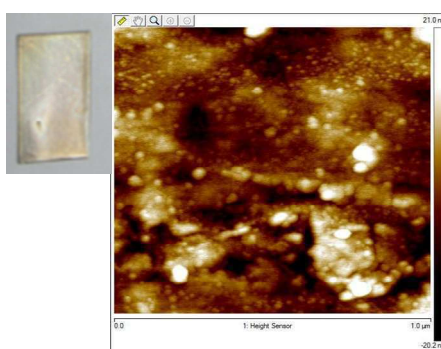


Figure 5. 8: AFM image of type I substrate treated with $\text{CeO}_2\text{-PAA}_{2k}$ with 0.1M NaNO_3 .

Applications

The AFM image seen in Figure 5. 8 showed that very few $\text{CeO}_2\text{-PAA}_{2k}$ NPs were adsorbed onto the Al substrate in the presence of 0.1M NaNO_3 . This peculiar result is certainly due the strong basicity of NaOH (formed by the combination of $-\text{OH}$ produced by the oxygen reduction with Na^+ cation of electrolyte) weakening the H-bonding interaction between hydroxyl ions and ceria NPs and thereby preventing the adhesion of the coating material (cathodic delamination)^[12]. As a result ceria NPs interact with nitrate anions forming then cerium nitrate as suggested by the brown precipitate seen at the surface of the substrate. No considerable difference is noticed in the UV-Vis spectra of the solutions before and after treatment with Al-substrate as precipitated cerium nitrates were excluded from the solution during the UV-Vis characterization (Figure 5.9).

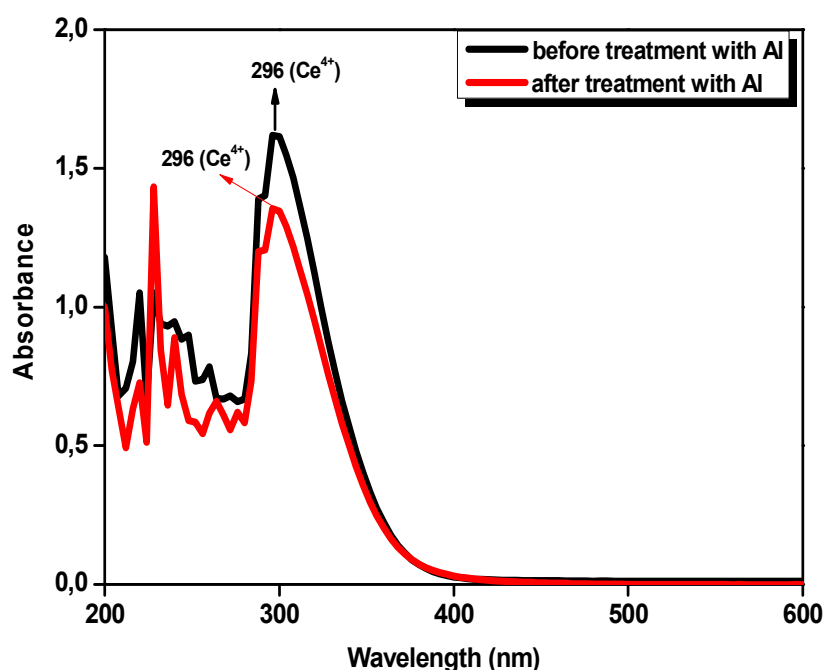


Figure 5.9: UV-Vis spectra of $\text{CeO}_2\text{-PAA}_{2k}$ containing 0.1 M NaNO_3 before (black) after (red) immersion of an Al substrate.

In parallel, LbL (4 bilayers) and SgL (at 0.62M NH_4Cl) multilayers were also grown on type I substrates from CeO_2 -the $\text{PAA}_{2k}/\text{PDDAC}$ pair. Both AFM images show the presence of NPs. But more accurate electrochemical investigations are needed to understand the effect of the hybrid multilayered coatings in the protection of Al alloys.

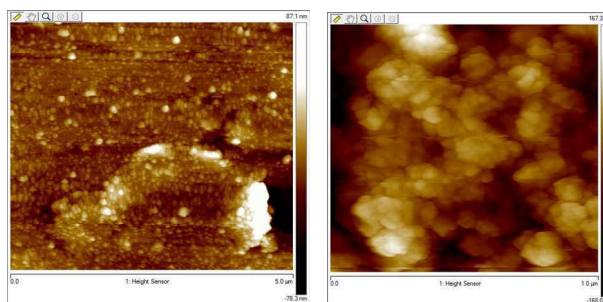


Figure 5.10: AFM images of $\text{CeO}_2\text{-PAA}_{2k}/\text{PDDAC}$ multilayer on type I substrate LbL (left) and SgL (right)

Estimation of the adsorbed ceria amount

The goal of this experiment was to determine the amount of ceria NPs adsorbed as individual entities, within clusters or multilayers on any substrate via UV-Vis spectroscopy. From many trial experiments, it was found that 10M HCl dissolves ceria NPs completely. In a separate experiment, few drops of “bare ceria NPs” stock solution (10 wt %) were allowed to dry on two model substrates: hydrophobic polypropylene and hydrophilic glass.

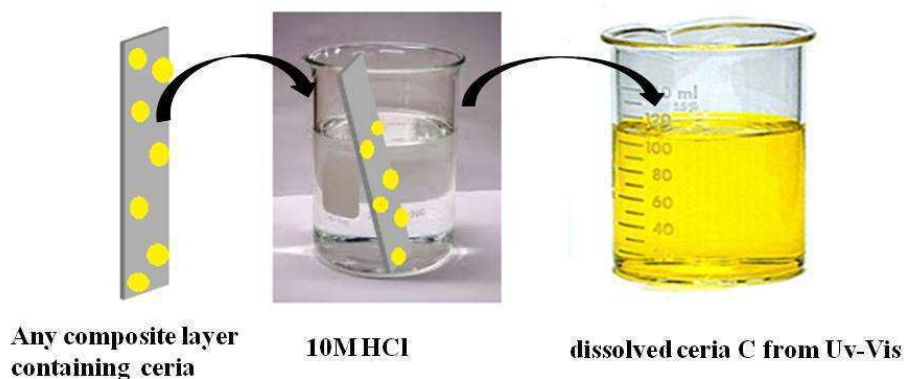


Figure 5.11: Schematic representation of the estimation of adsorbed amount of ceria NPs onto a given substrate.

After complete drying, the two substrates were separately immersed into a “known” volume of 10M HCl solution and allowed to rest for 1 day until complete dissolution of adsorbed ceria. Both solutions containing dissolved ceria were then subjected to UV-visible spectroscopy to cross-check the amount deposited on each substrate. The rather concentrated “unknown” solutions were first diluted and compared with calibration curves performed in 10M HCl. The amount of ceria dissolved in the acidic solutions was “determined” as a

Applications

function of concentration using extinction coefficient from the linear curve of absorption. The “determined” amount of ceria from UV-Vis was in close agreement within 20% with the “known” deposited amount. Measurement errors depend on various factors such as the dilution steps and the nature of the substrates.

This simple experiment can in principle estimate the amount of ceria NPs deposited on any substrate or hollow structure by dissolving the NPs material under any form into 10M HCl solution followed by rapid UV-Vis characterizations.

Carbon nanotubes system

Conductive properties

Table I and II shows the surface resistivity measured from the multilayered films of covalent and wrapped MWCNTs. The measured values indicate that the resistivity does not appear to be a linear function of number of bilayers for both LbL assembled PET films. This is due to the fact that the MWCNTs are inhomogeneously distributed within the films. Furthermore, the measurements were carried out on only 2 points where the tubes might have not been percolated. In agreement with the literature reports, the best way to increase the conductivity of the substrate is to improve the interconnectivity as well as the homogeneity of the film by establishing covalent bonds between the layers^[25, 26].

No of layers	(wPAA/wPEI) ₁	(wPAA) ₂ /(wPEI) ₁	(wPAA/wPEI) ₂	(wPAA) ₃ /(wPEI) ₂	(wPAA/wPEI) ₃
Resistivity (MΩ.□)	>100	37	>100	>100	1.86

Table 5.1: Resistivity of PET films fabricated from wrapped MWCNTs.

No of layers	(COOH/NH ₂) ₁	(COOH) ₂ /(NH ₂) ₁	(COOH/NH ₂) ₂
Resistivity (MΩ.□)	>100	0.19	1.18

Table 5.2: Resistivity of PET films fabricated from short ligands functionalized MWCNTs.

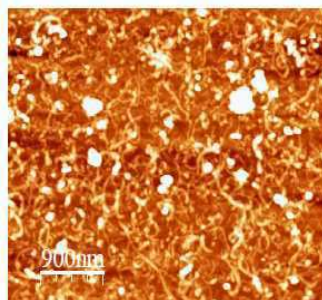


Figure 5.12: AFM image of percolated carbon nanotubes for a bilayer of MWCNT-COOH/MWCNT-NH₂

The COOH and -NH₂ functional groups (present in both pairs investigated) are well known to form covalent amide bond with heat treatment^[25] (see chapter 4). This cross-linking approach can provide better conductivity for both substrates. Unfortunately, due to lack of time we have not performed conductivity measurements on the cross-linked all-MWCNT thin films (MWCNT-COOH/MWCNT-NH₂)₁₆ fabricated in chapter 4.

On the other hand, the transparent film based on the short ligands functionalized MWCNTs (without cross-linking) exhibited resistivity of 100 kΩ.□ for 2 bilayers due to the percolated nanotubes network as shown in the Figure 5.12. This is much better than for wrapped MWCNTs composites, where the $\rho = >100 \text{ M}\Omega.\square$ for 2 bilayers. The reduced conductivity of wrapped composites is due to the non-conductive nature of the encapsulating PEs creating insulating barrier between the tubes reducing then the conductivity together with inhomogeneity. As mentioned earlier however, the heat treatment can increase the conductivity through the formation of covalent amide bonds between the layers, a result seen by Park *et al.*,^[26] for ester modified MWCNTs/PAH.

In the future this cross-linking approach can be extended for covalent MWCNTs BBs as well. Beyond, it gives some mechanical integrity to the film as seen in chapter 4. The other way to increase the conductivity is to use conducting PEs instead of non-conducting PEs, for surface functionalization of MWCNTs, as reported by Yang *et al.* Conducting PEs such as PANI, poly(phenylenevinylene) PPV could be the better alternatives in future^[36, 37].

Conclusions

Superhydrophilic and *almost*-superhydrophobic surfaces with extra anti-UV benefits were developed from oppositely charged *stable* ceria NPs via SgL through a combination of wetting and texturation.

Furthermore, nanoceria based coatings were carried out on aluminium foils to impart anti-corrosion protection. Preliminary investigations based on AFM analyses showed that a more efficient adsorption of anionic nanoceria on *Al*-substrates occurred in the presence of NH_4Cl salt; a rather unexpected result that highlights the importance of local basicity induced by the salt near the Al surface favouring the adhesion via H-bonding and subsequent anti-corrosive feature. Some electrochemical experiments are however needed to confirm this trend and shed some light on the exact mechanism at play.

Different *LbL* assemblies of *All*-MWCNTs were carried out on PET transparent substrates. Short ligand functionalized tubes showed interesting results with relatively low surface resistivity and the possibility to establish covalent bonds to improve even further the trend. The non conductive nature of regular PEs hinders the building of an effective conducting network and pledge for the development of CNT encapsulated with conjugated polymers.

Although further works are needed in the future, these encouraging preliminary experiments highlight the potential of both *LbL* and SgL growth to generate multilayers with diverse functionalities through simple and recyclable waterborne approaches.

References

1. Wojcik, A.B. and M. Messer, *Hybrid Glass as Protective Coating for Aerospace Optical Fibers and Cables: Validation Test Results*. Molecular Crystals and Liquid Crystals. **521**(1): p. 120-125.
2. Soutar, A.M., et al., *Mechanical and electrochemical properties of hybrid sol-gel protective coatings for copper substrates*. SIMTech technical reports, 2005. **6**(1): p. 50.
3. Schottner, G., *Hybrid Sol-Gel-Derived Polymers: Applications of Multifunctional Materials*. Chemistry of Materials, 2001. **13**(10): p. 3422-3435.
4. Xu, Q.F. and J.N. Wang, *A superhydrophobic coating on aluminium foil with an anti-corrosive property*. New Journal of Chemistry, 2009. **33**(4): p. 734-738.
5. Jung, Y.C. and B. Bhushan, *Mechanically Durable Carbon Nanotube-Composite Hierarchical Structures with Superhydrophobicity, Self-Cleaning, and Low-Drag*. ACS Nano, 2009. **3**(12): p. 4155-4163.
6. Cebeci, F.C., et al., *Nanoporosity-Driven Superhydrophilicity: A Means to Create Multifunctional Antifogging Coatings*. Langmuir, 2006. **22**(6): p. 2856-2862.
7. Rogach, A.L., et al., *Layer-by-Layer Assembled Films of HgTe Nanocrystals with Strong Infrared Emission*. Chemistry of Materials, 2000. **12**(6): p. 1526-1528.
8. Sorensen, P.A., et al., *Anticorrosive coatings: a review*. Journal of Coatings Technology and Research, 2009. **6**(2): p. 135-176.
9. Pagliaro, M., R. Ciriminna, and G. Palmisano, *Silica-based hybrid coatings*. Journal of Materials Chemistry, 2009. **19**(20): p. 3116-3126.
10. Yuan, S.J., et al., *Inorganic-Organic Hybrid Coatings on Stainless Steel by Layer-by-Layer Deposition and Surface-Initiated Atom-Transfer-Radical Polymerization for Combating Biocorrosion*. ACS Applied Materials & Interfaces, 2009. **1**(3): p. 640-652.
11. Steinsmo, U. and J.I. Skar, *Factors Influencing the Rate of Cathodic Disbonding of Coatings*. Corrosion, 1994. **50**(12): p. 934-939.
12. Sorensen, P.A., et al., *Influence of substrate topography on cathodic delamination of anticorrosive coatings*. Progress in Organic Coatings, 2009. **64**(2-3): p. 142-149.
13. Kendig, M., et al., *Role of hexavalent chromium in the inhibition of corrosion of aluminum alloys*. Surface and Coatings Technology, 2001. **140**(1): p. 58-66.
14. Kalenda, P., *Anticorrosion pigments and derived coating systems on their basis*. Dyes and Pigments, 1993. **23**(3): p. 215-223.
15. Aramaki, K., *A self-healing protective film prepared on zinc by treatment in a Ce(NO₃)₃ solution and modification with Ce(NO₃)₃*. Corrosion Science, 2005. **47**(5): p. 1285-1298.
16. Hamdy, A.S., *Advanced nano-particles anti-corrosion ceria based sol gel coatings for aluminum alloys*. Materials Letters, 2006. **60**(21-22): p. 2633-2637.
17. Schem, M., et al., *CeO₂-filled sol-gel coatings for corrosion protection of AA2024-T3 aluminium alloy*. Corrosion Science, 2009. **51**(10): p. 2304-2315.
18. Yue, X., L. Yingjie, and L. Sha, *Preparation and Characterization of Sol-Gel Coatings Doping with Cerium Ingredients on Aluminum Alloy Surface*. Journal of Rare Earths, 2007. **25**, (0): p. 193-196.
19. Zhang, D., et al., *Transparent, Conductive, and Flexible Carbon Nanotube Films and Their Application in Organic Light-Emitting Diodes*. Nano Letters, 2006. **6**(9): p. 1880-1886.
20. Small, W.R., et al., *Inkjet deposition and characterization of transparent conducting electroactive polyaniline composite films with a high carbon nanotube loading fraction*. Journal of Materials Chemistry, 2007. **17**(41): p. 4359-4361.
21. Gruner, G., *Carbon nanotube films for transparent and plastic electronics*. Journal of Materials Chemistry, 2006. **16**(35): p. 3533-3539.
22. Schnorr, J.M. and T.M. Swager, *Emerging Applications of Carbon Nanotubes* Chemistry of Materials, 2011. **23**(3): p. 646-657.

Applications

23. Zhang, M., et al., *Strong, Transparent, Multifunctional, Carbon Nanotube Sheets*. Science, 2005. **309**(5738): p. 1215-1219.
24. Yu, X., et al., *Carbon nanotube-based transparent thin film acoustic actuators and sensors*. Sensors and Actuators A: Physical, 2006. **132**(2): p. 626-631.
25. Lee, S.W., et al., *Layer-by-Layer Assembly of All Carbon Nanotube Ultrathin Films for Electrochemical Applications*. Journal of the American Chemical Society, 2008. **131**(2): p. 671-679.
26. Park, H.J., et al., *Preparation of Transparent Conductive Multilayered Films Using Active Pentafluorophenyl Ester Modified Multiwalled Carbon Nanotubes*. Langmuir, 2008. **24**(18): p. 10467-10473.
27. Zhang, L., et al., *Rapid and substrate-independent layer-by-layer fabrication of antireflection- and antifogging-integrated coatings*. Journal of Materials Chemistry. **20**(29): p. 6125-6130.
28. Goharshadi, E.K., et al, S. Samiee, and P. Nancarrow, *Fabrication of cerium oxide nanoparticles: Characterization and optical properties*. Journal of Colloid and Interface Science, 2011. **356**(2): p. 473-480.
29. Li, X. and J. He, *In situ Assembly of Raspberry- and Mulberry-like Silica Nanospheres toward Antireflective and Antifogging Coatings*. ACS Applied Materials & Interfaces. **4**(4): p. 2204-2211.
30. Ling, X.Y., et al., *Stable and Transparent Superhydrophobic Nanoparticle Films*. Langmuir, 2009. **25**(5): p. 3260-3263.
31. Zhai, L., et al., *Stable Superhydrophobic Coatings from Polyelectrolyte Multilayers*. Nano Letters, 2004. **4**(7): p. 1349-1353.
32. Soeno, T, I., K and Shiratori, S, *Ultra Water-Repellent Surface Resulting from Complicated Microstructure of SiO₂ nano particles*. Trans Mater Res Soc Jpn, 2003. **28**(4): p. 1207.
33. Ishizaki, T., Y. Masuda, and M. Sakamoto, *Corrosion Resistance and Durability of Superhydrophobic Surface Formed on Magnesium Alloy Coated with Nanostructured Cerium Oxide Film and Fluoroalkylsilane Molecules in Corrosive NaCl Aqueous Solution*. Langmuir. **27**(8): p. 4780-4788.
34. Koch, K. and W. Barthlott, *Superhydrophobic and superhydrophilic plant surfaces: an inspiration for biomimetic materials*. Philosophical Transactions of the Royal Society A: Mathematical, Physical and Engineering Sciences, 2009. **367**(1893): p. 1487-1509.
35. Karakoti, A.S., et al., *PEGylated Nanoceria as Radical Scavenger with Tunable Redox Chemistry*. Journal of the American Chemical Society, 2009. **131**(40): p. 14144-14145.
36. Xu, J., et al., *Synthesis and characterization of HCl doped polyaniline grafted multi-walled carbon nanotubes core-shell nano-composite*. Journal of Materials Science: Materials in Electronics, 2009. **20**(6): p. 517-527.
37. Ago, H., et al., *Composites of Carbon Nanotubes and Conjugated Polymers for Photovoltaic Devices*. Advanced Materials, 1999. **11**(15): p. 1281-1285.

Chapter 6: Conclusions and perspectives

Herein we summarize all the results obtained during the course of this Ph.D together with some perspectives of this work.

General conclusions

The main objective of this work was to generate versatile organic-inorganic hybrid functional layers at a fluid/solid interface via a novel Surface grown Layers or SgL approach through the salt triggered co-assembly of large variety of highly stable and oppositely charged building blocks. In this framework, highly stable cationic and anionic cerium oxide & silica nanoparticles, carbon nanotubes and polyelectrolytes were used as elementary building blocks in order to take advantage of their unique properties and potential applications in many fields.

At first we have investigated the *fundamentals of electrostatic complexation* (in chapter 1) between *pure* and oppositely charged PEs of asymmetric (weak/strong PEs) and symmetric (weak/weak, strong/strong PEs) systems with the help of the “desalting transition” process together with ITC experiments to gain more insight into the mechanism of inter polyelectrolyte complex formation (IPEC). The “desalting transition” concept was then successfully translated into *stable* colloids in chapter 3.

The “desalting transition” pathway triggered the electrostatic complexation at a critical salt concentration (I_b) between oppositely charged PEs of symmetric and symmetric for all pairs investigated and independently of their intrinsic features suggesting its universal character. The salt concentration required to completely turn off the electrostatic interaction for symmetric systems was higher than for asymmetric ones. Furthermore, salt acted as an efficient parameter to screen/tune the interaction when the complexation was solely driven by electrostatic forces. A neat split/spread in I_b was noticed between asymmetric and symmetric systems. The exact reason behind this split is beyond the scope of this work and deserves certainly more investigations in near future.

Nevertheless the I_b and sizes of the “organic” aggregates were found to strongly depend on the M_w and the nature of the PEs (block/homoPEs, weak/strong system and architecture such as linear or branched chains). Particularly, the complexation of weak PAA and *b*PEI chains was a two stages process corresponding to ion-pair and large aggregates

Conclusions & perspectives

formation. The *b*PEI conformation/architecture played an important role in shifting down the I_b .

Preliminary ITC experiments showed that the complexes formation was driven by entropy in all cases. Enthalpy in addition to entropy however participated to minimize the free energy of the complexation in symmetric systems (exotherms) suggesting the presence beyond the sole electrostatic interaction of secondary forces such as hydrophobic and/or hydrogen bonding. Indeed, the IPEC formation of the asymmetric system (PAA/PDDAC) was purely endothermic and consequently driven by the sole entropy associated with the counter ions (and water molecules) release. In the case of symmetric systems (PAA/*b*PEI & PSS/PDDAC), the IPEC formation was mainly exothermic indicating the contribution of secondary forces (hydrophobic & hydrogen bonding...) to the minimization of the free energy.

ITC experiments performed on the PAA/*b*PEI system have shown a two step process well in line with what was found through light scattering experiments. The absence of an end point in the the PAA/*b*PEI complex formation suggested that attention must be paid to estimate the effective charge ratio and pH at a given concentration to derive useful thermodynamic parameters. Finally, desalting and ITC experiments put forward that beyond electrostatic forces, secondary interactions play a key role in the IPEC formation.

In chapter 2, highly stable cationic & anionic hybrid nanoscale building blocks composed of inorganic nanomaterials such as cerium oxide, silica nanoparticles (NPs) or carbon nanotubes as core and cationic *b*PEI or anionic PAA as corona were formulated. The surface functionalization of inorganic nanomaterials with PEs improved their stability over a wide range of pH and ionic strengths (4M) via an efficient electro-steric stabilization.

Anionic ***cerium oxide nanoparticles*** (CNPs) were formulated by electrostatic (and coordination) adsorption of PAA_{2k} chains onto the surface of bare NPs via a direct precipitation-redispersion mixing protocol. Cationic *b*PEI functionalized CNPs were synthesized from anionic CNPs through the formation of covalent amide bonds by the robust carbodiimide chemistry via combination of a “*grafting to*” with a “*direct mixing*” approach.

FT-IR and NMR spectroscopic experiments gave strong evidences for the covalent attachment of *b*PEI_{25k} chains to the PAA corona of CPAA_{2k} NPs. Electrophoretic mobility

Conclusions & perspectives

showed that both cationic and anionic composites were stable under a broad range of pH. Furthermore PAA functionalization dramatically altered the IEP of inorganic materials towards lower pH, while the pKa of PAA chains was slightly shifted to lower pH values by CNPs. Light scattering experiments determined the differences in Mws, R_{HS} and the number of polymer chains per particle [$N_{ads} = 40$ PAA chains/CeO₂ NP].

Furthermore, TGA experiments have shown that 57% and 20% of CNPs were respectively present in anionic and cationic composites and allowed to determine the number of polymer chains grafted per NPs in the case of *b*PtEI chains coated NPs [$N_{ads} = 3$ *b*PtEI chains/CPAA_{2k}]. Excellent stability in high ionic strength up to 4M was exhibited by both PAA and *b*PtEI coated nano ceria. We then took advantage of this high saline stability to trigger the electrostatic co-assembly of such oppositely charged NPs in chapter 3.

In the past years, the dispersibility issues of CNTs were overcome via functionalization. Herein, for the first time, besides the sole dispersion in aqueous medium, we have shown a special concern on their stability features towards high ionic strength, an important criterion required to generate CNTs based functional surfaces. The impact of functionalization strategy as well as the features of the dispersants on MWCNTs stability was investigated using short ligands and charged macromolecules through both covalent and non-covalent grafting strategies.

The covalent attachment of short ligands such as carboxyl and amine groups via amide bonds to the oxidized CNTs tube surface were confirmed by cross FT-IR and DDLS experiments. In both cases, the occurrence of destabilization even under moderate concentration of salt (10⁻³M) indicated that the charge density, an essential parameter to get electrostatically stabilized dispersions, was not enough to exert a sufficient repulsion to overcome strong attractive van der Waals forces. This observation triggered the use of charged macromolecules and their electrosteric stabilization potential.

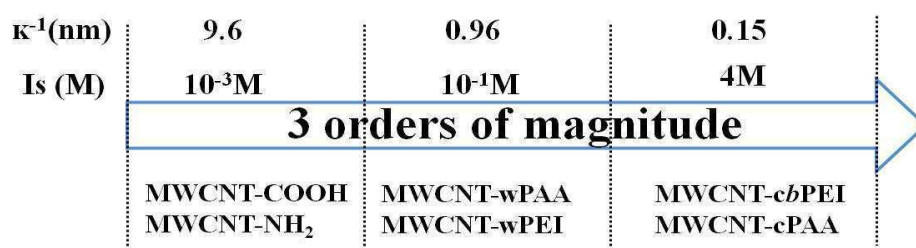
Non covalent MWCNTs-PEs composites were fabricated with the help of ultrasonication via the wrapping of cationic or anionic PEs over bare pristine CNT tubes. Significant FT-IR stretching bands together with increased tubes diameters measured by DDLS suggested a successful non-covalent functionalization of MWCNTs by PEs. Estimation of the final M_w of the macromolecules at the end of ultrasonication treatment step highlighted the key role of charges and PEs M_w on the dispersion stability. Indeed, large M_w

Conclusions & perspectives

PEs caused aggregation likely through bridging, whereas short chains were unable to fully wrap tubes surfaces.

Stability of non covalent CNT composite dispersions were improved up to two orders of magnitude (10^{-1}M) as compared to MWCNT-COOH and MWCNT-NH₂. The addition of salt during the wrapping step transiently (24 hrs) improved the stability up to 1M. The appearance of precipitation after 1 day suggested that long term stability could be efficiently accomplished by the covalent attachment of PEs to the surface of the MWCNTs.

Finally anionic PAA_{5k} and cationic *b*PEI_{25k} chains were covalently tethered on aminated and oxidized tubes respectively via amide linkage mediated by carbodiimide cross linkers. FT-IR and ¹H NMR characterization confirmed the successful covalent attachment of anionic and cationic PEs onto their respective parent tubes. DDLs and TEM experiments gave strong evidences for the presence of PEs chains on the tubes surface as shown by increased diameters. Furthermore nanocomposite solutions exhibited excellent stability in high ionic strength up to 4M of NH₄Cl for many months without any precipitation. Our observations allow to conclude that covalent attachment of weak anionic and cationic PEs is then a reliable way to generate stable CNT BBs. This stability aspect made CNTs as suitable candidates to fine tune their electrostatic interaction with other stable and oppositely charged BBs.



Stable *silica nanoparticles* were formulated by grafting PAA chains onto the APTES functionalized silica nanoparticles via amidation reaction mediated by carbodiimide cross linkers. Probing techniques confirmed the covalent attachment of anionic PAA chains onto the SiO₂-NH₂ NPs. Covalent grafting of PAA chains enhanced the stability of silica NPs under a wide pH and ionic strength (4M) range. The high stability of SiO₂-PAA_{5k} NPs triggered their use in electrostatically co-assembled structures with other oppositely charged stable building blocks. We have synthesized as well cationic *b*PEI functionalized silica NPs

Conclusions & perspectives

from anionic silica NPs. Their characterization was not entirely performed however by lack of time and will be achieved in the near future.

In *chapter 3*, we have investigated the bulk “desalting transition” approach using various stable & oppositely charged hybrid materials developed in chapter 2. The successful outcome proved that the desalting transition foreseen in chapter 1 for pure PEs was successfully translated into stable colloids. For the first time, we have shown that a fine tuning of electrostatic complexation was possible between *all*-nanoparticles/nanotubes hybrid systems.

As in chapter 1, the I_b value of each asymmetric and symmetric hybrid set put under scrutiny was found to differ according to the features of the interacting BBs such as their weak or strong character, architecture, M_{ws} and nature of the functional groups along the PE backbone. Stable and finite sized non-stoichiometric ($Z \neq 1$) electrostatic clusters were obtained for all the hybrid systems when one of the interacting components was weak PEs. Robotic experiments performed on asymmetric system have shown that I_b is indeed independent of the building blocks. In agreement with chapter 1, the complete “electrostatic” screening of oppositely charged components was possible when no secondary forces such as H-bonding or hydrophobic effect were at play in the complexation. Indeed, our experiments showed that H-bonding plays an essential role in the weak/weak PEs complexation where the interaction depends on the proton donor-acceptor characteristics of amine and acid functional groups. However, in some pairs the H-bonds formation at high I_s were controlled by the presence and nature of inorganic nanoparticles/tubes and the protonation state of functional groups induced by the added salt.

In line with the above discussions, in the asymmetric CPAA/PDDAC system the CeO_2 -PAA NPs in the presence of 1M of NH_4Cl are forbidden to engage hydrogen bonding with water, thereby allowing the NPs to interact strongly with PDDAC chains via electrostatic interaction during dilution as suggested by a slightly higher I_b value as compared to the pure PAA/PDDAC pair.

“*Real*” dormant solutions at I_0 were only obtained for symmetric systems of oppositely charged ceria NPs, MWCNT-*cb*PEI_{25k}/PAA_{2k} and SiO_2 -PAA_{5k}/ ℓ PEI_{2k}, where H-bonding interactions were not favored by protonated PAA and PEI chains. In the last pair, the lack of $-NH_2$ groups not only banned the H-bonding interactions at 4M but also generated

Conclusions & perspectives

relatively small and finite sized *reversible* hybrid complexes due to the weak interacting nature of $-NH$ in ℓPEI_{2k} . In case of oppositely charged covalent MWCNT-cPEs nanocomposites and SiO_2 -PAA_{5k}/*b*PEI_{25k}, H-bonding interaction even at I_0 was triggered by a large number of repeating units in both weak PEs, although they were rigid and protonated. This attribute put forward that H-bonding formation not only depends on the protonation states of the complementary functional groups but also on the M_w of the interacting PEs.

All these interesting bulk co-assembly features were then successfully transferred in chapter 4 to a substrate/solution interface in order to generate functional hybrid surfaces with unique properties and applications.

In *chapter 4*, we have grown hybrid functional layers at a solution/substrate interface both via conventional *LbL* and novel *SgL* approach through the interfacial electrostatic complexation of different oppositely charged hybrid materials formulated in chapter 2. The growth of the layers was monitored by QCM technique.

In a first part, the classical “electrostatic” Layer-*by*-Layer (*ELbL*) sequential adsorption method mostly used in the literature to grow *all*-organic PEs layer was taken here as a benchmark and helped us to generate organic/inorganic thin coatings. Beyond the nature and shape of the inorganic BBs, different key processing parameters such as pH and ionic strength of the solution and PEs nature were investigated. The different growth regimes (exponential vs. linear growth), final adsorbed amounts and volume fractions of inorganic material were shown to depend on the strength of the intermolecular interaction (ionic strength), the nature of functional groups, architecture of the PEs and most critically on the pH (ionization/protonation state) at which the different sequential adsorptions were performed. Counter intuitively, the assembly pH should be set at a value where at least one of the two interacting “weak” BBs is not fully charged in order to promote acid-basic interactions more efficient to grow thicker multilayers than the sole electrostatic interaction.

In a second part, we have transferred the *bulk* desalting transition concept investigated in chapter 3 to a solution/substrate interface and put forward a new assembly method called Surface grown Layers (*SgL*). The growth is here triggered at the onset of the bulk transition by fine-tuning the ionic strength (I_s) of the dispersions and through suitable experimental conditions (static vs. dynamic growth). The growth can be stopped by setting back to higher salt concentration and further resumed through a new dilution step. Different key parameters specific to the *SgL* growth such as charge ratio, physical-chemistry of the bare substrate and

Conclusions & perspectives

nature of the PEs were investigated specifically on the CeO₂-PAA_{2k}/PDDAC system. Below the critical bulk ionic strength I_b , the initial growth rate of the layer was shown to depend on the value of I_s . Relatively “thick” hybrid layers can be fabricated from a reactive solution prepared at charge stoichiometry. Furthermore, thicker films can be developed in *dynamic* conditions where shear forces at play favor a higher (formation and further) adsorption of the complexes. Finally, in most situations studied here, the as grown multilayers were very stable and did not disassemble in high ionic strength solution as pure *LbL* PEs multilayers do usually.

Although these studies must deepen in the near future, the encouraging results have shown that the simple and novel SgL approach is a very versatile method to generate thick hybrid layers in one-step. The complementary use of both SgL and *LbL* approaches together with very stable hybrid BBs opens pathway to generate smart functional surfaces with varying morphology, properties and novel applications.

Finally, in *chapter 5*, some preliminary and potential applications of hybrid functional surfaces developed by both *LbL* and SgL were put forward.

Superhydrophilic and *almost*-superhydrophobic surfaces with extra anti-UV benefits were developed from reactive solutions of oppositely charged *stable* ceria NPs via SgL approach through a combination of wetting and texturation.

Furthermore, nanoceria based coatings were carried out on aluminium foils to impart anti-corrosion protection. Preliminary investigations based on AFM analyses showed that a more efficient adsorption of anionic nanoceria on *Al*-substrates occurred in the presence of NH₄Cl salt; a rather unexpected result that highlights the importance of local basicity induced by the salt near the Al surface favouring the adhesion via H-bonding and subsequent anti-corrosive feature. Some electrochemical experiments are however needed to confirm this trend and shed some light on the exact mechanism at play.

Different *LbL* assemblies of *All*-MWCNTs were carried out on PET transparent substrates. Short ligand functionalized tubes showed interesting results with relatively low surface resistivity and the possibility to establish covalent bonds to improve even further the trend. The non conductive nature of regular PEs hinders the building of an effective

Conclusions & perspectives

conducting network and pledge for the development of CNT encapsulated with conjugated polymers.

Although further works are needed, these encouraging preliminary experiments highlighted the potential of both LbL and SgL approach to generate hybrid multilayers with diverse functionalities through simple and recyclable waterborne approaches.

Future perspectives

Beyond the sole core of this manuscript, electrostatic complexation is a spontaneous and ubiquitous process that needs to be precisely understood in order to control and tune the self/co-assembly of oppositely charged nano-objects in many different scientific and technological fields as seen throughout this manuscript.

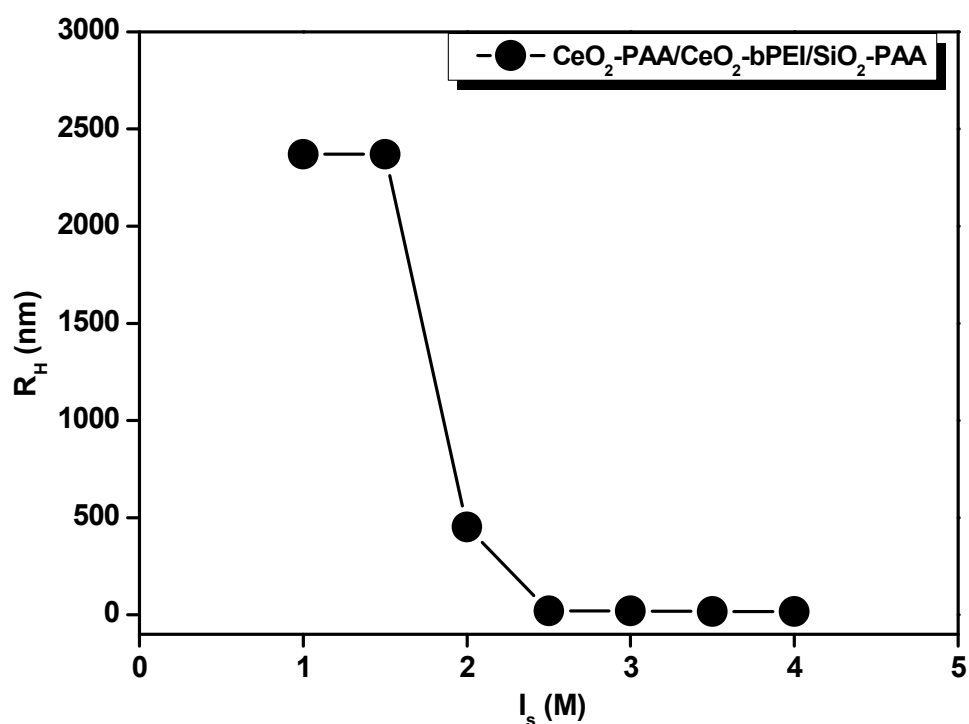
In chapter 1, our preliminary ITC experiments helped to understand the thermodynamics of PEs complex formation at low ionic strength. But in this thesis, as the electrostatic complexation was fine tuned through the ionic strength, in terms of future perspectives, it would be certainly very useful to perform the *salt triggered co-assembly process* via slow dilution directly inside an ITC cell. A way to better understand in general the mechanism(s) at play during the bulk desalting transition and in particular to study systematically the influence of both the ionic strength and the presence of secondary forces on the self/co-assembly thermodynamics.

In particular, as mentioned several times in chapter 1 & 3, H-bonding and hydrophobic interaction play a key role in the assembly process beyond the sole electrostatic forces. In the case of the PAA/bPEI pair, a system less documented in the literature, the real forces behind the complex formation has not been fully understood. During the course of the slow dilution, whether sole electrostatic forces or H-bonding or both are triggering the co-assembly? In order to sort things out, it is suggested to monitor the “desalting transition” of this specific pair through ITC in the presence of urea, a known H-bond breaker.

Furthermore, the split/spread in the critical ionic strength I_b observed in chapter 1 between asymmetric and symmetric systems is still mysterious and probably will deserve accurate and systematic “in-situ desalting transition” experiments as well.

Conclusions & perspectives

On a different perspective, unique properties of CNTs dragged them into different fields of applications. CNTs recently have been extensively used in drug delivery applications. LbL is a versatile and simple approach to fabricate stimuli responsive thin films based on carbon nanotubes for drug delivery. Several experimental and theoretical studies on the interaction of CNTs with DNA and nucleotide/DNA bases such as adenine, thymine, guanine and cytosine have been already performed. DNA base adenine intrinsically pair up with thymine via H-bonding, known as Watson-Crick base pairing principle. Based on this principle, we plan to covalently functionalize oxidized MWCNTs with adenine and thymine through the formation of amide bonds via carbodiimide cross-linkers or polyphosphate ester activation. Those nucleotide bases functionalized MWCNTs can then be used to build *specific interaction mediated* (H-bonding) multilayer thin films using LbL approach. The fabricated thin films envision to exhibit pH-dependent drug delivery properties.



The bulk and surface “desalting transition” investigated here have highlighted the formulation of *all*-nanoparticles/nanotubes hybrid clusters through the co-assembly of oppositely charged nanomaterials of the same type. The figure above shows a preliminary experiment on the complexation between hybrid materials of different types (functional CeO_2

Conclusions & perspectives

and SiO₂ NPs) through the bulk desalting transition process. Of course the structure of such hybrid clusters is unknown for the moment.

The salt triggered co-assembly of different types of hybrid materials provides the opportunity to formulate in a controlled way novel hybrid clusters carrying the intrinsic properties of different inorganic nanomaterials. Furthermore, it opens the way to generate/decorate functional substrates with a much larger variability and application range through the possible synergy between different BBs. For instance, functional surfaces will be generated in future from these co-assembled materials to show in the present case both anti-corrosive and superhydrophobic properties. In the same vein, it would be innovative to perform a bulk and surface complexation with 3 or more components with different aspect ratio (ceria, silica and CNTs that were developed in chapter 2 for example).

Finally, the novel SgL approach requires more investigations on the experimental conditions to fabricate “thick layers” (1 μm) and to figure out the exact mechanism behind the growth. Besides, the preliminary applications presented in chapter 5 must be investigated in great detail. The use of conjugated charged polymer can be a good idea to impart at the same time a high stability and a conductive nature to CNTs composite in order to develop easily thin and transparent conductive films. Anti-corrosive aluminum layers based on CNPs must be elaborated to understand the mechanism behind the anti-corrosive action. In order to fulfill the demand of ALCAN (end user), the SgL pathway to grow thick functional layers on Al substrate must be matured.

Appendix

Chapter 2

Appendix I

Polyethyleneimine functionalized Cerium oxide nanoparticles

Method I:

The anionic ceria nano particles were suspended as a powder in calculated amount of PEI of desired Mw. The pH of this mixture was adjusted to 8 with the help of HCl / NaOH. Slight turbidity was observed for all Mw. Despite, the synthesis was continued with the addition of aqueous solution of 2:2 equivalents of cross linkers (EDC/ NHS) calculated with respect to CPAA_{2k}. The reactant mixture was kept under stirring for 1 day at 50°C. The resulting yellow viscous liquid was precipitated in ethanol and centrifuged at 5000 rpm for 15 min to remove the unreacted PEI_x. This purification process was continued until the supernatant showed colorless solution with Ninhydrin reagent, which typically shows deep violet color with PEI_x. Afterwards, the paste (termed as CPEI_x) at the bottom of the centrifuge tube was collected and dried under vacuum to remove ethanol and finally dispersed in water. It resulted opaque solution due to presence of *large aggregates*. Those aggregates arose as the starting material (CPAA_{2k}) itself suspended in the aggregated form since they were introduced in their solid state. Therefore there was no individual dispersion of CPAA in PEI_x matrix even before the commencement of the reaction. As a result, functionalization of PEI_x has happened on aggregates of CPAA_{2k}. As the colloidal solution appeared turbid no other solution characterizations such as DLS and stability assessment were performed. FT-IR measurement on yellow paste CPEI_x (data not shown) proved that cationic polymer was successfully incorporated on particle surface. Although the chemistry was successful, one of the main needs of individual PEI functionalized nano particles were not reached. The synthesis was improved as follows to get stable dispersion.

Method II:

In order to avoid turbidity problems coming from the solid state dispersion, in this trial, CPAA_{2k} was handled in their solution state. The pH of the solution was adjusted to 8 with NH₄OH. As PAA chains are fully charged at this pH, unlike previous method, here the

Appendix

particles are distributed as individual colloids in aqueous medium before the reaction starts up. Functionalization on individual particles and it was carried out as follows.

The aqueous solution of CPAA_{2k} was added at one shot to the calculated amount of PEI_x (pH – 11.25) in the weight ratio of PAA to PEI_x of 1:40 (PEI_x was taken in excess since it could be removed by dialysis at the end). Sudden raise in pH and significant turbidity was noticed while stirring at room temperature for 15 min. The turbidity was slowly turned down to transparent when the pH of the reactant mixture was reset to ~8 from 11.1 with the drop by drop addition of 1M HCl. Appearance of transparency allows to further proceed with the addition of cross linkers as before. After stirring at 50°C for 24 hrs, the resulting intense yellow colored viscous liquid was precipitated with excess of ethanol and centrifuged, purified and dried as before. The dispersion of the resulting CPEI_x conjugates in water yielded slightly turbid solution for all Mw of PEI, with a comparatively better dispersion than in the previous method.

In the current method slight turbidity was caused by the presence of *small aggregates*. Those were formed as a consequence of sudden increase in pH of mixture to 11.1 while adding particle (pH 8) to polymer (pH 11.25). As a result of this drift, PAA were desorbed from the particle surface as there is no covalent bonds between PAA chains and ceria surface. Whilst the PAA uncovered particles tend to agglomerate and forms *small aggregates* due to the van der Waals attraction between them, indicated the appearance of a turbid solution. When the pH is readjusted to pH 8, the appearance of very slightly whitish transparent solution indicates that desorbed PAA chains were reabsorbed on *small aggregates*, because of their ability to form hydrogen bonds with ceria surface. But at the same time, those *small aggregates* will not turn back to individual NPs because of the irreversible process. Therefore PEI_x grafting takes place on *preformed small aggregates*. As the small clusters were in comparable size, filtration or centrifugation was not able to get rid of them. Hence the resulting solution appeared turbid and their colloidal stability was greatly influenced by an increase in pH and salt concentration.

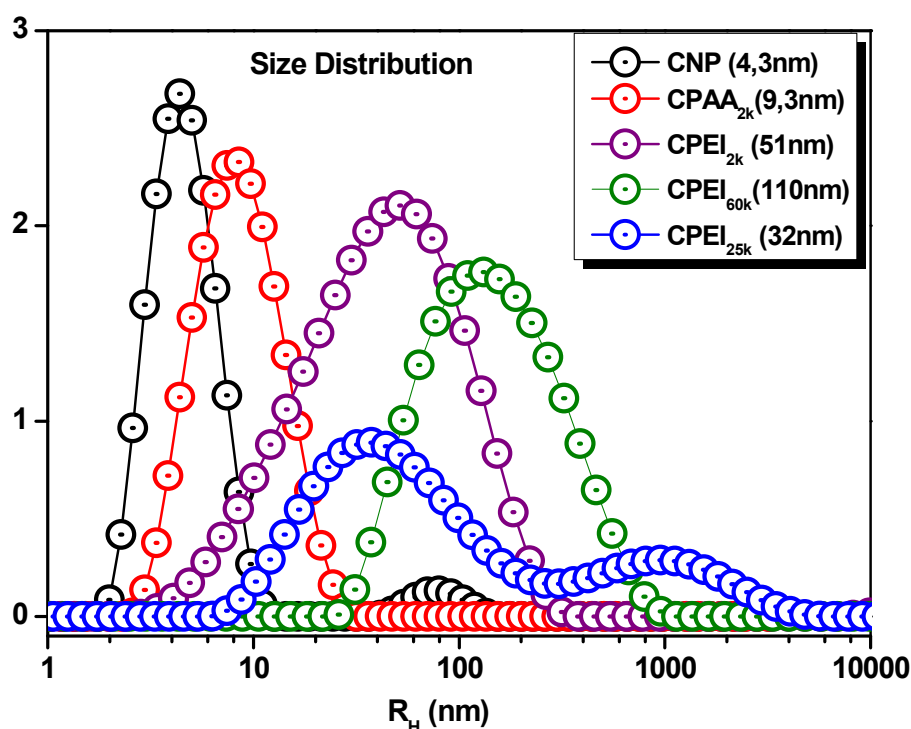


Figure 2A. 1 : DLS graph of Bare CNP (black), CPAA_{2k} (red), CPEI_x [$x = 2k$ (sky blue), 60k (green), 25k (blue)].

The above DLS measurements on colloidal solutions of CPEI_x proved that the hydrodynamic radii of resulting aggregates were larger than the expected value for individual wrapping with the corresponding polymers.

The increase in hydrodynamic radius of CPAA_{2k} in comparison with bare NPs was explained earlier (results & discussion of CPAA_{2k}). In case of CPEI_{2k}, the larger R_H (50 nm) than the corresponding contour length of PEI_x ($x = 2k$, ~10 nm) indicates the presence of aggregates. The situation is slightly different for large polyelectrolytes like PEI_{60k} and bPEI_{25k}, along with the aggregate formation coming from pH drift, where their large sizes can induce the wrapping of several small aggregates and destabilizing the dispersion. UV-Vis measurements determined that only 1 wt% of inorganic materials was present in the conjugate. This made Method II disadvantageous. The aggregate issue coming from pH drift was overcome by preadjustment of the pH of PEI with the help of HCl.

^1H NMR spectroscopy

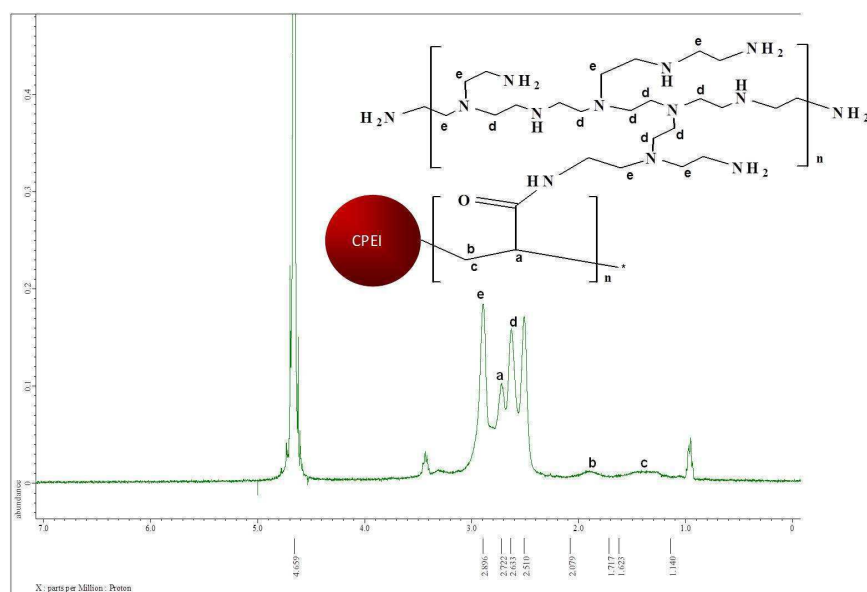


Figure 2A. 2 : ^1H NMR of of CPEI_{60k}

The ^1H NMR spectra is similar for all kinds of CPEI_x (spectra not shown for CPEI_{2k} and CPEI_{25k}). There is a small difference in the degree of modification of CPAA_{2k}. The shift of the peak from 2.5 ppm to 2.9 ppm indicates that successful formation of amide between CPAA_{2k} and PEI_x (detailed explanation is given below in NMR section of CPEI_{25kf}). But the intensity of acid peaks around 0.9-2.1 ppm, which normally should appear was very weak here due to the presence of low concentration of CPAA_{2k} as mentioned in the above section. From the integral value of all spectra recorded for other CPEI_x, it was determined that 80%, 70%, 75% of the carboxyl groups of CPAA_{2k} were modified with bPEI_{25k}, PEI_{2k} and PEI_{60k} respectively.

Appendix II

Polyethyleneimine functionalized silica nanoparticles

Various synthetic strategies were followed to obtain individual silica colloid encapsulated by bPEI_{25k}. The following section gives an overview of attempted methods. This might help in the future to develop a better dispersion.

Synthetic strategy I

Using aldehyde as linker

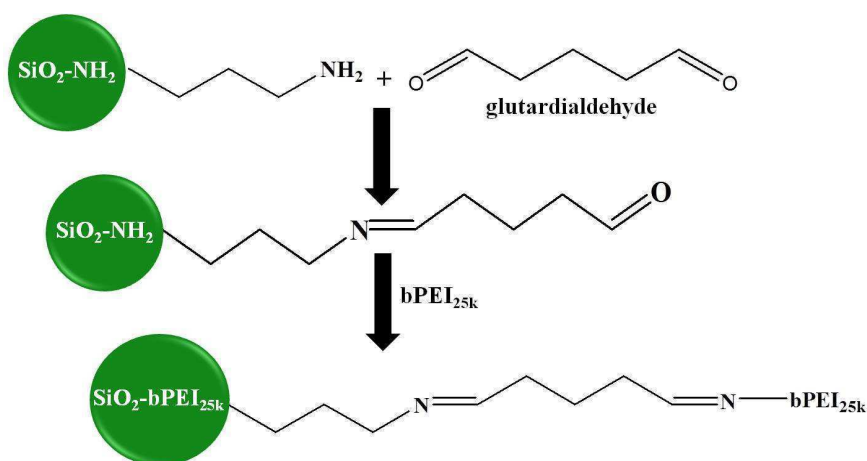


Figure 2A. 3 : *Synthesis of PEI functionalized silica nanoparticles via glutaraldehyde.*

Terminal amine groups of bPEI_{25k} were covalently functionalized with the surface amine groups of silica NPs via imine bonds using glutaraldehyde, a well known organic compound which cross links amine groups. The synthetic procedure is very similar to the method reported by McBain et al. The only difference is the Mw of PEI employed. In brief, APTES modified silica was three times washed with pyridine-HCl buffer. After the removal of buffer, the wet white powder was suspended in 5% glutaraldehyde and stirred at RT for three hours. The color of the solution turned from white to intense orange. At this stage the reason for such color change was not well understood. Bright colored particles were gently separated from the aldehyde solution with the help of magnet and washed again with buffer to remove any unreacted aldehyde. The particles bearing aldehyde were then suspended in aqueous solution of bPEI_{25k} and stirred at RT for 1 day. The loosely bound PEI chains were

Appendix

removed by simply washing the particles with water three times. The resulting orange paste was suspended in water and sonicated for 5 min to get homogenous dispersion. Unfortunately the particles were not dispersed well in both aqueous and organic solvents.

The formation of imine bond is generally indicated by the appearance of an orange color. But here the abnormal intense color change indicates that the aldehyde promoted the cross linking not only between the terminal amine groups of bPEI and surface amine groups of silica, but likely between individual NPs as they do possess amine functional groups. This inter particle association was indeed enhanced the formation of aggregates by aldehyde in excess.

Here we made several attempts with various concentrations of glutardialdehyde. The key of a successful functionalization is here a glutardialdehyde concentration very well optimized. In excess, it initiates the aggregation of the NPs. At low concentration, it limits the conversion from aminated silica to mono aldehyde, which further limits PEI functionalization. From many trials, we found that 0.5 equivalents of glutardialdehyde calculated with respect to amine moieties yielded a better result yet the presence of aggregates is notified by a slight color change. DLS measurements on the aqueous dispersion have shown an increase in R_H suggesting the individual functionalization. Whereas the broad second distribution curve with minimum intensity confirms the presence of aggregates. Unfortunately, the dispersion was not stable upon the addition of salt. More specifically the dispersion coagulated and precipitated beyond 0.5M NH_4Cl indicating likely an insufficient functionalization of the SiO_2-NH_2 NPs by the PEI chains.

In conclusion, synthesis of highly stable and individual silica nanoparticle functionalized by PEI chains based on the strategy I is very sensitive with respect to aldehyde concentration. The formation of aggregates by this method is inevitable as the aldehyde form imine bonds between the particles itself. Another strategy is put forward where no cross linkers are employed.

Synthetic strategy II

From TEOS

3 ml of TEOS was added at one shot to absolute ethanol. To which 3 ml of aqueous solution containing 1 ml of bPEI_{25k} (1 ml PEI in 3 ml) was added at one shot and kept for stirring at RT for 1 day. In order to remove free polymer chains, the suspension was

Appendix

centrifuged at 4000 rpm for 10 min. This purification process was continued until the supernatant gave a colorless solution with ninhydrin reagent. The white precipitate was dried and then suspended in water to make 0.1 wt% solution. The dispersion was then subjected to DLS and TEM characterizations.

In strategy I, PEI replaced NH_3 , a typical catalyst in silica NP formation. Whereas in strategy II, PEI acts as a base and catalyzes the hydrolysis and condensation of alkoxy silane. The main idea behind this replacement is that single NP functionalization by PEs chains can be achieved. Indeed if PEs functionalization occurs during the particle synthesis, they should easily get access and cover the particle surface.

But opposite results were observed from light scattering experiments. The measured R_H was about ~ 250 nm, which is quite larger than the contour length of the polymer chains, suggesting likely the aggregation of the NPs even though the PEs were used prior to particle formation. The reason may arise from the influence of the PEs chain length.

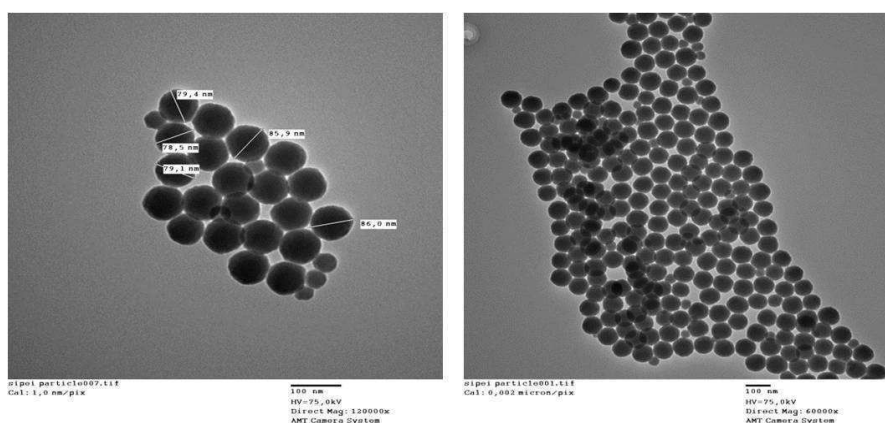


Figure 2A. 4 : HRTEM images of PEI functionalized silica nanoparticles from TEOS, high magnification (left), low magnification (right).

TEM experiment gave direct evidences for presence of aggregates. The sizes of aggregates measured from TEM images were however not in agreement with DLS. Indeed the size was much larger likely coming from the drying step known to enhance aggregation. Furthermore the size of NPs was also quite polydisperse due to the interruption of PEs during the nucleation and growth as explained in *one-pot synthesis* (introduction).

Chapter 3

Desalting transition via the Robotic platform on the $\text{CeO}_2\text{-PAA}_{2k}/b\text{PEI}_{25k}$ symmetric system

The sample preparation protocol is the same as for the $\text{CeO}_2\text{-PAA}/\text{PDDAC}$ system (chapter 3). The difference in this case is that strong and linear cationic PDDAC chains were replaced by weak and branched cationic $b\text{PEI}$ chains. As a result, the I_0 for separate stock solutions of $\text{CeO}_2\text{-PAA}$ and $b\text{PEI}$ at 1 wt% was set to 4M with the addition of NH_4Cl .

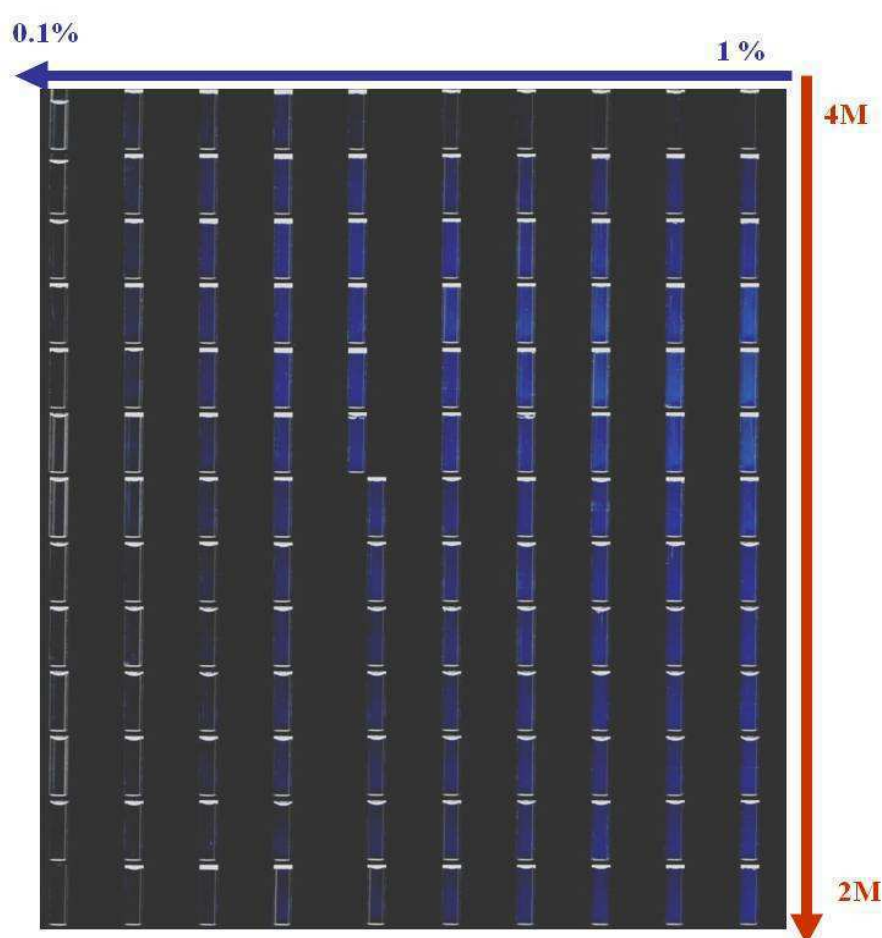


Figure 3A.1: Phase diagram of $\text{CeO}_2\text{-PAA}_{2k}/b\text{PEI}_{25k}I$. Top to bottom: I (M) = 4, 3.8, 3.6, 3.4, 3.2, 3, 2.8, 2.6, 2.4, 2.3, 2.2, 2.1, 2. Left to right: apparent c (%wt) = 0.1, 0.2, 0.3, 0.4, 0.5, 0.6, 0.7, 0.8, 0.9, 1.

Appendix

In step 2, separate solutions of CeO₂-PAA and *b*PEI at different *C* ranging from 0.1 wt% to 1 wt% (10 concentrations) were prepared by dilution of the respective stock solutions with DI water at the same *I*₀. The 2 solutions were then mixed at the same concentration and equal volume ratio to generate dormant solutions with concentration ranging from 0.1 wt% to 1 wt%. Step 3 was then performed in the robotic platform (Zinsser), where each dormant solution was sampled and later completed with pre-calculated volume of DI water, to generate formulation series with different *I*_s (M) (= 4, 3.8, 3.6, 3.4, 3.2, 3, 2.8, 2.6, 2.4, 2.3, 2.2, 2.1, 2). 10x13 =130 samples were obtained with different concentration and *I*_s. The robotic arm took the pictures of each sample for a period of 20 seconds and constructed the phase diagram as a function of *c* and *I*_s as shown in Figure 3.A.1.

Unfortunately, almost all the vials were whitish even at high *I*_s. At that time, the bulk complexation for the PAA/*b*PEI PEs pair was not performed yet and we were thinking that it should behave as PAA/*l*PEI pair, where *I*_b = 2.3M. The dilution was then only carried out from 4M to 2M. Later investigations on the PAA/*b*PEI system as explained in chapter 1 have shown that the whitishness was due to the formation of ion-pair complexes via the H-bonding interactions between weakly protonated –NH₂ groups of *b*PEI and –COOH groups of PAA. In future, dilution should be extended at least up to 1M to investigate the effect of the second transition (1.5M) on the size and stability of the complexes as a function of *c*.

Chapter 5

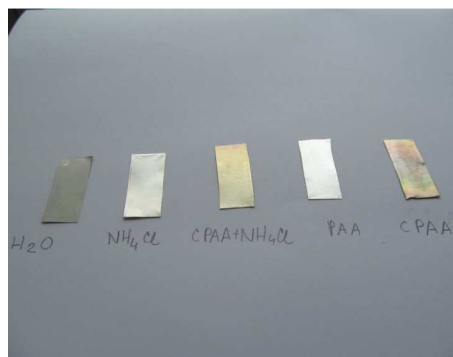


Figure 5A.1: Optical images of type II Al substrates (degreased and etched with KOH) after immersion into different solutions: water, 0.1M NH₄Cl, 0.1% CPAA + 0.1M NH₄Cl, 0.3% PAA and 0.1% CPAA

As seen in Figure 5A.1, type II substrates immersed into a CeO₂-PAA_{2k} +NH₄Cl dispersion gave a much more homogeneous and smooth appearance than type I substrates. This is due to the fact that the oxide layer on the top of the metallic substrate was uniformly distributed after KOH treatment. The uniform distribution plays a very important role in the corrosion protection.

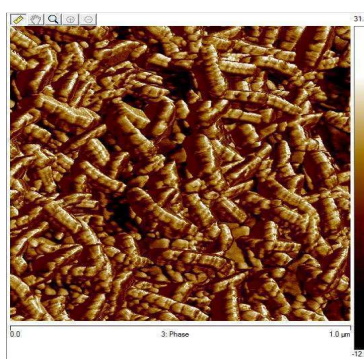


Figure 5A.2: AFM image of type III substrates without any coating material.

Figure 5A.2 evidences the formation of “thick oxide layer” on type III Al substrates treated with boiling water.

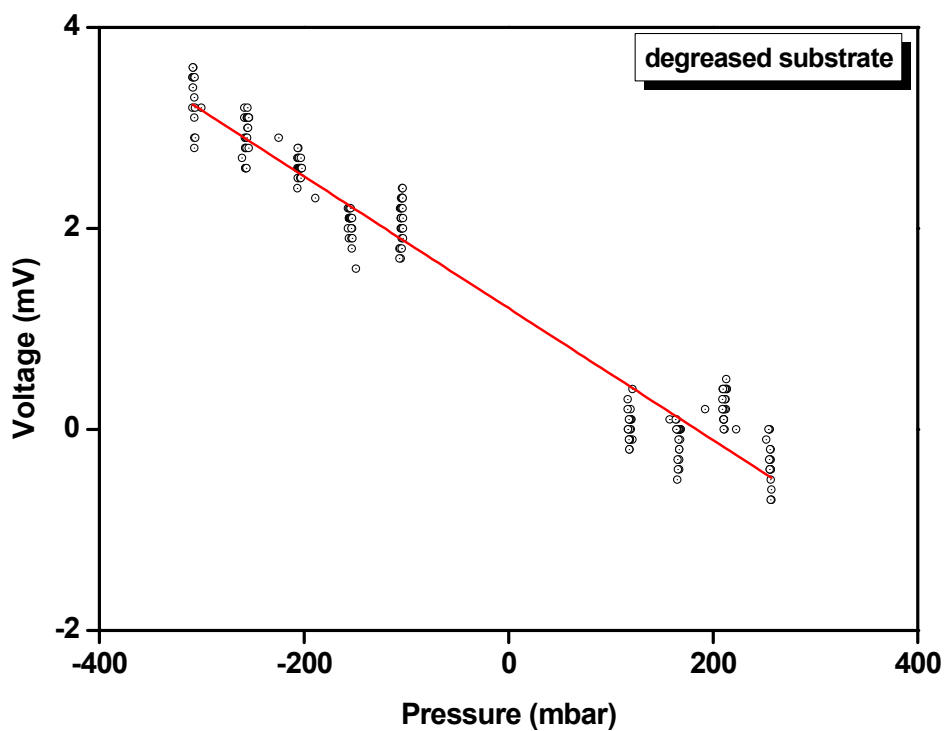


Figure 5A.3: *Generated potential difference ΔV as a function of the mechanical pressure difference ΔP driving the liquid flow on a type I substrate at pH 6 with 10mM NaCl.*

Figure 5A.3 clearly shows that type I substrate is negatively charged at pH 6 in the presence of 10mM NaCl indicating the presence of OH^- ions at the substrate.